Universidade do Estado do Rio de Janeiro
Centro de Tecnologia e Ciências
Instituto de Química

Nathalia Salles Vernin Barbosa

Poisson-Boltzmann equation and classical Density Functional Theory applied to electrolyte solutions: from biological systems to enhanced oil recovery

Rio de Janeiro
2019

Nathalia Salles Vernin Barbosa

Poisson-Boltzmann equation and classical Density Functional Theory applied to electrolyte solutions: from biological systems to enhanced oil recovery

Tese apresentada, como requisite parcial para obtenção de título de Doutor em Engenharia Química, ao Programa de Pós-graduação em Engenharia Química, da Universidade do Estado do Rio de Janeiro. Área de concentração: Processos Químicos, Petróleo e Meio Ambiente.

Orientadores: Prof. Dr. Eduardo Rocha de Almeida Lima

Prof. Dr. Frederico Wanderley Tavares

Rio de Janeiro

2019

CATALOGAÇÃO NA FONTE

UERJ / REDE SIRIUS / BIBLIOTECA CTC/Q

B238 Barbosa, Nathalia Salles Vernim.
Equação de Poisson-Boltzmann e teoria do funcional da densidade clássica aplicadas a sistemas eletrolíticos: desde sistemas biológicos até recuperação avançada de petróleo / Nathalia Salles Vernin Barbosa. – 2019.
204 f.

Orientador: Eduardo Rocha de Almeida Lima
Orientador: Frederico Wanderley Tavares
Tese (Doutorado) – Universidade do Estado do Rio de Janeiro. Instituto de Química.

1. Sistemas biológicos – Teses. 2. Eritrócitos – Teses. 3. Equação de Poisson-Boltzmann – Teses. I. Lima, Eduardo Rocha de Almeida. II. Tavares, Frederico Wanderley. III. Universidade do Estado do Rio de Janeiro. Instituto de Química. IV. Título.

bs CDU 577.3

Assinatura

08/04/2019

Data

Nathalia Salles Vernin Barbosa

Poisson-Boltzmann equation and classical Density Functional Theory applied to electrolyte solutions: from biological systems to enhanced oil recovery

Tese apresentada, como requisite parcial para obtenção de título de Doutor em Engenharia Química, ao Programa de Pós-graduação em Engenharia Química, da Universidade do Estado do Rio de Janeiro. Área de concentração: Processos Químicos, Petróleo e Meio Ambiente.

Aprovada em 18 de fevereiro de 2019.

Banca Examinadora:

Prof. Dr. Eduardo Rocha de Almeida Lima (Orientador)
Instituto de Química – UERJ

Prof. Dr. Frederico Wanderley Tavares (Orientador)
Universidade Federal do Rio de Janeiro

Dr. Lucas Gomes Pedroni
CENPES / Petrobras

Prof. Dr. Luciano Tavares da Costa
Universidade Federal Fluminense

Prof. Dr. Amaro Gomes Barreto Júnior
Universidade Federal do Rio de Janeiro

Prof. Dr. Pedro Henrique Rodrigues Alijó
0Instituto de Química – UERJ

Prof. Dr. Márcio Luis Lyra Paredes
Instituto de Química – UERJ

Rio de Janeiro

2019

DEDICATÓRIA

A meu pais, Verônica Salles e Paulo Roberto Rival, pelo amor, apoio e palavras sábias nos momentos mais difíceis da minha vida pessoal e profissional.

AGRADECIMENTOS

A Deus pela força e determinação para concluir mais uma etapa da minha vida profissional.

Aos meus pais, Verônica e Paulo Roberto, que tanto torceram por mim e me apoiaram em todas as decisões. Eles que sofreram com minha ausência durante o ano que estive nos Estados Unidos, mas nunca deixaram de me motivar mesmo a milhas de distância. Agradeço a eles pelo amor incondicional, carinho, conselhos, palavras; sem eles este sonho não seria possível.

À minha avó Terezinha e ao meu tio-avô José Francisco pelo carinho e amor.

Ao Leandro pelo amor e, principalmente, pela paciência ao longo desses anos. Ele que tantas vez ouviu que em um mês eu estaria mais tranquila; porém, esse tempo nunca chegou. Mas, ainda assim, sempre me apoiou e me deu forças nos momentos de exaustão e calma nos momentos de desespero.

Aos meus orientadores, Eduardo e Fred, pelo apoio, ensinamentos, disponibilidade e confiança depositada em mim desde o início desta caminhada. Eles foram fundamentais para meu amadurecimento profissional e pessoal.

Aos Drs. Edward Maginn e Yong Zhang pelos ensinamentos e orientação durante o período de doutorado sanduíche na Universidade de Notre Dame.

À Profª Lucienne Romanielo, que foi minha segunda mãe durante os meses de adaptação no exterior. Ela foi muito importante nesse processo, com suas palavras doces, coração maternal e pães de queijo e bolos mineiros.

Às minhas amigas Erika Queiros (*Casaquinho*), Marianne Teixeira e Danielle Valente pela amizade sincera.

Aos professores do PPGEQ/UERJ pelos conhecimentos transmitidos.

Aos grupos responsáveis pelo funcionamento e manutenção dos supercomputadores Santos Dumont, do Laboratório Nacional de Computação Científica, e Lobo Carneiro, do Núcleo de Atendimento a Computação de Alto Desempenho da COPPE/UFRJ, e ao "Center for Research Computing", da Universidade de Notre Dame, pelo suporte computacional.

Às agências de fomento FAPERJ e CNPq e à Petrobras pelo suporte financeiro.

RESUMO

BARBOSA, N. S. V. *Equação de Poisson-Boltzmann e teoria do funcional da densidade clássica aplicadas a sistemas eletrolíticos:* desde sistemas biológicos até recuperação avançada de petróleo. 2019. 204 f. Tese (Doutorado em Ciências em Engenharia Química) – Instituto de Química, Universidade do Estado do Rio de Janeiro, Rio de Janeiro, 2019.

As interações eletrostáticas desempenham um papel fundamental nos processos físicos, biológicos e químicos. Logo, o estudo de tais interações propicia um melhor entendimento de fenômenos contraintuitivos, além de nortear o desenvolvimento de novas soluções e estratégias em nível industrial. As técnicas utilizadas na modelagem de sistemas contendo eletrólitos podem ser classificadas em métodos implícitos, equações integrais e teoria do funcional da densidade clássica, métodos explícitos, e métodos híbridos. Nesta tese, utilizou-se a equação de Poisson-Boltzmann (PBE) e teoria do funcional da densidade clássica (DFT). Por meio da PBE, (i) avaliou-se a partição iônica transmembrana em um eritrócito com a inclusão das interações não eletrostáticas e do termo de Bohr, sendo possível contabilizar o efeito da mudança da constante dielétrica entre os meios intracelular e extracelular; (ii) investigou-se o comportamento elétrico da parede celular da bactéria *Bacillus brevis*, com a abordagem de regulação de carga no perfil de densidade volumétrica de carga fixa; e (iii) determinou-se o ângulo de contato e molhabilidade de um sistema constituído por três fases (dois líquidos e uma superfície sólida). Diferentemente dos dois primeiros sistemas, que possuem apelo biológico, o último foi desenvolvido visando a aplicação na recuperação avançada de petróleo por meio da injeção de uma solução eletrolítica aquosa. Além disso, um modelo baseado na DFT foi desenvolvido em domínio tridimensional com convoluções calculadas através da transformada de Fourier rápida e aplicado na análise da molhabilidade e ângulo de contato de um sistema caracterizado por salmoura/ hidrocarboneto/ rocha. A compreensão dos efeitos da injeção de água projetada é de suma importância para a recuperação de petróleo, uma vez que permite a seleção racional da composição desta água. Vale ressaltar, que essa aplicação da DFT para sistema líquido/ líquido/ sólido, assim como a inclusão do termo de Bohr na PBE e a abordagem volumétrica da regulação de carga são inovações na literatura, até onde se pôde rastrear. Conclui-se que o balanceamento das aproximações intrínsecas da PBE pode fazer com que as mesmas se anulem, promovendo uma excelente reprodução de dados experimentais, dependendo do sistema a ser estudado, como demonstrado na predição da partição iônica do íon Cl^-, que ocorre passivamente, no eritrócito e do potencial zeta da parede celular da bactéria *B. brevis*. Por outro lado, a DFT é primordial para sistemas complexos, tais como: sistemas confinados e com altas concentrações iônicas, uma vez que possui um maior nível de detalhamento.

Palavras-chave: Eletrólitos. Equação de Poisson-Boltzmann. Teoria do Funcional da Densidade. Interações não eletrostáticas. Teoria de Lifshitz.

ABSTRACT

BARBOSA, N. S. V. *Poisson-Boltzmann equation and classical Density Functional Theory applied to electrolyte systems:* from biological systems to enhanced oil recovery. 2019. 204 f. Tese (Doutorado em Ciências em Engenharia Química) – Instituto de Química, Universidade do Estado do Rio de Janeiro, Rio de Janeiro, 2019.

Electrostatic interactions play an indispensable role in physical, biological, and chemical processes. Therefore, the study of such interactions provides a better understanding of counterintuitive phenomena, as well as guiding the development of new solutions and strategies at the industrial level. The techniques used for modeling electrolyte systems can be classified as implicit methods, integral equations and classical density functional theory, explicit methods, and hybrid methods. In this thesis, the Poisson-Boltzmann equation (PBE) and the classical density functional theory (DFT) were used. At PBE level, (i) the transmembrane ion partition of an erythrocyte was evaluated through the inclusion of the non-electrostatic interactions and Bohr term, being possible to take into account the effects of the change in the dielectric constant between intra and extracellular environments; (ii) the electrical behavior of the *Bacillus brevis* cell wall was investigated with the charge-regulated volume bounded-charge density approach; and (iii) the contact angle and wetting of a three-phase system (two liquids and a solid surface) was determined. Unlike the former two systems, which have biological appeal, the latter was investigated aiming at the application in the enhanced oil recovery through the injection of an aqueous electrolyte solution. Furthermore, the DFT was developed in three-dimensional coordinates with convolutions calculated by the fast Fourier transform, and applied to the analysis of the wettability and contact angle of a system characterized by brine/ hydrocarbon/ rock. Understanding the effects of engineered water injection is of paramount importance to the oil recovery as it allows the rational selection of the composition of this water. It is worth mentioning that the application of DFT to study liquid/liquid/solid substrate system as well as the inclusion of the Bohr term in the PBE and the volumetric charge-regulated approach, as far as we could track, have not been performed in the literature. Finally, the balancing of the intrinsic approximations of the PBE might cancel them out, promoting an excellent reproduction of experimental data, depending on the system to be studied, as demonstrated in the prediction of the ionic partition of the Cl^- ion that occurs passively in the erythrocyte and zeta potential of *B. brevis* cell wall. On the other hand, the DFT is important to study complex systems, such as confined systems with high ionic concentrations, since it has a higher level of detail.

Keywords: Electrolyte. Poisson-Boltzmann Equation. Density Functional Theory. Non-electrostatic interactions. Lifshitz Theory.

LISTA DE FIGURAS

LISTA DE TABELAS

LISTA DE ABREVIATURAS E SIGLAS

3D-DFT	Tridimensional classical density functional theory
BFD	Bulk fluid density perturbation
BMCSL	Boublik-Mansoori-Carnahan-Starling-Leland equation of state
CCA	Contact-corrected approach
CSIII	Modified version of BMCSL
CD-MUSIC	Charge distribution multisite ion complexation
DCF	Direct correlation function
DFT	Classical density functional theory
DHH	Hole corrected Debye–Hückel theory
DIIS	Discrete inversion in iterative subspace
DLVO	Derjaguin-Laudau-Verwey-Overbeek theory
EDL	Electrical double layer
EOR	Enhanced oil recovery
EoS	Equation of state
EEW	Equilibrated engineered water
EW	Engineered water
FFT	Fast Fourier Transform
FMT	Fundamental measure theory
IEP	Isoelectric point
kgw	Kilogram of water
MC	Monte Carlo simulations
MD	Molecular dynamics simulations
MSA	Mean-spherical approximation
MSA-ER	Energy route MSA-based solution
OCP	One-component plasma
PBE	Poisson-Boltzmann equation
PMF	Potential of mean force
PY	Percus-Yevick compressibility equation of state
RF	Original fundamental measure theory
RF*	Antisymmetrized version of fundamental measure theory

RFD	Reference fluid density perturbation
RPM	Restricted primitive model
SCM	Surface complexation model
SPT	Scaled-particle theory
WB	White Bear version of fundamental measure theory
WBII	White-Bear mark II version of fundamental measure theory
WCA	Weighted correlation approach

LISTA DE SÍMBOLOS

The page in which the symbols are defined or used for the first time is presented in the last column.

Roman symbols:

a_i	Activity of the ith species	76
a_i^{α}	Activity of the ith species in the phase α	58
$\mathrm{å}_i$	Adjustable parameter of the extended Debye-Hückel model	76
$\mathrm{A_{DH}}$	Constant of the Debye-Hückel limiting law	76
A_f	Contact area of the film, *i.e.* interfacial area	77
A_{ob}	Contact area between oil and brine phases	106
A_s	Magnitude coefficient of structural forces	82
A_{sb}	Contact area between rock and brine phases	106
A_{so}	Contact area between rock and oil phases	104
b_i	Adjustable parameter of the extended Debye-Hückel model	76
$\mathscr{b}_i$	Effective characteristic radius of ith species according to MSA	164
$\mathrm{B_{DH}}$	Constant of the extended Debye-Hückel model	76
B_i	Dispersion parameter of the ith ion	55
$c^{(1)}$	First-order direct correlation function	36
$c_i^{(1)C}$	Direct Coulomb contribution to first-order direct correlation function	47
$c_i^{(1)el}$	Electrostatic screening contribution to first-order direct correlation function	49
$c_i^{(1)hs}$	Hard sphere contribution to first-order direct correlation function	42
$c_{ij}^{(2)el}$	Electrostatic screening contribution to second-order direct correlation function	49
$\overline{c}_{ij}^{(2)el}$	Electrostatic screening contribution to weighted second-order direct correlation function	51
e	Elementary charge	27
E	Surface energy	105
f_i^0	Fugacity of the pure ith species in its standard state	76

$\hat{\mathrm{f}}_i$	Fugacity of the ith species in a mixture	76
f_i^{el}	Electrostatic correlation Helmholtz energy of the ith particle	53
$\not{\nu}$	Inverse wavelength	155
F	Intrinsic Helmholtz energy	31
F^C	Excess Helmholtz energy functional due to direct Coulomb interactions	47
F^{el}	Excess Helmholtz energy functional due to charge distribution correlations	47
F^{ex}	Excess contribution to intrinsic Helmholtz energy functional	35
F^{hs}	Excess Helmholtz energy functional due to hard sphere exclusion volume	39
F^{id}	Ideal contribution to intrinsic Helmholtz energy functional	35
$\mathcal{F}$	Fourier transform	43
$\mathcal{F}^{-1}$	Inverse of Fourier transform	43
h	Planck's constant	33
h_d	Height of a spherical cap	104
H	Hamaker constant	81
$H_{\mathrm{non-ret}}$	Nonretarded Hamaker constant	81
$H_{\nu=0}$	Entropy contribution to Hamaker constant	81
$H_{\nu>0}$	Dispersion contribution to Hamaker constant	81
H_{scr}	Screened nonretarded Hamaker constant	81
H_{ret}	Hamaker constant considering retarded effects	82
$\mathcal{H}$	Hamiltonian	33
i	Imaginary number ($i = \sqrt{-1}$)	155
$I^{(m)}$	Ionic strength in mol per kilogram of water	76
k_B	Boltzmann constant	27
K	Kinetic energy	33
$K_{eq,j}$	Equilibrium constant of the jth reaction	61
K_{sp}	Solubility Product Constant	87
ℓ	Film thickness	78
ℓ_{eq}	Equilibrium film thickness	79
ℓ_s	Characteristic decay length of structural forces	82

m_j	Mass of the jth particle	33
m_i^b	Bulk molal concentration of the ith species	76
m_i^{eq}	Bulk molal concentration of the ith species at equilibrium	86
m_i^{in}	Input bulk molal concentration of the ith species	86
m^0	Equal to $1\ \frac{\text{mol solute}}{\text{kg of water}}$	76
$n_{RI,j}$	Refractive index in the visible of the jth material	55
$\mathbf{n}$	Unit normal vector	29
n_α	Weighted densities – $\alpha \in \{0,1,2,3,V1,V2\}$	39
$n_{\alpha,i}$	Weighted densities of the ith species – $\alpha \in \{0,1,2,3,V1,V2\}$	39
$\{\boldsymbol{n}\}$	Set of the number of mols of all species in the system	28
$n_{i,b}$	number of mols of the ith species in the bulk brine phase	78
$n_{i,f}$	number of mols of the ith species in the film	77
$n_{i,ob}$	number of mols of the ith species in the interface oil/brine	78
$n_{i,sb}$	number of mols of the ith species in the interface rock/brine	78
N	Total number of particles ($N \equiv \sum_i N_i$)	32
N_{av}	Avogadro constant	77
N_i	Number of particles of the ith species	33
$\mathcal{N}$	Number of grid points	43
$\mathcal{O}(x^{\mathrm{n}})$	Terms of order x^{n} or smaller	42
p	Pressure	28
$\mathbf{p}$	Molecular momentum vector	33
p_b	Pressure of the bulk brine phase	78
p_c	Capillary pressure	92
p_{EDL}	Bulk osmotic pressure of the electric double layer	52
p_f	Pressure of the film as a whole	77
p_{MSA}	Bulk osmotic pressure from MSA	52
$\mathcal{P}$	Density probability	152
$\mathcal{P}^{eq}$	Density probability at equilibrium	152
Q	Surface charge density	29
$Q_{Calcite}$	Surface charge density of calcite	88
Q_{Oil}	Surface charge density of oil	91
$\mathbf{r}$	Vector of position	27

$r_{B,i}$	Born radius of the ith species	68
$\mathbf{r}_j$	Position vector of the jth particle	33
$\mathbf{r}_\perp$	Perpendicular distance from the surface to the center of the sphere or surface	48
R_d	Radius of the droplet	104
R_{el}	Local electrostatic length scale	50
$\mathcal{S}$	Entropy of the system	32
S_b	Entropy of the bulk brine phase	78
S_f	Entropy of film as a whole	77
$S_{sb,ob}$	Excess entropy of the interface rock/brine and oil/brine	78
T	Absolute temperature	27
u_{ij}	Interaction potential between ith and jth particles	47
U	Internal energy	77
$\mathcal{U}$	Total interatomic potential energy	33
U_f	Internal energy of the film as a whole	77
V_i	External field contributions of the ith species	28
V_i^b	External field contributions of the ith species at bulk reservoir	28
v	One-body external potential	33
$\mathcal{V}$	Total volume of the system	31
$\mathcal{V}_b$	Volume of the bulk brine phase	78
$\mathcal{V}_d$	Volume of the droplet	104
$\mathcal{V}_f$	Volume of the film as a whole	77
$\mathcal{V}_i$	Volume of the spherical particle with diameter σ_i	40
x_m	Midplane between two parallel surfaces	80
z_i	Charge number of the ith ionic species	27

Greek symbols:

$\alpha_i^{el}(\mathbf{r})$	Characteristic functions of the RFD method	50
$\alpha_i^*(\nu)$	Excess polarizability of the ith ion at frequency ν	55
α_P	Mixing parameter of the Picard method	37
β	Inverse thermal energy ($\beta = (k_B T)^{-1}$)	33
$\gamma_i^{(m)}$	Molal activity coefficient of the ith species	76

γ_f	Interfacial tension of the film as a whole	77
γ_{ob}	Bulk interfacial tension of oil/brine interface	79
γ_{of}	Interfacial tension of oil/film interface	78
γ_{sb}	Bulk interfacial tension of rock/brine interface	79
γ_{sf}	Interfacial tension of rock/film interface	78
γ_{so}	Bulk interfacial tension of rock/oil interface	105
Γ	Parameter defined by the mean-spherical approximation	54
$\delta(r)$	Dirac-delta function	40
Δ	Interval between consecutive samples, *i.e.* increment	155
$\Delta\ell$	Increment in distance	92
$\Delta\mu_i^{Born}$	Chemical potential due to the transfer of the ith ion from a reference medium to other – Born correction energy	69
$\Delta\rho_c$	Residue of the contact-value theorem	52
$\Delta\rho_i(\mathbf{r})$	Local density deviation of ith particle from bulk density	49
$\Delta\rho_i^{ref}(\mathbf{r})$	Local density deviation of ith particle from reference density	50
ε	Dielectric constant of the solvent	27
$\varepsilon_j(\nu)$	Dielectric spectra of jth material at frequency ν	55
ε_0	Permittivity of vacuum	27
ε_{ref}	Dielectric constant of a reference fluid	68
ζ	Zeta potential	64
η	Parameter of the regularization function related to smoothness of the curve	61
θ	Contact angle	79
θ_{eq}	Equilibrium contact angle	106
$\theta(r)$	Heaviside step function	40
κ^{-1}	Debye length	51
λ_B	Bjerrum length	47
λ_{lw}^{-1}	London wavelength	82
Λ	Thermal de Broglie wavelength	34
μ	Chemical Potential	32
μ_i	Electrochemical potential of the ith species	28
μ_i^0	Standard electrochemical potential of the ith species	28

μ_i^b	Electrochemical potential of the ith species at bulk reservoir	28
$\mu_i^{b,el}$	Excess chemical potential of the i th species due to electrostatic screening at bulk reservoir	49
$\mu_i^{b,ex}$	Excess chemical potential of the ith species at bulk reservoir	36
$\mu_i^{b,hs}$	Excess chemical potential of the i th species due to hard sphere exclusion volume at bulk reservoir	41
$\mu_i^{b,id}$	Ideal chemical potential of the ith species at bulk reservoir	36
$\mu_i^{b,res}$	Residual chemical potential of the ith species at bulk reservoir	28
μ_i^{id}	Ideal chemical potential functional of the ith species	35
μ_i^{res}	Residual chemical potential of the ith species	28
ν	Frequency	55
$\nu_{e,j}$	Main electronic absorption frequency of the jth material in the UV	55
$\nu_{I,i}$	Ionization frequency of the ith ion	55
ν_{min}	First non-null frequency	55
ξ_α	Scaled-particle variables – $\alpha \in \{0,1,2,3\}$	40
ξ_j	Extent of reaction for the jth reaction	86
Ξ	Grand-canonical partition function	32
Ξ^{id}	Ideal grand-canonical partition function	38
Π	Total disjoining pressure	78
Π_{EDL}	Disjoining pressure due to the electrical double layer	79
Π_{vdW}	Disjoining pressure due to the van der Waals interaction between the interfaces	79
Π_s	Disjoining pressure due to the structural forces	79
ρ_i	Number density of the ith species	27
ρ_i^b	Number density of the ith species at bulk reservoir	27
ρ_i^{DFT}	Number density of the ith species computed from standard DFT	52
ρ_i^{eq}	E number density of the ith species	34
$\rho_{i,in}^{(k)}(\mathbf{r})$	Input density profile of the ith species at the kth iteration of Picard method	37
$\rho_{i,out}^{(k)}(\mathbf{r})$	Output density profile of the ith species at the kth iteration of Picard method	37
ρ_i^{ref}	Number density of the ith species in the reference fluid	50

$\rho_m^{\mathrm{s,max}}$	Maximum number density of the mth site of the bounded charge	62
$\tilde{\rho}_i$	Molar density of the ith species	61
$\tilde{\rho}^b$	Molar density of the ith species at bulk reservoir	110
$\tilde{\rho}_i^{cal}$	Local molar density of the ith species at the closest distance from the calcite surface	88
$\tilde{\rho}_i^{oil}$	Local molar density of the ith species at the closest distance from the oil surface	92
$\rho_w^{(m)}$	Volumetric mass density of water	77
ϱ	Volumetric density of charge	27
ϱ_{bn}	Volumetric density of fixed (bounded) charge	29
σ_i	Hard sphere diameter of the ith particle	40
σ_{ij}	Arithmetic mean between the diameters of the ith and jth particles	47
ς_m	Surface density of the mth surface site	88
$\varsigma_m^{\max}$	Maximum surface density of the mth surface site	88
$\upsilon_{i,j}$	Stoichiometric number of the ith species in the jth reaction	76
φ	One-body potential	34
ϕ_i^{DFT}	Local ionic volume fraction of the ith particle based on standard DFT	52
Φ^{el}	Reduced Helmholtz energy density due to electrostatic screening	54
Φ^{hs}	Reduced Helmholtz energy density due to hard sphere exclusion volume	39
ψ	Mean electrostatic potential	27
ψ^b	Mean electrostatic potential at the bulk reservoir (usually null)	28
ψ_D	Donnan potential	58
Ψ_i	Electric interaction between particle i and a charged planar surface	48
$\omega_i^{(\alpha)}$	Weighting functions of the ith species – $\alpha \in \{0,1,2,3,V1,V2\}$	39
$\widehat{\omega}_i^{(\alpha)}$	Weighting functions of the i th species in the reciprocal space– $\alpha \in \{0,1,2,3,V1,V2\}$	157
Ω	Grand potential	32
Ω^{id}	Ideal grand potential	38

SUMÁRIO

INTRODUCTION

Electrolyte systems and processes involving charges are ubiquitous. They encompass for example, our shampoos, the lithium battery of our cell phones, and even, the mechanism of information transfer in the nervous system. Therefore, the study of electrostatic phenomena is fundamental to the understanding of biological, chemical, and physical processes specially near interfaces.[1,2] A widespread theory developed to explain the interfacial behavior present in these systems is based on the concept of electrical double layer (EDL).

The EDL is a structure that arises on the surface of a macroparticle when it is exposed to an electrolyte solution. It is composed by an ionic layer firmly attached to the macroparticle (bounded charge on the surface), called potential determining ions, and an equivalent amount of oppositely charged ions from the electrolyte solution, the counterions. Although attracted to an oppositely charged surface, the counterions remain dispersed in the liquid medium near the interface due to entropic factors. The dispersed ions with the same sign of the potential determining ions are called coions. In summary, the charge on the surface of the macroparticle influences the ionic distribution near its vicinity: the counterions are attracted by the surface and the coions are repulsed from the surface by electrical forces. However, there is a dynamic equilibrium between the ions near the surface and the free ions of the same sign in the bulk liquid.[3–5]

Knowledge of microscopic structure and macroscopic properties of electrolyte systems is crucial to understand phenomena such as charge inversion, overload, and flocculation; and to develop more efficient processes and new products for pharmaceutical,[6–8] petrochemical,[9–14] and electronic[15–19] industries.

Different methods can be used to model electrolyte systems such as implicit methods, integral equations and classical density functional theory (DFT), and explicit methods, depending on the level of detail and the required computational time as shown in Figure 1.[20]

Implicit models consider the solvent as a continuous medium whose characteristics are described by a single parameter: the dielectric constant. With this analysis, the degree of freedom of the system is reduced. Example of implicit methods are: Poisson-Boltzmann Equation (PBE)[3,21–23], Coulomb's law and generalized Born methods[24].

Figure 1 – Level of detail and required computational time for implicit methods, integral equations and density functional theory, and explicit methods

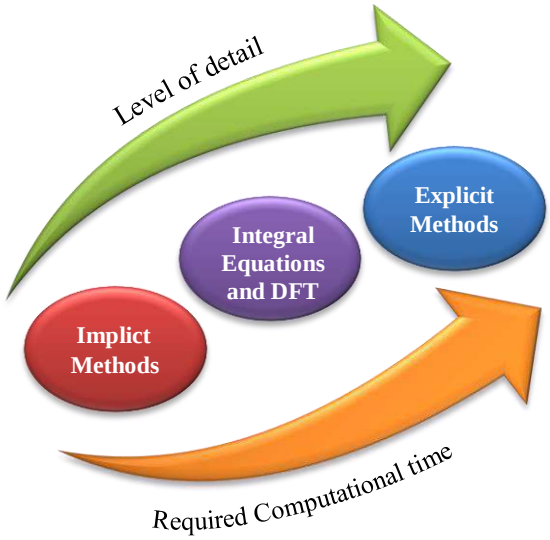

The investigation of electrolyte systems using DFT[25,26,35,36,27–34] and integral equations, such as hipernetted chain closure (HCN)[37], allows the inclusion of other contributions conventionally not addressed in the continuous mean-field theories, such as electrostatic correlations between ions. The solvent can be treated explicitly as hard spheres, for example, or implicitly.

Whereas the classical Poisson-Boltzmann equation predicts ion distributions dependent only on mean electrostatic potential, the classical density functional theory also considers electrostatic correlations and non-mean field contributions such as volume exclusion effects.[25,26,35,27–34] Together with the electrostatic correlations, they are responsible for many counterintuitive phenomena such as charge inversion,[35,38] attraction between like charged surfaces,[2,39–41] and long range oscillatory densities – multiple electric layers.[42]

Non-electrostatic interactions including, for instance, van der Waals interactions, self-image charge interactions, and hydration of ions, can be introduced in both DFT and modified PBE as external potentials.[22,43–45]

The explicit methods are based on statistical mechanics. They consider the solvent explicitly, *i.e.*, as individual molecules interacting among themselves and with solutes according to force fields. Although they present more realistic results, the increase in the degree of freedom causes a rise in the required computational time which, sometimes, can limit the capacity of those methods to generate convergent estimations to thermodynamic

phenomena.[46–48] Examples of explicit methods are Monte Carlo simulations (MC) and molecular dynamics simulations (MD) – however, both techniques can also be solved with implicit solvent, depending on the chosen force field.

Comparing DFT with MD, the former computes directly ensemble-averaged properties of interest, whereas the latter computes those average quantities based on the trajectories of the particles over long time simulations.

To address the time limitation, in recent years, there has been considerable interest in hybrid techniques that take advantage of different scale methods in order to improve results without an expressive increase in computational time.[43,44,49–51] For instance, potentials of mean force (PMF) from MD have been inserted in the modified PBE reaching better agreement with experimental data for the excess interfacial tension.[52–54]

Especially noteworthy is the numerical efficiency of PBE and DFT in systems with symmetry, in which the densities might only be analyzed in one, or even two, space variables. On the other hand, the explicit methods are usually performed in three dimensions.

The purpose of this thesis is the investigation of the interactions in electrolyte systems using PBE and DFT, in order to determine macroscopic properties of these systems. Basically, the analyzed cases can be divided into two categories: biological and petrochemical applications. The specific aims are:

a) Determination of the zeta potential of a bacterial cell wall into electrolyte solutions and its variation with pH using a smoothing function to describe the charge-regulated volume charge density;
b) Inclusion of a contribution due to the ionic hydration as function of dielectric constant of media – based on Bohr correction equation – for biological systems;
c) Investigation of ionic distribution confined in an aqueous solution between rock and oil using charge regulation at boundary conditions; and
d) Study of wettability and contact angle in oil/brine/rock systems using tridimensional density functional theory (3D-DFT);

In order to guarantee the linearity of this thesis, some studies developed over these years are not going to be presented in the next sections. For example:

a) we investigated the behavior of confined electrolyte systems using classical density functional theory;[20,55]

b) an AMBER-compatible transferable force field for poly(ethylene glycol) ethers (glymes) was also developed, more specifically during the year in the University of Notre Dame;[56] and
c) we also have investigated the potential of mean force for some ions at infinite dilution close to a graphene sheet, in order to insert into PBE and DFT, providing the integration of different scales.

After this introduction which presents the general aspects and objectives of this thesis, Chapter 1 describes two methods recurrently used during this work: Poisson-Boltzmann equation and classical density functional theory. A section is also reserved to comment about the non-electrostatic interactions since they were used in the development of this thesis.

The next two chapters have a general structure characterized by a brief introduction about the applications – biological or petrochemical –, and subsections divided into specific introduction, methodology, results and discussion, and partial conclusions applied to the research field of each subsection.

It is important to highlight that the biological applications discussed in this thesis is a continuation of the work initially developed in the master dissertation,[3] which analyzed the ionic partitioning in an erythrocyte using the modified PBE, with the addition of the Bohr correction.[21] Following the same line of inquiry, the electrostatic behavior of *Bacillus brevis* cell wall is also modeled in Chapter 2 using the PBE.[57]

The interest in the wettability of systems involving two liquids and a solid surface is well documented in the literature especially in the context of separation processes and oil extraction.[14,58–65] The latter case is the matter of concern of Chapter 3 which is dedicated to determining of the contact angle at the equilibrium for the oil/brine/rock systems using either PBE or DFT.

An interesting aspect is that all algorithms used here to solve the Poisson-Boltzmann equation and the classical density functional theory have been developed by us over the years since the Master.

Finally, the conclusion section summarizes the main contributions of this thesis to the literature and offers some suggestions to future studies.

1 THEORY

This chapter presents a literature review about the two methods used to investigate electrolyte systems in this thesis: Poisson-Boltzmann equation and classical density functional theory. As mentioned before, they have different levels of detail as shown in Figure 1. In Section 1.1, Gouy-Chapman theory, and classical and modified PBE are described, while Section 1.2 elucidates the key concepts of DFT and reviews some of the functionals conventionally used to compute the intrinsic Helmholtz energy.

It is interesting to mention that PBE and DFT were the topic of a chapter wrote to the "Reference module in chemistry, molecular sciences and chemical engineering", published by Elsevier.[20] This chapter can be found in APPENDIX A.

The last section of this chapter presents the non-electrostatic interactions between surfaces and ions that can be applied at PBE and DFT as external potentials.

1.1 Poisson-Boltzmann equation (PBE)

The DLVO (Derjaguin-Laudau-Verwey-Overbeek) theory provides the basis to model quantitatively the interactions between macroparticles in colloid science. It considers the action of two different types of electromagnetic forces: pure electrostatic forces from the EDL and the van der Waals forces. While the former occurs only in particles with charge, the latter occurs in all particles whether they are charged or not.[66,67] One model conventionally used to describe the EDL is treated in this section: the Gouy-Chapman model. On the other hand, the van der Waals potential, which is insensitive to the variation of ionic concentration and pH, in first approach, is briefly mentioned in Sections 1.3 and 3.1.2.2.

The presence of a charged surface immersed in an electrolyte solution contributes to an inhomogeneous distribution of ions close to that surface, constituting the EDL. Some theories have been proposed to describe, quantitatively and/or qualitatively, the structure of this layer, such as the Helmholtz-Perrin model, the Gouy-Chapman model, and the Stern model.[5,20,68] The main difference among them is how the structure of the counterion layer is considered.

According to the Gouy-Chapman theory, the solvent is treated as a continuum described by the dielectric constant and the finite dimensions of the ions are ignored. The counterions are scattered in the liquid phase within certain distance away from the surface due to a balance between the action of the electric field from the surface and the thermal motion. In the immediate vicinity of the surface the effect of the electric field is higher; as a result the concentration of counterions tends to rise in this region, while the concentration of coions decrease; however as the distance from the surface increases, the counterions become more scattered due to the thermal motion and the attenuation of the electric field's influence. At some distance far from the surface, the concentration of ions is equal to the bulk liquid concentration. By hypothesis, all surfaces are considered geometrically smooth and uniformly charged.[5,68]

The PBE, which is a second order elliptic partial differential equation, describes the mean electrostatic potential and the ion concentration as function of the distance from an interface according to the Gouy-Chapman model. Basically, it is a combination of the Poisson equation, which correlates the volumetric charge density ϱ with the mean electrostatic potential ψ,

$$\varepsilon_0 \nabla \cdot [\varepsilon \nabla \psi(\mathbf{r})] = -\varrho(\mathbf{r}) \equiv -e \sum_i z_i \rho_i(\mathbf{r}) \tag{1}$$

with the Boltzmann distribution

$$\rho_i(\mathbf{r}) = \rho_i^b \exp\left[-\frac{e z_i \psi(\mathbf{r})}{k_B T}\right] \tag{2}$$

yielding

$$\varepsilon_0 \nabla \cdot [\varepsilon \nabla \psi(\mathbf{r})] = -e \sum_i z_i \rho_i^b \exp\left(-\frac{e z_i \psi}{k_B T}\right) \tag{3}$$

where ε_0 is the permittivity of vacuum, ε is the dielectric constant of the solvent, e is the elementary charge, k_B is the Boltzmann constant, T is the absolute temperature of the system, ρ_i is the density of ion i (number of ions per unit volume), ρ_i^b is the bulk density of ion i, and z_i is the valence of ion i.

Despite its effectiveness in predicting some thermodynamic properties,[57] the classical PBE fails to explain phenomena such as the ion specificity, the potential inversion, the attraction between like-charged colloidal particles, the repulsion between opposite-charged particles, and multiple alternating layers of ions. This usually happens in concentrated systems and when the surface potential is high, since the Gouy-Chapman model neglects the finite size of the ions, the non-ideality of the solution, and any other type of interactions except the electrostatic one. These limitations have highlighted the importance of developing modifications to the classical version of the PBE in order to take into account several important effects such as dispersion forces, hydration, ion size effects, and electric correlation between ions.[43,50–52,69]

These additional contributions may be divided in two distinct classes: external field contributions, which are represented by V_i, and contributions depending on the interaction among ions – here referred as residual chemical potential, μ_i^{res}. These additional terms can be included in the description of the ion electrochemical potential μ_i as follows

$$\mu_i(p,T,\{\boldsymbol{n}\}) = \mu_i^0(p,T) + k_B T \ln \rho_i + e z_i \psi + V_i + \mu_i^{res}(p,T,\{\boldsymbol{n}\}) \tag{4}$$

where μ_i^0 is the standard electrochemical potential of the ion i and $\{\boldsymbol{n}\}$ represents the set of the number of mols of all species in the system. The additional contributions can be function of the ion's separation from the surface or even functional of the ion densities. At the bulk reservoir, the electrochemical potential of ion i, μ_i^b, is given by

$$\mu_i^b(p,T,\{\boldsymbol{n}\}) = \mu_i^0(p,T) + k_B T \ln \rho_i^b + e z_i \psi^b + V_i^b + \mu_i^{b,res}(p,T,\{\boldsymbol{n}\}) \tag{5}$$

here, ψ^b, V_i^b, and $\mu_i^{b,res}$ stand, respectively, for the electrostatic potential, the external potential of the ion i, and the residual chemical potential at the bulk reservoir. The two first contributions (ψ^b and V_i^b) usually are null. The modified Boltzmann distribution can be obtained by the combination of Eqs. (4) and (5), yielding[20]

$$\rho_i = \rho_i^b \exp\left[-\frac{z_i e(\psi - \psi^b) + V_i - V_i^b + \mu_i^{res} - \mu_i^{b,res}}{k_B T}\right] \tag{6}$$

Whereas the Boltzmann distribution of the ions is obtained solely on the basis of the electrical potential energy in the classical PBE, the extended version presented in Eq. (6) allows the inclusion of non-electrostatic energy contributions at the same level of the electrostatic potential.[20,50,69]

Another possible modification of the Gouy-Chapman model is the consideration of volumetric density of fixed charges, ϱ_{bn}, in the Poisson equation as follows

$$\varepsilon_0 \nabla \cdot [\varepsilon(\mathbf{r})\, \nabla\psi(\mathbf{r})] = -e \sum_i z_i\, \rho_i(\mathbf{r}) - \varrho_{bn}(\mathbf{r}) \equiv \varrho(\mathbf{r}) \tag{7}$$

Here the term "fixed" denotes charges that are fixed in space (immobile), but not necessarily with a constant value. In addition, the dielectric constant may be uniform, as in the Gouy-Chapman model, or a function of the position. The scale integration can provide useful information for the definition of the local dielectric constant function.[20]

Consequently, the modified PBE is given by the combination of Eqs. (6) and (7):

$$\varepsilon_0 \nabla \cdot [\varepsilon(\mathbf{r})\, \nabla\psi(\mathbf{r})] = -e \sum_i z_i\, \rho_i^b \exp\left[-\frac{z_i e(\psi - \psi^b) + V_i - V_i^b + \mu_i^{res} - \mu_i^{b,res}}{k_B T}\right] - \varrho_{bn}(\mathbf{r}) \tag{8}$$

It is important to highlight that the modified PBE is also applicable to uncharged surfaces or interfaces.

The boundary conditions usually associated with Eq. (8) can be of three types: Dirichlet boundary (potential specified at the boundary), Neumann boundary (derivative of the potential specified at the boundary), and Robin boundary (a weighted combination of Dirichlet boundary conditions and Neumann boundary conditions).[20]

The Dirichlet boundary is straightforward and the electrostatic potential at the specified boundary is set *a priori*. On the other hand, the Neumann boundary condition is related to the surface charge density Q by

$$[\varepsilon(\mathbf{r})\, \nabla\psi(\mathbf{r})]|_{\text{surface}} \cdot \mathbf{n} = -\frac{Q}{\varepsilon_0} \tag{9}$$

where **n** is the unit normal vector to the corresponding surface. In a distance far from the surface or interface, the electrostatic potential or the surface charge density is usually set to zero.

Nevertheless, constant potential or constant surface charge density boundary conditions are rarely found in real surfaces. To address this problem, Robin boundary conditions described by charge regulation can be used especially for systems with surface charge density susceptible to pH or the presence of other ions close to the surface. Examples of such surfaces are proteins,[70–72] carbonate rocks, sandstone rocks,[73] some ionic membranes,[74] etc.

For Cartesian coordinates with one planar surface, uniform dielectric constant, symmetrical electrolyte, and Dirichlet boundary conditions, the classical PBE can be solved analytically.[68] For other coordinate systems or conditions, different numerical techniques can be used to solve the PBE equation such as finite difference method,[75,76] finite volume method,[4,77] second order spline finite elements method,[3,78] and finite element method.[73,75]

Even with such modifications, the PBE fails sometimes to predict some structural and thermodynamics properties particularly in concentrated systems and/or with high surface charge density. In this context, models with higher level of details based on explicit consideration of the ion and/or the solvent structures may be an option to overcome these limitations. One of the methods that can be used to consider a higher level of detail, beyond PBE, is the classical density functional theory, presented in the next section. For instance, in Figure 3 of the APPENDIX A, the density profiles of monovalent ions as a function of the distance from a flat wall with surface charge equal to –0.35C/m² are presented. For a bulk concentration of 2.0 M, DFT predicts an inversion in the volumetric charge density agreeing with Monte Carlo simulation,[79] whereas PBE is unable to predict this inversion as expected.[20]

1.2 Classical density functional theory (DFT)

Similar to the PBE, the classical DFT – also known as statistical mechanics DFT since it is based on statistical mechanics – provides information about the microscopic behavior and thermodynamic properties of the system of interest, making possible the connection with well-established phenomenological equations to model macroscopic phenomena. Using classical DFT, besides electrolyte and colloidal systems (treated in this thesis), it is also

possible to model systems with uncharged particles (or molecules) explicitly. Indeed the classical DFT is a versatile tool able to analyze multiple length scales ranging, for example, from molecular events to macroscopic phase transitions.[32,33]

The main concept of the classical DFT comes from the electronic density functional theory (also called quantum mechanics DFT), which was established by the works of Hohenberg, Kohn and Sham.[80,81] Based on the observation of Thomas[82] and Fermi[83], in which the energy of an electronic system can be directly computed by the electron density profile, Hohenberg and Kohn[80] proved mathematically that the intrinsic ground-state molecular energy is a unique functional of the ground-sate electron probability density. Following that work, Kohn and Sham[81] proposed a method to compute the electronic density considering a fictitious reference system without interactions among electrons, under the same external potential energy for all of them. Therefore, the ground-state electronic energy is defined by the nuclear attraction potential energy for the electrons, the Coulombic repulsions, the average kinetic energy of the reference system, and the so called exchange-correlation energy.[81,84] The latter term encompasses the kinetic correlation energy, the exchange energy, the Coulombic correlation energy, and a self-interaction correction.

Whereas the density of the electronic DFT refers to the electrons, in the classical approach it refers to the atoms, ions, molecules or even the unit of polymers. Unfortunately, in the literature, the same acronym is used to both theories. For the purpose of this thesis, the acronym DFT, without explicit denomination of being electronic or classical, will be adopted as a reference to the classical DFT.

According to the Hohenberg–Kohn theorem applied to the classical DFT, in an open system with specified temperature T, total volume $\mathcal{V}$, and chemical potential of all constituent species μ_i, the external potential is uniquely determined by the equilibrium density of the species $\rho_i(\mathbf{r})$.[33,85–87] Additionally, the intrinsic Helmholtz energy $F[\{\rho_k(\mathbf{r})\}]$, which is independent of the external potential, is uniquely defined as a functional of the densities. Here, $\{\rho_k(\mathbf{r})\}$ is the set of the density functions of all species in the system. More information about the Hohenberg–Kohn theorem can be found in APPENDIX B.

The first studies of the DFT for classical systems were conducted in 1976 to model the liquid-vapor surface tension and the wettability of a Lennard-Jones fluid[88,89] and since then much progress has been made for more accurate formulation of the Helmholtz energy functional applicable not only to simple but also to complex fluids, such as polymers, polyelectrolytes and biomacromolecules.[32,90,99,91–98]

1.2.1 Grand canonical potential

In order to correlate thermodynamic properties of an open system to the density profiles $\rho(\boldsymbol{r})$, some features and definitions of the statistical thermodynamics are necessary. The grand canonical ensemble, in which the phase space is defined by the union of phase spaces corresponding to all values of the variable N with T and $\mathcal{V}$ given, is adopted. Hence, the number of molecules N in a system can range over all possibilities since the systems of the ensemble are allowed to come to equilibrium with a reservoir with which they can exchange both heat and matter.[100,101]

For a one-component open system in the absence of external field, the thermodynamic state is defined by specifying the values of $\mathcal{V}$, T, and μ, in which the corresponding thermodynamics function is the grand potential Ω defined by:[100,101]

$$\Omega = F - N\mu \tag{10}$$

Moreover, the grand potential is related to the total volume $\mathcal{V}$ and total pressure p of the system in a uniform fluid by

$$\Omega = -(p\mathcal{V}) = -\frac{1}{\beta}\ln \Xi \tag{11}$$

where Ξ is the grand-canonical partition function.

According to classical thermodynamics, the change in internal energy arising from infinitesimal changes in N, $\mathcal{V}$ and $\mathcal{S}$ for an open isothermal system that can perform only mechanical work is given by[102]

$$\mathrm{d}U = T\mathrm{d}\mathcal{S} - p\mathrm{d}\mathcal{V} + \mu\mathrm{d}N \tag{12}$$

where $\mathcal{S}$ is the entropy of the system. Since $F = U - T\mathcal{S}$, the differential form of the grand potential is expressed as

$$\mathrm{d}\Omega = \mathrm{d}F - \mu \mathrm{d}N - N\mathrm{d}\mu = \mathrm{d}U - T\mathrm{d}\mathcal{S} - \mathcal{S}\mathrm{d}T - \mu \mathrm{d}N - N\mathrm{d}\mu \tag{13}$$

By substituting Eq. (12) into Eq. (13) we have[100,101]

$$\mathrm{d}\Omega = -p\mathrm{d}\mathcal{V} - \mathcal{S}\mathrm{d}T - N\mathrm{d}\mu \tag{14}$$

After, this brief definition of the grand canonical ensemble, we expand the analysis to a heterogeneous, multicomponent system in the presence of external potentials. For the classical approach, the grand-canonical partition function for an n-component mixture containing N_i spherical particles of type i is given by[103,104]

$$\Xi = \sum_{N_1, N_2 \ldots N_n} \frac{1}{h^{3N}} \left[\prod_{i=1}^{n} \frac{1}{N_i!} \exp(\beta \mu_i N_i) \right] \int \exp[-\beta \mathcal{H}(\mathbf{r}^N, \mathbf{p}^N)] \, \mathrm{d}\mathbf{r}^N \mathrm{d}\mathbf{p}^N \tag{15}$$

where h is the Planck's constant, $\mathcal{H}(\mathbf{r}^N, \mathbf{p}^N)$ is the Hamiltonian of the n-component mixture in the configuration $\mathbf{r}^N$, $\mathbf{p}$ is the momentum, $\beta = 1/(k_B T)$, and $N \equiv \sum_i N_i$. The Hamiltonian in the presence of an external potential considers the contributions from the kinetic energy $K(\mathbf{p}^N)$, the total interatomic potential energy $\mathcal{U}(\mathbf{r}^N)$, and the one-body external potential $v(\mathbf{r})$ as[105]

$$\mathcal{H}(\mathbf{r}^N, \mathbf{p}^N) = K(\mathbf{p}^N) + \mathcal{U}(\mathbf{r}^N) + \sum_{j=1}^{N} v(\mathbf{r}_j) \tag{16}$$

where $\mathbf{r}_j$ is the position vector of the jth particle,

$$K(\mathbf{p}^N) = \sum_{j=1}^{N} \frac{|\mathbf{p}_j|^2}{2m_j} \tag{17}$$

and m_j is the mass of the jth particle. Combining Eqs. (15) – (17) and solving the integration over momenta,[87] the grand-canonical partition function can be written as

$$\Xi = \sum_{N_1,N_2\ldots N_n} \left[\prod_{i=1}^{n} \frac{1}{N_i!\,\Lambda_i^{3N_i}}\right] \int \exp\left[-\beta\left(\mathcal{U}(\mathbf{r}) + \sum_{j=1}^{N} \varphi(\mathbf{r}_j)\right)\right] \mathrm{d}\mathbf{r}^N \tag{18}$$

where $\Lambda_i = \left(\frac{\mathrm{h}^2}{2\pi m_i k_B T}\right)^{0,5}$ is the thermal de Broglie wavelength and the one-body potential is defined by $\varphi(\mathbf{r}_j) \equiv v(\mathbf{r}_j) - \mu(\mathbf{r}_j)$. Hence the density function of the component i can be written as[106,107]

$$\begin{aligned}\rho_i(\mathbf{r}) &= \frac{1}{\Xi} \sum_{N_1,N_2\ldots N_n} \left[\prod_{k=1}^{n} \frac{1}{N_k!\,\Lambda_k^{3N_k}}\right] \int \left[\sum_{j=1}^{N_i} \delta\left(\mathbf{r} - \mathbf{r}_j^{(i)}\right)\right] \exp\left[-\beta\mathcal{U}(\mathbf{r}) - \beta\sum_{j=1}^{N} \varphi(\mathbf{r}_j)\right] \mathrm{d}\mathbf{r}^N \\ &= -\frac{1}{\beta\Xi}\frac{\delta\Xi}{\delta\varphi_i(\mathbf{r})}\end{aligned} \tag{19}$$

in which $\mathbf{r}_j^{(i)}$ is the vector position of the jth particle of type i,

$$\varphi_i(\mathbf{r}) \equiv \int \sum_{j=1}^{N_i} \varphi\left(\mathbf{r}_j^{(i)}\right)\delta\left(\mathbf{r} - \mathbf{r}_j^{(i)}\right) \mathrm{d}\mathbf{r}^N \tag{20}$$

and $\frac{\delta\Xi}{\delta\varphi_i(\mathbf{r})}$ is a functional derivative of Ξ. For more details about the definition of the density as a functional derivative of Ξ, see APPENDIX B. The density function can also be derived from the grand potential Ω as[86,107]

$$\rho_i(\mathbf{r}) = \frac{\delta\Omega}{\delta\varphi_i(\mathbf{r})} \tag{21}$$

Using the Legendre transformation to correlate the grand potential Ω and the intrinsic Helmholtz energy, yields[20,86,87]

$$\Omega = F + \int \sum_{i=1}^{n} \rho_i^{eq}(\mathbf{r})\varphi_i(\boldsymbol{r})\mathrm{d}\mathbf{r} \tag{22}$$

where ρ_i^{eq} is the equilibrium number density of ion i. As a matter of fact, according to the Hohenberg–Kohn theorem (discussed in Section 1.2 and presented in APPENDIX B), the one-body potential $\varphi_i(\boldsymbol{r})$ can be uniquely determined by the density function $\rho_i(\mathbf{r})$. Based on this definition, we can expand the concept to every system independently of being at equilibrium or not, using the variational grand potential functional $\Omega[\{\rho_k(\mathbf{r})\}]$ and the variational intrinsic Helmholtz energy functional $F[\{\rho_k(\mathbf{r})\}]$:[20,86,87,107]

$$\Omega[\{\rho_k(\mathbf{r})\}] = F[\{\rho_i(\mathbf{r})\}] + \int \sum_{i=1}^{n} \rho_i(\mathbf{r})\varphi_i(\mathbf{r})\,\mathrm{d}\mathbf{r} \tag{23}$$

For equilibrium density profiles, Eq. (23) reduces to the grand potential of the system expressed by Eq. (22); conversely, for any other density profiles, the functional $\Omega[\{\rho_k(\mathbf{r})\}]$ reduces to a value that is larger than the grand potential. In other words, in an open system, the grand potential is a minimum at equilibrium; hence, $\rho_i^{eq}(\mathbf{r})$ must satisfy the Euler-Lagrange equation,[20,86,87,107]

$$\left.\frac{\delta\Omega[\{\rho_k(\mathbf{r})\}]}{\delta\rho_i(\mathbf{r})}\right|_{\rho_i^{eq}} = 0 \tag{24}$$

for the inhomogeneous density profile $\rho_i(\mathbf{r})$ of all species i, which is equivalent to

$$\mu_i - v_i(\mathbf{r}) = \frac{\delta F[\{\rho_k(\mathbf{r})\}]}{\delta\rho_i(\mathbf{r})} \tag{25}$$

with the constraining

$$\nabla\mu_i(\mathbf{r}) = 0 \tag{26}$$

i.e. the electrochemical potential for each species μ_i is constant and equal to its value at the bulk solution, μ_i^b. The intrinsic Helmholtz energy can be split into two contributions: ideal F^{id} and excess F^{ex}. In addition, the functional derivative of the ideal Helmholtz energy is equivalent to the ideal chemical potential μ_i^{id}, while the functional derivative of the excess

Helmholtz energy is related to the first-order direct correlation function (DCF) $c^{(1)}$, as follows

$$c_i^{(1)}(\mathbf{r}) \equiv -\beta \frac{\delta F^{ex}[\{\rho_k(\mathbf{r})\}]}{\delta \rho_i(\mathbf{r})} \tag{27}$$

For each contribution considered in the computation of the intrinsic Helmholtz energy functional, there must be an equivalent contribution to the chemical potential. Replacing these definitions into Eq. (25), we obtain

$$\mu_i = v_i(\mathbf{r}) - \beta^{-1} c^{(1)}(\mathbf{r}) + \mu_i^{id}(\mathbf{r}) \tag{28}$$

The term $-\beta^{-1} c^{(1)}(\mathbf{r})$ can be interpreted as the local excess chemical potential due to the intermolecular interactions, which are absent in the ideal gas.

By solving the functional derivative of the ideal Helmholtz energy, we obtain[107]

$$\rho_i^{eq}(\mathbf{r}) = \frac{1}{\Lambda_i^3} \exp\left[\beta\mu_i - \beta v_i(\mathbf{r}) - \frac{\beta \delta F^{ex}}{\delta \rho_i^{eq}(\mathbf{r})}\right] = \frac{1}{\Lambda_i^3} \exp\left[\beta\mu_i - \beta v_i(\mathbf{r}) + c^{(1)}(\mathbf{r})\right] \tag{29}$$

Consequently, given the external potential and the excess Helmholtz energy functional – or the first-order direct correlation function -, the equilibrium density profile can be obtained. At equilibrium μ_i, which can also be split into ideal ($\mu_i^{b,id}$) and excess ($\mu_i^{b,ex}$) contributions, is equivalent to the bulk chemical potential of the species i. Furthermore, the ideal chemical potential of the species i at the bulk reservoir is given by

$$\mu_i^{b,id} = \beta^{-1} \ln\left(\Lambda_i^3 \rho_i^b\right) \tag{30}$$

Replacing Eq. (30) into Eq. (29), we have

$$\rho_i^{eq}(\mathbf{r}) = \rho_i^b \exp\left[\beta\mu_i^{b,ex} - \beta v_i(\mathbf{r}) + c^{(1)}(\mathbf{r})\right] \tag{31}$$

The different versions of DFT reflect some of the assumptions made about the calculation of the excess intrinsic Helmholtz energy, since, in the DFT calculation, there is no

generic procedure in order to compute F^{ex}. Thus, many approximations are available; however, all the versions are generally based on the minimization of the grand potential Ω, which can be denominated as free minimization or parameterized minimization. In the former, the density profile is discretized and, in the latter, it is a parameterized function form, *e.g.* Gaussians.[20,86,108,109]

Two methods are commonly described in the literature to solve Eq. (29): Picard method and Newton method. The Picard method has no guarantee to converge, nevertheless for many choices of external potentials, it does converge to a solution with the inclusion of a mixing parameter $\alpha_P \in \{0, \dots, 1\}$. Therefore, the input density profile of the new iteration k, $\rho_{i,in}^{(k)}(\mathbf{r})$ is a weighted combination between the input density profile $\rho_{i,in}^{(k-1)}(\mathbf{r})$ and the output density profile $\rho_{i,out}^{(k-1)}(\mathbf{r})$ of the previous iteration:[110]

$$\rho_{i,in}^{(k)}(\mathbf{r}) = \alpha_P \, \rho_{i,out}^{(k-1)}(\mathbf{r}) + (1 - \alpha_P) \, \rho_{i,in}^{(k-1)}(\mathbf{r}) \tag{32}$$

According to Knepley *et al.*, Picard iteration requires more iteration steps to converge compared to Newton method (which has a quadratic convergence); however, the latter needs more computer storage and each iteration usually takes longer than a Picard iteration.[108] Even with variable mixing parameters along the simulation, there are some cases in which Picard presents difficulty to converge. Oettel and co-works suggested a procedure based in a Picard-DIIS (discrete inversion in iterative subspace) hybrid algorithm for such situations.[111]

Edelmann and Roth recently proposed a Picard-Broyden-hybrid algorithm, in which, for the initial steps, Picard method is applied and, after a certain threshold is reached, a switch to the Broyden method is performed.[112] Thus, the main idea is to execute the Picard iteration until the density profiles are sufficiently close to their equilibrium values and take the advantage of the convergence speed of the Broyden method, which is a quasi-Newton method.[112]

It is worthwhile to note that the equilibrium point corresponding to the minimum of the grand potential is obtained by the necessary condition represented by Eq. (24).

1.2.2 Ideal gas contribution to the intrinsic Helmholtz energy functional

The intrinsic Helmholtz energy functional of an ideal gas can be expressed as a functional of the density profile. For an open system with n-component mixture containing N_i spherical particles of type i, the ideal grand-canonical partition function is given by

$$\begin{aligned}\Xi^{id} &= \sum_{N_1,N_2\ldots N_n}\left[\prod_{i=1}^{n}\frac{1}{N_i!\,\Lambda_i^{3N_i}}\right]\int \exp\left[-\beta\sum_{j=1}^{N}\varphi(\mathbf{r}_j)\right]\mathrm{d}\mathbf{r}^N \\ &= \exp\left[\sum_{i=1}^{n}\int\frac{\exp[-\beta\varphi_i(\mathbf{r})]}{\Lambda_i^3}\,\mathrm{d}\mathbf{r}\right]\end{aligned} \tag{33}$$

in which the concept of power series to define the exponential $\left(\exp x = \sum_m \frac{x^m}{m!}\right)$ is used. Thus, the ideal grand potential can be written as

$$\beta\Omega^{id} = -\ln\Xi^{id} = -\sum_{i=1}^{n}\int\frac{\exp[-\beta\varphi_i(\mathbf{r})]}{\Lambda_i^3}\,\mathrm{d}\mathbf{r} \tag{34}$$

while the equilibrium density profile of an ideal gas is

$$\rho_i(\mathbf{r}) = -\frac{1}{\beta}\frac{\delta\ln\Xi^{id}}{\delta\varphi_i(\mathbf{r})} = \frac{\exp[-\beta\varphi_i(\mathbf{r})]}{\Lambda_i^3} \tag{35}$$

Applying Eq. (23) for the ideal system and combining with the definitions in Eqs. (34) and (35), the ideal gas contribution to the intrinsic Helmholtz energy functional F^{id} is given by[86]

$$\beta F^{id}[\{\rho_k(\mathbf{r})\}] = \beta\Omega^{id} - \beta\int\sum_{i=1}^{n}\rho_i(\mathbf{r})\varphi_i(\mathbf{r})\,\mathrm{d}\mathbf{r} = \sum_{i=1}^{n}\int\rho_i(\mathbf{r})\{\ln[\rho_i(\mathbf{r})\Lambda_i^3]-1\}\mathrm{d}\mathbf{r} \tag{36}$$

and depends only on the local density of the species.

The functional derivative of $F^{id}[\{\rho_k(\mathbf{r})\}]$ with respect to $\rho_i(\mathbf{r})$ is given by

$$\frac{\delta\beta F^{id}[\{\rho_k(\mathbf{r})\}]}{\delta\rho_i(\mathbf{r})} = \ln[\rho_i(\mathbf{r})\Lambda_i^3] \tag{37}$$

Thus, the ideal gas contribution of the component i to the chemical potential in the bulk solution can be deduced resulting in Eq. (30).

1.2.3 Short-range repulsion

The short-range repulsion among molecules can be conveniently represented by a hard sphere model, in which the overlap of the atoms/molecules is prohibited.

A notable class of methods based on the fundamental geometric measures of the hard particle has been highlighting over the years: the fundamental measure theory (FMT)[113,114], which was first introduced by Rosenfeld[113] in 1989. Since then, numerous modifications have been proposed in order to improve the determination of the structure and thermodynamic properties especially of condensed systems.[115–118]

The FMT was constructed on physical foundation combining the ideas from the scaled-particle theory (SPT) and the Percus-Yevick (PY) compressibility equation of state. According to this theory, the excess Helmholtz energy functional due to the hard sphere exclusion volume F^{hs} is defined by [113]

$$\beta F^{hs}[\{\rho_k(\mathbf{r})\}] = \int \Phi^{hs}(\{n_\alpha(\mathbf{r})\})\mathrm{d}\mathbf{r} \tag{38}$$

where Φ^{hs} is the reduced Helmholtz energy density and $\{n_\alpha(\mathbf{r})\}$ is the set of the weighted densities for the n-component mixture given by

$$n_\alpha(\mathbf{r}) = \sum_{i=1}^{n} n_{\alpha,i}(\mathbf{r}) = \sum_{i=1}^{n} \int \rho_i(\mathbf{r}')\omega_i^{(\alpha)}(\mathbf{r}-\mathbf{r}')\,\mathrm{d}\mathbf{r}' \tag{39}$$

where the integral is taken over all the space and $\alpha \in \{0,1,2,3,V1,V2\}$. The indexes $V1$ and $V2$ refer to the vector-like weighted densities. The dimension of n_α is equal to $[\text{volume}]^{\frac{(\alpha-3)}{3}}$. The weighting functions $\omega_i^{(\alpha)}(\mathbf{r})$ are related to the fundamental geometric measures of the hard spheres by[113,114]

$$\omega_i^{(0)}(\mathbf{r}) = \frac{\omega_i^{(2)}(\mathbf{r})}{\pi {\sigma_i}^2} \tag{40}$$

$$\omega_i^{(1)}(\mathbf{r}) = \frac{\omega_i^{(2)}(\mathbf{r})}{2\pi\sigma_i} \tag{41}$$

$$\omega_i^{(2)}(\mathbf{r}) = \delta\left(\frac{\sigma_i}{2} - |\mathbf{r}|\right) \tag{42}$$

$$\omega_i^{(3)}(\mathbf{r}) = \theta\left(\frac{\sigma_i}{2} - |\mathbf{r}|\right) \tag{43}$$

$$\boldsymbol{\omega}_i^{(V1)}(\mathbf{r}) = \frac{\boldsymbol{\omega}_i^{(V2)}(\mathbf{r})}{2\pi\sigma_i} \tag{44}$$

$$\boldsymbol{\omega}_i^{(V2)}(\mathbf{r}) = \frac{\mathbf{r}}{|\mathbf{r}|}\delta\left(\frac{\sigma_i}{2} - |\mathbf{r}|\right) \tag{45}$$

Here σ_i is the hard sphere diameter of the component i in the mixture, $\theta(r)$ is the Heaviside step function, and $\delta(r)$ is the Dirac-delta function. Integrations over $\omega_i^{(3)}(\mathbf{r})$, $\omega_i^{(2)}(\mathbf{r})$, $\omega_i^{(1)}(\mathbf{r})$, and $\omega_i^{(0)}(\mathbf{r})$ give respectively the volume ($\mathcal{V}_i$), the surface area, the mean radius of curvature, and the Euler characteristics (equal to 1) of the sphere. The vector function $\boldsymbol{\omega}_i^{(V2)}(\mathbf{r})$ refers to the variance across the particle surface. Moreover, the integrals over the vector-like weighting functions vanish.[113,114] Particularly interesting is that the weighting functions are independent of the density distributions.

In the limit of the homogeneous system, the scalar weighted densities are equivalent to the SPT variables ξ_α in which[113,114]

$$n_0 \equiv \xi_0 = \sum_i \rho_i^b \tag{46}$$

$$n_1 \equiv \xi_1 = \frac{1}{2}\sum_i \rho_i^b \sigma_i \tag{47}$$

$$n_2 \equiv \xi_2 = \pi \sum_i \rho_i^b \, \sigma_i^2 \tag{48}$$

$$n_3 \equiv \xi_3 = \frac{\pi}{6}\sum_i \rho_i^b \sigma_i^3 \tag{49}$$

ξ_3 is also denominated the total packing fraction.

Regarding the reduced Helmholtz energy density Φ^{hs}, a dimensional analysis defines that

$$\Phi^{hs} = f_1(n_3)n_0 + f_2(n_3)n_1 n_2 + f_3(n_3)\,\mathbf{n}_1 \cdot \mathbf{n}_2 + f_4(n_3)n_2^3 + f_5(n_3)n_2 \mathbf{n}_2 \cdot \mathbf{n}_2 \tag{50}$$

here, the coefficients $\{f_0, \ldots, f_5\}$ are functions of n_3 and each term in Eq. (50) has dimension of [length]$^{-3}$. The difference between the original FMT proposed by Rosenfeld[113] and its modifications[116–120] is related to these coefficients. The reduced Helmholtz energy densities for some versions of FMT are presented in Table 1.

The original FMT (RF) failed to account for the freezing transition of the hard-sphere fluid into a solid or in systems with strong-confining external potentials due to a divergence in the excess Helmholtz energy density. The first attempts to overcome this problem consist in the dimensional crossover whereby the three dimensional functional was used to model two-, one-, and zero-dimensional densities, such as hard sphere confined in a slit pore, cylindrical pore or even, a cavity.[119–122] Examples are the antisymmetrized version of the original FMT (RF*)[119] and the approach developed by Tarazona,[122] which considers the inclusion of an additional tensorial weight function.

Furthermore, some modifications of the FMT involve the introduction of other equations of state (EoS) instead of the PY, like EoS developed for mixtures. The White-Bear (WB) version of the FMT is based on the Boublik-Mansoori-Carnahan-Starling-Leland equation of state (BMCSL) and presents more agreement to data from computer simulation mainly for confined fluids.[115,117,118] However the SPT differential equation,

$$\lim_{\sigma_i \to \infty} \frac{\beta \mu_i^{b,hs}}{\mathcal{V}_i} = \frac{\partial \Phi^{hs}}{\partial n_3} = \beta p \tag{51}$$

which plays an important role to the derivation of the original FMT, cannot be satisfied in the WB version, leading to a slight inconsistency. Here, $\mu_i^{b,hs}$ refers to the excess chemical potential due to the hard sphere exclusion volume at bulk reservoir.

In Table 1, it is possible to observe the difference between the pressures estimated by the FMT and the EoS by comparing the columns $\frac{\partial \Phi^{hs}}{\partial n_3}$ and "Bulk Pressure based on the EoS". Since $\mathbf{n}_{V1}$ and $\mathbf{n}_{V2}$ vanish at the bulk solution, it is rather clear that the original FMT and the antisymmetrized version presented in Table 1 satisfy Eq. (51). In order to take advantage of like- BMCSL equation of state and keeping the consistency for pressure, Hansen-Goos and Roth[123] proposed the White-Bear mark II version of the FMT (WBII), whereby the expansion of the logarithm term of the $\frac{\partial \Phi^{hs}}{\partial n_3}$ in a series

$$\ln(1-n_3) = -n_3 - \frac{n_3^2}{2} - \mathcal{O}(n_3^3) \tag{52}$$

leads to the reproduction of the pressure defined by the CSIII (modified version of the BMCSL), where $\mathcal{O}(n_3^3)$ refers to terms of order n_3^3 or smaller.

The FMT has also been developed to geometries different from the hard sphere, such as hard platelets and hard rods.[114,124,125]

Moreover, a method based on the Carnahan-Starling equation of state applied to simple fluids[126] and on the integration of the generalized Flory equation of state[127] with the addiction of the hard sphere interaction to characterize polymeric fluids has been used in the literature especially to model the exclusion volume in polymeric solutions: the so-called Forsman, Woodward and Freasier method (FWF).[128]

The hard-sphere contribution to the first-order direct correlation function is equal to

$$c_i^{(1)hs}(\mathbf{r}) = -\frac{\delta \beta F^{hs}[\Phi^{hs}(\{n_\alpha\})]}{\delta \rho_i(\mathbf{r})} = -\sum_\alpha \int \frac{\partial \Phi^{hs}(\{n_\alpha\})}{\partial n_\alpha} \frac{\delta n_\alpha(\mathbf{r}')}{\delta \rho_i(\mathbf{r})} \mathrm{d}\mathbf{r}' \tag{53}$$

in which, for Cartesian coordinates, the functional derivative of $n_\alpha(\mathbf{r}')$ with respect to $\rho_i(\mathbf{r})$ reduces to

$$\frac{\delta n_\alpha(\mathbf{r}')}{\delta \rho_i(\mathbf{r})} = \frac{\delta}{\delta \rho_i(\mathbf{r})} \sum_i \int \rho_i(\mathbf{r}'') \omega_i^{(\alpha)}(\mathbf{r}' - \mathbf{r}'') \, \mathrm{d}\mathbf{r}'' = \omega_i^{(\alpha)}(\mathbf{r}' - \mathbf{r}) \tag{54}$$

It is worthwhile to note that the argument in the weighting function in Eq. (39) is different from Eq. (53). For the scalar weighting functions, it is irrelevant since they are even functions; however the vector weighting functions are odd functions, resulting in[117]

$$\boldsymbol{\omega}_i^{(\alpha)}(\mathbf{r}' - \mathbf{r}) = -\boldsymbol{\omega}_i^{(\alpha)}(\mathbf{r} - \mathbf{r}') \tag{55}$$

The partial derivative of $\Phi^{hs}(\{n_\alpha\})$ with respect to $\{n_\alpha\}$ for some versions of the FMT are shown in Table 2. In addition, the hard-sphere contribution to the chemical potential at the bulk fluid is

$$\beta\mu_i^{b,hs} = \sum_\alpha \frac{\partial\Phi^{hs}}{\partial n_\alpha}\frac{\partial n_\alpha}{\partial \rho_i^b} = \frac{\partial\Phi^{hs}}{\partial n_0} + \frac{\partial\Phi^{hs}}{\partial n_1}\frac{\sigma_i}{2} + \frac{\partial\Phi^{hs}}{\partial n_2}\pi\sigma_i^2 + \frac{\partial\Phi^{hs}}{\partial n_3}\frac{\pi\sigma_i^3}{6} \tag{56}$$

The integrals in Eqs. (39) and (54) are convolutions; therefore, they can be evaluated in the real or reciprocal space. Writing the weighted densities and the hard-sphere contribution to first-order direct correlation function using the Fourier transform and the convolution theorem yields, respectively,

$$n_\alpha(\mathbf{r}) = \sum_{i=1}^{n} \mathcal{F}^{-1}\left[\mathcal{F}(\rho_i)\cdot\mathcal{F}\left(\omega_i^{(\alpha)}\right)\right] = \mathcal{F}^{-1}\left[\sum_{i=1}^{n}\mathcal{F}(\rho_i)\cdot\mathcal{F}\left(\omega_i^{(\alpha)}\right)\right] \tag{57}$$

$$c_i^{(1)hs}(\mathbf{r}) = -\sum_\alpha \mathcal{F}^{-1}\left\{\mathcal{F}\left[\frac{\partial\Phi^{hs}[\{n_\alpha\}]}{\partial n_\alpha}\right]\cdot\mathcal{F}\left[\pm\omega_i^{(\alpha)}\right]\right\} \tag{58}$$

where $\mathcal{F}$ and $\mathcal{F}^{-1}$ denote, respectively, the Fourier transform and its inverse.[108,114,117]

The calculation of these convolutions in reciprocal space has a couple of advantages compared to real space, including computational speed and numerical accuracy.[108,129–131] The former is justified by the reduction of the number of operations from $\mathcal{O}(\mathcal{N}^2)$ in the real space to $\mathcal{O}(\mathcal{N}\log\mathcal{N})$ using fast Fourier transform (FFT), where $\mathcal{N}$ is the number of grid points.[132] Furthermore, the convolutions of densities inside and at the surface of the spheres are not computed with sufficient accuracy in real-space, mainly in two- and three-dimensional systems, even with very fine discretization.[108] For example, if bulk concentrations are used in Eq. (39), the geometric measures of the sphere are not recovered with usual real methods. However, specialized quadrature might reverse this scenario.[108,117] On the other hand, since

$\mathcal{F}\left(\omega_i^{(\alpha)}\right)$ are distributions, it is not trivial to represent them on the rectangular grid using FFT with excellent accuracy. To address this problem, Knepley *et al*.[108] suggested the calculation of each weighting function analytically on the same mesh as the fast Fourier transform (in order to be consistent with $\hat{\rho}_i$ computed by the FFT). This alternative is able to reproduce the geometric measures of the spheres when the weighting functions are convoluted with constant densities. Moreover real space methods are more sensitive to grid size than reciprocal space methods.[108,131]

Table 1 – Excess free energy density for theories based on FMT

FMT	Φ	$\frac{\partial \Phi}{\partial n_3}$	Bulk Pressure based on the EoS βp
RF	$-n_0 \ln(1-n_3) + \frac{n_1 n_2 - \mathbf{n}_{V1}\cdot\mathbf{n}_{V2}}{1-n_3} + \frac{n_2^3 - 3n_2 \mathbf{n}_{V2}\cdot\mathbf{n}_{V2}}{24\pi(1-n_3)^2}$	$\frac{n_0}{1-n_3} + \frac{n_1 n_2 - \mathbf{n}_{V1}\cdot\mathbf{n}_{V2}}{(1-n_3)^2} + \frac{n_2^3 - 3n_2\mathbf{n}_{V2}\cdot\mathbf{n}_{V2}}{12\pi(1-n_3)^3}$	$\frac{n_0}{1-n_3} + \frac{n_1 n_2}{(1-n_3)^2} + \frac{n_2^3}{12\pi(1-n_3)^3}$
RF*	$-n_0 \ln(1-n_3) + \frac{n_1 n_2 - \mathbf{n}_{V1}\cdot\mathbf{n}_{V2}}{1-n_3} + \frac{n_2^3}{24\pi(1-n_3)^2}\left(1 - \frac{\mathbf{n}_{V2}\cdot\mathbf{n}_{V2}}{n_2^2}\right)^3$	$\frac{n_0}{1-n_3} + \frac{n_1 n_2 - \mathbf{n}_{V1}\cdot\mathbf{n}_{V2}}{(1-n_3)^2} + \frac{n_2^3}{12\pi(1-n_3)^3}\left(1 - \frac{\mathbf{n}_{V2}\cdot\mathbf{n}_{V2}}{n_2^2}\right)^3$	
WB	$-n_0 \ln(1-n_3) + \frac{n_1 n_2 - \mathbf{n}_{V1}\cdot\mathbf{n}_{V2}}{1-n_3} + (n_2^3 - 3n_2\,\mathbf{n}_{V2}\cdot\mathbf{n}_{V2}) \times \frac{n_3 + (1-n_3)^2\ln(1-n_3)}{36\pi\, n_3^2 (1-n_3)^2}$	$\frac{n_0}{1-n_3} + \frac{n_1 n_2 - \mathbf{n}_{V1}\cdot\mathbf{n}_{V2}}{(1-n_3)^2} - (n_2^3 - 3n_2\mathbf{n}_{V2}\cdot\mathbf{n}_{V2}) \times \left[\frac{2 + n_3(n_3-5)}{36\pi\, n_3^2(1-n_3)^3} + \frac{\ln(1-n_3)}{18\pi\, n_3^3}\right]$	$\frac{n_0}{1-n_3} + \frac{n_1 n_2}{(1-n_3)^2} + \frac{n_2^3\left[1 - \frac{1}{3}n_3\right]}{12\pi(1-n_3)^3}$
WBII	$-n_0 \ln(1-n_3) + \frac{n_1 n_2 - \mathbf{n}_{V1}\cdot\mathbf{n}_{V2}}{1-n_3}\phi_2(n_3) + \frac{n_2^3 - 3n_2\mathbf{n}_{V2}\cdot\mathbf{n}_{V2}}{24\pi\,(1-n_3)^2}\phi_3(n_3)$	$\frac{n_0}{1-n_3} + \frac{n_1 n_2 - \mathbf{n}_{V1}\cdot\mathbf{n}_{V2}}{(1-n_3)^2}\left(1 + \frac{1}{3}n_3^2\right) + \frac{n_2^3 - 3n_2\mathbf{n}_{V2}\cdot\mathbf{n}_{V2}}{12\pi(1-n_3)^3}\left(1 - \frac{2}{3}n_3 + \frac{1}{3}n_3^2\right)$	$\frac{n_0}{1-n_3} + \frac{n_1 n_2\left(1 + \frac{1}{3}n_3^2\right)}{(1-n_3)^2} + \frac{n_2^3\left(1 - \frac{2}{3}n_3 + \frac{1}{3}n_3^2\right)}{12\pi(1-n_3)^3}$

Legend: RF is the original FMT,[113] RF* is the antisymmetrized version of RF,[119] WB is the White-Bear version,[115] and WBII is the White-Bear mark II.[123] $\phi_2(n_3) = 1 + 3n_3^{-1}[2n_3 - n_3^2 + 2(1-n_3)\ln(1-n_3)]$, $\phi_3(n_3) = 1 - 3n_3^{-2}[2n_3 - 3n_3^2 + 2n_3^3 + 2(1-n_3)^2\ln(1-n_3)]$. For $\partial\Phi^{\mathrm{WBII}}/\partial n_3$, the logarithm term was expanded as $\ln(1-n_3) = -n_3 - \frac{n_3^2}{2} - \mathcal{O}(n_3^3)$.

Table 2 – Partial derivative of the excess free energy density for theories based on FMT

FMT	$\frac{\partial\Phi}{\partial n_0}$	$\frac{\partial\Phi}{\partial n_1}$	$\frac{\partial\Phi}{\partial n_2}$	$\frac{\partial\Phi}{\partial \mathbf{n}_{V1}}$	$\frac{\partial\Phi}{\partial \mathbf{n}_{V2}}$
RF	$-\ln(1-n_3)$	$\frac{n_2}{1-n_3}$	$\frac{n_1}{1-n_3}+\frac{n_2^2-\mathbf{n}_{V2}\cdot\mathbf{n}_{V2}}{8\pi(1-n_3)^2}$	$-\frac{\mathbf{n}_{V2}}{1-n_3}$	$-\frac{\mathbf{n}_{V1}}{1-n_3}-\frac{n_2\mathbf{n}_{V2}}{4\pi(1-n_3)^2}$
RF*	$-\ln(1-n_3)$	$\frac{n_2}{1-n_3}$	$\frac{n_1}{1-n_3}+\frac{n_2^2}{8\pi(1-n_3)^2}\left(1-\frac{\mathbf{n}_{V2}\cdot\mathbf{n}_{V2}}{n_2^2}\right)^3+\frac{\mathbf{n}_{V2}\cdot\mathbf{n}_{V2}}{4\pi(1-n_3)^2}\left(1-\frac{\mathbf{n}_{V2}\cdot\mathbf{n}_{V2}}{n_2^2}\right)^2$	$-\frac{\mathbf{n}_{V2}}{1-n_3}$	$-\frac{\mathbf{n}_{V1}}{1-n_3}-\frac{n_2\mathbf{n}_{V2}}{4\pi(1-n_3)^2}\left(1-\frac{\mathbf{n}_{V2}\cdot\mathbf{n}_{V2}}{n_2^2}\right)^2$
WB	$-\ln(1-n_3)$	$\frac{n_2}{1-n_3}$	$\frac{n_1}{1-n_3}+(n_2^2-\mathbf{n}_{V2}\cdot\mathbf{n}_{V2})\times\frac{n_3+(1-n_3)^2\ln(1-n_3)}{12\pi\, n_3^2(1-n_3)^2}$	$-\frac{\mathbf{n}_{V2}}{1-n_3}$	$-\frac{\mathbf{n}_{V1}}{1-n_3}-n_2\,\mathbf{n}_{V2}\frac{n_3+(1-n_3)^2\ln(1-n_3)}{6\pi\, n_3^2(1-n_3)^2}$
WBII	$-\ln(1-n_3)$	$\frac{n_2}{1-n_3}\phi_2(n_3)$	$\frac{n_1}{1-n_3}\phi_2(n_3)+\frac{n_2^2-\mathbf{n}_{V2}\cdot\mathbf{n}_{V2}}{8\pi\,(1-n_3)^2}\phi_3(n_3)$	$-\frac{\mathbf{n}_{V2}}{1-n_3}\phi_2(n_3)$	$-\frac{\mathbf{n}_{V1}}{1-n_3}\phi_2(n_3)-\frac{n_2\mathbf{n}_{V2}}{4\pi\,(1-n_3)^2}\phi_3(n_3)$

Legend: RF is the original FMT,[113] RF* is the antisymmetrized version of RF,[119] WB is the White-Bear version,[115] and WBII is the White-Bear mark II.[123] $\phi_2(n_3)=1+3n_3^{-1}[2n_3-n_3^2+2(1-n_3)\ln(1-n_3)]$, $\phi_3(n_3)=1-3n_3^{-2}[2n_3-3n_3^2+2n_3^3+2(1-n_3)^2\ln(1-n_3)]$.

1.2.4 Electrostatics

The electrostatic contribution to the intrinsic Helmholtz energy functional can be divided into two parts: one is related to the direct Coulomb interactions (F^C), which is similar to the electrostatic interactions in the PBE, and the other one refers to the charge distribution correlations (F^{el}). The latter is an attractive van der Waals-like interaction that gives rise to attraction between equally charged particles, for example.

The interaction potential u_{ij} between any pair of spheres i and j in the system is usually represented by

$$\beta u_{ij}(\mathbf{r}) = \begin{cases} \infty & |\mathbf{r}| < \sigma_{ij} \\ \dfrac{\lambda_B z_i z_j}{|\mathbf{r}|} & |\mathbf{r}| \geq \sigma_{ij} \end{cases} \tag{59}$$

where σ_{ij} is the arithmetic average between the diameters of particles i and j, and λ_B is the so-called Bjerrum length, defined as

$$\lambda_B = \frac{\beta e^2}{4\pi\varepsilon\varepsilon_0} \tag{60}$$

which represents the distance between the centers of two elementary charges in a medium with dielectric constant ε and with Coulomb potential equal to the thermal energy – $k_B T$. Consequently, the direct Coulomb contribution F^C is defined by[25,34]

$$\beta F^C[\{\rho_k(\mathbf{r})\}] = \frac{\lambda_B}{2} \sum_i \sum_j \iint \frac{z_i z_j \rho_i(\mathbf{r}) \rho_j(\mathbf{r}')}{|\mathbf{r} - \mathbf{r}'|} \mathrm{d}\mathbf{r}\mathrm{d}\mathbf{r}' \tag{61}$$

and the local first-order direct correlation function due to the direct Coulomb contribution, $c_i^{(1)C}(\mathbf{r})$ is[109]

$$c_i^{(1)C}(\mathbf{r}) = -\lambda_B z_i \sum_j \int \frac{z_j \rho_j(\mathbf{r}')}{|\mathbf{r} - \mathbf{r}'|} \mathrm{d}\mathbf{r}' \tag{62}$$

Furthermore the interaction Ψ_i between the charged sphere i and a charged planar surface is usually equivalent to[25,109]

$$\beta\Psi_i(\mathbf{r}) = \begin{cases} \infty & \mathbf{r}_\perp < \dfrac{\sigma_i}{2} \\ -\dfrac{2\pi\lambda_B z_i Q}{e}\mathbf{r}_\perp & \mathbf{r}_\perp \geq \dfrac{\sigma_i}{2} \end{cases} \tag{63}$$

where $\mathbf{r}_\perp$ is the perpendicular distance from the surface to the center of the sphere i. The combination of the direct Coulomb interaction and the external electric potential due to the charged surface gives the mean electrostatic potential:[25]

$$z_i e\psi(\mathbf{r}) = \Psi_i(\mathbf{r}) + \frac{\delta F^C[\{\rho_k(\mathbf{r})\}]}{\delta\rho_i(\mathbf{r})} \tag{64}$$

To avoid divergence during the computation, the mean electrostatic potential is calculated by Poisson equation – Eq. (1) – instead of the explicit contributions from $F^C[\{\rho_k(\mathbf{r})\}]$ and Ψ.

Neglecting the size and electrostatic correlations effects and considering only the contributions due to the direct Coulomb interactions, Eq. (31) reduces to the well-known Boltzmann Equation, Eq. (2).

For Cartesian coordinates with symmetry in $\hat{\mathbf{y}}$ and $\hat{\mathbf{z}}$ directions and boundary conditions equal to $\mathrm{d}\psi(x)/\mathrm{d}x|_{x\to\infty} = 0$ e $\psi(x \to \infty) = 0$, the mean electrostatic potential can be written as[25]

$$\beta e\psi(x) = 4\pi\lambda_B \int_x^\infty (x - x') \sum_i z_i \rho_i(x')\,\mathrm{d}x' \tag{65}$$

based on the Poisson equation. More information about the derivation of Eq. (65) is presented in the APPENDIX D.

Since the electrostatic correlations play an important role in systems with electric double layers, many approaches have been developed in order to quantify these effects such as perturbation methods,[34,114,133–135] one-component plasma (OCP) model,[98,136–139] energy

route MSA-based solution (MSA-ER),[140–143] and functional integration with the DCFs from the MSA.[109,144]

The bulk fluid density perturbation (BFD) is the most traditional method to take into account the ion-ion correlation.[34,114,133] It is based on a quadratic functional expansion in Taylor series around the densities at the bulk solution applied only to the long-range component of the ionic interactions:

$$\beta F^{el}[\{\rho_k(\mathbf{r})\}] = \beta F^{el}\left[\{\rho_k^b\}\right] - \sum_i \int c_i^{(1)el}\left[\{\rho_k^b\}\right]\Delta\rho_i(\mathbf{r})\mathrm{d}\mathbf{r} - \frac{1}{2}\sum_i\sum_j \iint c_{ij}^{(2)el}\left[\{\rho_k^b\}; |\mathbf{r}-\mathbf{r}'|\right]\Delta\rho_i(\mathbf{r})\Delta\rho_j(\mathbf{r}')\mathrm{d}\mathbf{r}\mathrm{d}\mathbf{r}' \tag{66}$$

where $\Delta\rho_i(\mathbf{r}) = \rho_i(\mathbf{r}) - \rho_i^b$ and the bulk DCFs are defined by

$$c_i^{(1)el}\left[\{\rho_k^b\}\right] \equiv -\left.\frac{\delta\beta F^{el}[\{\rho_k(\mathbf{r})\}]}{\delta\rho_i(\mathbf{r})}\right|_b = -\beta\mu_i^{b,el} \tag{67}$$

$$c_{ij}^{(2)el}\left[\{\rho_k^b\}; |\mathbf{r}-\mathbf{r}'|\right] \equiv -\left.\frac{\delta^2\beta F^{el}[\{\rho_k(\mathbf{r})\}]}{\delta\rho_i(\mathbf{r})\delta\rho_j(\mathbf{r}')}\right|_b \tag{68}$$

whereas the local first-order direct correlation function due to the electrostatic screening interactions is represented by

$$c_i^{(1)el}(\mathbf{r}) = -\beta\mu_i^{b,el} + \sum_j \int c_{ij}^{(2)el}\left[\{\rho_k^b\}; |\mathbf{r}-\mathbf{r}'|\right]\Delta\rho_j(\mathbf{r}')\mathrm{d}\mathbf{r}' \tag{69}$$

Here $\mu_i^{b,el}$ is the excess chemical potential due to the ion-ion correlation at the bulk solution. According to Eq. (69), $c_i^{(1)el}(\mathbf{r})$ is linearly proportional to the local density deviation. The second-order direct correlation function is conventionally calculated on the basis of the mean-spherical approximation (MSA).[145–147] For more information about MSA, see APPENDIX E.

In contrast with typical mean-field theory based on modifications of the PBE, the quadratic expansion is able to detect some counterintuitive phenomena as, for example, the charge inversion near a macroparticle and attraction between same like-charged particles.[26,133,148] Even so, this approach has some limitations especially for systems weakly

inhomogeneous as those with neutral or slightly charged surfaces.[27,29,133] In light of these unexpected findings, new approaches have been proposed in order to improve the contact densities in systems where the BFD fails.

Patra e Gosh[149,150] were the pioneers to implement a perturbation expansion around position-dependent weighted densities; nevertheless the behavior was similar to the BFD. Almost one decade after this first attempt, Gillespie and coworkers[134,135] successfully proposed the reference fluid density perturbation (RFD) method, which is very similar to the BFD; however, instead of the expansion around a uniform value of density equivalent to the bulk, a reference fluid profile is chosen:

$$\rho_i^{ref}[\{\rho_k(\mathbf{r})\};\mathbf{r}] = \frac{3}{4\pi R_{el}^3(\mathbf{r})}\int \alpha_i^{el}(\mathbf{r}')\rho_i(\mathbf{r}')\theta\big(|\mathbf{r}'-\mathbf{r}| - R_{el}(\mathbf{r})\big)\mathrm{d}\mathbf{r}' \tag{70}$$

in which R_{el} is the local electrostatic length scale and $\{\alpha_i^{el}\}$ are chosen in order to guarantee that the fluid with densities $\{\alpha_i^{el}(\mathbf{r})\rho_i(\mathbf{r})\}$ is electroneutral and has the same ionic strength of the original fluid over the whole space.

According to the RFD approach, the intrinsic Helmholtz energy functional due to the charge distribution correlations is

$$\begin{aligned}\beta F^{el}[\{\rho_k(\mathbf{r})\}] = {}& \beta F^{el}\big[\{\rho_k^{ref}(\mathbf{r})\}\big] - \sum_i \int c_i^{(1)el}\big[\{\rho_k^{ref}(\mathbf{r})\};\mathbf{r}\big]\Delta\rho_i^{ref}(\mathbf{r})\mathrm{d}\mathbf{r} \\ & -\frac{1}{2}\sum_i\sum_j \iint c_{ij}^{(2)el}\big[\{\rho_i^{ref}(\mathbf{r})\};|\mathbf{r}-\mathbf{r}'|\big]\Delta\rho_i^{ref}(\mathbf{r})\Delta\rho_j^{ref}(\mathbf{r}')\mathrm{d}\mathbf{r}\mathrm{d}\mathbf{r}'\end{aligned} \tag{71}$$

while the local first-order direct correlation function is described by[134,135]

$$c_i^{(1)el}(\mathbf{r}) = c_i^{(1)el}\big[\{\rho_k^{ref}\};\ \mathbf{r}\big] + \sum_j \int c_{ij}^{(2)el}\big[\{\rho_k^b\};|\mathbf{r}-\mathbf{r}'|\big]\Delta\rho_j^{ref}(\mathbf{r}')\mathrm{d}\mathbf{r}' \tag{72}$$

where $\Delta\rho_i^{ref}(\mathbf{r}) = \rho_i(\mathbf{r}) - \rho_i^{ref}(\mathbf{r})$ and the direct correlation functions in a point of the reference fluid is defined analogously to Eqs. (67) and (68). Since the local electroneutrality is satisfied everywhere in the whole system, the DCFs can also be computed by the MSA.[145–147]

Gillespie, Valiskó and Boda[135] reported an improvement in the density profiles using RFD compared to the BFD for systems with uncharged or slightly charged surfaces; however, both methods are unable to predict the liquid-vapor phase transition.[151,152]

Similar to the BFD and RFD approaches, the weighted correlation approach (WCA) defines the local first-order DFC as a linear response of the density deviation, even though it is a non-perturbative method based on weighted second-order DCF $\overline{c}_{ij}^{(2)el}$.[109,144]

According to the WCA, which follows the integration path, the local first-order direct correlation function is described by[109,144]

$$c_i^{(1)el}(\mathbf{r}) = -\beta\mu_i^{b,el} + \sum_j \int \overline{c}_{ij}^{(2)el}[\{\rho_k\}; \mathbf{r}, \mathbf{r}']\Delta\rho_j(\mathbf{r}')\mathrm{d}\mathbf{r}' \tag{73}$$

where

$$\overline{c}_{ij}^{(2)el}[\{\rho_k\}; \mathbf{r}, \mathbf{r}'] = \frac{\int \kappa^2(\mathbf{r}'')\, c_{ij}^{(2)el}[\{\rho_k(\mathbf{r}'')\}; |\mathbf{r}-\mathbf{r}'|]\, \theta\big(|\mathbf{r}-\mathbf{r}''| - \sigma_{ij}\big)\, \mathrm{d}\mathbf{r}''}{\int \kappa^2(\mathbf{r}'')\ \theta\big(|\mathbf{r}-\mathbf{r}''| - \sigma_{ij}\big)\, \mathrm{d}\mathbf{r}''} \tag{74}$$

and the local Debye length $\kappa^{-1}(\mathbf{r})$ defined as

$$\kappa^2(\mathbf{r}) = 4\pi\lambda_B \sum_i z_i^2 \rho_i(\mathbf{r}) \tag{75}$$

Although the electroneutrality at every point of the local densities $\{\rho_k(\mathbf{r})\}$ is not guaranteed, Wang and coworkers[109,144] compute the second-order DCF using MSA and, surprisingly, they showed that WCA predicts with good agreement the densities close to surfaces and the pressure between charged surfaces compared to molecular simulation data. At this point, it is important to highlight that MSA was developed for bulk electrolytes (APPENDIX E). [145–147]

The contact-corrected approach[152,153] (CCA) is based on the framework of the WCA; however, instead of using the original density profiles to compute the $c_{ij}^{(2)el}$ and the local Debye length, it uses the local reference densities defined by Gillespie and coworkers.[134] Therefore, according to the CCA, the local first-order direct correlation function can be written as[152,153]

$$c_i^{(1)el}(\mathbf{r}) = c_i^{(1)el}\left[\{\rho_k^{ref}\};\ \mathbf{r}\right] + \sum_j \int \overline{c}_{ij}^{(2)el}\left[\{\rho_k^{ref}(\mathbf{r}')\};\mathbf{r},\mathbf{r}'\right]\Delta\rho_j^{ref}(\mathbf{r}')\mathrm{d}\mathbf{r}' \tag{76}$$

Another improvement of this model is the incorporation of an empirical nonlinear interpolation that modifies the ion density profiles from the standard DFT calculation in order to assure the contact value theorem.[152,153] For electrolytes in contact with a planar surface, the contact-value theorem establishes that the sum of the ion densities at the minimum distance from surface, $\rho_i\left(\frac{\sigma_i}{2}\right)$, is related to the bulk osmotic pressure p_{EDL} and the surface charge density as[67,107,154]

$$k_B T \sum_i \rho_i\left(\frac{\sigma_i}{2}\right) = p_{\mathrm{EDL}} + \frac{Q^2}{2\varepsilon_0\varepsilon} \tag{77}$$

In contrast with the BFD, RFD, and WCA, CCA presents a consistency between the bulk osmotic pressure described by MSA[155], p_{MSA}, and the one computed from the contact-value theorem. As a matter of fact, this is expected since the methodology involves a mixing step between the density profiles ρ_i^{DFT} calculated from the Euler-Lagrange using standard DFT and the deviation $\Delta\rho_c$ of the contact-value theorem:

$$\rho_i(x) = \rho_i^{DFT}(x) + f_i(x)\Delta\rho_c \tag{78}$$

where

$$\Delta\rho_c \equiv \beta p_{\mathrm{MSA}} + \frac{\beta Q^2}{2\varepsilon_0\varepsilon} - \sum_i \rho_i^{DFT}\left(\frac{\sigma_i}{2}\right) \tag{79}$$

and $f_i(x)$ is the empirical interpolation function given by[152]

$$f_i(x) = \phi_i^{DFT}(x)\exp\left[1 - \left(\frac{x}{\sigma_i} - 0.5\right)^{\frac{\beta\left(p_{\mathrm{EDL}} + \frac{Q^2}{2\varepsilon_0\varepsilon}\right)}{\sum_i \rho_i^b}}\right] \tag{80}$$

Here, ϕ_i^{DFT} is the local ionic volume fraction according to the standard DFT. It is worthwhile to note that the CCA was developed to one-dimensional systems in the presence of a planar surface. For other geometries, this theory is not straightforward; one possibility of generalization would involve Maxwell equations and the pressure tensor.

Following a different route from the previous methods, the contributions from the electrostatic interactions in the intrinsic Helmholtz functional can be evaluated on the basis of the hole corrected Debye–Hückel theory (DHH) to one-component plasma (OCP), given by[98,136–139]

$$\beta F^{el}[\{\rho_k(\mathbf{r})\}] = \beta \sum_i \int \rho_i(\mathbf{r}) f_i^{el}\left(\rho_i^{ref}(\mathbf{r})\right) \mathrm{d}\mathbf{r} \tag{81}$$

where f_i^{el} is the electrostatic correlation Helmholtz energy of the ith particle, given by

$$f_i^{el}\left(\rho_i^{ref}(\mathbf{r})\right) = \frac{1}{4}\left[1 + \frac{2\pi}{3\sqrt{3}} - \ln 3 + \ln\left(\omega_i^2 + \omega_i + 1\right) - \omega_i^2 - \frac{2}{\sqrt{3}}\tan^{-1}\left(\frac{2\omega_i + 1}{\sqrt{3}}\right)\right] \tag{82}$$

with

$$\omega_i(\mathbf{r}) = \left(1 + |z_i|^3 (3\lambda_B)^{3/2} \sqrt{\frac{4\pi\rho_i^{ref}(\mathbf{r})}{3}}\right)^{1/3} \tag{83}$$

The density of the reference fluid is defined by Eq. (70) with constant $\alpha_i^{el}(\mathbf{r}) = 1$. Here the local electrostatic length scale is equivalent to the diameter of the correlation hole and can be approximated by the particle diameter or computed by an iterative method according to DHH.[136]

It should be pointed out that DHH assumes an approximate constant range of the ions correlations in the whole system, which in turn is governed by high density regimes where like-charged ions are packed relatively close together. [136] Thus, at high densities, some corrections due to steric effects should be included; however, they are usually neglected. Besides, it presents some deviations regarding the contact-value theorem. [136]

Notwithstanding its limitations, DHH is able to reproduce satisfactorily the molecular simulation data of bulk pressure, differential capacitance and density profiles for some complex systems, like confined ionic liquids.[98,136,137]

The framework of the energy route is similar to the FMT. Hence, the intrinsic Helmholtz functional is related to the reduced Helmholtz energy density as[143,147]

$$\beta F^{el}[\{\rho_k(\mathbf{r})\}] = \int \Phi^{el}\left(\{\rho_k^{ref}(\mathbf{r})\}\right)\mathrm{d}\mathbf{r} \tag{84}$$

where Φ^{el} is the reduced Helmholtz energy density due to electrostatic correlations, given by[143,147]

$$\Phi^{el}\left(\{\rho_k^{ref}(\mathbf{r})\}\right) = -\lambda_B \sum_i z_i \rho_i^{ref}(\mathbf{r}) \frac{\Gamma(\mathbf{r})}{1+\Gamma(\mathbf{r})\sigma} + \frac{\Gamma(\mathbf{r})^3}{3\pi} \tag{85}$$

for restricted primitive model (RPM), where Γ is defined in the context of the mean-spherical approximation (APPENDIX E).

1.3 Non-electrostatic interactions between ions and surface

For the purpose of this thesis, non-electrostatic interactions refer to all non-Coulomb interactions, *i.e.* except the interactions from purely electrostatic forces.[3,4] Such interactions are responsible for the ionic specificity observed, for example, when two ions of the same valence affect differently the stability of colloidal systems. The first systematic research to study this effect was conducted by Hofmeister in 1887, who observed the precipitation of egg lysozyme in an aqueous dispersion by different salts at different concentrations.[66,67,156]

In the context of ions-surface interactions, the main approaches conventionally used to take into account this contribution in PBE and/or DFT are the inclusion of dispersion potentials from: Lifshitz theory,[21,65,157,158] potential of mean force (PMF) from molecular simulation,[43,50,52] and insertion of a direct potential, such as hard-wall,[109,118,141] Yukawa,[159,160] and Lennard-Jones.[97,98,161–164]

The Lifshitz theory ignores the atomic structure and the discrete nature of the solvent. As a consequence, the forces between particles are treated in a continuous medium described by the dielectric constant and the refractive index of the solvent and macroparticles (or surfaces).[67] The behavior of the particles is more appropriate represented by this theory when surfaces are farther away than molecular dimensions. The importance of this theory is related to the ability to calculate the Hamaker constant.[67,165]

For the calculation of the non-electrostatic potential between an ion i and a planar surface on the basis of the Lifshitz theory, we have[4,21,66,157]

$$V_i(\mathbf{r}) = -\frac{B_i}{\mathbf{r}_\perp{}^3} \qquad \mathbf{r}_\perp \geq \frac{\sigma_i}{2} \tag{86}$$

where B_i is the dispersion parameter of the ith ion, given by[165]

$$\beta B_i = \frac{\alpha_i^*(0)}{4\varepsilon_3(0)}\left[\frac{\varepsilon_2(0)-\varepsilon_3(0)}{\varepsilon_2(0)+\varepsilon_3(0)}\right] + \frac{h}{4\pi k_B T}\int_{\nu_{min}}^{\infty}\frac{\alpha_i^*(\nu)}{\varepsilon_w(\nu)}\left[\frac{\varepsilon_2(\nu)-\varepsilon_3(\nu)}{\varepsilon_2(\nu)+\varepsilon_3(\nu)}\right]d\nu \tag{87}$$

where $\varepsilon_j(0)$ and $\varepsilon_j(\nu)$ are the dielectric spectra of the j at the frequencies 0 and ν, respectively, $\alpha_i^*(0)$ and $\alpha_i^*(\nu)$ are the excess polarizabilities of the ion i at the frequency 0 and ν, and ν_{min} is the first non-null frequency ($\nu_{min} = 2\pi k_B T/h$). The subscript 2 refers to the surface or macroparticle and 3 is the solvent. The polarizability and dielectric constant vary with frequency much in the same way as a harmonic-oscillator model:[66,157]

$$\alpha_i^*(\nu) = \frac{\alpha_i^*(0)}{1+\left(\nu^2/\nu_{I,i}^2\right)} \tag{88}$$

$$\varepsilon_j(\nu) = 1 + \frac{n_{RI,j}^2 - 1}{1+\left(\nu^2/\nu_{e,j}^2\right)} \tag{89}$$

where $\nu_{I,i}$ is the ionization frequency of the ith ion, and $\nu_{e,j}$ is the main electronic absorption frequency in the UV and $n_{RI,j}$ is the refractive index in the visible of the jth medium. The ionization energy of ions in solution can be estimated based on the hydration Gibbs energy of these ions.[157]

By a closer look at Eq. (87), we can attest that the influence on the stability of colloidal systems by different salts in the same medium is directly related to the polarizability of the ions in solution.[4]

According to Ninham and Lo Nostro,[66] Eq. (86) is valid when the center of the ion is at least one or two diameters away from the surface. For positive values of B_i, the interaction is attractive, promoting, in general, an adsorption of the ion at the interface. On the other hand, negative values of B_i indicate a repulsion, and, consequently, an ion depletion on the surface.

The use of hybrid techniques, such as the insertion of PMF obtained from molecular simulation data in PBE and DFT, can improve considerably the prediction of both density profiles and thermodynamic properties. The PMF may account for the self-image potential, van der Waals interactions between ions, water and surface, ionic hydration effects, and effects from preferential orientation of water molecules.[52]

Horinek and Netz[52,53] obtained the PMF for some ions at infinite dilution in the vicinity of the interface between the aqueous solution and air or self-assembled monolayers of $C_{20}H_{42}$, using umbrella sampling and the weighted histogram analysis method. The PMFs were interpolated, and the provided functions were used to calculate the excess interfacial tension,[52,53] density profiles,[43,52,53] and double layer pressure between two surfaces.[50,51]

Especially for DFT, the hard wall potential is widely used and defines the minimum distance from the center of the ion to the surface as[109,118,141]

$$V_i(\mathbf{r}) = \begin{cases} \infty & \mathbf{r}_\perp < \dfrac{\sigma_i}{2} \\ 0 & \mathbf{r}_\perp \geq \dfrac{\sigma_i}{2} \end{cases} \tag{90}$$

Other famous potentials were also applied in DFT based on force fields from molecular simulation, such as the 9−3 and 12−6 Lennard-Jones potentials.[97,98,161–164,166]

2 APPLICATIONS TO BIOLOGICAL SYSTEMS

One important feature of biological systems is the ion partitioning observed between two different environments (*e.g.* intra- and extracellular environments), which originates the Donnan potential. Many important mechanisms for life, such as muscular contractions and synapses, only exist due to this difference.[167]

The Donnan potential occurs

a) in the presence of a selectively permeable membrane, which promotes an unequal distribution of ions between two electrolyte solutions, *i.e.*, it allows certain ions to move freely between the two solutions, whereas others are not allowed;

b) between two regions characterized by a solution with free ions and a charged membrane (or charged macromolecules).

The former situation is illustrated in Figure 2A by a lipid bilayer separating two different environments. The left compartment has some negatively charged proteins represented by "Ptn"; the membrane in the scheme is impermeable to these polyelectrolytes, while it is permeable to K^+ and Cl^- due to the presence of the ion channels. On the other hand, Figure 2B exemplifies the latter case with one region defined by polyelectrolyte brushes, solvent and free ions; whereas the other region only contains the solvent and mobile ions.

Figure 2 – Ion partitioning in biological systems: the Donnan potential

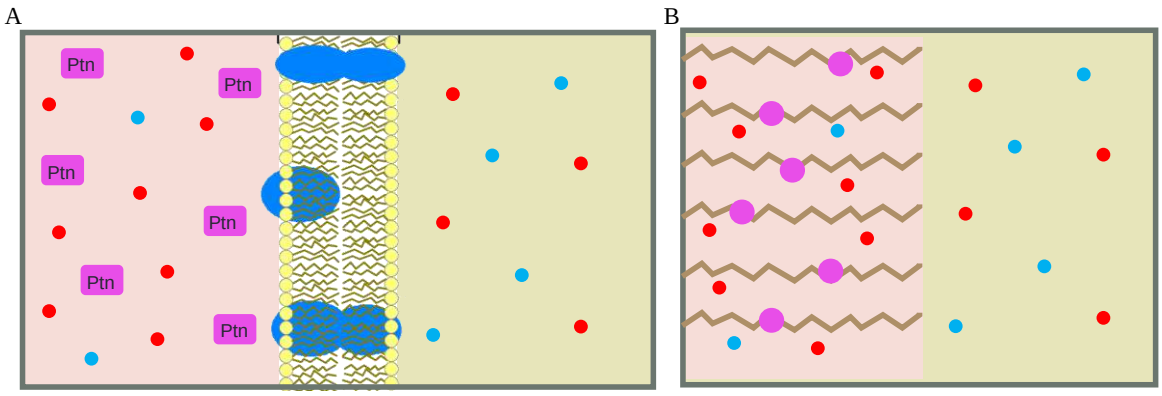

Legend: In (A), a lipid bilayer, which is impermeable to the polyelectrolyte "Ptn" with negative charge and permeable to K^+ (red circle) and Cl^- (blue circle), is separating two different compartments. In (B), the difference between the two compartments is due to the presence of polyelectrolyte brushes in one of them. The figure is not drawn to scale.

In other words, the Donnan potential occurs not only in the membrane equilibria but also in any situation in which there is a tendency to produce an ion partitioning.[57] It is worthwhile to note that the distribution of ions obeys the laws of thermodynamics and the principle of electroneutrality between the two compartments.[168,169]

According to the classical approach of the Donnan potential, there is a discontinuous potential gap between the two regions of interest, which can be computed by the Nernst equation as[102,170]

$$\psi_D = \frac{k_B T}{e z_i} \ln \frac{a_i^{\beta}}{a_i^{\alpha}} \tag{91}$$

where ψ_D is the Donnan potential and a_i is the activity of ion i in a phase (α or β).

Mauro[169] proposed a continuous Donnan potential using the PBE applied to two compartments adjacent to each other: one containing fixed charge completely ionized and another one without fixed charge. The Donnan potential calculated via PBE for remote regions is equal to the potential difference predict by the Nernst equation.[169,171] The strategy often found in the literature consists of solving the PBE for each side of the interface with boundary conditions that ensure the continuity of the electrostatic potential between the two phases.[169,170,172–174] For more information about the common boundary conditions reported in the literature, see APPENDIX F.[57]

The PBE was used to study two different biological systems. In the first (subsection 2.1), the potential profile across the *Bacillus brevis* cell wall was evaluated as a function of the solution pH, depending on the ionization of the cell wall functional groups (APPENDIX F). We introduced the concept of charge-regulated volume charge density to model the bacterial cell wall. For the second system, which is a continuation of the work developed during the Master, the membrane potential and ion partitioning in an erythrocyte were analyzed (subsection 2.2). The innovation refers to the inclusion of the Born correlation contribution in the PBE (APPENDIX G).

2.1 Electrostatic behavior of *Bacillus brevis* cell wall

2.1.1 Introduction

The electrical properties of bacterial cells are determined by a set of factors such as the type and the concentration of specific functional groups on the cell walls, the pH value, the composition and the ionic strength of electrolytes, and the separation distance from nearby surfaces.[74,175,176]

The presence of acidic and basic functional groups in the bacterial cell, including carboxyl, phosphoryl, hydroxyl and amine groups, is responsible for the charge on the surface.[177–179] In the cell walls of Gram-positive bacteria, these functional groups are associated with rigid and relatively thick layer of peptidoglycan and anionic polymers[180] – *e.g.* teichoic acid and theichuronic acid – as in the schematic structure presented in Figure 3.

Figure 3 – Scheme of the cell wall of Gram-positive bacteria

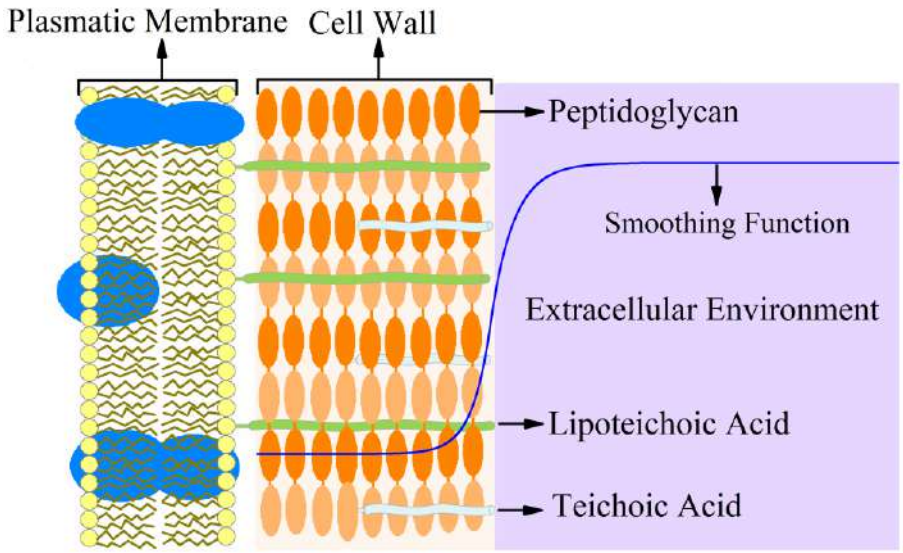

Note: The figure is not drawn to scale.
Source: Adapted from Barbosa, Lima and Tavares (2015).[57]

In the literature, some usual approximations to model the charge of the cell wall (or even, membrane or polyelectrolyte brushes) are: (i) charge regulation on the surface,[74] and (ii) constant volume charge density (*i.e.* charge uniformly distributed) for cell wall thickness much greater than the Debye length.[170,181] In the former assumption, the layer is treated as a

surface, neglecting its thickness, and the latter ignores the acid-base and (di)association reactions that can occur within the layer. In this thesis, we address these problems by the introduction of the charge-regulated volume charge density concept, which is characterized by bounded charges with uniform volume density of sites spread out in a part of the domain considering the dependence on the ionization of the functional groups as a function of the local concentration of free ions. Moreover, to avoid the resolution of the PBE for each adjacent compartment, we propose the use of a smoothing function to describe charged-regulated volume charge density profile in systems containing polyelectrolytes dispersed distinctively between two phases. In this context, the Donnan potential automatically arises from the resolution of the PBE for the two environments (with and without the polyelectrolytes) simultaneously. To evaluate the proposed strategy, the electrostatic potential profile across the *Bacillus brevis* (a gram-positive bacteria) cell wall is analyzed and the zeta potential is compared to experimental data.

2.1.2 Methodology

As previously mentioned, instead of solving the PBE twice (one for each side of the interface), we proposed the use of a smoothing function to describe the fixed volume charge density profile.

Smoothing functions – also known as regularization functions – are used to join two different functions of the same independent variable in order to generate a continuous function over the entire range of the spatial variable.[20,182] Considering two generic functions $g(x)$ and $h(x)$, such that

$$f(x) = \begin{cases} g(x), & \text{for } x < x^* \\ h(x), & \text{for } x > x^* \end{cases} \tag{92}$$

the goal is to convert the discontinuous function $f(x)$ into a continuous function $F(x)$ using, *e.g.*, a hyperbolic tangent function, as follows[182]

$$F(x,\eta) = t(x,\eta)h(x) + [1 - t(x,\eta)]g(x) \tag{93}$$

where

$$t(x,\eta) = \frac{1 + \tanh\left(\frac{x - x^*}{\eta}\right)}{2} \tag{94}$$

The parameter η is a positive factor related to the smoothness of the curve. High values of η generate smoother curves, while low values generate steep curves.

The cell wall is modeled implicitly as a fixed polyelectrolyte layer in which charges vary as a function of the ionization of their functional groups – carboxyl, phosphoryl, hydroxyl, and amino groups – being, consequently, dependent on pH.[57]

Considering both acid and base sites of the cell wall, the volume charge density of fixed sites ϱ_{bn} is related to the following dissociation reactions:[178,179]

$$> \mathrm{R}_{aj}\mathrm{H} \quad \rightleftharpoons \quad > \mathrm{R}_{aj}^{-} \quad + \quad \mathrm{H}^{+} \tag{95}$$

$$> \mathrm{R}_{bm}\mathrm{H}^{+} \quad \rightleftharpoons \quad > \mathrm{R}_{bm} \quad + \quad \mathrm{H}^{+} \tag{96}$$

where $> \mathrm{R}_{aj}$ are the acid ionizable sites of type j, which can be represented by phosphoryl, carboxyl or hydroxyl groups; and $> \mathrm{R}_{bm}$ is the base ionizable sites of type m, represented by the amine group. Considering the activity of H^{+} and the functional groups of the cell wall equal to their concentrations, the dissociation constants (K_{eq}) for each reaction can be expressed as[183,184]

$$K_{eq,aj} = \frac{\tilde{\rho}_{R_{aj}^{-}}\tilde{\rho}_{H^{+}}}{\tilde{\rho}_{R_{aj}H}} \tag{97}$$

$$K_{eq,bm} = \frac{\tilde{\rho}_{R_{bm}}\tilde{\rho}_{H^{+}}}{\tilde{\rho}_{R_{bm}H^{+}}} \tag{98}$$

where $\tilde{\rho}_i$ is the molar concentration of the ith species.

By the assumption of uniformly distributed sites within the wall (*i.e.*, the number of acid sites of type j and base sites of type m per unit of volume are constant inside the bacteria cell wall) the volume charge density of fixed sites can be written as[57]

$$\varrho_{bn}(x) = e[1 - t(x)]\left[\sum_m \frac{10^{-\mathrm{pH}}\rho_m^{\mathrm{s,max}}(x)}{10^{-\mathrm{pH}} + K_{eq,bm}\exp\left[\frac{ez_{\mathrm{H}^+}\psi(x)}{k_B T}\right]} - \sum_j \frac{K_{aj}\rho_j^{\mathrm{s,max}}(x)}{K_{eq,aj} + 10^{-\mathrm{pH}}\exp\left[-\frac{ez_{\mathrm{H}^+}\psi(x)}{k_B T}\right]}\right] \quad (99)$$

where $10^{-\mathrm{pH}}$ is considered equal to the concentration of H^+ at an infinitely large distance from the interface, $\rho_j^{\mathrm{s,max}}$ and $\rho_m^{\mathrm{s,max}}$ are defined, respectively, as the maximum number density of acid sites of type *j* and base sites of type *m*, and z_{H^+} is equal to 1 (valence of H^+). It is worthwhile to note that the distribution of sites over the whole space is described by the smoothing function – within the wall it is positive and constant and, in the surrounding, it is null. More details can be found in APPENDIX F.[57]

2.1.3 Results and discussion

The PBE together with the volume charge density function – Eq.(99) – and Neumann boundary conditions at $x \to \pm\infty$ were solved using a second order spline finite elements method in a one-dimensional Cartesian coordinate system for various bulk pH values. We took advantage of the symmetry in the non-perpendicular directions to the interface cell wall/ extracellular media. The four site model proposed by Hong and Brown[185] was adopted (Table 3). They analyzed potentiometric titration data from a washed suspension of *B. brevis* in 0.1 M NaCl solution. Bacterial cultures were grown in a minimal media consisted of 5.44 g KH_2PO_4 and 0.6 ml of salt solution (10.0 g/L $MgSO_4{\cdot}7H_2O$, 0.1 g/L $CaCl_2{\cdot}2H_2O$, 0.4 g/L $FeSO_4{\cdot}7H_2O$, and 1.0 g/L $MnCl_2{\cdot}2H_2O$) in 1L of water with the addition of 2.0 g glucose and 0.5 g NH_4Cl. Three pK_{eq} values (3.81, 5.31, and 7.01) are associated with functional groups that can be negatively charged, whereas the fourth (9.81) is associated with functional groups that can be either negatively charged (hydroxyl) or positively charged (amine). On the basis of the isoelectric point (IEP) of *B.brevis* – approximately 4.0 – it was possible to estimate the

concentration of hydroxyl and amine groups related to these pK_{eq}.[74] The values of pK_{eq} and site concentrations are shown in Table 3.

We assumed that the acid and base sites are uniformly smeared out over the cell wall with thickness of 75 nm.[176] The cell wall thickness was used to estimate the cell wall volume together with the cell dimensions: 1.60±0.31 μm length and 0.60±0.05 μm width.[74] To calculate the site concentration in mol per m³ (Table 3), we used the cell wall volume and the ratio of cell numbers to dry mass,[74] which, for *B. brevis*, is equal to 4.0×10^{12} cell per g.[57]

Table 3 – Dissociation constants and site concentrations for the cell surface of *B. brevis*

	a_1 [a]	a_2 [a]	a_3 [a]	a_4 [a,b]	b [a,b]
Dissociation Constant (pK_{eq})	3.81	5.31	7.01	9.81	9.81
Site concentrations (10^{-4} mol/g)	3.77	1.53	2.19	1.14	2.36
Site concentrations (10^2 mol/m³)	2.94	1.19	1.71	0.89	1.84

Legend: [a] a_i refers to acid site i and b refers to base site. [b] $\rho_{a4}^{\max} + \rho_b^{\max} = \rho_4^{\max}$ and p$K_{eq,a4}$ = p$K_{eq,b}$ = p$K_{eq,4}$, in which $\rho_4^{\max}$ is the overall site concentrations for the fourth pK_{eq} value given by Hong and Brown[185]. $\rho_{a4}^{\max}$ and $\rho_b^{\max}$ were calculated through the IEP of *B.brevis*.
Source: Hong and Brown (2006)[185] and Barbosa, Lima and Tavares (2015)[57].

Figure 4 shows the electrostatic potential as a function of the distance from the cell surface for bulk ionic strength equal to 0.1 M. The solutions were obtained by a mixture of NaCl, HCl, and NaOH. At pH values lower than IEP, the potential inside the cell wall is positive. On the other hand, at pH values greater than IEP, the potential is negative inside cell wall.[57] Because the thickness of bacterial wall is much greater than the Debye length κ^{-1}, the potential deeply inside the surface layer becomes the Donnan potential.[186]

A similar study has been carried out by Wasserman and Felmy[187] These authors analyzed the electrostatic potential profile for some bacteria and the theoretical impact of trace amounts of divalent and trivalent cations at very low concentrations (10^{-6} M) in the electrostatic profile. To obtain the electrostatic profile, they solved Poisson–Boltzmann equation (without considering the fixed charge of cell wall as a function of the ionization of the functional groups) for the membrane and solution, using continuity conditions in the boundary of the two environments (membrane and surrounding electrolyte solution).

Figure 4 – Electrostatic potential as a function of the distance from the cell surface for *B. brevis* at bulk pH ranging from 2.0 to 9.0

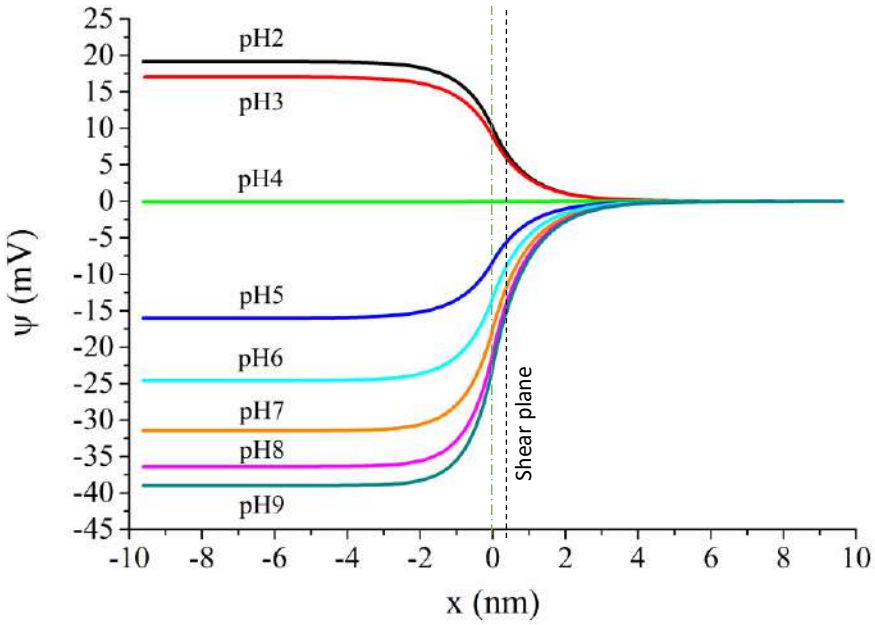

Legend: The cell surface is located at x = 0 nm. Bulk ionic strength is equal to 0.1 M. Negative values of x are located inside the cell wall and positive values outside the cell.
Source: Barbosa, Lima and Tavares (2015).[57]

On the other hand, Hong and Brown[74] proposed the location of all sites on the surface of the cell and they found the effective site numbers by an iterative method: the real density of the acid/base groups has been uniformly reduced until the surface potential was equal to the zeta potential (ζ), which is the potential at the surface of the shear plane also known as the region of rapidly viscosity change.

In Figure 5, we show that the zeta potential computed with the methodology proposed here is in good agreement with the zeta potential estimated by the Smoluchowski equation based on experimental electrophoretic mobility data.[74] We consider that the shear plane is located 0.4 nm from the interface. As a matter of fact, we introduced no parameter such as effective site number coefficient to enforce the experimental ζ, unlike the Hong and Brown's approach.[74] However it is important to highlight that Smoluchowski equation is based on a simple DLVO model to correlate mobility to ζ potential.[5,188]

Figure 5 – Zeta Potential of *B. brevis* as a function of bulk pH ranging from 2.0 to 9.0 and bulk ionic strength of 0.1 M

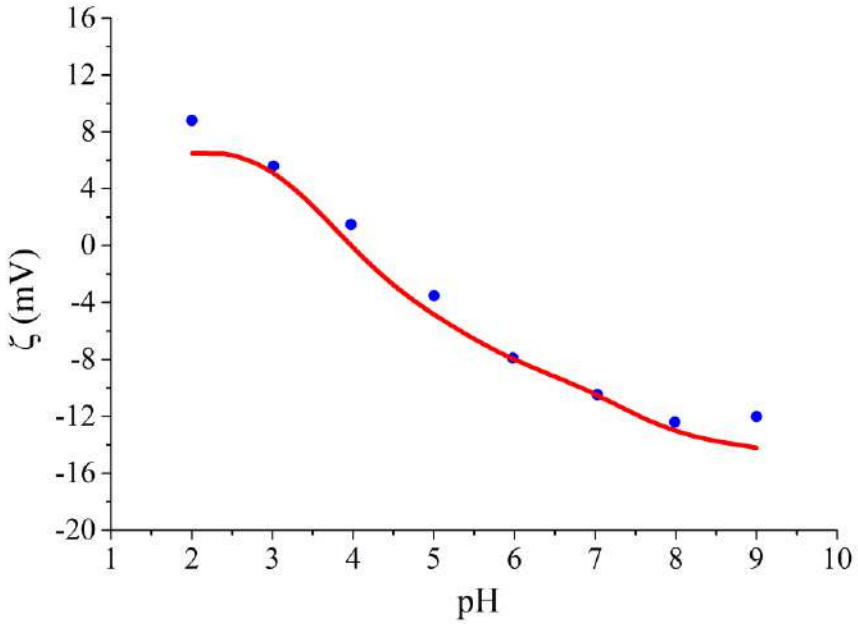

Legend: Circles refer to ζ estimated by the Smoluchowski equation based on experimental electrophoretic mobility data[74] and line refers to the model. Bulk ionic strength equal to 0.1 M.
Source: Barbosa, Lima and Tavares (2015).[57]

2.1.4 Conclusion

We have successfully developed a membrane ion charge model based on the Poisson-Boltzmann description of charge density profiles, including a volume charge density inside the membrane together with an electrolyte solution outside the membrane. With this methodology, the zeta potential of *B. brevis* cell wall for various pH values was predicted in good agreement with experimental data. Information about the zeta potential of a bacteria immersed in an electrolyte solution is useful in the investigation of the metal uptake from solution, the biofilm and biofouling formations, the biocorrosion process, and even in the development of new drugs. The model proposed here allows the estimation of the stability of Gram positive bacteria in various electrolyte solutions without the need for numerous experimental measures.

Typically charge density profiles are only calculated in the electrolyte region between surfaces. Less commonly two calculations can be coupled to obtain the diffuse layer profiles on either side of a membrane in which the charge of the membrane itself is routinely handled

as a simple surface charge density. Any distribution of charges inside a surface (or membrane) is commonly ignored. These distributions of charges are modelled here and, as consequence, the Donnan potential is naturally obtained in this model, rather than having to be artificially imposed. Moreover, the membrane charge is not simply treated as a fixed volume charge density, but varies with the specific local conditions (the electrostatic potential) inside the membrane, smoothing out the transition of the electrostatic potential and the charge densities across the interface between the membrane and electrolyte solution. This is analogous to the charge regulation condition often applied to surface charges.

2.2 Membrane potential and ion partitioning in an erythrocyte

2.2.1 Introduction

In virtually all mammal cells, a much higher concentration of potassium ions inside the cell and vice versa for sodium ions is observed.[189] Usually, this difference in the ion partitioning across a cell membrane is attributed exclusively to a balance between active and passive transport processes.[167] In this context, an active ion transporter stands out: the Na^+K^+ATPase. It couples the phosphorylation and dephosphorylation of an amino acid residue to the simultaneous movement of two K^+ ions inward and three Na^+ ions outward across the plasma membrane (the ions are moved against their electrochemical gradients).[190,191]

However, the classical theories ignore the specific ion effects and the difference in the thermodynamic reference states between intracellular and extracellular environments.[21] Considering that both phenomena – active transport by Na^+K^+ATPase and specific ion effects – occur in mammal cells, the aim of this subsection is to investigate how much the specific ion effects and solvation energy contribute to ion partitioning in human erythrocytes.

Erythrocytes, also denominated red blood cells, are responsible for carrying almost all the oxygen required by the cells from the lungs to the tissues.[167] Due to the absence of nucleus and other organelle, they are considered classical models for studying how ions and other compounds are distributed between intra and extracellular environments. Their cytoplasm comprises nearly close-packed hemoglobin, which is one of the most soluble proteins in the

cell and constitutes more than 98% of the erythrocyte protein by mass.[66,192] It is also important to highlight that hemoglobin is a protein of high surface area.[66]

2.2.2 Methodology

The system containing an erythrocyte was analyzed using a modified PBE in Cartesian coordinates. The Lifshitz theory was used to quantify the dispersion interactions between ions and macromolecules, while the Born theory was used to change the reference state from the intracellular composition to extracellular environment. Moreover, an extra potential that takes into account the difference in ion permeability of the erythrocyte membrane and the presence of active transporters at the plasma membrane was included in the modified PBE as a residual chemical potential.

The main assumptions used to model the erythrocyte in the plasma were[21]

a) temperature equal to 310.15 K;
b) erythrocyte described by a sphere with equivalent radius of 2.673 μm;
c) thickness of the plasma membrane plus glycocalyx equal to 10 nm;
d) surface charge density on the outer surface (glycocalyx) equal to 0.02 C/m^2;[193]
e) surface charge density on the inner membrane surface equal to that of outer membrane plus glycocalyx;
f) intracellular dielectric constant equal to 65.22[194] or 57.0;[195]
g) extracellular dielectric constant equal to the aqueous dielectric constant at the system's temperature;
h) only Na^+, K^+ and Cl^- ions presented in the system;
i) the plasma membrane considered as a flat plane;
j) the average distance between ions and cytoplasm proteins equal to 5Å; and
k) equilibrium between intracellular and extracellular environments.

The main contribution of the paper presented in APPENDIX G to this thesis comprises the inclusion of the Born correction in the analysis; thus, this topic is covered in some detail

here, whereas other information about the methodology, as well as other results, can be found in the paper.[21]

2.2.2.1 Born Correction

In situations in which two different liquid phases containing electrolytes are in equilibrium, special attention must be given to the reference states. The total environment effect on the transfer of an ion from a finite concentration in one liquid phase to a similar concentration in another phase takes into account two main contributions. One results from a difference in ion-ion interactions in the two solvents, while the other one results from a difference in ion-medium interactions. In implicit models, the different environments are characterized mainly by their dielectric response; thus the ion-solvent interactions, which can be described by the Born energy, should be largely dependent on the dielectric constant.[21,196,197]

The Born energy is equivalent to the electrostatic contribution for the solvation energies and can be calculated by a hypothetic process characterized by: (i) the discharging of a sphere (represented by an ion) in the reference medium with dielectric constant ε_{ref}, in which

$$\mu_{ref,i}^{Born} = \int_{ez_i}^{0} \frac{q}{4\pi\varepsilon_0\varepsilon_{ref}r_{B,i}}\,\mathrm{d}q = -\frac{e^2z_i^2}{8\pi\varepsilon_0 r_{B,i}}\frac{1}{\varepsilon_{ref}} \tag{100}$$

(ii) the transference of this neutral sphere to another environment with dielectric constant ε_{mix}; and, subsequent, (iii) charging up to its full charge:

$$\mu_{mix,i}^{Born} = \int_{0}^{ez_i} \frac{q}{4\pi\varepsilon_0\varepsilon_{ref}r_{B,i}}\,\mathrm{d}q = \frac{e^2z_i^2}{8\pi\varepsilon_0 r_{B,i}}\frac{1}{\varepsilon_{mix}} \tag{101}$$

Therefore the change in the chemical potential on transferring an ion from a medium of dielectric constant ε_{ref} to one of dielectric constant ε_{mix} is given by[67,196–198]

$$\Delta\mu_i^{Born} = -\frac{e^2 z_i^2}{8\pi\varepsilon_0 r_{B,i}}\left(\frac{1}{\varepsilon_{ref}} - \frac{1}{\varepsilon_{mix}}\right) \quad (102)$$

where $r_{B,i}$ is the Born radius of ion i. The Born model implicitly accounts for the molecular nature of the solvent and it can predict the partition of ions in different solvents; however, the explicit features of the medium defined by its structural and dynamic molecular properties are not included.

Considering the problem studied here, if the extracellular solution is chosen as the reference state, we need to correct the change of the reference state from the intracellular composition to extracellular solution. To this end, we assumed that the Born radii of the ions are equal in both solutions.[21]

2.2.3 Results and Discussion

In the literature, the difference in the ion partitioning of Na^+ and K^+ is generally attributed to the action of the Na^+K^+ATPase pump. In order to analyze the potential required to describe the experimental ion partitioning, the inclusion of a residual chemical potential μ_i^{res} in the modified Boltzmann equation was proposed.[21] Here, the μ_i^{res} potential takes into account the difference in reference states between intracellular and extracellular environments $\Delta\mu_i^{Born}$ (Born effects), the difference in ion permeability of the erythrocyte membrane, and short-range hydration forces. It is computed by an iterative procedure aiming the reproduction of the experimental intracellular concentration[199–201] values. The modified Poisson-Boltzmann equation with the inclusion of this term was presented in Eq. (8). More information about the iterative process is presented in APPENDIX G.

Using the modified PBE with Neumann boundary conditions in a discontinuous system that mimics an erythrocyte immersed in an infinite bath with bulk concentrations equivalent to extracellular medium, it is possible to obtain the electrostatic potential and concentrations profiles as functions of the distance from the membrane (Figure 6). As expected, inside the cell there is more K^+ than Na^+ and outside cell inverse occurs. Extracellular μ_i^{res} for all ions are considered equal to zero. Intracellular values of μ_i^{res} for each ion can be seen in Table 4.

Figure 6 – Electrostatic behavior of an erythrocyte using discontinuous approach

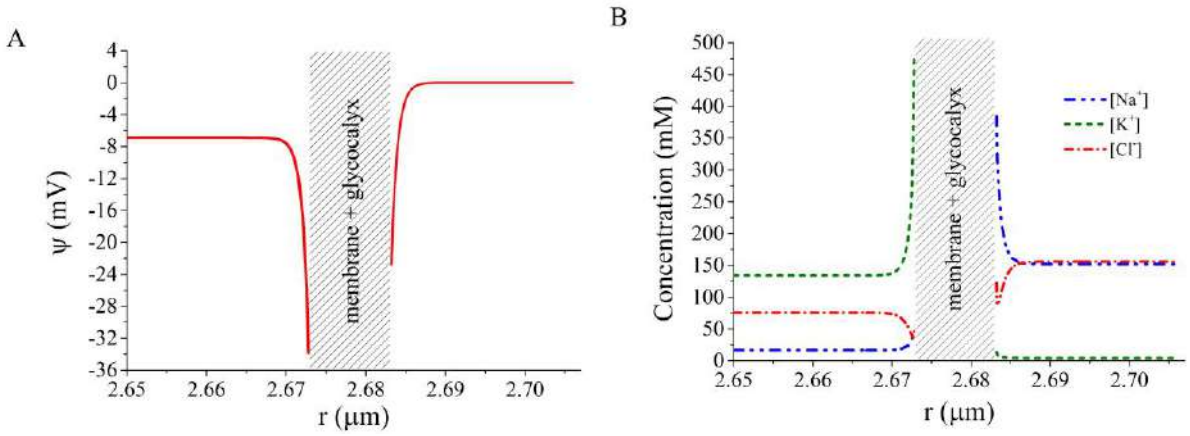

Legend: (A) Electrostatic potential profile and (B) ion concentration profile near erythrocyte plasma membrane in a discontinuous system between intracellular and extracellular environment considering μ_i^{res} potential. Surface charge densities equal to -0.02 C/m². Plasma membrane plus glycocalyx are represented by hatching.
Source: Barbosa *et al.* (2015).[21]

Since the dielectric constants of intracellular and extracellular environments are not the same, it is necessary to introduce a correction due to the change of the reference state, which can be described by the Born correction. Table 4 shows the values of Born term for Na^+, K^+ and Cl^- using two different values of intracellular dielectric constant for normal erythrocytes reported in the literature.[194,195] Di Biasio and Cametti obtained the dielectric spectra measures using a Hewlett–Packard precision impedance analyzers[202] and the dielectric constant was estimated by a fitting procedure based on the Levenberg–Marquardt method for complex functions.[194] On the other hand, Gascoyne and coworkers used the Nelder-Mead simplex method to fit the single-shell oblate-spheroid dielectric model to electrorotation spectra measures obtained experimentally, and then they computed the cytoplasmic dielectric constant of the normal erythrocyte.[195]

Comparing Born correction terms for each ion for both intracellular dielectric constant values, it is possible to note that despite the influence of the dielectric constant in the correction terms, the orders of magnitude are the same (Table 4). The values of the μ_i^{ex} potential and $\Delta\mu_i^{Born}$ for Cl^- are similar with respect to order of magnitude, suggesting that the difference between intracellular concentration of Cl^- observed experimentally in the literature and theoretically in this work can be assigned to the change of the thermodynamic reference state.[21] It is important to note that the active transport of Cl^- across the plasmatic membrane is irrelevant in agreement with experimental evidences.[167]

Table 4 – Intracellular values of U_i, μ_i^{res} and Born term for Na^+, K^+ and Cl^-

Ion	βV_i	$\beta\mu_i^{res}$	$\beta\Delta\mu_i^{Born}$	
			$\varepsilon_{in} = 65.22$[a]	$\varepsilon_{in} = 57$[b]
Na^+	0.009	2.484	0.296	0.651
K^+	0.036	-3.191	0.230	0.503
Cl^-	0.067	0.531	0.257	0.564

Legend: ε_{in} is the dielectric constant of intracellular environment. [a]Dielectric constant from Di Biasio and Cametti[194]. [b]Dielectric constant from Gascoyne *et al.*[195]
Source: Barbosa *et al.* (2015).[21]

Indeed, this conclusion confirms the statement of Bernhardt and Weiss,[203] in which, under physiological condition, the net ion movement of K^+ and Na^+ in comparison to Cl^- across the erythrocyte membrane is very small (about 2 orders of magnitude lower), *i.e.* net Cl^- permeability across membrane is larger than K^+ and Na^+ permeability. The difference between μ_i^{res} and $\Delta\mu_i^{Born}$ for Cl^- can be attributed to the consideration of all anions present in the extracellular environment as chloride (including bicarbonates, sulfates, organic phosphates, proteins, etc.), as well as, the real value of the intracellular dielectric constant.[21]

Table 4 also shows the contribution of the non-electrostatic potential to the ion partitioning of sodium and potassium; however, it is very small compared to μ_i^{res} (0.4% for Na^+, 1.1% for K^+). The contribution of Born correction term is more evident than non-electrostatic interaction, at least with respect to Cl^-. On the other hand, neither non-electrostatic interactions nor Born correction term can explain intracellular K^+ and Na^+ concentrations. Then, the presence of the pump Na^+K^+ATPase is clear.

2.2.4 Conclusion

The study developed to analyze the electric behavior of an erythrocyte is briefly commented here, since it is a continuation of the Master dissertation. However the introduction of the Born correction, proposed for this thesis, could explain the partition of Cl^- observed experimentally.

The inclusion of the Born term in the same level of electrostatic potential in the PBE is an important contribution to the investigation of the total mean field potential in systems with an implicit local variation of the dielectric constant.

3 APPLICATIONS TO ENHANCED OIL RECOVERY

The oil recovery refers to the displacement of petroleum from the reservoir toward and out the production oil well due to a gradient of pressure between the reservoir and the borehole. According to the producing life of a reservoir, the oil recovery can be classified as primary, secondary, and tertiary recovery. In the primary recovery, this process happens naturally; whereas, in the secondary recovery, a fluid is injected (*e.g.* water or gas) to keep the pressure of the reservoir above the saturation pressure, aiding or driving an efficient recovery. Tertiary recovery is characterized by the recovery after secondary recovery and encompasses the injection of special fluids such as chemicals, gases, and/or the injection of thermal energy.[204–206] On the other hand, enhanced oil recovery (EOR) is not restricted to a particular phase in the producing life of the reservoir, *i.e.* it can be applied at any moment of the production in order to increase the recovery of a reservoir by advanced techniques that improve the oil displacement.[205] However, the term is sometimes used interchangeably with tertiary recovery.[204,206]

The EOR techniques can be classified as thermal recovery,[61,62,207] gas injection[208–210] and chemical injection.[14,60,62–64] Of particular interest is the injection of aqueous electrolyte solutions with a different composition from the connate water. During this process, the pre-established chemical equilibrium due to precipitation, dissolution and/or adsorption reactions that occur in bulk solution and on rock/fluid interface might be modified, providing favorable conditions to the oil recovery. The simplest composition of water to be injected is the sea water, mainly in offshore productions due to its abundance. A closer look at the physical and chemical mechanisms behind this improvement, reveals a possible correlation with oil expansion, decrease of oil viscosity, fines migration, multicomponent ion exchange, and/or alteration of surface properties such as interfacial tension, elasticity of interfaces, double layer expansion, and ζ potential. There is not a unique composition of water that enhances the oil recovery for all reservoirs, independently of the rock, oil and connate water compositions, temperature, and pressure. This statement gives origin to the concept of engineered water (EW) waterflooding, which is characterized by the injection of water with a specific composition of electrolyte into the oil reservoir in order to enhance the oil recovery.[14,60,61]

Hence, it is crucial to understand the phenomena to predict the composition of the EW for each reservoir of interest. While several mechanisms have been proposed to explain the EOR using EW, alteration of the wettability seems to be one of most prevalence. It refers to

the relative preference of one liquid over another to spread on a surface due to the interplay of molecular and ionic interactions among three phases and it is often expressed as the macroscopic contact angle.[211]

The first picture that usually comes to mind when we study the wettability among three phases is similar to Figure 7A, in which all three phases are in contact with each other. The situation illustrated in Figure 7A may happen when the brine film collapse due to unfavorable conditions on the surface.[212] Nevertheless, especially noteworthy in reservoir engineering field, is the consensus in which the pores of rock saturated with oil have a residual thin brine film between the oil and the rock as represented in Figure 7B. It has origin in the formation of the oil and in the geological evidence that the reservoir was originally occupied by water before the migration of the oil.[213,214]

For the wettability regime, in both situations, we consider the contact angle between 0º and 70º as water-wet, from 70º to 110º as neutral and from 110º to 180º as oil-wet, following the definition adopted by Santos and coworkers.[215]

Figure 7 – Sketch of the oil droplet immersed in brine resting on a flat solid surface

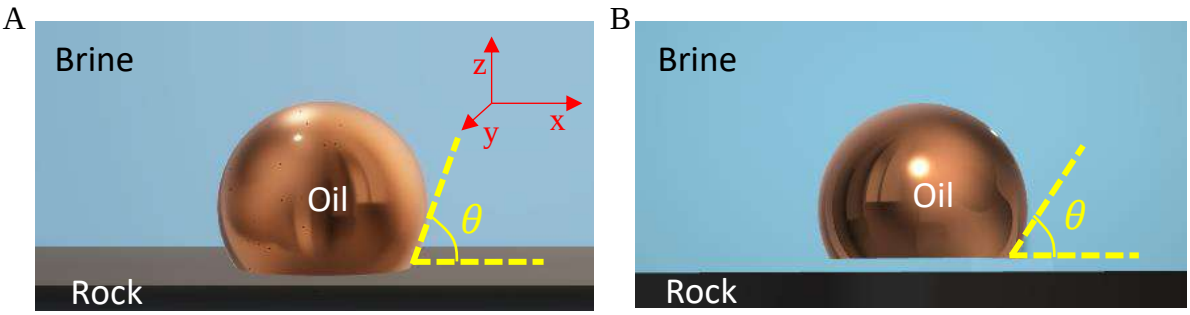

Legend: In (B), there is an aqueous film between the rock and oil droplet, unlike (A). θ is the contact angle among the three phases. The figures are not drawn to scale.
Source: Adapted from Barbosa, Lima and Tavares (2019).[65]

We used two different strategies to analyze the wettability and contact angle in three-phase contact systems. In Section 3.1, the capillary pressure, the contact angle and the disjoining pressure are correlated by the thermodynamics of thin films. The electric component of the disjoining pressure was calculated by the PBE. For validation, the surface charge density, electrostatic potential, and the disjoining pressure for a system characterized by a thin brine film between sandstone and oil were studied. Furthermore, the contact angle and wettability for carbonates were investigated. On the other hand, 3D-DFT was the method chosen in Section 3.2. At the level of reservoir engineering, the object of study is simpler than

the one in Section 3.1 due to the absence of the film, similar to Figure 7A. However, 3D-DFT gives a greater possibility to understand some phenomena that are limited by a mean-field approach. It is worthwhile to note that the study in Section 3.2 is the first step in a bigger scenario, in which we start to work with 3D-DFT and Fourier transforms to compute the innumerous convolutions in the density functional theory. Results of this initial study were recently published in "Fluid Phase Equilibria" (APPENDIX H).

3.1 Charge-regulation models using PBE

3.1.1 Introduction

The EW waterflooding can alter the wettability of sandstone and carbonates. However, unlike sandstone rocks, carbonates are highly reactive and can dissolve in brine to produce, for instance, Ca^{2+}, Mg^{2+}, CO_3^{2-}, HCO_3^-, H_2CO_3 , and SO_4^{2-} depending on the composition of the rock, which consists mainly of crystalline calcite ($CaCO_3$), nevertheless it can also include smaller amounts of dolomite ($CaMg(CO_3)_2$) and anhydrite ($CaSO_4$).[214,216] Hence, the composition of the injected brine is considerably shifted by dissolution/precipitation reactions and the pH of the solution is buffered toward basic values quite independent of the engineered water pH.[216,217] According to Yutkin and coworkers,[216] the kinetic of rock dissolution is fast (order of seconds) for both high and low permeability zones. Moreover, the carbon dioxide content of the reservoir, which can be originated from CO_2-rich crude oil and gas cap, also plays an important role in the composition of the equilibrated engineered water (EEW).

Depending on the concentration and type of electrolytes, the EEW might have meaningful effects on the wetting state, expanding, for example, the two electrical double layers in the film (one at the brine/oil interface and another at the brine/rock interface), increasing the electrostatic repulsion between these two interfaces of the brine film, and, finally, releasing the oil previously bounded to the rock surface. In other words, the rock becomes less oil wet, in direction to a more hydrophilic condition.[214,218–220]

In this work, we are especially interested in carbonate systems, since more than 50% of the known oil reservoirs are composed by this rock, and, in most of them, the wettability ranges from neutral to oil-wet.[204,211] In Brazil, with the exploration of the pre-salt layer, an

exponential increase of carbonate reservoirs has happened. Some examples of predominantly carbonaceous fields are:[221]

a) “Tartaruga verde”, “tubarão azul”, and “tubarão martelo” in Campos Basin;
b) “Lula”, “Sapinhoá”, and “Mero” in Santos Basin;
c) “Harpia” and “Guará” in Sergipe-Alagoas Basin;
d) “Lagoa Piabanha” in Espírito Santo Basin.

In order to investigate the wettability on carbonates, we modeled the disjoining pressure and with the augmented Young-Laplace equation, we computed the contact angle. The electrostatic potential was described by the PBE with charge regulation at the boundary conditions, whereas the van der Waals interaction between the surfaces was described by the Lifshitz theory. For the sake of simplicity, we assumed that the carbonate rock is exclusively composed by calcite.

The plan of this chapter is as follows. Section 3.1.2 describes some backgrounds about chemical equilibria, electrolyte solution, and thermodynamics of thin films. Moreover, it presents a brief review about the surface complexation model for carbonaceous rock in the vicinity of brine. In Section 3.1.3 a theoretical methodology is constructed which is designed to capture the wettability of calcite/brine/oil system. The proposed strategy is validated for a sandstone rock, and after is applied to calcite rocks in Section 3.1.4. Finally, Section 3.1.5 presents the more remarkable conclusions and offers some suggestions for improvement.

3.1.2 Background

3.1.2.1 Chemical equilibria and activity coefficients

One criterion of equilibrium for chemical reactions indicates that the sum of products of the chemical potential of each component multiplied by its stoichiometric number ($\upsilon_{i,j}$) for a reaction j is zero:[222]

$$\sum_i v_{i,j}\mu_i = 0 \quad \forall j \tag{103}$$

The chemical potential of any component i as function of the fugacity can be expressed by[102,222]

$$\mu_i = \mu_i^0 + RT \ln \frac{\hat{\mathrm{f}}_i}{\mathrm{f}_i^0} = \mu_i^0 + RT \ln a_i \tag{104}$$

where μ_i^0 is standard state chemical potential of i, f_i^0 is the fugacity of pure component i in this standard state, $\hat{\mathrm{f}}_i$ is the fugacity of the component i in a mixture, and a_i is the activity coefficient of i.

Substituting Eq. (104) into Eq. (103), we have[222]

$$K_{eq,j}(T) = \prod_i a_i^{v_{i,j}} \tag{105}$$

where $K_{eq,j}(T)$ is the equilibrium constant of the jth reaction at temperature T. For the solute i in the liquid phase, except for high pressure, the activity can be approximated by the product between the molal activity coefficient, $\gamma_i^{(m)}$, and the bulk molal concentration of the species i in the solution, m_i^b, as

$$a_i = \frac{\gamma_i^{(m)} m_i^b}{m^0} \tag{106}$$

in which the unsymmetrical normalization convention for the activity coefficient is used. Here, m^0 is equal to 1 mol of solute i per kilogram of water and ensures the dimensionless of the activity

The molal activity coefficient of ions may be computed based on an extended Debye-Hückel model with the inclusion of a linear term as[102,196,222,223]

$$\ln \gamma_i^{(m)} = -\frac{\mathrm{A_{DH}} z_i^2 \sqrt{I^{(m)}}}{1 + \mathrm{B_{DH}} \mathring{a}_i \sqrt{I^{(m)}}} + b_i I^{(m)} \tag{107}$$

where

$$\mathrm{A_{DH}}\left[\sqrt{\mathrm{kg/mol}}\right] = \sqrt{500\, N_{av}\lambda_B^3\rho_w^{(m)}} \tag{108}$$

$$\mathrm{B_{DH}}\left[\sqrt{\mathrm{kg/mol}}\,\mathrm{Å}^{-1}\right] = \sqrt{8\pi\, N_{av}\lambda_B\rho_w^{(m)}10^{-17}} \tag{109}$$

N_{av} is the Avogadro constant, $\mathrm{å}_i$ and b_i are ion-specific parameters with units equal to 10^{-10} m and kilogram of water (kgw) per mol, respectively, $I^{(m)}$ is the ionic strength in mol/kgw, and $\rho_w^{(m)}$ is the volumetric mass density of water at T. For ion-pair and low ionic strength, the Setschenow equation can be used:[224]

$$\ln\gamma_i^{(m)} = b_i I^{(m)} \tag{110}$$

The activity of water can be estimated by an approximation based on Raoult's law:[223]

$$a_{\mathrm{H_2O}} = 1 - 0.017\sum_i \frac{m_i^b}{m_0} \tag{111}$$

where the sum is over all the charged and uncharged solutes in liquid phase.

3.1.2.2 Thermodynamics of thin liquids

There are two common approaches to represent thin films: single diving surface or two Gibbs dividing surfaces. In the former, the differential of the energy (dU) of the open film system is given by[213,218]

$$\mathrm{d}U_f = T\mathrm{d}S_f - p_f\mathrm{d}\mathcal{V}_f + \sum_i \mu_i\mathrm{d}n_{i,f} + \gamma_f\mathrm{d}A_f \tag{112}$$

where S is the entropy, $n_{i,f}$ is the number of mols of i in the film, γ is the interfacial tension, A is the area, and the superscript f indicates that the variables are applied to the film as a whole. On the other hand, for the later approach, the film thickness ℓ appears explicitly and the differential of the energy of the film is equal to the sum of the contributions from the brine phase and the surface excess quantities as

$$\begin{aligned} \mathrm{d}U_f = T\left(\mathrm{d}S_b + \mathrm{d}S_{sb,ob}\right) - p_b \mathrm{d}\mathcal{V}_b + \sum_i \mu_i \left(\mathrm{d}n_{i,b} + \mathrm{d}n_{i,sb} + \mathrm{d}n_{i,ob}\right) \\ + \left(\gamma_{sf} + \gamma_{of}\right)\mathrm{d}A_f - A_f \Pi \mathrm{d}\ell \end{aligned} \tag{113}$$

where the subscripts b, o, and s indicate, respectively, brine, oil and rock surface, and Π is the total disjoining pressure. The relation between thickness, volume and area of the film can be expressed as

$$\mathrm{d}\mathcal{V}_b = A_f \mathrm{d}\ell + \ell \mathrm{d}A_f \tag{114}$$

Eliminating $\mathrm{d}\ell$ of Eq. (113) using Eq. (114) yields

$$\begin{aligned} \mathrm{d}\mathcal{U}_f = T\left(\mathrm{d}S_b + \mathrm{d}S_{sb,ob}\right) - (p_b + \Pi)\mathrm{d}\mathcal{V}_b + \sum_i \mu_i \left(\mathrm{d}n_{i,b} + \mathrm{d}n_{i,sb} + \mathrm{d}n_{i,ob}\right) \\ + \left(\gamma_{sf} + \gamma_{of} + \Pi\ell\right)\mathrm{d}A_f \end{aligned} \tag{115}$$

which in turn can be compared to Eq. (112) resulting in the following relationships:

$$\mathrm{d}S_f = \mathrm{d}S_b + \mathrm{d}S_{sb,ob} \tag{116}$$

$$\mathrm{d}\mathcal{V}_f = \mathrm{d}\mathcal{V}_b \tag{117}$$

$$p_f = p_b + \Pi \tag{118}$$

$$\mathrm{d}n_{i,f} = \mathrm{d}n_{i,b} + \mathrm{d}n_{i,sb} + \mathrm{d}n_{i,ob} \tag{119}$$

$$\gamma_f = \gamma_{sf} + \gamma_{of} + \Pi\ell \tag{120}$$

According to Churaev, Dergajin and Muller[225] the disjoining pressure is equal to the difference between the normal component of the pressure tensor within the film and the bulk pressure of the phase from which the film has been formed by thinning out at mechanical

equilibrium. The relation between Π and a flat film thickness at constant T and chemical potential of all species in the system is defined by[213,226]

$$\Pi = -\left[\frac{\partial\left(\gamma_{sf} + \gamma_{of}\right)}{\partial \ell}\right]_{T,\mu_i} \tag{121}$$

For a film thickness large enough, the interfacial tensions γ_{sf} and γ_{of} are equal to the bulk interfacial tensions, γ_{sb} and γ_{ob}, (*i.e.* film acts exclusively as a bulk brine fluid) and the disjoining pressure is null.

Integrating Eq. (121) from ∞ to an equilibrium thickness, ℓ_{eq}, we have

$$\gamma_{sf} + \gamma_{of} = \gamma_{sb} + \gamma_{ob} - \int_{\infty}^{\ell_{eq}} \Pi(\ell)\mathrm{d}\ell \tag{122}$$

Combining Eq. (120) with Eq. (122) yields

$$\gamma_f = \gamma_{sb} + \gamma_{ob} + (\Pi\ell)_{eq} - \int_{\infty}^{\ell_{eq}} \Pi(\ell)\mathrm{d}\ell \tag{123}$$

In an extrapolated situation where $\ell = 0$, the interfacial tension of the film can be written by the Young's equation as[213]

$$\gamma_f = \gamma_{ob}\cos\theta + \gamma_{sb} \tag{124}$$

Finally, combining Eq. (123) with Eq. (124) , we obtain[213,227,228]

$$\cos\theta = 1 + \frac{(\Pi\ell)_{eq} - \int_{\infty}^{\ell_{eq}} \Pi(\ell)\mathrm{d}\ell}{\gamma_{ob}} \tag{125}$$

that expresses the relation between the contact angle and the disjoining pressure.

For three-phase systems, the disjoining pressure is usually decomposed into contributions from the electric double layer (Π_{EDL}), the van der Waals interaction between the surfaces (Π_{vdW}) and the structural forces (Π_s).

$$\Pi(\ell) = \Pi_{EDL}(\ell) + \Pi_{vdW}(\ell) + \Pi_s(\ell) \tag{126}$$

The electric component of the disjoining pressure is the difference between the pressure of two charged surfaces (or interfaces) at a distance ℓ and the pressure when these surfaces are far from each other ($\ell' \to \infty$). The pressure due to the electric double layer at any position x between the two surfaces is

$$\left(\frac{\partial p}{\partial \ell'}\right)_{x,T,n} = \rho_i(x)\left(\frac{\partial \mu_i}{\partial \ell'}\right)_{x,T,n} \tag{127}$$

where ℓ' is the distance between the surfaces varying from ℓ to $\ell' \to \infty$. The chemical potential is described by Eq. (4) and the ideal solution approximation is used, except by the non-ideality of the ion charge. Thus, the disjoining pressure can be estimated by bringing two plates from an infinity separation distance between them to a distance equal to ℓ as[67]

$$\begin{aligned}\Pi_{EDL}(x,\ell) &= -\int_{\ell}^{\infty}\sum_i \rho_i(x)\left(\frac{\partial \mu_i}{\partial \ell'}\right)_{x,T,n} \mathrm{d}\ell' \\ &= \left[-\frac{1}{2}\varepsilon_0\varepsilon\left(\frac{\mathrm{d}\psi}{\mathrm{d}x}\right)_{x,\ell}^2 + \frac{1}{\beta}\sum_i \rho_i(x,\ell)\right] - \left[-\frac{1}{2}\varepsilon_0\varepsilon\left(\frac{\mathrm{d}\psi}{\mathrm{d}x}\right)_{x,\infty}^2 + \frac{1}{\beta}\sum_i \rho_i(x,\infty)\right]\end{aligned} \tag{128}$$

Here, we disregarded the contributions of the external potential and residual chemical potential. The term inside the parentheses with subscript x means that the values are calculated at x when the distance between the surfaces is ℓ or ∞. The first term inside the bracket of Eq. (128) is the contribution from the electrostatic field, whereas the second term refers to the entropic (osmotic) contribution.

In addition, at equilibrium, the disjoining pressure should be independent of the position x.[67] Considering x located at the midplane (x_m) of the slit pore, we have

$$\Pi_{EDL}(\ell) = -\frac{1}{2}\varepsilon_0\varepsilon\left(\frac{\mathrm{d}\psi}{\mathrm{d}x}\right)_{x_m,\ell}^2 + \frac{1}{\beta}\sum_i \left[\rho_i(x_m,\ell) - \rho_i^b\right] \tag{129}$$

When the two surfaces have the same charge, Eq. (129) is reduced to

$$\Pi_{EDL}(\ell) = \frac{1}{\beta}\sum_{i}\left[\rho_i(x_m,\ell) - \rho_i^b\right] \tag{130}$$

The van der Waals interaction between two surfaces in a medium can be described on the basis of the Lifshitz theory.[229] For two planar surfaces, Π_{vdW} is defined as function of the distance ℓ between them and the Hamaker constant H as[67]

$$\Pi_{vdW}(\ell) = \frac{\mathrm{d}}{\mathrm{d}\ell}\left(\frac{H}{12\pi\ell^2}\right) \tag{131}$$

For a system characterized by two phases 1 and 2 interacting across a medium 3, the nonretarded Hamaker constant ($H_{\mathrm{non-ret}}$) can be approximated as[67]

$$\begin{aligned} H_{\mathrm{non-ret}} &= H_{\nu=0} + H_{\nu>0} \\ &\approx \frac{3}{4\beta}\left(\frac{\varepsilon_1-\varepsilon_3}{\varepsilon_1+\varepsilon_3}\right)\left(\frac{\varepsilon_2-\varepsilon_3}{\varepsilon_2+\varepsilon_3}\right) \\ &+ \frac{3h\nu_e}{8\sqrt{2}}\frac{\left(n_{RI,1}^2-n_{RI,3}^2\right)\left(n_{RI,2}^2-n_{RI,3}^2\right)}{\sqrt{\left(n_{RI,1}^2+n_{RI,3}^2\right)\left(n_{RI,2}^2+n_{RI,3}^2\right)}\left[\sqrt{\left(n_{RI,1}^2+n_{RI,3}^2\right)}+\sqrt{\left(n_{RI,2}^2+n_{RI,3}^2\right)}\right]} \end{aligned} \tag{132}$$

assuming the same absorption frequencies for all three phases, where ε_j and $n_{RI,j}$ are the dielectric constant and refractive index of the jth phase, and the subscript ν refers to the frequency.

The presence of electrolytes in the medium 3 affects the Hamaker constant by screening the entropic contribution, *i.e.* $H_{\nu=0}$. Hence, the screened nonretarded Hamaker constant $H_{\mathrm{scr}}$is given by[67]

$$H_{\mathrm{scr}}(\ell) \approx \underset{\nu=0}{H_{\mathrm{non-ret}}}\exp(-\kappa\ell) + \underset{\nu>0}{H_{\mathrm{non-ret}}} \tag{133}$$

The retardation effects are significant at distance greater than 5nm, approximately, where the contribution from $\nu > 0$ to the van der Walls force begins to decay more intensely. The resolution of the full Lifshitz theory considering the retarded effects is not trivial, particularly for the interactions across a dielectric media. This fact stimulated the

development of some approximations as the one proposed by Gregory (1981),[230] which calculates the Hamaker constant in the transition region from nonretarded to retarded forces by

$$H_{\substack{\text{ret} \\ \nu>0}}(\ell) \approx \frac{H_{\substack{\text{non-ret} \\ \nu>0}}}{1 + 5.3\,\lambda_{lw}^{-1}\,\ell} \tag{134}$$

where λ_{lw}^{-1} is the London wavelength, usually set to 100 nm.

Combining Eqs. (131) – (134), the van der Waals interaction between two flat surfaces in a medium can be written as

$$\Pi_{vdW}(\ell) = -\frac{H_{\nu=0}\exp(-\kappa\ell)\,(2+\kappa\ell)}{12\pi\ell^3} - \frac{H_{\nu>0}(2 + 15.9\,\lambda_{lw}^{-1}\,\ell)}{12\pi\ell^3(1 + 5.3\,\lambda_{lw}^{-1}\,\ell)^2} \tag{135}$$

The last contribution, but not least important, to total disjoining pressure is due to the structural forces, *i.e.* the short-range solvation forces between the two surfaces, which is represented by an exponential function as[213,227]

$$\Pi_s(\ell) = A_s \exp\left(-\frac{\ell}{\ell_s}\right) \tag{136}$$

where A_s is a coefficient associated with the magnitude of the structural forces and ℓ_s is a characteristic length. Typical values for these parameters are, respectively, 1.5 $\times 10^5$ bar and 0.5 Å.[213]

3.1.2.3 Surface complexation models

The equilibrium reactions at solid/liquid interfaces have been frequently described in the literature by the surface complexation model (SCM), characterized by the bond between species dissolved in the liquid phase with ions exposed on the surface of the solid phase. This model has been successfully applied in the literature to describe the thermodynamic

equilibrium between carbonaceous surfaces – such as calcite, magnesite and dolomite – and aqueous electrolyte solutions.[231,232,241,233–240]

Van Cappellen and coworkers[231] developed a SCM for divalent metal carbonates (rhodochrosite, siderite and calcite) based on the protonation and the deprotonation of hydrated surface sites using 1:1 stoichiometry between the carbonate and metal sites on the surface. The equilibrium constant values for rhodochrosite ($MnCO_3$) and siderite ($FeCO_3$) were derived from the optimization of the SCM based on the constant capacitance model to reproduce surface charge data obtained experimentally by acid/base titration. The equilibrium constants for calcite ($CaCO_3$) were estimated to reproduce the IEP equal to 8.2 for a suspension of calcite at 298.15 K and partial pressure of carbon dioxide equal to 3.3×10^{-4}.[231] According to Van Cappellen and coworkers the suggested hydration of species corroborated with the findings obtained by X-ray photoelectron spectroscopy[242] and diffuse reflectance infrared Fourier transform spectroscopy.[232,235]

Pokrovcky and coworkers[232–234,236] applied the same set of reactions proposed by Van Cappellen *et al.*[231] to a large set of divalent metal carbonates (Ca, Mg, Sr, Ba, Mn, Fe, Co, Ni, Zn, Cd, and Pb) and dolomite [$CaMg(CO_3)_2$]. For all of the aforementioned crystals, except calcite, the equilibrium constants were estimated based on a constant capacitance model using surface charge data obtained from potentiometric titration at 25±0.2°C in a limited residence time reactor, and ζ potential obtained as a function of pH and ionic strength.[232–234,236] On the other hand, the equilibrium constants for calcite were determined based on ζ potential and IEP data in solutions with different compositions[232,243] due to the fast kinetics of dissolution of $CaCO_3$ and the buffering effect of the carbonate ions in solution, which would affect the acid/base titration results.

Brady, Krumhansl and Mariner[238] used the same reactions proposed by Van Cappellen *et al.*[231] and Pokrovcky *et al.*[232–234,236]; however, motivated by the Pierre's findings[244] – in which the sulfate decreases the surface charge of the calcite, particularly near the IEP – they added reactions involving this ion.

The dissolution and dissociation constants involving calcite at high temperatures, pressures, and salinity were predicted by Hiorth, Cathles e Madland[237] using the Helgeson-Kirkham-Flowers equation of state.[245] One of the hypotheses adopted consisted in the same dependence on the temperature between the equilibrium constants at the surface and in analogous reactions in bulk phase. The ζ potential values obtained by the model were compared to experimental data, and a good agreement was observed.[237]

Recently, Eftekhari *et al.* (2017)[241] optimized the equilibrium constants of the surface complexation reactions to adjust the theoretical surface charge density to ζ potential data of pulverized Stevns Klint chalk (canyon located southwest of Store Heddinge on the Danish island of Zealand).[61,246,247] The theoretical ζ potential was calculated according to the Debye-Hückel equation from the linearization of the analytical solution of the Poisson-Boltzmann equation for the electric double layer model of Gouy-Chapman.[67] The shear plane was considered 3 Å away from surface.[248] In order to correctly predict the ζ potential signal, the restriction $\zeta_i^{calc}\zeta_i^{exp} \geq 0$ was imposed for all *i*, ranging over the experimental data ζ_i^{exp} and computed ζ potentials (ζ_i^{calc}).[241] The optimized parameters were used to model the single-phase multicomponent reactive flow of the brine through the Stevns Klint rock and the results obtained were compared to the concentration history of a chromatographic experiment.[246] There was a divergence between the values analyzed, which can be explained by an undesirable modification in the surface properties of the Stevns Klint rock during the pulverization (remembering that the ζ potential measurements were obtained on the pulverized rock). Thus, Eftekhari and coworkers[241] proposed a new set of equilibrium constants in order to reproduce the history concentration obtained by chromatography.

Heberling *et al.* (2011)[240] developed a SCM related to the Stern electric double layer model. A set of ζ potentials as a function of the pH at different partial CO_2 pressures and of streaming potential as a function of pH and calcium concentration (added as $CaCl_2$) were measured. In addition, it was possible to evaluate the 3D crystal structure of the calcite (1 0 4)/brine interface *in situ* at similar conditions to those used to measure the ζ potential by surface diffraction measurements.[240] Thus, the Stern EDL was used to calculate the equilibrium constants of the reactions, capacitance of the Stern layer, and the shear plane distances (for each ionic strength) based on experimental data of ζ and streaming potentials, and structurally consistent with the results of the surface diffraction experiments.[240] In the first plane, in contact with the surface, only protonation and deprotonation reactions were considered. It was assumed that all other ion-surface interactions occur in the transition plane between the adsorption layer and the diffuse layer. Moreover, it is known that the calcium atom exposed on the surface of the calcite crystal ideally has +1/3 charge instead of +1 due to the calcite structure – Ca atoms are octahedrally coordinated by O from six different CO_3 groups –when the bonds between the Ca atom and the oxygen atoms of the neighbors CO_3^{2-} are purely ionic.[249] However, according to bond valence calculations based on surface diffraction measurements, the exposed calcium atom on the calcite surface has a partial charge of +0.25.[240]

Song *et al.* (2017)[239] expanded the reactions of the SCM of the synthetic calcite proposed by Heberling *et al.*[240] by the inclusion of reactions with Ca^{2+}, CO_3^{2-}, Mg^{2+} and SO_4^{2-}; however, they considered that all reactions occur in the outer layer of the model, *i.e.* the surface potential is equivalent to the potential in the outer Helmholtz plane in which all the ions were considered adsorbed. For the model of the diffuse layer, the Debye-Hückel equation was considered with a fixed distance from the shear plane equal to 0.33 nm for ionic strength of 0.1 M.[239]

Wolthers *et al.*[250] proposed a more sophisticated SCM by the charge distribution multisite ion complexation (CD-MUSIC), which considers three planes to describe the charge distribution at the rock/brine interface. This model allows the inclusion of different crystallographic coordination sites on the surface, and it is necessary to specify which crystal face is exposed and which types of site are present on the mineral surface. The charges on the mineral surface are described by the valence bond theory.[250]

3.1.3 Methodology

3.1.3.1 Bulk equilibria reactions

The equilibrium reactions for the EW/calcite/oil system include the reactions that occur in the bulk phase and those on the interfaces. For the former, there are some databases available in the literature, such as PHREEQC,[224] WATEQ4F,[251] SC-Database,[252] JESS,[253] and EQ3/6.[254] The set of reactions at the bulk phase is fundamental to define the species and their concentrations in the EEW, which in turn is used to calculate the electrical component of the disjoining pressure.

Numerous aqueous species and reactions are involved in the equilibrium chemistry of the EW. Considering the ions in their totally ionized form, the EW studied here may have Ca^{2+}, Mg^{2+}, Na^{+}, H^{+}, CO_3^{2-}, SO_4^{2-}, Cl^{-}, and OH^{-}. Thus, a set of sixteen equilibrium reactions in the aqueous phase were specified, totalizing the possibility of occurrence of twenty two aqueous species as shown in Table 5, besides Cl^{-} that was considered inert for the reactions.

Table 5 – Reactions and equilibrium constants in bulk phase at 298.15 K

	Reaction	pK_{eq} [a]
1	$CO_{2(aq)} + H_2O \rightleftharpoons CO_3^{2-} + 2H^+$	16.681
2	$CO_3^{2-} + H^+ \rightleftharpoons HCO_3^-$	–10.329
3	$Ca^{2+} + CO_3^{2-} + H^+ \rightleftharpoons CaHCO_3^+$	–11.435
4	$Ca^{2+} + CO_3^{2-} \rightleftharpoons CaCO_{3(aq)}$	–3.224
5	$Mg^{2+} + CO_3^{2-} + H^+ \rightleftharpoons MgHCO_3^+$	–11.399
6	$Mg^{2+} + CO_3^{2-} \rightleftharpoons MgCO_{3(aq)}$	–2.98
7	$Na^+ + HCO_3^- \rightleftharpoons NaHCO_3$	0.25
8	$Na^+ + CO_3^{2-} \rightleftharpoons NaCO_3^-$	–1.27
9	$H_2O \rightleftharpoons OH^- + H^+$	14.0
10	$Ca^{2+} + H_2O \rightleftharpoons CaOH^+ + H^+$	12.78
11	$Mg^{2+} + H_2O \rightleftharpoons MgOH^+ + H^+$	11.44
12	$SO_4^{2-} + H^+ \rightleftharpoons HSO_4^-$	–1.988
13	$Ca^{2+} + SO_4^{2-} \rightleftharpoons CaSO_{4(aq)}$	–2.30
14	$Ca^{2+} + HSO_4^- \rightleftharpoons CaHSO_4^+$	–1.08
15	$Mg^{2+} + SO_4^{2-} \rightleftharpoons MgSO_{4(aq)}$	–2.37
16	$Na^+ + SO_4^{2-} \rightleftharpoons NaSO_4^-$	–0.7
17[b]	$CaCO_{3(s)} \rightleftharpoons Ca^{2+} + CO_3^{2-}$	8.48
18[b]	$CO_{2(g)} \rightleftharpoons CO_{2(aq)}$	1.468

Source: [a]Equilibrium constants from Nordstrom *et al* (1990).[255] [b]The last two reactions are only considered for the EEW.

In the beginning, we should specify the temperature, pressure, composition, and concentration of the injected EW; and check whether the reactions are at equilibrium or not.

If Eq. (105) is not satisfied for all possible reactions in the EW based on the specified species, then the composition and molalities referred to the equilibrium condition should be computed. For this end, we chose the stoichiometric formulation: for each independent reaction, we have one non-linear equation described by Eq. (105). The molalities of the solutes at equilibrium, m_i^{eq}, are defined by[222,256]

$$m_i^{eq} = m_i^{in} + \sum_j \upsilon_{i,j}\, \xi_j \tag{137}$$

where the sum is over all the independent reactions and ξ_j is the extent of reaction for the jth reaction. The set of non-linear reactions was solved for $\boldsymbol{\xi}$ using the multivariate Newton-Raphson method.[256]

The ion-specific parameters of the extended Debye-Hückel equation, which have been estimated based on the mean salt activity coefficient and MacInnes assumption,[223] are summarized in Table 6. For uncharged species, a constant value of 2.303×10^{-1} kgw/mol was considered for b_i.[224]

Given the composition and concentration of the EW at equilibrium, the next step consists in the estimation of the EEW composition. Since calcite is highly reactive, the EEW might be quite different from the injected EW. Besides the reactions in Table 5, in this step, the precipitation/dissolution reaction of calcite ($K_{sp} = 10^{-8.48}$)[255] and dissolution of carbon dioxide in the liquid phase ($K_{eq} = 10^{-1.468}$)[255] are considered for the equilibrium state. We should also pay attention to the possibility of precipitation of solid species not initially present in the system, such as dolomite, aragonite, gypsum, anhydrite, and halite.

Table 6 – Ion-specific parameters of the extended Debye-Hückel model

Species	a_i	b_i	Species	a_i	b_i
H^+	9.00	0.0	$MgOH^+$	6.50[a]	0.0
Na^+	4.00	1.727×10^{-1}	$MgHCO_3^+$	4.00	0.0
$NaHCO_{3(aq)}$	–	2.303×10^{-1}	$MgCO_{3(aq)}$	–	2.303×10^{-1}
$NaCO_3^-$	5.40	0.0	$MgSO_{4(aq)}$	–	2.303×10^{-1}
$NaSO_4^-$	5.40	0.0	Cl^-	3.50	3.453×10^{-2}
Ca^{2+}	5.00	3.779×10^{-1}	OH^-	3.50	0.0
$CaOH^+$	6.00	0.0	$CO_{2(aq)}$	–	2.303×10^{-1}
$CaHCO_3^+$	6.00	0.0	HCO_3^-	5.40	0.0
$CaCO_{3(aq)}$	–	2.303×10^{-1}	CO_3^{2-}	5.40	0.0
$CaHSO_4^+$	3.04[a]	0.0	HSO_4^-	4.50	0.0
$CaSO_{4(aq)}$	–	2.303×10^{-1}	SO_4^{2-}	5.00	-9.210×10^{-2}
Mg^{2+}	5.50	4.605×10^{-1}			

Source: Parameters from Truesdell and Jones (1974)[223] and Parkhurst and Appelo (2013)[224].

After the estimation of the molalities in the EEW, it is necessary to compute the density of the electrolyte solution. We used the methodology proposed by Appelo and

coworkers, [257] in which the density of the electrolyte solution is related to the density of the pure water at the same pressure and temperature of the system and to the apparent molar volume of the dissolved salt, which in turn was obtained according to the Redlich equation expanded to the modified Debye-Hückel theory.[257,258] Then, with the density of the electrolyte solution, it is possible to determine the molarities, which in turn are the input data to solve the PBE, whose solution is used to calculate the disjoining pressure due to the EDL.

It is worthwhile to note that the composition of the connate water was neglected in the equilibrium reactions, as well as, the existence of tracer of Ba^{+2}.

3.1.3.2 Surface complexation reactions

We adopted the charge regulation boundary condition for both the surfaces of calcite and oil. Two models were used for the calcite: Eftekhari's model[241] and Song's model.[239]

According to the model proposed by Eftekhari *et al.*[241], the maximum surface densities of carbonaceous ($\varsigma_{CO_3}^{max}$) and calcium (ς_{Ca}^{max}) sites are described by

$$\varsigma_{CO_3}^{max} = \varsigma_{CO_3H} + \varsigma_{CO_3^-} + \varsigma_{CO_3Ca^+} + \varsigma_{CO_3Mg^+} = 2\ \mathrm{nm}^{-2} \tag{138}$$

$$\varsigma_{Ca}^{max} = \varsigma_{CaOH} + \varsigma_{CaHCO_3} + \varsigma_{CaOH_2^+} + \varsigma_{CaO^-} + \varsigma_{CaCO_3^-} + \varsigma_{CaSO_4^-} = 2\ \mathrm{nm}^{-2} \tag{139}$$

where ς_m is the number surface density of the mth site on the surface. Moreover, the reactions and equilibrium constants for the model are summarized in Table 7, where > represents the mineral surface.

The charge density on the calcite surface is determined by the surface densities of the charged sites and their charge number. Thus we have

$$Q_{Calcite} = e\left[\varsigma_{CO_3Ca^+} + \varsigma_{CO_3Mg^+} - \varsigma_{CO_3^-} + \varsigma_{CaOH_2^+} - \varsigma_{CaO^-} - \varsigma_{CaCO_3^-} - \varsigma_{CaSO_4^-}\right] \tag{140}$$

Here, unlike in the bulk equilibria, we assume that the activity of the species i in the solution is equal to its local molar density at the surface ($\tilde{\rho}_i^{cal} = \rho_i(x)|_{x\to \mathrm{calcite}}$); and, for the surface sites, the activity is equivalent to its molar surface density.

Table 7 – Reactions and equilibrium constants for the Eftekhari's model

	Reactions	pK_{eq} [a]
E1	$> CO_3H \rightleftharpoons\ > CO_3^- + H^+$	4.5
E2	$> CO_3H + Ca^{2+} \rightleftharpoons\ > CO_3Ca^+ + H^+$	1.29
E3	$> CO_3H + Mg^{2+} \rightleftharpoons\ > CO_3Mg^+ + H^+$	2.04
E4	$> CaOH \rightleftharpoons\ > CaO^- + H^+$	17.09
E5	$> CaOH + H^+ \rightleftharpoons\ > CaOH_2^+$	–14.08
E6	$> CaOH_2^+ + CO_3^{2-} \rightleftharpoons\ > CaCO_3^- + H_2O$	–3.33
E7	$> CaOH_2^+ + HCO_3^- \rightleftharpoons\ > CaHCO_3 + H_2O$	–0.48
E8	$> CaOH_2^+ + SO_4^{2-} \rightleftharpoons\ > CaSO_4^- + H_2O$	–1.45

Source: [a]Equilibrium constants from Eftekhari *et al.* (2017).[241]

Combining Eqs. (105) and (140) yields

$$Q_{Calcite} = e\left[\varsigma_{CO_3H}\left(\frac{K_{eq,E2}\tilde{\rho}_{Ca^{2+}}^{cal} + K_{eq,E3}\tilde{\rho}_{Mg^{2+}}^{cal} - K_{eq,E1}}{\rho_{H^+}}\right) + \varsigma_{CaOH}\left(-\frac{K_{eq,E4}}{\tilde{\rho}_{H^+}^{cal}} + K_{eq,E5}\tilde{\rho}_{H^+}^{cal}\left(1 - K_{eq,E6}\tilde{\rho}_{CO_3^{2-}}^{cal} - K_{eq,E8}\tilde{\rho}_{SO_4^{2-}}^{cal}\right)\right)\right] \quad (141)$$

Expressing ς_{CO_3H} and ς_{CaOH} as functions of $\varsigma_{CO_3}^{max}$ and ς_{Ca}^{max} and substituting these variables in Eq.(141), we obtain the surface charge density on the calcite as function of the local densities of the free ions at the surface, the maximum surface density of the sites and the equilibrium constant of the surface reactions:

$$Q_{Calcite} = e\left[\varsigma_{CO_3}^{max}\frac{K_{eq,E2}\tilde{\rho}_{Ca^{2+}}^{cal} + K_{eq,E3}\tilde{\rho}_{Mg^{2+}}^{cal} - K_{eq,E1}}{K_{eq,E2}\tilde{\rho}_{Ca^{2+}}^{cal} + K_{eq,E3}\tilde{\rho}_{Mg^{2+}}^{cal} + K_{eq,E1} + \tilde{\rho}_{H^+}^{cal}} + \frac{\varsigma_{Ca}^{max}}{D}\left(K_{eq,E5}\left(\tilde{\rho}_{H^+}^{cal}\right)^2\left(1 - K_{eq,E6}\tilde{\rho}_{CO_3^{2-}}^{cal} - K_{eq,E8}\tilde{\rho}_{SO_4^{2-}}^{cal}\right) - K_{eq,E4}\right)\right] \quad (142)$$

where

$$D = K_{eq,E5}\left(\tilde{\rho}_{\mathrm{H^+}}^{cal}\right)^2\left(1 + K_{eq,E6}\tilde{\rho}_{\mathrm{CO_3^{2-}}}^{cal} + K_{eq,E7}\tilde{\rho}_{\mathrm{HCO_3^-}}^{cal} + K_{eq,E8}\tilde{\rho}_{\mathrm{SO_4^{2-}}}^{cal}\right) + K_{eq,E4} + +\tilde{\rho}_{\mathrm{H^+}}^{cal} \quad (143)$$

For the complexation model proposed by Song *et al.*[239] the site densities on the surface are

$$\begin{aligned}\varsigma_{\mathrm{CO_3}}^{\max} &= \varsigma_{\mathrm{CO_3}H^{+0.75}} + \varsigma_{\mathrm{CO_3^{-0.25}}} + \varsigma_{\mathrm{CO_3H\cdots CO_3^{-1.25}}} + \varsigma_{\mathrm{CO_3H\cdots SO_4^{-1.25}}} + \varsigma_{\mathrm{CO_3H\cdots HCO_3^{-0.25}}} \\ &\quad + \varsigma_{\mathrm{CO_3H\cdots Cl^{-0.25}}} = 4.95\ \mathrm{nm^{-2}}\end{aligned} \quad (144)$$

$$\begin{aligned}\varsigma_{\mathrm{Ca}}^{\max} &= \varsigma_{\mathrm{CaOH^{-0.75}}} + \varsigma_{\mathrm{CaOH_2^{+0.25}}} + \varsigma_{\mathrm{CaOH\cdots Ca^{+1.25}}} + \varsigma_{\mathrm{CaOH\cdots Mg^{+1.25}}} + \varsigma_{\mathrm{CaOH\cdots Na^{+0.25}}} \\ &= 4.95\ \mathrm{nm^{-2}}\end{aligned} \quad (145)$$

Note that the valences of the sites are fractioned numbers. The reactions and equilibrium constants can be found in Table 8. Hence, following the same procedure made for Eftekhari's model, we can obtain the surface charge density on the calcite as function of $\varsigma_{\mathrm{CO_3}}^{\max}$, $\varsigma_{\mathrm{Ca}}^{\max}$, equilibrium constants and local densities of the free ions:

$$\begin{aligned}Q_{Calcite} = 0.25e\Big[&3\,\varsigma_{\mathrm{CO_3}H^{+0.75}} - \left(\varsigma_{\mathrm{CO_3^{-0.25}}} + \varsigma_{\mathrm{CO_3H\cdots HCO_3^{-0.25}}} + \varsigma_{\mathrm{CO_3H\cdots Cl^{-0.25}}}\right) \\ &- 5\left(\varsigma_{\mathrm{CO_3H\cdots CO_3^{-1.25}}} + \varsigma_{\mathrm{CO_3H\cdots SO_4^{-1.25}}}\right) + \varsigma_{\mathrm{CaOH_2^{+0.25}}} + \varsigma_{\mathrm{CaOH\cdots Na^{+0.25}}} \\ &+ 5\left(\varsigma_{\mathrm{CaOH\cdots Ca^{+1.25}}} + \varsigma_{\mathrm{CaOH\cdots Mg^{+1.25}}}\right) - 3\,\varsigma_{\mathrm{CaOH^{-0.75}}}\Big]\end{aligned} \quad (146)$$

$$\begin{aligned}Q_{Calcite} = 0.25e\Bigg[&\frac{\varsigma_{\mathrm{CO_3}}^{\max}}{D_1}\Big(\Big(3 - 5\,K_{eq,S2}\tilde{\rho}_{\mathrm{CO_3^{2-}}}^{cal} - 5\,K_{eq,S3}\tilde{\rho}_{\mathrm{SO_4^{2-}}}^{cal} - K_{eq,S4}\tilde{\rho}_{\mathrm{HCO_3^-}}^{cal} \\ &- K_{eq,S5}\tilde{\rho}_{\mathrm{Cl^-}}^{cal}\Big) - K_{eq,S1}\Big) \\ &+ \frac{\varsigma_{\mathrm{Ca}}^{\max}}{D_2}\left(-3 + K_{eq,S6}\tilde{\rho}_{\mathrm{H^+}}^{cal} + 5\,K_{eq,S7}\tilde{\rho}_{\mathrm{Ca^{2+}}}^{cal} + 5\,K_{eq,S8}\tilde{\rho}_{\mathrm{Mg^{2+}}}^{cal} + K_{eq,S9}\tilde{\rho}_{\mathrm{Na^+}}^{cal}\right)\Bigg]\end{aligned} \quad (147)$$

where

$$D_1 = K_{eq,S1} + \tilde{\rho}_{\mathrm{H^+}}^{cal}\left(1 + K_{eq,S2}\tilde{\rho}_{\mathrm{CO_3^{2-}}}^{cal} + K_{eq,S3}\tilde{\rho}_{\mathrm{SO_4^{2-}}}^{cal} + K_{eq,S4}\tilde{\rho}_{\mathrm{HCO_3^-}}^{cal} + K_{eq,S5}\tilde{\rho}_{\mathrm{Cl^-}}^{cal}\right) \quad (148)$$

$$D_2 = 1 + K_{eq,S6}\tilde{\rho}_{\mathrm{H^+}}^{cal} + K_{eq,S7}\tilde{\rho}_{\mathrm{Ca^{2+}}}^{cal} + K_{eq,S8}\tilde{\rho}_{\mathrm{Mg^{2+}}}^{cal} + K_{eq,S9}\tilde{\rho}_{\mathrm{Na^+}}^{cal} \quad (149)$$

Table 8 – Reactions and equilibrium constants for the Song's model

	Reactions	pK_{eq} [a]
S1	$> CO_3H^{+0.75} \rightleftharpoons > CO_3^{-0.25} + H^+$	13.5
S2	$> CO_3H^{+0.75} + CO_3^{2-} \rightleftharpoons > CO_3H \cdots CO_3^{-1.25}$	–2.23
S3	$> CO_3H^{+0.75} + SO_4^{2-} \rightleftharpoons > CO_3H \cdots SO_4^{-1.25}$	–1.00
S4	$> CO_3H^{+0.75} + HCO_3^- \rightleftharpoons > CO_3H \cdots HCO_3^{-0.25}$	–0.09
S5	$> CO_3H^{+0.75} + Cl^- \rightleftharpoons > CO_3H \cdots Cl^{-0.25}$	0.64
S6	$> CaOH^{-0.75} + H^+ \rightleftharpoons > CaOH_2^{+0.25}$	–0.30
S7	$> CaOH^{-0.75} + Ca^{2+} \rightleftharpoons > CaOH \cdots Ca^{+1.25}$	–1.74
S8	$> CaOH^{-0.75} + Mg^{2+} \rightleftharpoons > CaOH \cdots Mg^{+1.25}$	–1.62
S9	$> CaOH^{-0.75} + Na^+ \rightleftharpoons > CaOH \cdots Na^{+0.25}$	–0.14

Source: [a]Parameters from Song *et al.* (2017).[239]

For the oil/brine interface, we adopted the SCM proposed by Brady and coworkers, which considers the interaction of the basic and acidic sites of the oil with the ions H^+, Ca^{2+}, and Mg^{2+} (Table 9).[12,238,259]

Table 9 – Reactions and equilibrium constants for the oil/brine interface

	Reactions	pK_{eq} [a]
B1	$-NH^+ \rightleftharpoons -N + H^+$	6.0
B2	$-COOH \rightleftharpoons -COO^- + H^+$	5.0
B3	$-COOH + Ca^{2+} \rightleftharpoons -COOCa^+ + H^+$	3.8
B4	$-COOH + Mg^{2+} \rightleftharpoons -COOMg^+ + H^+$	4.0

Source: [a]Parameters from Brady *et al.* [12,238,259]

Following the same procedure as for the brine/rock surface, the surface charge density on the oil/brine interface, Q_{Oil}, can be described by

$$Q_{Oil} = e\left[\varsigma_{COO}^{\max}\frac{K_{eq,B3}\tilde{\rho}_{Ca^{2+}}^{oil} + K_{eq,B4}\tilde{\rho}_{Mg^{2+}}^{oil} - K_{eq,B2}}{K_{eq,B3}\tilde{\rho}_{Ca^{2+}}^{oil} + K_{eq,B4}\tilde{\rho}_{Mg^{2+}}^{oil} + K_{eq,B2} + \tilde{\rho}_{H^+}^{oil}} + \varsigma_N^{\max}\frac{\tilde{\rho}_{H^+}^{oil}}{\tilde{\rho}_{H^+}^{oil} + K_{eq,B1}}\right] \quad (150)$$

where $\tilde{\rho}_i^{oil}$ is the molar density of the ith species at the closest distance from the oil surface.

3.1.3.3 Wettability and Contact angle

From Eq. (125), we observe that it is necessary the profile of the disjoining pressure as function of the film thickness from a long distance until the equilibrium thickness to calculate the contact angle. The van der Waals and structural components of the disjoining pressure are straightforward, since both are computed directly from Eqs. (135) and (136), respectively. On the other hand, the electric component is computed using the solution of the PBE for various thickness of the film. In practice, we solved the PBE, with a distance increment $\Delta\ell$ of 0.02 nm, from $\ell^0 = 100$ nm until reach the equilibrium thickness, *i.e.*, the distance in which the total disjoining pressure is equal to the capillary pressure (p_c) defined as input data, as outlined in Figure 8.

Figure 8 – Computational strategy used to compute the disjoining pressure and the contact angle

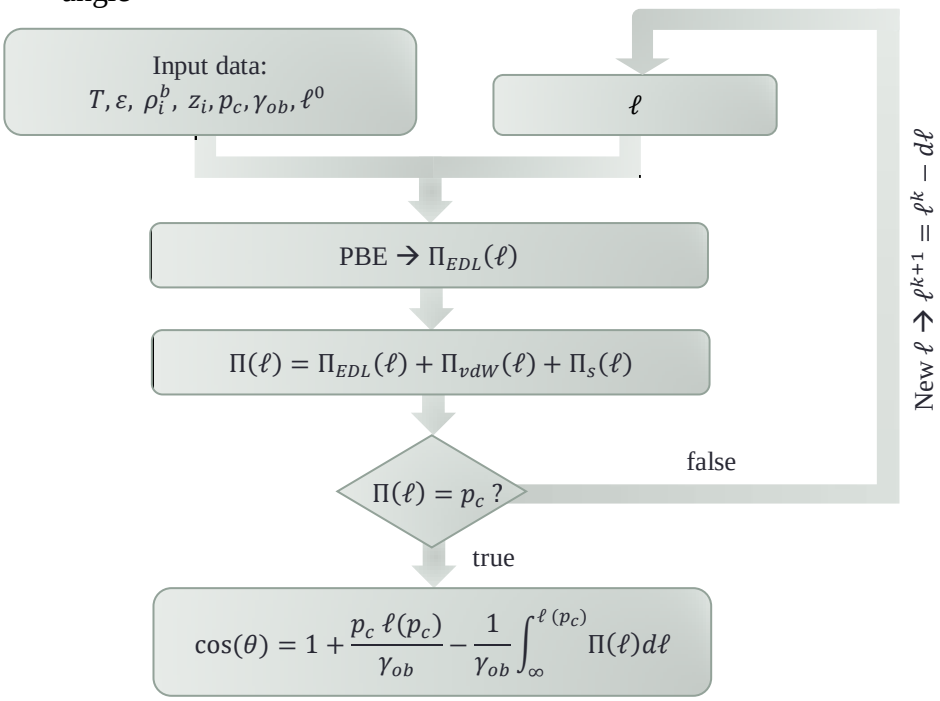

Sadeqi-Moqadam, Riahi, and Bahramian[219] reported that capillary pressure does not have any significant effect on the predicted contact angle even for capillary pressures

differing by two orders of magnitude, *e.g.* 0.02 bar to 2 bar. On the basis of these findings, we adopted an input capillary pressure equal to 0.3 bar.

3.1.4 Results and Discussion

3.1.4.1 Validation of the methodology to compute the disjoining pressure

In order to validate the program to obtain the total disjoining pressure, especially the electric component, we reproduced the results reported by Lima, Murad and Domingues.[73] The system consists of a clay surface located at $x = 0$ and an oil/brine interface located at the end of the space domain, which is variable for each case analyzed. The brine between these two interfaces is composed by Na^+, H^+, Ca^{2+}, Cl^-, and OH^-. For sandstones, the bulk equilibria between the rock and the injected EW is not relevant, since the kinetic of dissolution/precipitation reactions is not fast; in other words, the clay surface is not highly reactive. Thus the composition and concentrations of the EEW are considered equal to the injected EW. The set of reactions on the clay and oil surfaces, as well as the surface charge equations for the regulation charge boundary conditions, can be found in the original paper of Lima, Murad and Domingues.[73]

In Figure 9, the impact of the bulk concentration of Ca^{2+} in the electric potential profile is investigated for two different values of pH for a film of 5 nm. Unless otherwise specified, the bulk concentration of Na^+ is 0.1 M, while the concentration of Cl^- is set to guarantee the electroneutrality. For pH equal to 4.0, the calcite and oil interfaces have opposite surface electric potential, whereas, in Figure 9B, both surfaces have the same sign for the surface electric potential, except for bulk concentration of Ca^{2+} equal to 0.1 M.

Figure 9 – Effect of the bulk Ca^{2+} concentration in the electric potential profile for sandstones systems

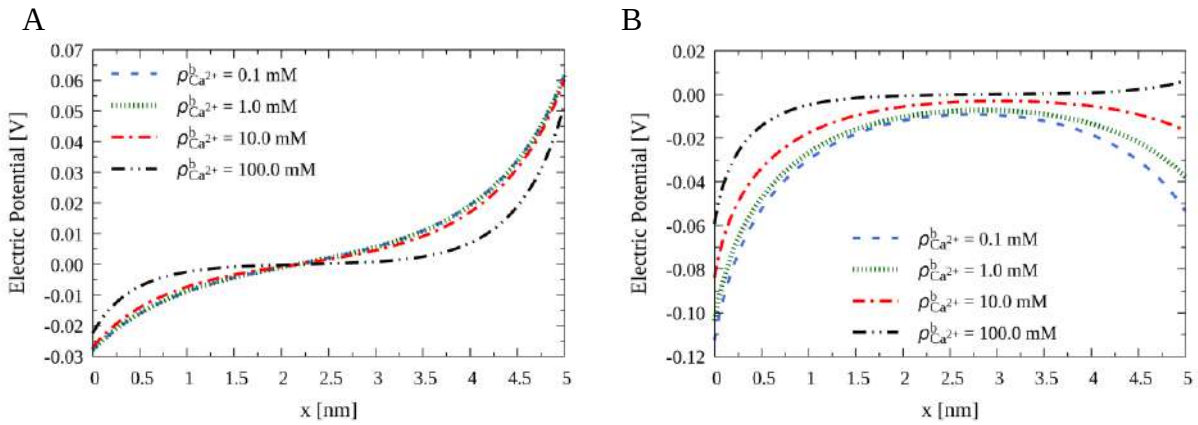

Legend: In A, bulk pH equal to 4.0, whereas, in B, it is 7.0 Film thickness equal to 5 nm and bulk concentration of ion sodium is 0.1 M.

Figure 10 shows that pH has a notable influence in the surface charge of the oil/brine interface, since for acidic pH it presents positive charge; and near to neutral pH, slightly positive or negative surface charges are observed depending on the bulk concentration of Ca^{2+}. On the other hand, for the clay surface, only values of pH close to 3.0 are able to change the surface charge towards positive values for the brine compositions analyzed. Unlike Figure 9, the film thickness in Figures 10 and 11 is equal to 3 nm, following the results provided by Lima, Murad and Domingues.[73]

Figure 10 – Effect of the bulk Ca^{2+} concentration in the surface charge of the clay and the oil as a function of pH for a film thickness of 3 nm

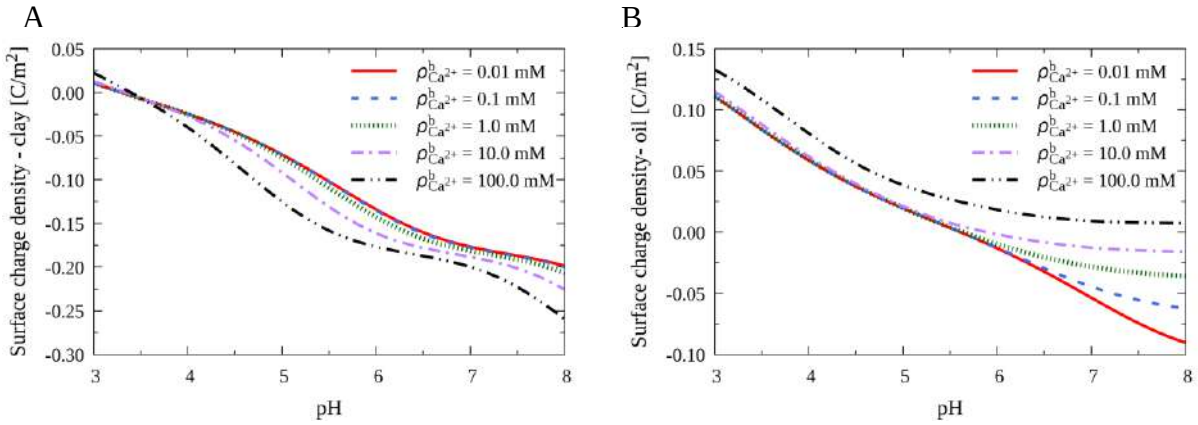

Legend: Surface charge density of clay, in A; whereas, in B, the surface charge density of the oil is presented. Bulk concentration of ion sodium is 0.1 M.

For Ca^{2+} concentration equal to 0.01, 0.1, and 1.0 mM, the entropic contributions to the electric disjoining pressure is dominant for pH >5.5, and, therefore, the disjoining pressure is positive. In other words, the contributions from the electrostatic field are always attractive independently of the system and, since the result disjoining pressures for pH >5.5 are repulsive (*i.e.* positive), the entropic contributions prevail over the electrostatic (Figure 11). The same behavior happens for pH values lower than 3.4. It is worthwhile to note that the non-entropic contribution to the electric disjoining pressure is always attractive, contributing to decrease the value of Π_{EDL}.

Figure 11 – Effect of the bulk Ca^{2+} concentration in the electric double layer disjoining pressure as a function of pH for a film thickness of 3 nm

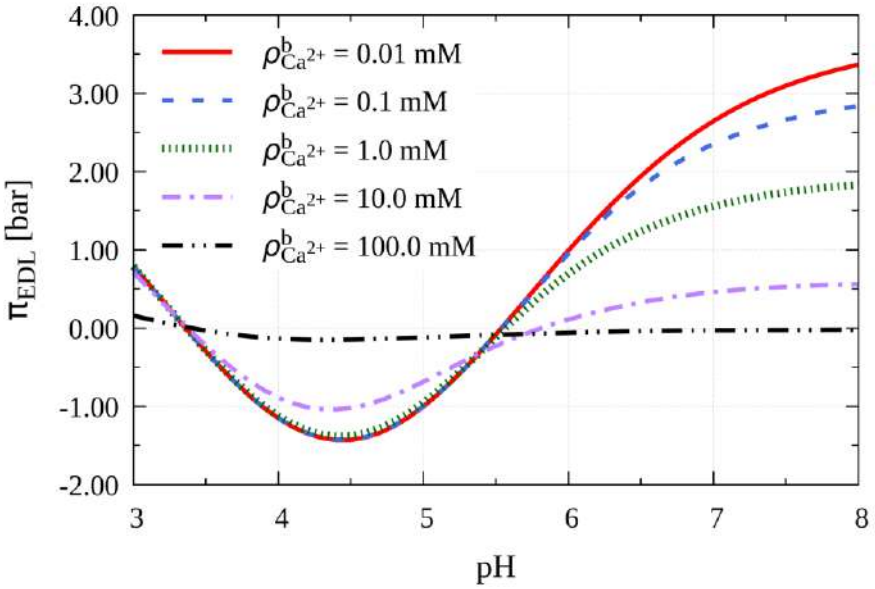

Legend: Bulk concentration of ion sodium is 0.1 M.

Finally, we evaluated the electric, van der Waals, and structural components of the disjoining pressure as function of the $\log \ell$ for pH equal to 4.0 and 7.0, and bulk Ca^{2+} concentration equal to 0.1 mM and 0.01 mM. All the results displayed in Figure 12 reproduced with excellent agreement those reported by Lima, Murad and Domingues.[73]

They considered only the nonretarded van der Waals interaction, without the screening effects. Thus, Π_{vdW} exhibits the same profile for all conditions, independently of the brine composition. The same is valid to Π_S. However, the structural forces are always repulsive and short-ranged forces. Moreover, they are dominant over the other components of the disjoining pressure for very small film thickness.

Figure 12 – Electric, van der Waals, and structural components of the disjoining pressure for different values of pH and bulk Ca^{2+} concentration for sandstones systems

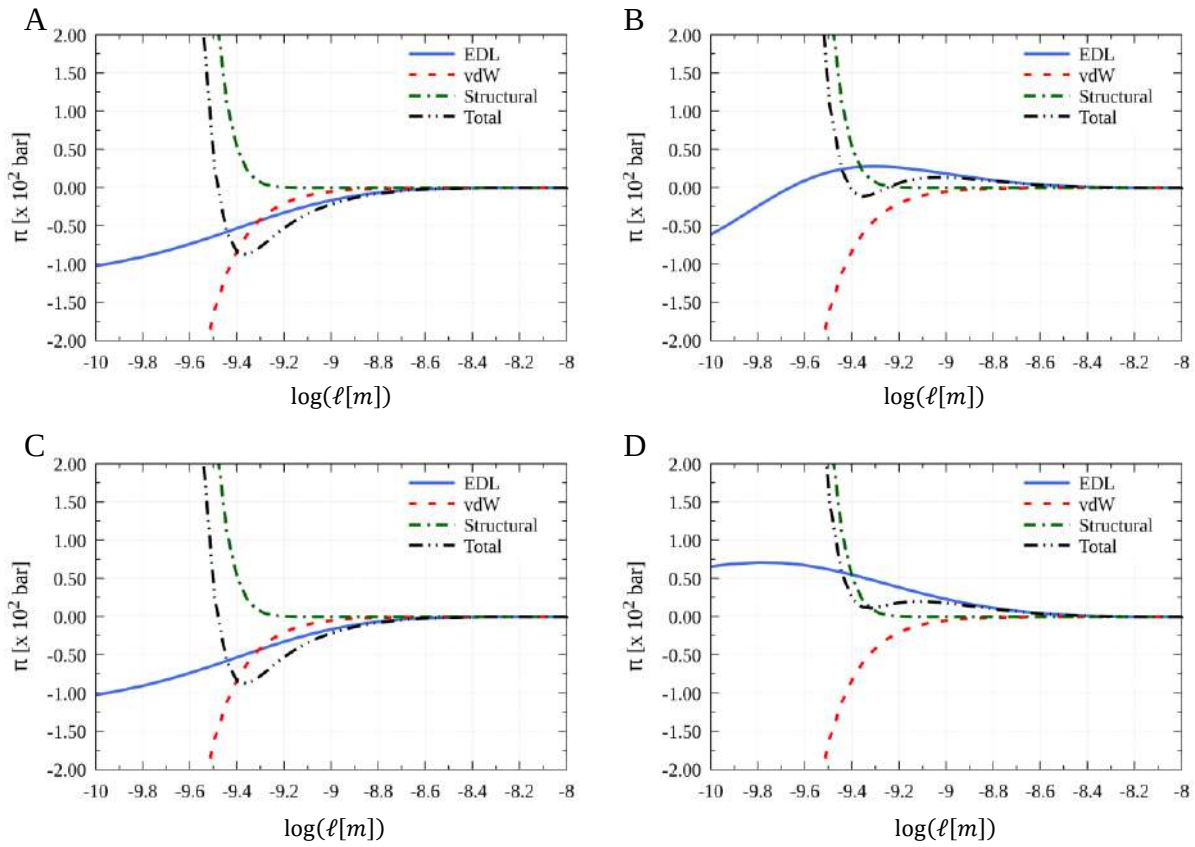

Legend: In A and B, the bulk Ca^{2+} concentration is 0.1 mM, whereas in C and D, it is 0.01 mM. The pH is equal to 4.0 for the graphics A and C. On the other hand C and D represent the neutral pH.

3.1.4.2 Wettability of calcite/brine/oil systems

The IEP of the calcite in pure water varies from 7 to 12, depending on the analyzed condition of the mineral; consequently, the calcite surface has a strong tendency to be positively charged compared to sandstone.[214,239] On the other hand, as exposed in the previous section, the oil has a tendency to be negatively charged particularly in pH greater than 5.5. Since the surface charge density of the oil is very sensitive to pH and the calcite promotes a buffering toward basic pH (favoring a negative oil/water interface), it would be interesting to inject an electrolyte solution that changes the surface charge density of calcite to more negative values in order to increase the electrostatic repulsion between both surfaces.

Following the experimental observations, in which the calcite surface charge decreases with the increase in the concentration of SO_4^{2-},[61,239] we analyzed the interfacial properties over

different concentrations of sulfate in the EW for different values of ionic strength at 298.15 K. Thus, for each curve in Figures 13 – 19, the ionic strength is kept constant and for a specified initial concentration of Na_2SO_4, we calculated the corresponding concentration of NaCl to be added to the mixture. The pH was determined to maintain the electroneutrality of the EW. As can be seen in Figure 13, an increase in the injection of SO_4^{2-} causes a rise in pH. Moreover, for the same concentration of SO_4^{2-} in the injected EW, the pH is greater at lower ionic strength. Both behaviors are strongly related to the equilibrium reaction between sulfate and bisulfate; additionally, the latter observation is also related to the equilibrium reaction involving Na^+, SO_4^{2-}, and $NaSO_4^-$ ions.

Figure 13 – Variation of the engineered water pH as function of the initial SO_4^{2-} concentration for different ionic strengths

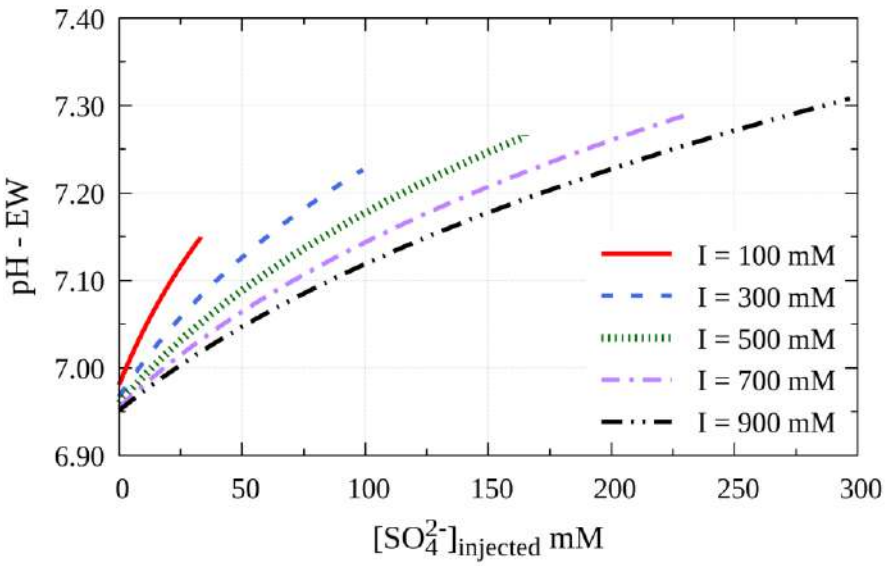

Legend: In the key I is the ionic strength of the initial composition expressed in mol/m³.

Here, we do consider a fast kinetics between the EW and the calcite as reported by some authors.[216,232] Therefore, the pH of the injected EW is quite different from the EEW pH as shown in Figure 14. It varies more than 1.3 units in the scale. Besides, a CO_2 partial pressure of $10^{-3.4}$ atm – equivalent to atmospheric CO_2 – was adopted.[239,241]

Figure 14 – Variation of the equilibrated engineered water pH as function of the initial SO_4^{2-} concentration for different ionic strengths

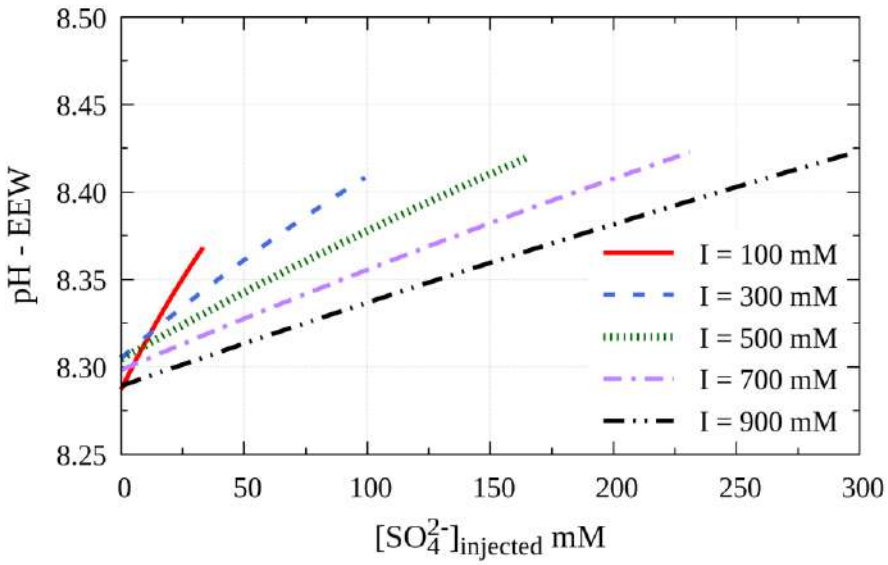

Legend: In the key I is the ionic strength of the initial composition expressed in mol/m³.

After the bulk equilibrium between calcite and engineered water (dissolution/ precipitation reactions), we could calculate the surface charge density on the calcite in the EEW by PBE with charge regulation, as presented in Figure 15 for the two sets of reactions used in this work (Song's model[239] and Eftekhari's model[241]), observing that the adsorption of SO_4^{2-} places negative charges near the calcite surface.

The range of variation of the calcite surface charge is larger for the Song's model[239] compared to the Eftekhari's model[241] (Figure 15), what does not mean that one model is better than other. They were reported for different samples of rock using different complexation reactions and methodologies, as mentioned in section 3.1.2.3. However, qualitatively, both models exhibit similar behaviors.

For comparison, Figure 16 shows the surface charge density of the oil for the same electrolyte compositions of Figure 15 and, as expected, the surface charge is negative in this case. Besides, the profiles are almost constant or with a slight inclination, reflecting the buffering effects of calcite over the EW solution since the oil surface is highly sensitive to pH. In other words, since the absolute variation of the EEW pH is not pronounced, then, the oil surface charge does not vary considerably.

Figure 15 – Surface charge density on the calcite as function of the initial SO_4^{2-} concentration for Song's and Eftekhari's reactions model

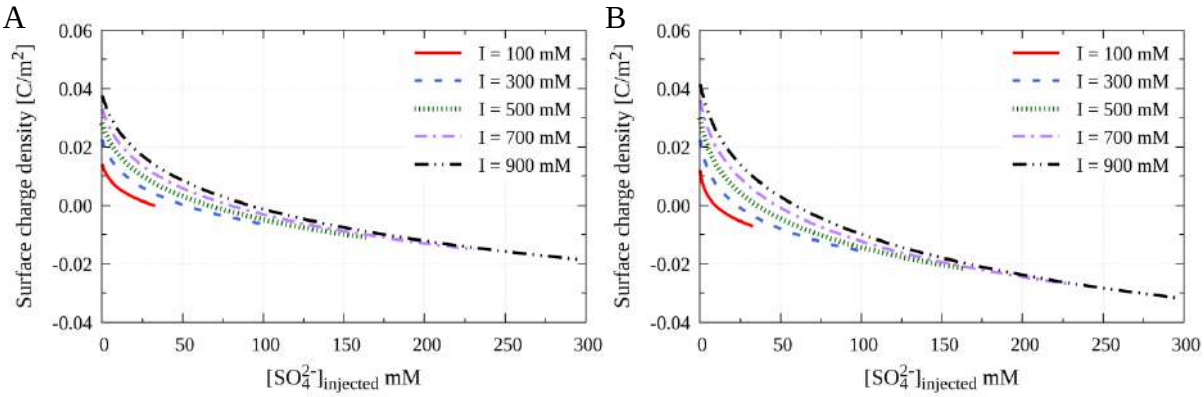

Legend: Surface charge density of calcite using charge regulation with set of reactions reported by Eftekhari *et al.* (Eftekhari's model)[241] in A; whereas, in B, the set of reactions are those reported by Song *et al.* (Song's model)[239]. In the key I is the ionic strength of the initial composition expressed in mol/m³.

Figure 16 – Surface charge density on oil as function of the initial SO_4^{2-} concentration

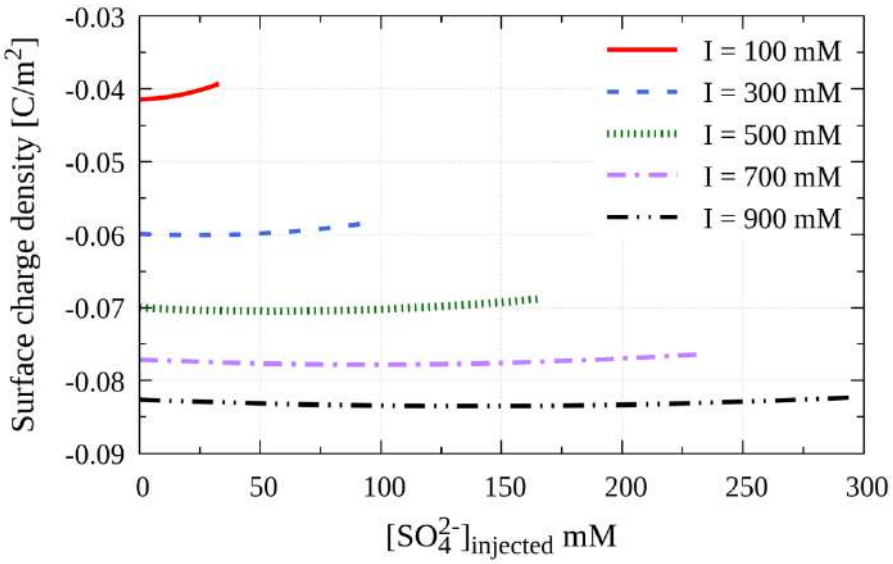

Legend: Surface charge density of oil using charge regulation with set of reactions reported by Brady *et al.* (2012, 2015).[12,238,259] In the key I is the ionic strength of the initial composition expressed in mol/m³.

In order to evaluate the contact angle, it is necessary to know the Hamaker constant of the interaction between calcite and oil across the electrolyte solution. As demonstrated in Eq. (132), the non-retarded Hamaker constant depends on the refractive index and dielectric constant of the phases. For calcite, due to its anisotropy, instead of a singular value of dielectric constant, we have a tensor with diagonal components equal to 8.67, 8.69, and

8.31;[260] and, for the refractive index, calcite has two components: one from the ordinary rays (1.6584) [260] and other from extraordinary rays (1.4864).[260]

Specifically for the dielectric constant of the calcite, single values (ε_{11}, ε_{22}, or ε_{33}) or combinations of them do not impact considerably the entropic contribution of the Hamaker constant. Thus, we adopted a value of 8.68. However, Figure 17 reveals that the refractive index of calcite has a considerable impact on the contact angle. For the Eftekhari's model, a decrease of the contact angle is observed using the extraordinary refractive index to compute the Hamaker constant (Figure 17A). The same is valid for the Song's model with the difference that the ionic strength of 900 mM using the extraordinary refractive index changes the wettability toward completely water wet (Figure 17B), with an increase of the film thickness as displayed in Figure 18B.

Figure 17 – Effect of the calcite refractive index and ionic strength on the contact angle

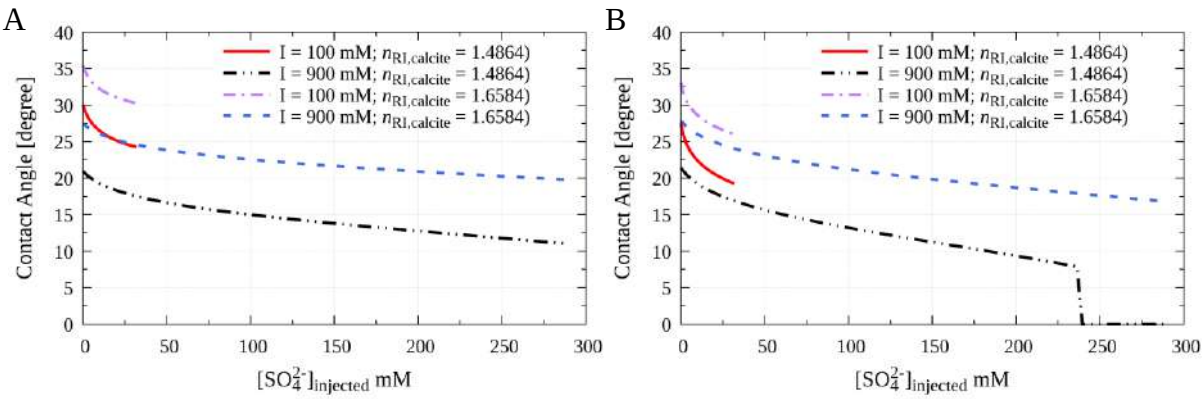

Legend: Surface charge density of calcite using charge regulation with set of reactions reported by Eftekhari *et al.* (Eftekhari's model)[241] in A; whereas, in B, the set of reactions are those reported by Song *et al.* (Song's model)[239]. In the key I is the ionic strength of the initial composition expressed in mol/m³.

Regarding the oil, both parameters are dependent on the composition, varying from one sample to another. Here we considered the dielectric constant and refractive index of the oil equal to 1.925 and 1.455, respectively.[261]

In the literature, the EW is frequently referred as low-salinity water;[13,14,214,216] however, as can be seen in Figures 17 and 18, moderate-salinity water was able to modify completely the wettability toward water-wet. Here, the effect is directly related to the concentration of SO_4^{2-} which acts as a potential determining ion.

Figure 18 – Impact of the calcite refractive index and ionic strength on the equilibrium film thickness

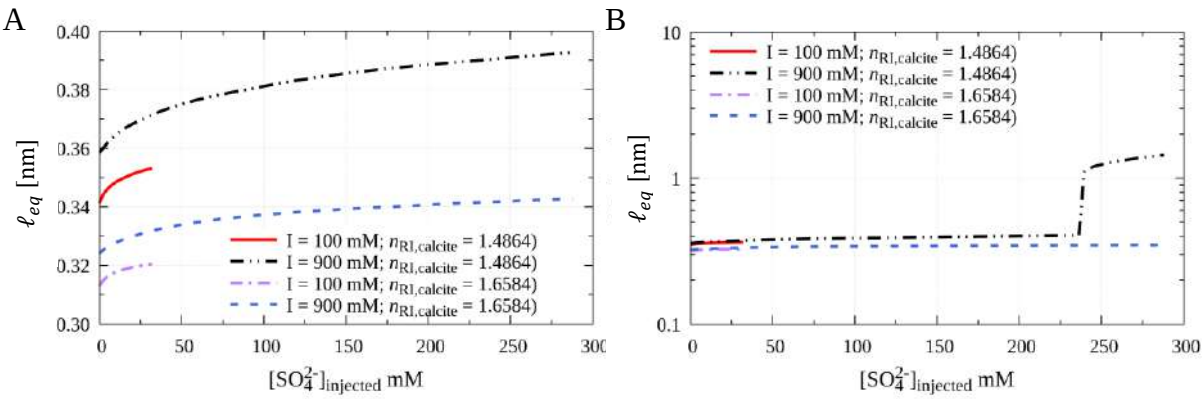

Legend: Surface charge density of calcite using charge regulation with set of reactions reported by Eftekhari *et al.* (Eftekhari's model)[241] in A; whereas, in B, the set of reactions are those reported by Song *et al.* (Song's model)[239]. In the key I is the ionic strength of the initial composition expressed in mol/m³.

Figure 19 shows the electric potential profile as a function of the distance to a width pore of 1.1 nm for both 100 mM and 900 mM ionic strengths with initial sulfate concentration equal to 2.66 mM and 239 mM, respectively, and charge regulation on calcite described by Song's model.

Figure 19 – Electric potential profile as function of the distance for a film thickness equal to 1.1 nm

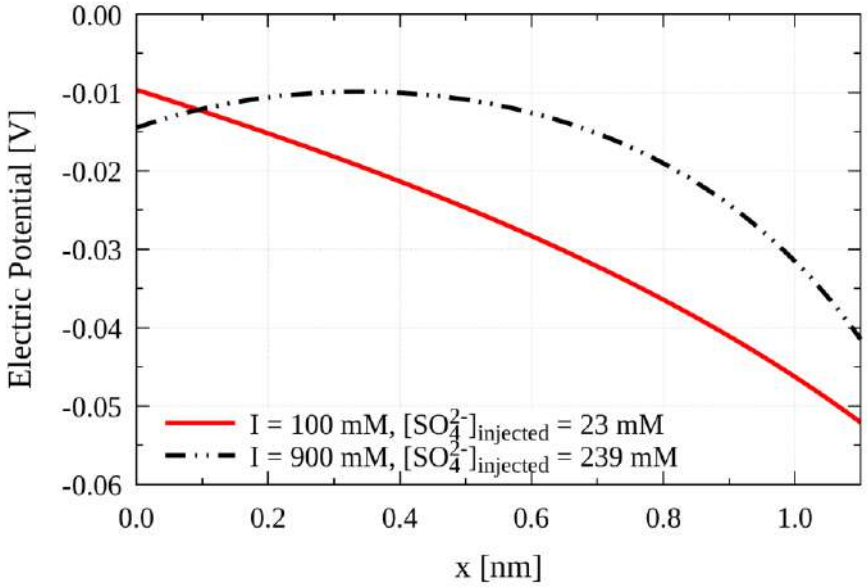

Legend: Surface charge density of calcite using charge regulation with set of reactions reported by (Song's model).[239] In the key I is the ionic strength of the initial composition expressed in mol/m³.

In order to analyze the electric disjoining pressure, let us consider the distance of about 0.32 nm, where the electric potential profile, for an ionic strength equal to 900 mM, has a maximum. At this point, for 900 mM ionic strength, the non-entropic contribution to Π_{EDL} is zero; whereas, for 100 mM, it is negative. Regarding the entropic component, it is repulsive for both cases; however, for ionic strength of 100 mM, the contribution is lower, not being enough to overcome the attractive contribution of the non-entropic term. Consequently, the resulting electric disjoining pressure is attractive for ionic strength equal to 100 mM with initial sulfate concentration equal to 2.66 mM (Figure 20). On the other hand, it is repulsive for ionic strength equal to 900 mM with initial sulfate concentration equal to 239 mM (Figure 20).

Figure 20 – Effect of ionic strength in the electric double layer disjoining pressure as a function of the initial SO_4^{2-} concentration for a film thickness of 1.1 nm

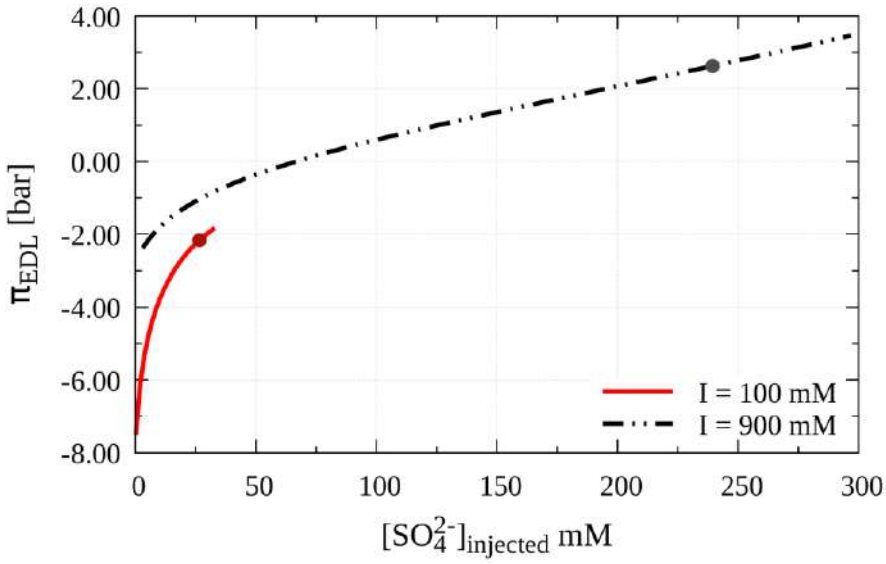

Legend: Surface charge density of calcite using charge regulation with set of reactions reported by (Song's model).[239] In the key I is the ionic strength of the initial composition expressed in mol/m³.

3.1.5 Conclusion

This is a broad work that involves thermodynamics of electrolytes, chemical equilibria in bulk phase and on surfaces, thermodynamics of thin films, and interfacial phenomena. With this methodology it is possible to compute the contact angle at equilibrium and the wetting behavior of a rock surface. The wetting properties have a considerable influence on the oil

displacement by water since they are correlated to the capillary pressure, interfacial tensions, and electrical properties in the pores.

We could observe a higher tendency toward water-wet calcite with the injection of EW containing sulfate. In the literature, the EW is frequently referred as low-salinity water; however, this is not always true, as reported here. It is important to highlight that at temperature of about 60°C, it was experimentally verified that the rock tends to be more water wet.[262] Thus it would be interesting to expand this analysis to higher temperatures besides room temperature. At this point, we have the limitation of the unknown surface reactions enthalpies or reaction equilibrium constants at higher temperatures.

Therefore, with this methodology, we could reassure some hypotheses that have been made over the years to explain the enhanced oil recovery by EW.

3.2 Contact angle of rock/brine/oil system using 3D-DFT

3.2.1 Introduction

DFT has been used to investigate the wettability in vapor/liquid/solid substrate systems because of its versatility to determine the equilibrium structure and corresponding thermodynamic quantities of systems subjected to external potentials.[159–161,263–266] However, the application of DFT to study the wettability and contact angle of liquid/liquid/solid substrate as far as we could track has not been performed.

Moreover, in systems with little or no symmetry, the resolution of DFT in tridimensional coordinate is required. However, the high number of convolutions has impact ion the efficiency of the 3D-DFT; thus, it is interesting to use the fast Fourier transform (FFT) in an attempt to overcome this limitation.[65,108]

The aim of this work, which is fully presented in APPENDIX H, is the determination of the most probable contact angle of a system characterized by an oil phase, ionic aqueous solution and an uncharged planar solid surface using 3D-DFT. More than expose a quantitative value, we are interested in providing a different approach to study these kinds of system using classical tridimensional DFT. Here the characteristics of the oil and the solid surface are defined by external potentials between them and the ions in solution. Two

strategies were used to describe the external potential: hard-surfaces and non-electrostatic interactions with the dispersion constant described by the Lifshitz theory. For the latter, a hypothetical rock surface of silica and an oil phase composed by pure pentane were considered, in order to compute the dispersion parameters between the ions and the surfaces.[65]

3.2.2 Methodology

In the following derivations, we consider a liquid droplet of oil resting on a flat solid surface surrounded by ionic aqueous solution as presented in Figure 7B. It is assumed that the chemical and physical characteristics of the substrate are not changed because of the contact with the fluid molecules. Neglecting the gravitational field, the shape of the droplet may be visualized rather close to a spherical cap. If θ is the contact angle between the droplet of volume $\mathcal{V}_d$ and the solid, then the radius R_d, the height h_d of the cap and the area of the droplet in contact with the solid (A_{so}) can be written as[263,267]

$$R_d^3 = \frac{3\mathcal{V}_d}{\pi(1+\cos\theta)^2(2-\cos\theta)} \tag{151}$$

$$h_d = R_d(1+\cos\theta) \tag{152}$$

$$A_{so} = \pi R_d^2 \sin^2\theta \tag{153}$$

The geometric representation of these measures is found in Figure 21.

Figure 21 – Geometric measure representation of spherical cap

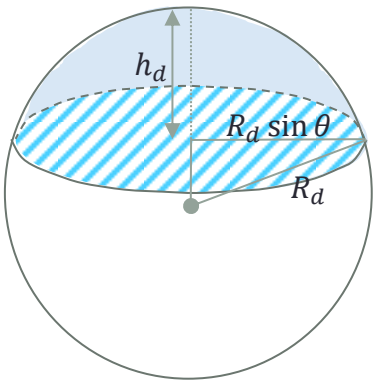

Legend: The spherical cap is in blue. θ, R_d, and h_d are the contact angle, the radius and the height, respectively. The hatched area corresponds to the area of the base circle of the cap, A_{so}.
Source: Adapted from Barbosa, Lima and Tavares (2019).[65]

For the sake of simplicity, we consider the mean density inside the droplet to be uniform, *i.e.*, the oil droplet is incompressible. We also assume, *a priori*, the absence of thin brine film between the solid surface and the oil.

Given an infinitesimal change in area $\mathrm{d}A$, the change in the surface energy $\mathrm{d}E$ of the system in Figure 7B is given

$$\mathrm{d}E = (\gamma_{so} - \gamma_{sb} - \gamma_{ob}\cos\theta)\mathrm{d}A \tag{154}$$

where γ_{sb}, γ_{so}, and γ_{ob} are the solid/brine, solid/oil, and oil/brine interfacial tensions, respectively. The balance of forces in the $\hat{\mathbf{x}}$ direction correlates the interfacial tensions with the contact angle by the Young equation[211]

$$\cos\theta = \frac{\gamma_{so} - \gamma_{sb}}{\gamma_{ob}} \tag{155}$$

The nature of the contact angle is determined by the relative affinity of the two liquid phases for the solid, expressed by their interfacial tensions.[65]

3.2.2.1 Simulation Details

Our approach is based on a classical DFT of inhomogeneous fluids in three dimensions[65,108,129] which treats the rock and the oil as external potentials acting on the ions in the brine. The convergence criterion for the grid was based on the analysis of the density profiles.

For the hard sphere contribution, we used the WB version of the FMT.[117,118] The convolutions were solved in reciprocal space as presented in Eqs. (57) and (58).

As mentioned before, several approaches are available in the literature to take into account the contributions from electrostatic correlations.[134,135,144,136–143] However, for the sake of simplicity, here we use the BFD model,[114] although it presents well-known limitations.[27,29,133,152] It is a classical approximation and we are interested in presenting a strategy to calculate the contact angle of a liquid/liquid/solid system, independently of the

functionals used to describe the excess Helmholtz energy. The second order DCFs were computed based on the equations developed by Blum and Rosenfeld.[147]

As well as the contributions from hard sphere interactions, the convolutions of $\delta F^{el}/\delta\rho_i$ and the Poisson equation were calculated in the Fourier domain, following the strategy proposed by Knepley and coworkers.[108]

The dielectric constant was treated as uniform in each phase, in order to determine the Hamaker constant between the ions and interfaces. However, the image effects were neglected.

The oil droplet and the brine adopt the configuration that minimizes the grand potential

$$\Omega = -p\mathcal{V} + \gamma_{sb}A_{sb} + \gamma_{so}A_{so} + \gamma_{ob}A_{ob} \tag{156}$$

which is conveniently divided into bulk and surface contributions, where A_{ij} is the surface area between phases i and j, and the subscripts s, b, and o correspond to the solid, brine and oil phases, respectively. The line tension was neglected. In order to provide the equilibrium contact angle θ_{eq} among the three phases, we simulated a set of systems with a constant droplet volume varying the contact angle θ' (Figure 22).

Figure 22 – Variation of the radius with the contact angle for a constant droplet volume

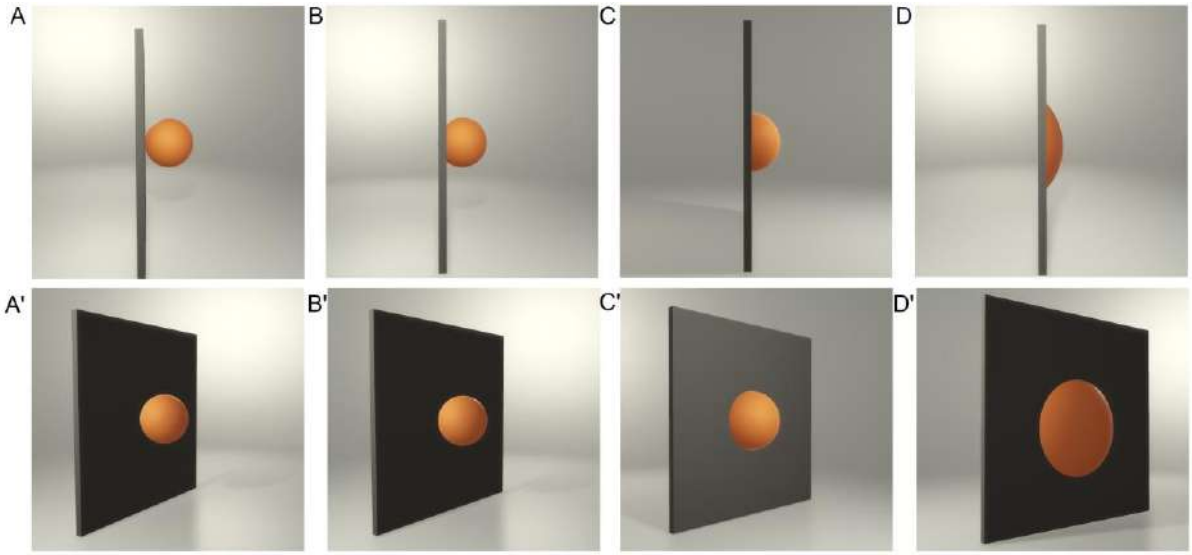

Legend: The upper and lower figures in each column are equivalent, only the perspective of the observer changes. The contact angles are 0º, 45º, 90º, and 135º, respectively.
Source: Barbosa, Lima and Tavares (2019).[65]

An increase in the droplet radius with increasing θ' is observed to maintain the constant volume. Thus, θ' is an input data for each simulation in a set, along with the volume, temperature, dielectric constant, bulk densities, ionic valences, ionic diameters, and droplet volume, whereas the density distribution of ions outside the droplet and the grand potential provided by DFT are the output data. The latter does not include the contribution to the total grand potential due to the interaction between solid/oil ($\gamma_{so}A_{so}$), which in turn is added *a posteriori*, as shown in Figure 23. We assume, for the sake of simplicity, that the density of the oil inside the droplet is uniform for all the systems in a set. With this information, θ_{eq} is calculated by the analysis of the angle that minimizes Ω.

Figure 23 – Computational strategy used to compute the equilibrium contact angle

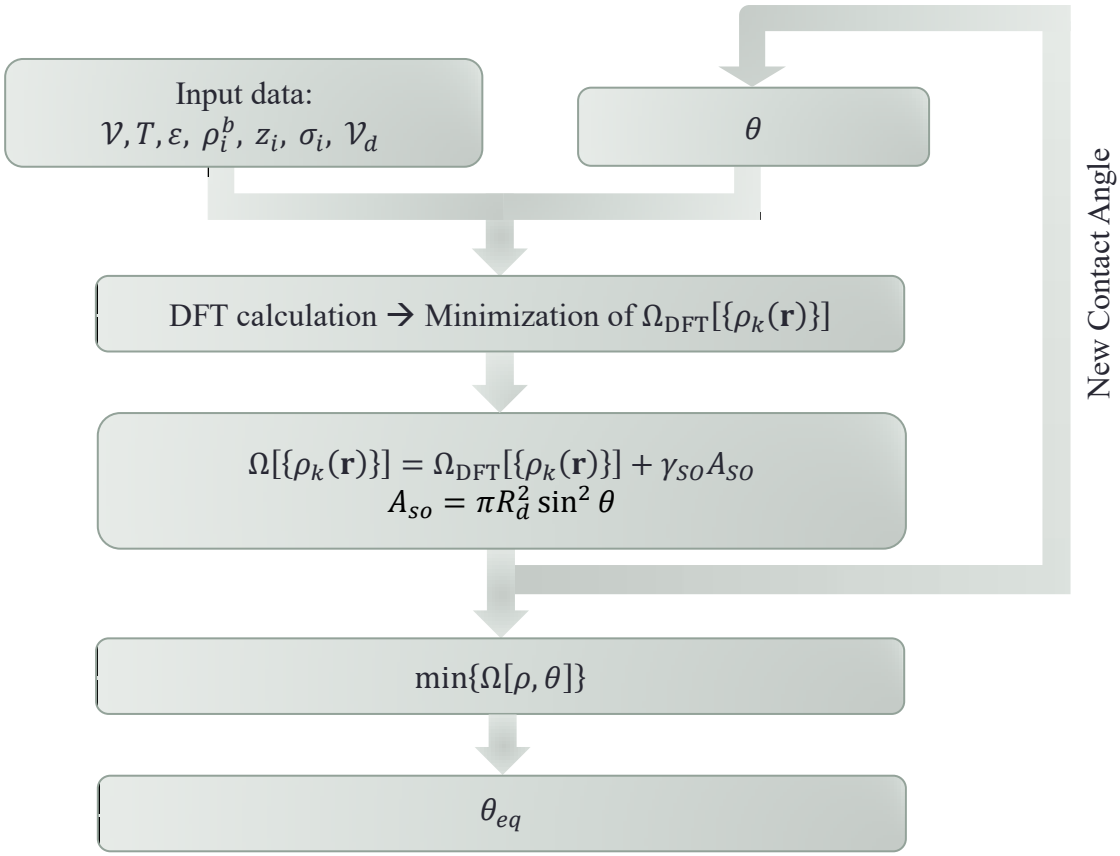

Source: Barbosa, Lima and Tavares (2019).[65]

3.2.3 Results and Discussion

For our simulations, we examined an aqueous NaCl solution (1:1) at 298.15 K. The ionic diameters are equal to 0.198 nm and 0.362 nm for cation (σ_+) and anion (σ_-), respectively.[260] The simulation cell has the dimensions of 6 × 6 × 6 nm^3 and the flat surface is placed at z equal to 0 nm. The volume of the droplet was set to 3.0 nm^3. The dielectric constant of the solvent is equal to 78.5. Periodic boundary conditions were considered in $\hat{\mathbf{x}}$ and $\hat{\mathbf{y}}$ directions, whereas in $\hat{\mathbf{z}}$ direction both boundaries are delimited by the presence of planar surfaces.

Figures 24 and 25 present the density profiles of cations and anions, respectively, near to the droplet and solid surface with contact angle equal to 34.4° and bulk ionic strength, ρ^b, of 1.0 M. To evidence the vicinity of the droplet, only half of z axis is shown. The distances are adimensionalized by the cationic diameter. We used the hard wall potential to take into account the interactions between brine/solid surface and brine/oil droplet. The discrete increase of the cation concentration close to the interfaces (see Figure 24) is due to the BFD theory used to describe the electrostatic correlation. Comparatively with data from molecular simulation, this increase is qualitatively incorrect and has motivated the development of other theories to compute the electrostatic correlations.[134,135,144,136–143] It is interesting to note that because the cation is smaller than the anion by a factor of 0.55, the former can get closer to the interfaces. Consequently, a more pronounced increase in concentration of anions can be observed in the vicinity of the interfaces (Figure 25), attracted by the first layer composed by the cations. It is important to remember that in this study both surfaces are supposed to be neutral, so there is no electrostatic interaction between ions and surfaces.

We analyzed a range of contact angle from 0.1 to 2.4 rad (5.7° to 137.5º) for bulk ionic strength equal to 0.5 and 1.0 M, and the grand potential provided by DFT (Ω_{DFT}) was determined in this process. In order to find the contact angle, it is necessary to add the contribution of oil/solid surface to the grand potential given by

$$\Omega[\{\rho_k(\mathbf{r})\}] = \Omega_{\mathrm{DFT}}[\{\rho_k(\mathbf{r})\}] + \gamma_{SO}A_{SO} \tag{157}$$

Figure 24 – Density profile of cations near a droplet for a bulk ionic strength of 1.0 M

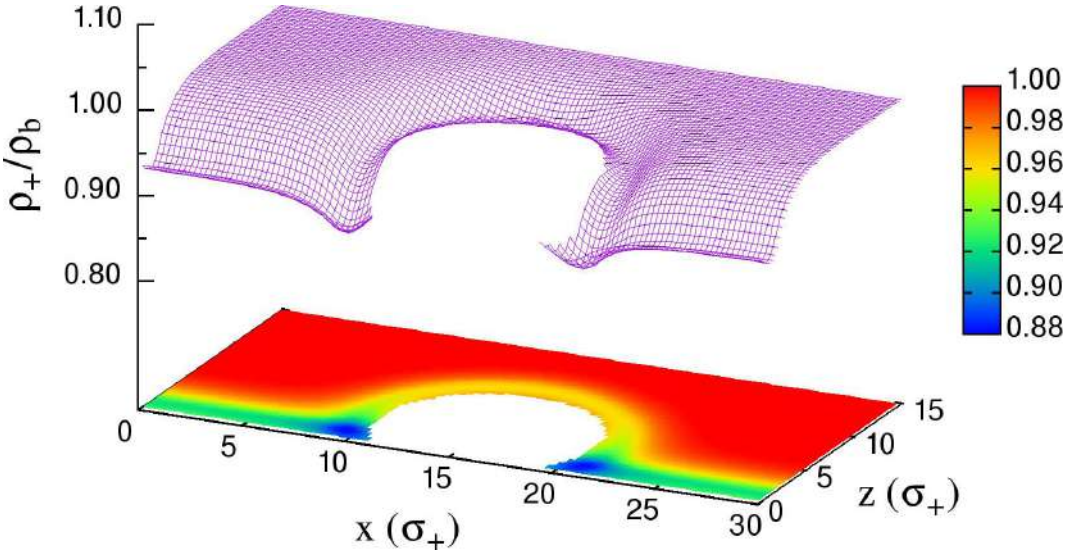

Legend: Contact angle between the rock and droplet equal to 0.6 rad (34.4°).
Source: Barbosa, Lima and Tavares (2019).[65]

Figure 25 – Density profile of anions near a droplet for a bulk ionic strength of 1.0 M

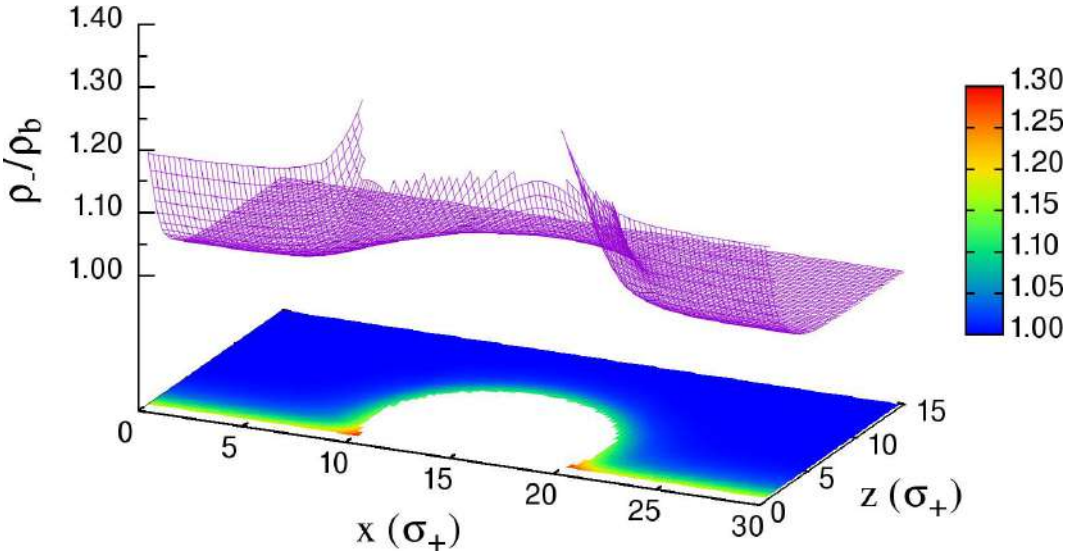

Legend: Contact angle between the rock and droplet equal to 0.6 rad (34.4°).
Source: Barbosa, Lima and Tavares (2019).[65]

Increasing the contact angle increases the basal area of the spherical cap; therefore, depending on the magnitude of γ_{so}, the profile of $\Omega[\{\rho_k(\mathbf{r})\}]$ presents a minimum within the range of contact angle analyzed. The impact of different values of γ_{so} (0.5, 1.0 and 2.0 mN/m) is shown in Figures 26 and 27 and Table 10 for bulk ionic strength equal to 0.5 and 1.0 M, respectively.

Table 10 – Summary of equilibrium contact angle (in degrees) for different concentrations and external potentials

γ_{so} [mN/m]	Hard Wall		Lifshitz	
	0.5 M	1.0 M	0.5 M	1.0 M
0.5	103	126	103	130
1.0	69	103	66	105
2.0	< 5	69	< 5	69

Source: Barbosa, Lima and Tavares (2019).[65]

Figure 26 – Grand potential for the oil/brine ($\tilde{\rho}^b = 0.5$ M)/rock system with hard-wall interaction between brine and rock

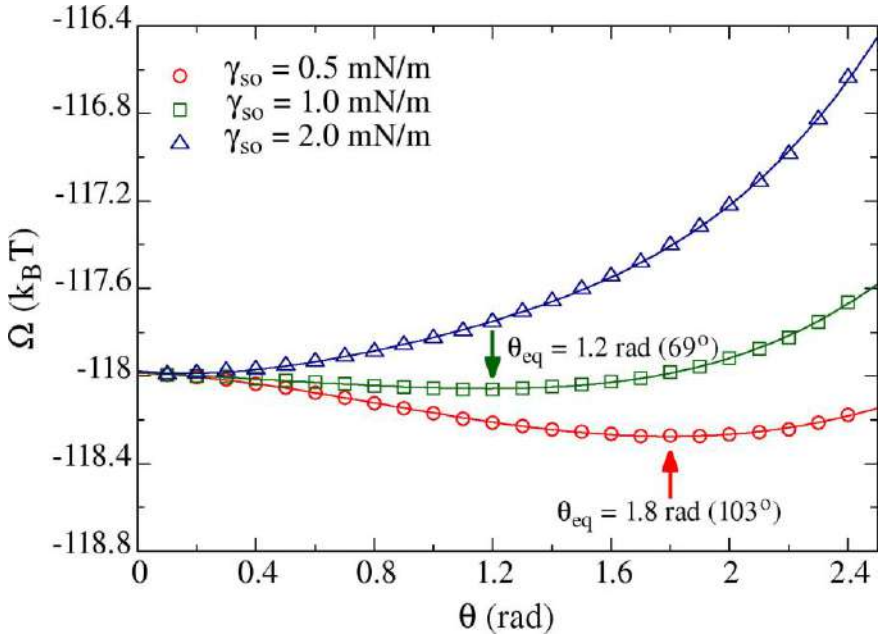

Legend: The arrows refer to the equilibrium contact angle.
Source: Barbosa, Lima and Tavares (2019).[65]

Not surprisingly, considerable differences are observed between systems with different γ_{so}, however the impact of this contribution is much more pronounced than the contribution between solid/brine and brine/oil interfaces. Considering γ_{so} equal to 2.0 mN/m the system is completely water-wet for ρ^b equal to 500 mol/m^3 as observed in Figure 26. Thus, for the estimation of the wettability following the methodology proposed here, it is necessary to know γ_{so}. However, with the experimental measure of this property, it is possible to predict the effect of different electrolyte solutions on the wettability of the system rock/brine/oil.

Figure 27 – Grand potential for the oil/brine ($\tilde{\rho}^b = 1.0$ M)/rock system with hard-wall interaction between brine and rock

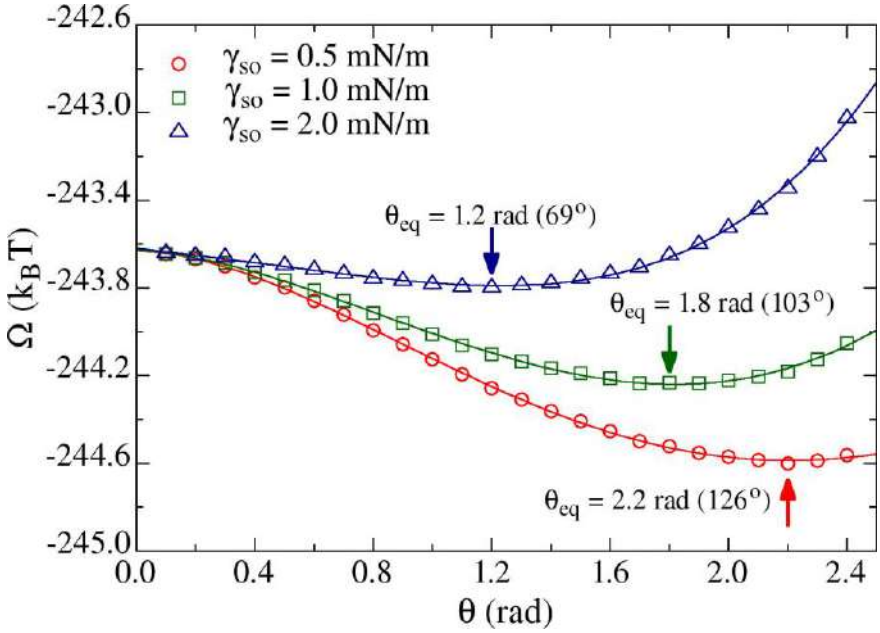

Legend: The arrows refer to the equilibrium contact angle.
Source: Barbosa, Lima and Tavares (2019).[65]

Table 11 gives the constants necessary to calculate the Hamaker constant by Lifshitz theory for Na^+ and Cl^- interacting with silica and n-pentane. According to the value of Hamaker constant both ions are attracted by silica. However, this effect is about 7 times stronger for chloride. Dispersion coefficients are presented in Table 12.

Nevertheless, as it can be seen in Table 10, the dispersion interactions have little influence on the equilibrium contact angle compared to the hard wall potential, considering the ions, solid and oil analyzed. Other salt components could provide different results.

Table 11 – Physical properties for water, silica, n-pentane and ions

	Dielectric constant	Refractive index	Polarizability [Å^3]	Ionization energy [10^{12} erg]
Water	78.5[a]	1.333[a]	–	20[a]
n-pentane	1.84[a]	1.349[a]	–	20[a]
Silica	3.8[a]	1.448[a]	–	20[a]
Na^+	–	–	0.1485[b]	54.7[b,c]
Cl^-	–	–	3.764[b]	9.15[b,c]

Legend: [a]Physical properties from Israelachvili[67]. [b] Physical properties from Tavares *et al.*[157] [c]Ionization energy in water.

Table 12 – Hamaker coefficients for ions

	$\beta B_{ion-pentane}$ [Å^3]	$\beta B_{ion-silica}$ [Å^3]
Na^+	0.0678	0.578
Cl^-	0.552	4.248

Source: Barbosa, Lima and Tavares (2019).

3.2.4 Conclusion

There are also several avenues for improvement of the model here proposed. The assumption of constant density and, hence, of a constant volume of oil droplet containing a given number of molecules was employed, however it is possible to refine the model aiming to consider the oil molecules explicitly inside the droplet. In such analysis the contribution due to the oil/solid surface interactions would be automatically included into the 3D-DFT. Another important contribution is the inclusion of charge on the solid surface, or even, on the oil surface.

The description of electrostatic correlation by more sophisticated theories is straightforward. Nevertheless it is important to evaluate the advantages of this change for each particular system, because, in general, they demand more computation time, especially for 3D-DFT. We conclude that the approach presented here is promising to investigate the contact angle of different electrolyte solutions and the impact of the bulk concentration and ionic valence on the wettability. The tridimensional treatment turns the method versatile and provides options for inclusion of some peculiarities such as roughness on the solid surface and the presence of a thin film of brine between the oil and the solid as represented by Figure 7B.

GENERAL CONCLUSIONS

On the basis of the results obtained on this thesis, it is possible to conclude that the Poisson-Boltzmann equation is a useful tool to analyze systems in which the Donnan potential is present, as well as, the wettability of systems containing two liquid phases and a solid surface.

Regarding the biological line of this thesis, two papers were published. The first, published in "The Journal of Physical Chemistry B", addressed the ionic partitioning across an erythrocyte, evaluating the contribution of non-electrostatic interactions and the difference in dielectric constant between the intracellular and extracellular media for this partition.[21] A new modification was developed for the PBE by the insertion of the Born correction term due to the dielectric constant difference between the two media involved. This last modification was implemented during the doctoral research, being an important advance of this thesis, which also complemented the study realized in the master.

The second paper, which analyses the electric behavior of the *B. brevis*, was submitted to the journal "Colloids and Surfaces B: Biointerfaces". The cell wall was treated by a charge regulation method applied to the volumetric charge density profile. The zeta potential profile as a function of pH within the fluid phase was evaluated, showing a good agreement with experimental data.[57]

Part of the results obtained by the application of PBE to investigate the wettability of rock/brine/oil was presented in the "XI Iberoamerican Conference on Phase Equilibria and Fluid Properties for Process Design" in 2018[268] and a paper involving this theme is being written. We showed that engineered water is a better denomination over low salinity water to characterize the electrolyte solution to be injected in the reservoir in order to enhance the oil recovery. Besides, we reassured the dominant role of the sulfate in this process.

The balancing of the intrinsic approximations of the PBE might cancel them out, promoting an excellent reproduction of experimental data, depending on the system to be studied. However, especially for concentrated systems, polyelectrolytes, and/or highly confined systems, a method with a higher level of detail, such as DFT, should be considered.

In this context, we also studied the wettability using the classical density functional theory. It has been used to investigate the wettability in vapor/liquid/solid substrate systems over the years because of its versatility to determine the equilibrium structure and corresponding thermodynamic quantities of systems subjected to external potentials.

However, the application of DFT to study the wettability and contact angle of liquid/liquid/solid substrate as far as we could track had not been performed until the publication of our paper "Wettability of rock, oil and brine system based on density functional theory" in the journal "Fluid Phase Equilibria".[65] This topic was also presented in the "IX Congresso Brasileiro de Termodinâmica Aplicada", in 2017.[269]

As mentioned before, in order to guarantee the linearity of this thesis, the fundamental results obtained for confined electrolyte systems using classical density functional theory were only mentioned briefly in the introduction. However, this thematic was also studied during these years and a work entitled "Estudo de sistemas eletrolíticos através da teoria do funcional da densidade clássica" was presented in the "XXI Congresso Brasileiro de Engenharia Química".[55]

Following the same argument, only now we comment about a paper developed during the year in the University of Notre Dame. There, an AMBER-compatible transferable force field for poly(ethylene glycol) ethers (glymes) was developed.[56] The initial plan was to apply this force field to the development of potential electrochemical devices using a mixture of ionic liquid and glyme; what we will be done soon, in future works. The paper in fully presented in APPENDIX I.[56]

We also have investigated the potential of mean force for some ions at infinite dilution close to a graphene sheet, in order to insert into PBE and DFT, providing the integration of different scales. This is fantastic since allows taking advantage of the high level of detail of sophisticated methods such as MD, which are more demanding, and use this information in methods that require low computational time such as PBE and DFT.

Other future perspectives include the development of an algorithm to optimize the engineered water composition and concentration, the inclusion of charged surfaces in the 3D-DFT, and the parallelization of the 3D-DFT code in order to study larger systems without the limitation of the grid size.

REFERENCES

1. LEVIN, Y. Electrostatic correlations: from plasma to biology. *Rep. Prog. Phys.*, v. 65, p. 1577–1632, 2002.

2. NAJI, A. et al. Electrostatic interactions in strongly coupled soft matter. *Physica A*, v. 352, n. 1, p. 131–170, 2005.

3. BARBOSA, N. S. V. *Aplicação da equação de Poisson-Boltzmann modificada em sistemas biológicos: análise da partição iônica em um eritrócito*. 2014. 152 f. Dissertação (Mestrado em Engenharia Química) – Instituto de Química, Universidade do Estado do Rio de Janeiro, Rio de Janeiro, 2014.

4. LIMA, E. R. A. *Cálculo de Propriedade físico-químicas de sistemas coloidais via equação de Poisson-Boltzmann*. 2008. 144 f. Tese (Doutorado em Engenharia Química) – Programa de Pós-graduação em Engenharia Química, COPPE, Universidade Federal do Rio de Janeiro, Rio de Janeiro, 2008.

5. VOYUTSKY, S. S. *Colloid chemistry*. Tradução de N. Brobov. Moscow: Mir Publishers, 1978.

6. BUNKER, A.; MAGARKAR, A.; VIITALA, T. Rational design of liposomal drug delivery systems, a review: combined experimental and computational studies of lipid membranes, liposomes and their PEGylation. *Biochim. Biophys. Acta*, v. 1858, p. 2334–2352, 2016.

7. GUPTA, A. et al. Combatting antibiotic-resistant bacteria using nanomaterials. *Chem. Soc. Rev.*, v. 48, p. 415–427, 2019.

8. DE OLIVEIRA, J. F. A. et al. Defeating bacterial resistance and preventing mammalian cells toxicity through rational design of antibiotic-functionalized nanoparticles. *Sci. Rep.*, v. 7, n. 1326, 2017.

9. AL-ANSSARI, S. et al. Wettability of nanofluid-modified oil-wet calcite at reservoir conditions. *Fuel*, v. 211, p. 405–414, 2018.

10. AUSTAD, T.; REZAEIDOUST, A.; PUNTERVOLD, T. Chemical mechanism of low salinity water flooding in sandstone reservoirs. In: SPE IMPROVED OIL RECOVERY

SYMPOSIUM, 2010, Tulsa, OK. Society of Petroleum Engineers, 2010. Disponível em: <http://www.onepetro.org/doi/10.2118/129767-MS>. Acesso em: 28 dez. 2017.

11. NASRALLA, R. A.; ALOTAIBI, M. B.; NASR-EL-DIN, H. A. Efficiency of oil recovery by low salinity water flooding in sandstone reservoirs. In: SPE WESTERN NORTH AMERICAN REGIONAL MEETING, 2011, Anchorage, AK. Society of Petroleum Engineers, 2011. Disponível em: <http://www.onepetro.org/doi/10.2118/144602-MS>. Acesso em: 28 dez. 2018.

12. BRADY, P. V. et al. Electrostatics and the low salinity effect in sandstone reservoirs. *Energy Fuels*, v. 29, n. 2, p. 666–677, 2015.

13. QIAO, C.; JOHNS, R.; LI, L. Modeling low-salinity waterflooding in chalk and limestone reservoirs. *Energy Fuels*, v. 30, n. 2, p. 884–895, 2016.

14. FATHI, S. J.; AUSTAD, T.; STRAND, S. "Smart water" as a wettability modifier in chalk: the effect of salinity and ionic composition. *Energy Fuels*, v. 24, n. 4, p. 2514–2519, 2010.

15. UENO, K. Categorizing molten salt complexes as ionic liquids and their applications to battery electrolytes. *Electrochemistry*, v. 84, n. 9, p. 674–680, 2016.

16. UENO, K. et al. A design approach to lithium-ion battery electrolyte based on diluted solvate ionic liquids. *J. Electrochem. Soc.*, v. 164, n. 1, p. A6088–A6094, 2017.

17. GIFFIN, G. A. Ionic liquid-based electrolytes for "beyond lithium" battery technologies. *J. Mater. Chem. A*, v. 4, n. 35, p. 13378–13389, 2016.

18. SHAO, Y. et al. Nanocomposite polymer electrolyte for rechargeable magnesium batteries. *Nano Energy*, v. 12, p. 750–759, 2015.

19. XU, H. et al. Modeling of all-porous solid oxide fuel cells with a focus on the electrolyte porosity design. *Appl. Energy*, v. 235, p. 602–611, 2019.

20. BARBOSA, N. S. V.; LIMA, E. R. A.; TAVARES, F. W. Molecular modeling in chemical engineering. In: REEDIJK, J. (Ed.). *Reference module in chemistry, molecular sciences and chemical engineering*. [S.l.]: Elsevier, 2017. Disponível em: <https://doi.org/10.1016/B978-0-12-409547-2.13915-0>. Acesso em: 22 jan. 2018.

21. BARBOSA, N. S. V. et al. Membrane potential and ion partitioning in an erythrocyte using the Poisson–Boltzmann equation. *J. Phys. Chem. B*, v. 119, n. 21, p. 6379–6388, 2015.

22. LIMA, E. R. A.; BISCAIA, E. C.; TAVARES, F. W. Modelagem computacional de sistemas coloidais. In: NETO, F. M. et al. (Ed.). *Modelagem computacional em materiais*. Rio de Janeiro: Ciência Moderna, 2010. cap. 7, p. 133–152.

23. BAKER, N. A. Improving implicit solvent simulations: a Poisson-centric view. *Curr. Opin. Struct. Biol.*, v. 15, n. 2, p. 137–143, 2005.

24. FEIG, M.; BROOKS, C. L. Recent advances in the development and application of implicit solvent models in biomolecule simulations. *Curr. Opin. Struct. Biol.*, v. 14, n. 2, p. 217–224, 2004.

25. LI, Z.; WU, J. Density functional theory for planar electric double layers: closing the gap between simple and polyelectrolytes. *J. Phys. Chem. B*, v. 110, n. 14, p. 7473–7484, 2006.

26. YU, Y.-X.; WU, J.; GAO, G.-H. Ionic distribution, electrostatic potential and zeta potential at electrochemical interfaces. *Chinese J. Chem. Eng.*, v. 12, n. 5, p. 688–695, 2004.

27. HENDERSON, D. et al. Density functional study of the electric double layer formed by a high density electrolyte. *J. Phys. Chem. B*, v. 115, n. 44, p. 12911–12914, 2011.

28. HENDERSON, D.; WU, J. Electrochemical properties of the double layer of an ionic liquid using a dimer model electrolyte and density functional theory. *J. Phys. Chem. B*, v. 116, n. 8, p. 2520–2525, 2012.

29. BHUIYAN, L. B. et al. Monte Carlo simulation for the double layer structure of an ionic liquid using a dimer model: a comparison with the density functional theory. *J. Phys. Chem. B*, v. 116, n. 34, p. 10364–10370, 2012.

30. HENDERSON, D. et al. Application of density functional theory to study the double layer of an electrolyte with an explicit dimer model for the solvent. *J. Phys. Chem. B*, v. 116, n. 36, p. 11356–11361, 2012.

31. HENDERSON, D. et al. The tail effect on the shape of an electrical double layer differential capacitance curve. *J. Chem. Phys.*, v. 138, n. 14, p. 144704, 2013.

32. WU, J. Density functional theory for chemical engineering: from capillarity to soft materials. *AIChE J.*, v. 52, n. 3, p. 1169–1193, 2006.

33. EVANS, R. Density functionals in the theory of nonuniform fluids. In: HENDERSON, D. (Ed.). *Fundamentals of inhomogeneous fluids*. New York: Marcel Dekker, 1992. cap. 3, p. 85–116.

34. LI, Z.; WU, J. Density-functional theory for the structures and thermodynamic properties of highly asymmetric electrolyte and neutral component mixtures. *Phys. Rev. E*, v. 70, n. 3, p. 031109, 2004.

35. LI, Z.; WU, J. Density functional theory for polyelectrolytes near oppositely charged surfaces. *Phys. Rev. Lett.*, v. 96, n. 4, p. 048302, 2006.

36. LAMPERSKI, S. et al. Influence of anisotropic ion shape on structure and capacitance of an electric double layer: a Monte Carlo and density functional study. *J. Chem. Phys.*, v. 139, n. 5, p. 054703, 2013.

37. KJELLANDER, R. et al. Double layer interactions in mono- and divalent electrolytes: a comparison of the anisotropic HNC theory and Monte Carlo simulations. *J. Chem. Phys.*, v. 97, p. 1424–1431, 1992.

38. RAVINDRAN, S.; WU, J. Overcharging of nanoparticles in electrolyte solutions. *Langmuir*, v. 20, n. 17, p. 7333–7338, 2004.

39. WU, J. Z. et al. Monte Carlo simulation for the potential of mean force between ionic colloids in solutions of asymmetric salts. *J. Chem. Phys.*, v. 111, n. 15, p. 7084–7094, 1999.

40. WU, J.; BRATKO, D.; PRAUSNITZ, J. M. Interaction between like-charged colloidal spheres in electrolyte solutions. *Proc. Natl. Acad. Sci.*, v. 95, n. 26, p. 15169–15172, 1998.

41. WANG, L.; LIANG, H.; WU, J. Electrostatic origins of polyelectrolyte adsorption: theory and Monte Carlo simulations. *J. Chem. Phys.*, v. 133, n. 4, p. 044906, 2010.

42. WU, J. et al. A classical density functional theory for interfacial layering of ionic liquids. *Soft Matter*, v. 7, n. 23, p. 11222–11231, 2011.

43. LIMA, E. R. A. et al. Co-ion and ion competition effects: ion distributions close to a hydrophobic solid surface in mixed electrolyte solutions. *Langmuir*, v. 24, n. 8, p. 3944–3948, 2008.

44. TAVARES, F. W. et al. Ion-specific thermodynamic properties of colloids and proteins. *Fluid Phase Equilib.*, v. 296, n. 2, p. 99–105, 2010.

45. BOSTRÖM, M. et al. Anion-specific partitioning in two-phase finite volume systems: possible implications for mechanisms of ion pumps. *J. Phys. Chem. B*, v. 113, n. 23, p. 8124–8127, 2009.

46. MAGINN, E.; ELLIOTT, J. Historical perspective and current outlook for molecular dynamics as a chemical engineering tool. *Ind. Eng. Chem. Res.*, v. 49, p. 3059–3078, 2010.

47. GUBBINS, K. E.; MOORE, J. D. Molecular modeling of matter: impact and prospects in engineering. *Ind. Eng. Chem. Res.*, v. 49, p. 3026–3046, 2010.

48. BAKER, N. A.; BASHFORD, D.; CASE, D. A. Implicit solvent electrostatics in biomolecular simulation. In: LEIMKUHLER, B. et al. (Ed.). *New algorithms for macromolecular simulation*. Heidelberg: Springer, 2006. cap. 5, p. 263–295.

49. LIMA, E. R. A. et al. Ion specific forces between charged self-assembled monolayers explained by modified DLVO theory. *Colloids Surf. A*, v. 346, p. 11–15, 2009.

50. LIMA, E. R. A. et al. Specific ion adsorption and surface forces in colloid science. *J. Phys. Chem. B*, v. 112, p. 1580–1585, 2008.

51. LIMA, E. R. A. et al. Forces between air-bubbles in electrolyte solution. *Chem. Phys. Lett.*, v. 458, p. 299–302, 2008.

52. HORINEK, D.; NETZ, R. R. Specific ion adsorption at hydrophobic solid surfaces. *Phys. Rev. Lett.*, v. 99, n. 22, p. 226104, 2007.

53. HORINEK, D. et al. Specific ion adsorption at the air/water interface: the role of hydrophobic solvation. *Chem. Phys. Lett.*, v. 479, n. 4–6, p. 173–183, 2009.

54. NETZ, R. R.; HORINEK, D. Progress in modeling of ion effects at the vapor/water interface. *Annu. Rev. Phys. Chem.*, v. 63, p. 401–418, 2012.

55. BARBOSA, N. S. V.; LIMA, E. R. A.; TAVARES, F. W. Estudo de sistemas eletrolíticos através da teoria do funcional da densidade clássica. In: CONGRESSO BRASILEIRO DE ENGENHARIA QUÍMICA, 21., 2016, Fortaleza. *Anais*... Fortaleza: COBEQ, 2016.

56. BARBOSA, N. S. V. et al. Development of an AMBER-compatible transferable force field for poly(ethylene glycol) ethers (glymes). *J. Mol. Model.*, v. 23, n. 6, p. 194, 2017.

57. BARBOSA, N. S. V.; LIMA, E. R. A.; TAVARES, F. W. The electrostatic behavior of the bacterial cell wall using a smoothing function to describe the charge-regulated volume charge density profile. *Colloids Surf. B* , v. 134, p. 447–452, 2015.

58. XUE, Z. et al. A novel superhydrophilic and underwater superoleophobic hydrogel-coated mesh for oil/water separation. *Adv. Mater.*, v. 23, n. 37, p. 4270–4273, 2011.

59. XUE, Z. et al. Special wettable materials for oil/water separation. *J. Mater. Chem. A*, v. 2, n. 8, p. 2445–2460, 2014.

60. ASLAN, S.; FATHI NAJAFABADI, N.; FIROOZABADI, A. Non-monotonicity of the contact angle from NaCl and $MgCl_2$ concentrations in two petroleum fluids on atomistically smooth surfaces. *Energy Fuels*, v. 30, n. 4, p. 2858–2864, 2016.

61. ZHANG, P.; AUSTAD, T. Wettability and oil recovery from carbonates: effects of temperature and potential determining ions. *Colloids Surf. A*, v. 279, n. 1–3, p. 179–187, 2006.

62. JABBARI, H. et al. Thermally-induced wettability alteration from hot-water imbibition in naturally fractured reservoirs—Part 1: numerical model development & 1D models. *Fuel*, v. 208, p. 682–691, 2017.

63. AMIRPOUR, M. et al. Experimental investigation of wettability alteration on residual oil saturation using nonionic surfactants: capillary pressure measurement. *Petroleum*, v. 1, p. 289–299, 2015.

64. MAGHZI, A. et al. Monitoring wettability alteration by silica nanoparticles during water flooding to heavy oils in five-spot systems: a pore-level investigation. *Exp. Therm. Fluid Sci.*, v. 40, p. 168–176, 2012.

65. BARBOSA, N. S. V.; LIMA, E. R. A.; TAVARES, F. W. Wettability of rock, oil and

brine system based on density functional theory. *Fluid Phase Equilib.*, v. 479, n. 1, p. 99–105, 2019.

66. NINHAM, B. W.; LO NOSTRO, P. *Molecular forces and self assembly*. Cambrigde: Cambridge University Press, 2010.

67. ISRAELACHVILI, J. N. *Intermolecular and surface forces*. 3. ed. Burlington: Academic Press, 2011.

68. MASLIYAH, J. H.; BHATTACHARJEE, S. *Electrokinetic and colloidal transport phenomena*. New Jersey: Wiley, 2006.

69. BOSTRÖM, M.; WILLIAMS, D. R. M.; NINHAM, B. W. Ion specificity of micelles explained by ionic dispersion forces. *Langmuir*, v. 18, p. 6010–6014, 2002.

70. LIMA, E. R. A. et al. Osmotic second virial coefficients and phase diagrams for aqueous proteins from a much-improved Poisson-Boltzmann equation. *J. Phys. Chem. C*, v. 111, p. 16055–16059, 2007.

71. BOSTRÖM, M. et al. Why forces between proteins follow different Hofmeister series for pH above and below pI. *Biophys. Chem.*, v. 117, n. 3, p. 217–224, 2005.

72. PARSONS, D. F.; DUIGNAN, T. T.; SALIS, A. Cation effects on haemoglobin aggregation: balance of chemisorption against physisorption of ions. *Interface Focus*, v. 7, p. 20160137, 2017.

73. LIMA, S. A.; MURAD, M. A.; DOMINGUES, R. A new multiscale computational model for low salinity alkaline waterflooding in clay-bearing sandstones. In: SPE RESERVOIR SIMULATION CONFERENCE, 2017, Montgomery, TX. Society of Petroleum Engineers, 2017. Disponível em: <http://www.onepetro.org/doi/10.2118/182651-MS>. Acesso em: 5 fev. 2018.

74. HONG, Y.; BROWN, D. G. Electrostatic behavior of the charge-regulated bacterial cell surface. *Langmuir*, v. 24, p. 5003–5009, 2008.

75. FOGOLARI, F.; BRIGO, A.; MOLINARI, H. The Poisson-Boltzmann equation for biomolecular electrostatics: a tool for structural biology. *J. Mol. Recognit.*, v. 15, p. 377–392, 2002.

76. MAGNICO, P. Ion size effects on electric double layers and ionic transport through ion-exchange membrane systems. *J. Memb. Sci.*, v. 415–416, p. 412–423, 2012.

77. LIMA, E. R. A.; TAVARES, F. W.; BISCAIA, E. C. Finite volume solution of the modified Poisson-Boltzmann equation for two colloidal particles. *Phys. Chem. Chem. Phys.*, v. 9, p. 3174–3180, 2007.

78. BARBOSA, N. S. V.; LIMA, E. R. A.; TAVARES, F. W. Analysis of finite element solution of the Poisson–Boltzmann equation. In: CONGRESSO BRASILEIRO DE ENGENHARIA QUÍMICA, 20., 2014, São Paulo. *Anais*... São Paulo: Blucher, 2014. p. 15283–15290.

79. TORRIE, G. M.; VALLEAU, J. P. Electrical double layers. I. Monte Carlo study of a uniformly charged surface. *J. Chem. Phys.*, v. 73, n. 11, p. 5807–5816, 1980.

80. HOHENBERG, P.; KOHN, W. Inhomogeneous electron gas. *Phys. Rev.*, v. 136, n. 3B, p. B864–B871, 1964.

81. KOHN, W.; SHAM, L. J. Self-Consistent equations including exchange and correlation effects. *Phys. Rev.*, v. 140, n. 4A, p. A1133–A1138, 1965.

82. THOMAS, L. H. The calculation of atomic fields. *Math. Proc. Cambridge Philos. Soc.*, v. 23, n. 5, p. 542–548, 1927.

83. FERMI, E. Eine statistische methode zur bestimmung einiger eigenschaften des atoms und ihre anwendung auf die theorie des periodischen systems der elemente. *Zeitschrift für Phys.*, v. 48, n. 1–2, p. 73–79, 1928.

84. LEVINE, I. N. *Quantum Chemistry*. 7. ed. Upper Saddle River: Pearson Education, 2014.

85. EVANS, R. The nature of the liquid-vapour interface and other topics in the statistical mechanics of non-uniform, classical fluids. *Adv. Phys.*, v. 28, n. 2, p. 143–200, 1979.

86. WU, J. Z. Density functional theory for liquid structure and thermodynamics. In: LU, X.; HU, Y. (Ed.). *Molecular thermodynamics of complex systems*. Berlin, Heidelberg: Springer-Verlag Berlin Heidelberg, 2009. p. 1–73. (Structure and Bonding, v. 131). Disponível em: <http://www.springerlink.com/index/10.1007/978-3-540-69116-7>. Acesso em: 12 mar. 2015.

87. HANSEN, J.-P.; MCDONALD, I. R. *Theory of Simple Liquids*. 3. ed. Burlington: Academic Press, 2006.

88. EBNER, C.; SAAM, W. F.; STROUD, D. Density-functional theory of simple classical fluids. I. Surfaces. *Phys. Rev. A*, v. 14, n. 6, p. 2264–2273, 1976.

89. SAAM, W. F.; EBNER, C. Density-functional theory of classical systems. *Phys. Rev. A*, v. 15, n. 6, p. 2566–2568, 1977.

90. YU, Y.-X.; WU, J. A fundamental-measure theory for inhomogeneous associating fluids. *J. Chem. Phys.*, v. 116, n. 16, p. 7094–7103, 2002.

91. YU, Y.-X. X.; WU, J. Density functional theory for inhomogeneous mixtures of polymeric fluids. *J. Chem. Phys.*, v. 117, n. 5, p. 2368–2376, 2002.

92. YU, Y.-X.; WU, J. Extended test-particle method for predicting the inter- and intramolecular correlation functions of polymeric fluids. *J. Chem. Phys.*, v. 118, n. 8, p. 3835–3842, 2003.

93. JIANG, T.; WU, J. Self-organization of multivalent counterions in polyelectrolyte brushes. *J. Chem. Phys.*, v. 129, n. 8, p. 084903, 2008.

94. JIANG, T.; WANG, Z.-G.; WU, J. Electrostatic regulation of genome packaging in human hepatitis B virus. *Biophys. J.*, v. 96, n. 8, p. 3065–3073, 2009.

95. LIMA, E. R. A.; JIANG, T.; WU, J. A theoretical study of colloidal forces near amphiphilic polymer brushes. *Colloids Surf. A*, v. 384, n. 1–3, p. 115–120, 2011.

96. HENDERSON, D. et al. Structure and capacitance of an electric double layer of an asymmetric valency dimer electrolyte: a comparison of the density functional theory with Monte Carlo simulations. *J. Mol. Liq.*, v. 228, p. 236–242, 2017.

97. SZPARAGA, R.; WOODWARD, C. E.; FORSMAN, J. Ionic liquids and ionic liquid+solvent mixtures, studies by classical density functional theory. In: DEAN, D. et al. (Ed.). *Electrostatics of soft and disordered matter*. Singapura: Pan Stanford Publishing, 2014. cap. 7, p. 81–92.

98. FORSMAN, J.; WOODWARD, C. E.; TRULSSON, M. A classical density functional theory of ionic liquids. *J. Phys. Chem. B*, v. 115, n. 16, p. 4606–4612, 2011.

99. FORSMAN, J.; WOODWARD, C. E.; FREASIER, B. C. Density functional study of surface forces in athermal polymer solutions with additive hard sphere interactions: solvent effects, capillary condensation, and capillary-induced surface transitions. *J. Chem. Phys.*, v. 117, n. 4, p. 1915–1926, 2002.

100. MCQUARRIE, D. A. *Statistical mechanics*. Mill Valley: University Science Books, 2000.

101. HILL, T. L. *An introduction to statistical thermodynamics*. [S.l.]: Dover, 2013. (New York).

102. PRAUSNITZ, J. M.; LICHTENTHALER, R. N.; AZEVEDO, E. G. *Molecular thermodynamics of fluid-phase equilibria*. 3. ed. Upper Saddle River: Prentice Hall, 1999.

103. ALLEN, M. P.; TILDESLEY, D. J. *Computer simulation of liquids*. 2. ed. New York: Oxford University Press, 2017.

104. FRENKEL, D.; SMIT, B. *Understanding molecular simulation*. San Diego: Academic Press, 2002.

105. HENDERSON, D. (Ed.). *Fundamentals of Inhomogeneous Fluids*. New York: Marcel Dekker, 1992.

106. EU, B. C. *Kinetic theory of nonequilibrium ensembles, irreversible thermodynamics, and generalized hydrodynamics*. [S.l.]: Springer International Publishing, 2016. v. 1.

107. DAVIS, H. T. *Statistical mechanics of phases, interfaces and thin films*. New York: Wiley-VCH, 1996.

108. KNEPLEY, M. G. et al. An efficient algorithm for classical density functional theory in three dimensions: ionic solutions. *J. Chem. Phys.*, v. 132, n. 12, p. 124101, 2010.

109. WANG, Z.; LIU, L.; NERETNIEKS, I. The weighted correlation approach for density functional theory: a study on the structure of the electric double layer. *J. Phys. Condens. Matter*, v. 23, n. 17, p. 175002, 2011.

110. YU, Y.-X. et al. Structures and correlation functions of multicomponent and polydisperse hard-sphere mixtures from a density functional theory. *J. Chem. Phys.*, v.

121, n. 3, p. 1535–1541, 2004.

111. OETTEL, M. et al. Description of hard-sphere crystals and crystal-fluid interfaces: a comparison between density functional approaches and a phase-field crystal model. *Phys. Rev. E*, v. 86, p. 021404, 2012.

112. EDELMANN, M.; ROTH, R. A numerical efficient way to minimize classical density functional theory. *J. Chem. Phys.*, v. 144, n. 7, p. 074105, 2016.

113. ROSENFELD, Y. Free-energy model for the inhomogeneous hard-sphere fluid mixture and density-functional theory of freezing. *Phys. Rev. Lett.*, v. 63, n. 9, p. 980–983, 1989.

114. ROSENFELD, Y. Free energy model for inhomogeneous fluid mixtures: Yukawa-charged hard spheres, general interactions, and plasmas. *J. Chem. Phys.*, v. 98, n. 10, p. 8126–8148, 1993.

115. ROTH, R. et al. Fundamental measure theory for hard-sphere mixtures revisited: the White Bear version. *J. Phys. Condens. Matter*, v. 14, n. 46, p. 12063–12078, 2002.

116. ROSENFELD, Y. Geometrically based density functional theory of liquids. *J. Phys. Condens. Matter*, v. 8, n. 47, p. 9289–9292, 1996.

117. ROTH, R. Fundamental measure theory for hard-sphere mixtures: a review. *J. Phys. Condens. Matter*, v. 22, n. 6, p. 063102, 2010.

118. YU, Y.-X.; WU, J. Structures of hard-sphere fluids from a modified fundamental-measure theory. *J. Chem. Phys.*, v. 117, n. 22, p. 10156–10164, 2002.

119. ROSENFELD, Y. et al. Dimensional crossover and the freezing transition in density functional theory. *J. Phys. Condens. Matter*, v. 8, n. 40, p. 577–581, 1996.

120. TARAZONA, P.; ROSENFELD, Y. From zero-dimension cavities to free-energy functionals for hard disks and hard spheres. *Phys. Rev. E*, v. 55, n. 5, p. R4873–R4876, 1997.

121. SCHMIDT, M. et al. Density functional for a model colloid-polymer mixture. *Phys. Rev. Lett.*, v. 85, n. 9, p. 1934–1937, 2000.

122. TARAZONA, P. Density functional for hard sphere crystals: a fundamental measure approach. *Phys. Rev. Lett.*, v. 84, n. 4, p. 694–697, 2000.

123. HANSEN-GOOS, H.; ROTH, R. Density functional theory for hard-sphere mixtures: the White Bear version mark II. *J. Phys. Condens. Matter*, v. 18, n. 37, p. 8413–8425, 2006.

124. ROSENFELD, Y. Free-energy model for the inhomogeneous hard-sphere fluid in D dimensions: structure factors for the hard-disk (D=2) mixtures in simple explicit form. *Phys. Rev. A*, v. 42, n. 10, p. 5978–5989, 1990.

125. ESZTERMANN, A.; REICH, H.; SCHMIDT, M. Density functional theory for colloidal mixtures of hard platelets, rods, and spheres. *Phys. Rev. E*, v. 73, n. 1, p. 011409, 2006.

126. WOODWARD, C. E. A density functional theory for polymers: application to hard chain–hard sphere mixtures in slitlike pores. *J. Chem. Phys.*, v. 94, n. 4, p. 3183–3191, 1991.

127. WICHERT, J. M.; GULATI, H. S.; HALL, C. K. Binary hard chain mixtures. I. Generalized Flory equations of state. *J. Chem. Phys.*, v. 105, n. 17, p. 7669–7682, 1996.

128. FORSMAN, J.; WOODWARD, C. E. Evaluating the accuracy of a density functional theory of polymer solutions with additive hard sphere diameters. *J. Chem. Phys.*, v. 120, n. 1, p. 506–510, 2004.

129. FRINK, L. J. D. et al. Numerical challenges in the application of density functional theory to biology and nanotechnology. *J. Phys. Condens. Matter*, v. 14, n. 46, p. 12167–12187, 2002.

130. SEARS, M. P.; FRINK, L. J. D. A new efficient method for density functional theory calculations of inhomogeneous fluids. *J. Comput. Phys.*, v. 190, n. 1, p. 184–200, 2003.

131. ROTH, R.; DIETRICH, S. Binary hard-sphere fluids near a hard wall. *Phys. Rev. E*, v. 62, n. 5, p. 6926–6936, 2000.

132. NUSSBAUMER, H. J. *Fast Fourier transform and convolution algorithms*. 2. ed. Berlin: Springer-Verlag Berlin Heidelberg, 1982. (Information Sciences, v. 2).

133. YU, Y.-X.; WU, J.; GAO, G.-H. Density-functional theory of spherical electric double layers and ζ potentials of colloidal particles in restricted-primitive-model electrolyte solutions. *J. Chem. Phys.*, v. 120, n. 15, p. 7223–7233, 2004.

134. GILLESPIE, D.; NONNER, W.; EISENBERG, R. S. Density functional theory of charged, hard-sphere fluids. *Phys. Rev. E*, v. 68, n. 3, p. 031503, 2003.

135. GILLESPIE, D.; VALISKÓ, M.; BODA, D. Density functional theory of the electrical double layer: the RFD functional. *J. Phys. Condens. Matter*, v. 17, p. 6609–6626, 2005.

136. FORSMAN, J. Density functional theories of surface interactions in salt solutions. *J. Chem. Phys.*, v. 130, p. 064901, 2009.

137. TURESSON, M. et al. Classical density functional theory & simulations on a coarse-grained model of aromatic ionic liquids. *Soft Matter*, v. 10, p. 3229–3237, 2014.

138. NORDHOLM, S. Simple analysis of the thermodynamic properties of the one-component plasma. *Chem. Phys. Lett.*, v. 105, n. 3, p. 302–307, 1984.

139. PENFOLD, R. et al. A simple analysis of the classical hard sphere one component plasma. I. Hole corrected Debye–Hückel theory. *J. Chem. Phys.*, v. 95, n. 3, p. 2048–2055, 1991.

140. PIZIO, O.; SOKOŁOWSKI, S. Restricted primitive model for electrolyte solutions in slit-like pores with grafted chains: microscopic structure, thermodynamics of adsorption, and electric properties from a density functional approach. *J. Chem. Phys.*, v. 138, p. 204715, 2013.

141. PIZIO, O.; SOKOŁOWSKI, S. Phase behavior of the restricted primitive model of ionic fluids with association in slitlike pores. Density-functional approach. *J. Chem. Phys.*, v. 122, p. 144707, 2005.

142. PATRYKIEJEW, A.; SOKOŁOWSKI, S.; PIZIO, O. The liquid-vapor interface of the restricted primitive model of ionic fluids from a density functional approach. *Condens. Matter Phys.*, v. 14, n. 1, p. 13603, 2011.

143. PIZIO, O.; PATRYKIEJEW, A.; SOKOŁOWSKI, S. Phase behavior of ionic fluids in slitlike pores: a density functional approach for the restricted primitive model. *J. Chem. Phys.*, v. 121, n. 23, p. 11957–11964, 2004.

144. WANG, Z.; LIU, L.; NERETNIEKS, I. A novel method to describe the interaction pressure between charged plates with application of the weighted correlation approach. *J. Chem. Phys.*, v. 135, p. 244107, 2011.

145. BLUM, L. Mean spherical model for asymmetric electrolytes I. Method of solution. *Mol. Phys.*, v. 30, n. 5, p. 1529–1535, 1975.

146. HIROIKE, K. Supplement to Blum's theory for asymmetric electrolytes. *Mol. Phys.*, v. 33, n. 4, p. 1195–1198, 1977.

147. BLUM, L.; ROSENFELD, Y. Relation between the free energy and the direct correlation function in the mean spherical approximation. *J. Stat. Phys.*, v. 63, n. 5–6, p. 1177–1190, 1991.

148. TANG, Z.; SCRIVEN, L. E.; DAVIS, H. T. Interactions between primitive electrical double layers. *J. Chem. Phys.*, v. 97, n. 12, p. 9258–9266, 1992.

149. PATRA, C. N.; GHOSH, S. K. A nonlocal density functional theory of electric double layer: symmetric electrolytes. *J. Chem. Phys.*, v. 100, n. 7, p. 5219–5229, 1994.

150. PATRA, C. N.; GHOSH, S. K. A nonlocal density-functional theory of electric double layer: charge-asymmetric electrolytes. *J. Chem. Phys.*, v. 101, n. 5, p. 4143–4149, 1994.

151. GROH, B.; EVANS, R.; DIETRICH, S. Liquid-vapor interface of an ionic fluid. *Phys. Rev. E*, v. 57, n. 6, p. 6944–6954, 1998.

152. JIANG, J. et al. Revisiting density functionals for the primitive model of electric double layers. *J. Chem. Phys.*, v. 140, n. 4, p. 044714, 2014.

153. JIANG, J. et al. A contact-corrected density functional theory for electrolytes at an interface. *Phys. Chem. Chem. Phys.*, v. 16, n. 9, p. 3934–3938, 2014.

154. HENDERSON, D.; BLUM, L. Some exact results and the application of the mean spherical approximation to charged hard spheres near a charged hard wall. *J. Chem. Phys.*, v. 69, n. 12, p. 5441–5449, 1978.

155. SIMONIN, J.-P.; BERNARD, O.; BLUM, L. Real ionic solutions in the mean spherical approximation. 3. Osmotic and activity coefficients for associating electrolytes in the

primitive model. *J. Phys. Chem. B*, v. 102, n. 22, p. 4411–4417, 1998.

156. KUNZ, W.; HENLE, J.; NINHAM, B. W. 'Zur Lehre von der Wirkung der Salze' (about the science of the effect of salts): Franz Hofmeister's historical papers. *Curr. Opin. Colloid Interface Sci.*, v. 9, n. 1–2, p. 19–37, 2004.

157. TAVARES, F. W. et al. Ion-specific effects in the colloid−colloid or protein−protein potential of mean force: role of salt−macroion van der Waals interactions. *J. Phys. Chem. B*, v. 108, n. 26, p. 9228–9235, 2004.

158. LIMA, E. R. A. et al. Ion-specific forces between a colloidal nanoprobe and a charged surface. *Langmuir*, v. 23, p. 7456–7458, 2007.

159. EVANS, R.; MARCONI, U. M. B.; TARAZONA, P. Capillary condensation and adsorption in cylindrical and slit-like pores. *J. Chem. Soc. Faraday Trans. 2*, v. 82, p. 1763–1787, 1986.

160. RÖCKEN, P. et al. Two-stage capillary condensation in pores with structured walls: a nonlocal density functional study. *J. Chem. Phys.*, v. 108, n. 20, p. 8689–8697, 1998.

161. WANG, L. et al. The mechanism of roughness-induced CO_2 microbubble nucleation in polypropylene foaming. *Phys. Chem. Chem. Phys.*, v. 19, n. 31, p. 21069–21077, 2017.

162. LI, Z.; WU, J. Toward a quantitative theory of ultrasmall liquid droplets and vapor-liquid nucleation. *Ind. Eng. Chem. Res.*, v. 47, n. 15, p. 4988–4995, 2008.

163. SZPARAGA, R.; WOODWARD, C. E.; FORSMAN, J. Theoretical prediction of the capacitance of ionic liquid films. *J. Phys. Chem. C*, v. 116, p. 15946–15951, 2012.

164. SZPARAGA, R.; WOODWARD, C. E.; FORSMAN, J. Capillary condensation of ionic liquid solutions in porous electrodes. *J. Phys. Chem. C*, v. 117, p. 1728–1734, 2013.

165. NINHAM, B. W.; YAMINSKY, V. Ion binding and ion specificity: the Hofmeister effect and Onsager and Lifshitz theories. *Langmuir*, v. 13, p. 2097–2108, 1997.

166. MA, K.; WOODWARD, C. E.; FORSMAN, J. Classical density functional study on interfacial structure and differential capacitance of ionic liquids near charged surfaces. *J. Phys. Chem. C*, v. 118, p. 15825–15834, 2014.

167. NELSON, D. L.; COX, M. M. *Lehninger: principles of biochemistry*. 5. ed. New York: W. H. Freeman and Company, 2008.

168. KRYSINSKI, P.; TI TIEN, H. Membrane electrochemistry. *Prog. Surf. Sci.*, v. 23, n. 4, p. 317–412, 1986.

169. MAURO, A. Space charge regions in fixed charge membranes and the associated property of capacitance. *Biophys. J.*, v. 2, p. 179–198, 1962.

170. OHSHIMA, H.; OHKI, S. Donnan potential and surface potential of a charged membrane. *Biophys. J.*, v. 47, n. 5, p. 673–678, 1985.

171. CHEIN, R.; CHEN, H.; LIAO, C. Investigation of ion concentration and electric potential distributions in charged membrane/electrolyte systems. *J. Memb. Sci.*, v. 342, n. 1–2, p. 121–130, 2009.

172. OHSHIMA, H. Double layer interaction between soft particles. In: OHSHIMA, H. (Ed.). *Theory of colloid and interfacial electric phenomena*. London: Elsevier, 2006. cap. 16, p. 390–408.

173. DUVAL, J. F. L. Electrokinetics of diffuse soft interfaces. 2. Analysis based on the nonlinear Poisson-Boltzmann equation. *Langmuir*, v. 21, n. 8, p. 3247–3258, 2005.

174. OHSHIMA, H.; KONDO, T. Electrophoretic mobility and Donnan potential of a large colloidal particle with a surface charge layer. *J. Colloid Interface Sci.*, v. 116, n. 2, p. 305–311, 1987.

175. DZIUBAKIEWICZ, E. et al. Study of charge distribution on the surface of biocolloids. *Colloids Surf. B* , v. 104, p. 122–127, 2013.

176. VAN DER WAL, A. et al. Electrokinetic potential of bacterial cells. *Langmuir*, v. 13, p. 165–171, 1997.

177. DAUGHNEY, C. J.; FEIN, J. B. The effect of ionic strength on the adsorption of H^+, Cd^{2+}, Pb^{2+}, and Cu^{2+} by Bacillus subtilis and Bacillus licheniformis: a surface complexation model. *J. Colloid Interface Sci.*, v. 198, p. 53–77, 1998.

178. YEE, N.; FEIN, J. Cd adsorption onto bacterial surfaces: a universal adsorption edge? *Geochim. Cosmochim. Acta*, v. 65, n. 13, p. 2037–2042, 2001.

179. FEIN, J. B. et al. A chemical equilibrium model for metal adsorption onto bacterial surfaces. *Geochim. Cosmochim. Acta*, v. 61, n. 16, p. 3319–3328, 1997.

180. BROWN, L. et al. Through the wall: extracellular vesicles in Gram-positive bacteria, mycobacteria and fungi. *Nat. Rev. Microbiol.*, v. 13, n. 10, p. 620–630, 2015.

181. VAN DER WAL, A. et al. Determination of the total charge in the cell walls of Gram-positive bacteria. *Colloids Surf. B* , v. 9, p. 81–100, 1997.

182. FREITAS, T. C. et al. An Efficient Adjoint-Free Dynamic Optimization Methodology for Batch Processing using Pontryagin's Formulation. In: EUROPEAN SYMPOSIUM ON COMPUTER AIDED PROCESS ENGINEERING, 22., 2012, Amsterdam. Elsevier, 2012. Disponível em: <https://doi.org/10.1016/B978-0-444-59520-1.50118-4>. Acesso em: 20 mar. 2014. p. 1297–1301.

183. DUNHAM-CHEATHAM, S. et al. The effect of chloride on the adsorption of Hg onto three bacterial species. *Chem. Geol.*, v. 373, p. 106–114, 2014.

184. CHANG, Y.-I.; HSU, J.-P. Effect of multivalent cations on the adhesion rate of cellular surfaces bearing ionizable groups. *Colloids Surf. A*, v. 96, p. 155–163, 1995.

185. HONG, Y.; BROWN, D. G. Cell surface acid-base properties of Escherichia coli and Bacillus brevis and variation as a function of growth phase, nitrogen source and C:N ratio. *Colloids Surf. B* , v. 50, n. 2, p. 112–119, 2006.

186. OHSHIMA, H. The Donnan potential-surface potential relationship for a cylindrical soft particle in an electrolyte solution. *J. Colloid Interface Sci.*, v. 323, n. 2, p. 313–316, 2008.

187. WASSERMAN, E.; FELMY, A. R. Computation of the Electrical Double Layer Properties of Semipermeable Membranes in Multicomponent Electrolytes. *Appl. Environ. Microbiol.*, v. 64, n. 6, p. 2295–2300, 1998.

188. OHSHIMA, H. Electrokinetic phenomena of soft particles. *Curr. Opin. Colloid Interface Sci.*, v. 18, n. 2, p. 73–82, 2013.

189. ALBERTS, B. et al. *Molecular biology of the cell*. 5. ed. New York: Garland Science, 2008.

190. LODISH, H. et al. *Molecular cell biology*. 4. ed. New York: W. H. Freeman and Company, 2000.

191. SKOU, J. C. The identification of the Sodium-Potassium Pump (Nobel Lecture). *Biosci. Rep.*, v. 18, n. 4, p. 155–169, 1998.

192. FREEDMAN, J. Membrane transport in red blood cells. In: SPERELAKIS, N. (Ed.). *Cell physiology sourcebook: a molecular approach*. 3. ed. Ohio: Academic Press, 2001. cap. 23, p. 377–392.

193. DONATH, E.; LERCHE, D. 309 - Electrostatic and structural properties of the surface of human erythrocytes. I-cell-electrophoretic studies following neuraminidase treatment. *Bioelectrochem. Bioenerg.*, v. 7, n. 1, p. 41–53, 1980.

194. DI BIASIO, A.; CAMETTI, C. On the dielectric relaxation of biological cell suspensions: the effect of the membrane electrical conductivity. *Colloids Surf. B* , v. 84, n. 2, p. 433–441, 2011.

195. GASCOYNE, P. et al. Dielectrophoretic detection of changes in erythrocyte membranes following malarial infection. *Biochim. Biophys. Acta*, v. 1323, p. 240–252, 1997.

196. ROBINSON, R. A.; STOKES, R. H. *Electrolyte solutions*. New York: Dover, 2002.

197. CHEN, C.-C.; SONG, Y. Generalized electrolyte-NRTL model for mixed-solvent electrolyte systems. *AIChE J.*, v. 50, n. 8, p. 1928–1941, 2004.

198. DILL, K. A. *Molecular driving forces: statistical thermodynamics in chemistry and biology*. New York: Garland Science, 2003.

199. FUNDER, J.; WEITH, J. Potassium, sodium and water in normal human red blood cells. *Scand. J. Clin. Lab. Investig.*, v. 18, n. 2, p. 167–180, 1966.

200. FUNDER, J.; WEITH, J. Chloride and hydrogen ions distribution between human red cell and plasma. *Acta Physiol. Scand.*, v. 98, n. 2, p. 234–245, 1966.

201. ARIBI, M. et al. Clinical evaluation of lipids , lipoproteins and red blood cells sodium and potassium in patients with different grades of hypertension. *Clin. Biochem.*, v. 43, p. 942–947, 2010.

202. DI BIASIO, A.; CAMETTI, C. D-glucose-induced alterations in the electrical parameters of human erythrocyte cell membrane. *Bioelectrochemistry*, v. 77, n. 2, p. 151–157, 2010.

203. BERNHARDT, I.; WEISS, E. Passive membrane permeability for ions and membrane potential. In: BERNHARDT, I.; ELLORY, J. C. (Ed.). *Red cell membrane transport in health and disease*. Heidelberg: Springer, 2003. cap. 4, p. 83–119.

204. DONALDSON, E. C.; CHILINGARIAN, G. V.; YEN, T. F. (Ed.). *Enhanced oil recovery: fundamentals ans analyses*. New York: Elsevier Science, 1985. (Developments in petroleum science, v. 17A).

205. SHENG, J. *Modern chemical enhanced oil recovery: theory and practice*. Burlington: Elsevier, 2011.

206. PEDRONI, L. G. *Experimental study of mobility control by foams: potential of a FAWAG process in pre-salt reservoir conditions*. 2017. 184 f. Tese (Doutorado em Geociências) – Université Pierre et Marie Curie, Paris, 2017.

207. BRANDT, A. R.; UNNASCH, S. Energy intensity and greenhouse gas emissions from thermal enhanced oil recovery. *Energy Fuels*, v. 24, p. 4581–4589, 2010.

208. BLUNT, M.; FAYERS, F. J.; ORR, F. M. Carbon dioxide in enhanced oil recovery. *Energy Convers. Manag.*, v. 34, n. 9–11, p. 1197–1204, 1993.

209. JIN, L. et al. Advancing CO_2 enhanced oil recovery and storage in unconventional oil play—Experimental studies on Bakken shales. *Appl. Energy*, v. 208, p. 171–183, 2017.

210. YU, W. et al. CO_2 injection for enhanced oil recovery in Bakken tight oil reservoirs. *Fuel*, v. 159, p. 354–363, 2015.

211. MORROW, N. R. (Ed.). *Interfacial Phenomena in petroleum recovery*. New York (NY): Marcel Dekker, 1991.

212. KALLEL, W. et al. Pore-scale modeling of wettability alteration during primary drainage. *Water Resour. Res.*, v. 53, p. 1891–1907, 2017.

213. HIRASAKI, G. J. Thin films and three-phase contact angle. In: MORROW, N. R. (Ed.). *Interfacial Phenomena in Petroleum Recovery*. New York (NY): Marcel Dekker,

1991. cap. 2, p. 23–76.

214. MYINT, P. C.; FIROOZABADI, A. Thin liquid films in improved oil recovery from low-salinity brine. *Curr. Opin. Colloid Interface Sci.*, v. 20, n. 2, p. 105–114, 2015.

215. DOS SANTOS, R. G. et al. Contact angle measurements and wetting behavior of inner surfaces of pipelines exposed to heavy crude oil and water. *J. Pet. Sci. Eng.*, v. 51, n. 1–2, p. 9–16, 2006.

216. YUTKIN, M. P. et al. Bulk and surface aqueous speciation of calcite: implications for low-salinity waterflooding of carbonate reservoirs. *SPE J.*, v. 23, n. 1, p. 84–101, 2017.

217. SARAJI, S.; GOUAL, L.; PIRI, M. Dynamic adsorption of asphaltenes on quartz and calcite packs in the presence of brine films. *Colloids Surf. A*, v. 434, p. 260–267, 2013.

218. MYINT, P. C.; FIROOZABADI, A. Thermodynamics of flat thin liquid films. *AIChE J.*, v. 61, n. 9, p. 3104–3115, 2015.

219. SADEQI-MOQADAM, M.; RIAHI, S.; BAHRAMIAN, A. An investigation into the electrical behavior of oil/water/reservoir rock interfaces: the implication for improvement in wettability prediction. *Colloids Surf. A*, v. 490, p. 268–282, 2016.

220. MORROW, N. R. Wettability and its effect on oil recovery. *J. Pet. Technol.*, v. 42, n. 12, p. 1476–1484, 1990.

221. ABELHA, M. *Brazilian carbonate oil fields: a perspective*. Rio de Janeiro, 2015. Disponível em: <http://www.anp.gov.br/wwwanp/?dw=75786>. Acesso em: 1 nov. 2018.

222. TESTER, J. W.; MODELL, M. *Thermodynamics ans its applications*. 3. ed. Upper Saddle River: Prentice Hall, 1997.

223. TRUESDELL, A. H.; JONES, B. F. WATEQ, a computer program for calculating chemical equilibria of natural waters. *J. Res. U.S. Geol. Surv.*, v. 2, n. 2, p. 233–248, 1974.

224. PARKHURST, D. L.; APPELO, C. A. J. Description of input and examples for PHREEQC version 3—A computer program for speciation, batch-reaction, one-dimensional transport, and inverse geochemical calculations. In: *Techniques and*

Methods, book 6. Denver: U.S. Geological Survey, 2013. cap. A43.

225. CHURAEV, N. V.; DERJAGUIN, B. V.; MULLER, V. M. *Surface Forces*. New York: Springer Science + bussiness media, 1987.

226. FEIJTER, J. A. Thermodynamics of thin liquid films: fundamentals and applications. In: IVANOV, I. (Ed.). *Thin liquid films*. New York: Marcel Dekker, 1988. cap. 1.

227. HIRASAKI, G. J. Wettability: fundamentals and surface forces. *SPE Form. Eval.*, v. 6, n. 2, p. 217–226, 1991.

228. FIROOZABADI, A. *Thermodynamics and applications in hydrocarbon energy production*. New York: McGraw-Hill Education, 2016.

229. LIFSHITZ, E. M. The theory of molecular attractive forces between solids. *J. Exp. Theor. Phys.*, v. 2, n. 1, p. 73–83, 1956.

230. GREGORY, J. Approximate expressions for retarded van der Waals interaction. *J. Colloid Interface Sci.*, v. 83, n. 1, p. 138–145, 1981.

231. VAN CAPPELLEN, P. et al. A surface complexation model of the carbonate mineral-aqueous solution interface. *Geochim. Cosmochim. Acta*, v. 57, n. 15, p. 3505–3518, 1993.

232. POKROVSKY, O. S. Surface speciation of Ca and Mg carbonate minerals in aqueous solutions: a combined potentiometric, electrokinetic, and DRIFT surface spectroscopy approach. *Mineral. Mag.*, v. 62A, p. 1196–1197, 1998.

233. POKROVSKY, O. S.; SCHOTT, J.; THOMAS, F. Processes at the magnesium-bearing carbonates/solution interface. I. A surface speciation model for magnesite. *Geochim. Cosmochim. Acta*, v. 63, n. 6, p. 863–880, 1999.

234. POKROVSKY, O. S.; SCHOTT, J.; THOMAS, F. Dolomite surface speciation and reactivity in aquatic systems. *Geochim. Cosmochim. Acta*, v. 63, n. 19–20, p. 3133–3143, 1999.

235. POKROVSKY, O. S. et al. Surface speciation models of calcite and dolomite/aqueous solution interfaces and their spectroscopic evaluation. *Langmuir*, v. 16, n. 6, p. 2677–2688, 2000.

236. POKROVSKY, O. S.; SCHOTT, J. Surface chemistry and dissolution kinetics of divalent metal carbonates. *Environ. Sci. Technol.*, v. 36, n. 3, p. 426–432, 2002.

237. HIORTH, A.; CATHLES, L. M.; MADLAND, M. V. The impact of pore water chemistry on carbonate surface charge and oil wettability. *Transp. Porous Media*, v. 85, n. 1, p. 1–21, 2010.

238. BRADY, P. V; KRUMHANSL, J. L.; MARINER, P. E. Surface complexation modeling for improved oil recovery. In: SPE IMPROVED OIL RECOVERY SYMPOSIUM, 2012, Tulsa, OK. Society of Petroleum Engineers, 2012. Disponível em: <http://www.onepetro.org/doi/10.2118/153744-ms>. Acesso em: 28 dez. 2017.

239. SONG, J. et al. Surface complexation modeling of calcite zeta potential measurements in brines with mixed potential determining ions (Ca^{2+}, CO_3^{2-}, Mg^{2+}, SO_4^{2-}) for characterizing carbonate wettability. *J. Colloid Interface Sci.*, v. 506, p. 169–179, 2017.

240. HEBERLING, F. et al. Structure and reactivity of the calcite-water interface. *J. Colloid Interface Sci.*, v. 354, n. 2, p. 843–857, 2011.

241. EFTEKHARI, A. A. et al. Thermodynamic analysis of chalk-brine-oil interactions. *Energy Fuels*, v. 31, p. 11773–11782, 2017.

242. STIPP, S. L.; HOCHELLA, M. F. Structure and bonding environments at the calcite surface as observed with X-ray photoelectron spectroscopy (XPS) and low energy electron diffraction (LEED). *Geochim. Cosmochim. Acta*, v. 55, n. 6, p. 1723–1736, 1991.

243. CICERONE, D. S.; REGAZZONI, A. E.; BLESA, M. A. Electrokinetic properties of the calcite/water interface in the presence of magnesium and organic matter. *J. Colloid Interface Sci.*, v. 154, n. 2, p. 423–433, 1992.

244. PIERRE, A. et al. Calcium as potential determining ion in aqueous calcite suspensions. *J. Dispers. Sci. Technol.*, v. 11, n. 6, p. 611–635, 1990.

245. HELGESON, H. C.; KIRKHAM, D. H.; FLOWERS, G. C. Theoretical prediction of the thermodynamic behavior of aqueous electrolytes by high pressures and temperatures: IV. Calculation of activity coefficients, osmotic coefficients, and apparent molal and standard and relative partial molal properties to 600^{o}C. *Am. J. Sci.*, v. 281, n. 10, p. 1249–1516, 1981.

246. ZHANG, P.; TWEHEYO, M. T.; AUSTAD, T. Wettability alteration and improved oil recovery by spontaneous imbibition of seawater into chalk: Impact of the potential determining ions Ca^{2+}, Mg^{2+}, and SO_4^{2-}. *Colloids Surf. A*, v. 301, n. 1–3, p. 199–208, 2007.

247. ZHANG, P.; TWEHEYO, M. T.; AUSTAD, T. Wettability alteration and improved oil recovery in chalk: the effect of calcium in the presence of sulfate. *Energy Fuels*, v. 20, n. 5, p. 2056–2062, 2006.

248. MEGAWATI, M.; HIORTH, A.; MADLAND, M. V. The impact of surface charge on the mechanical behavior of high-porosity chalk. *Rock Mech. Rock Eng.*, v. 46, n. 5, p. 1073–1090, 2013.

249. STIPP, S. L. S. Toward a conceptual model of the calcite surface: hydratation, hydrolysis, and surface potential. *Geochim. Cosmochim. Acta*, v. 19/20, n. 63, p. 3121–3131, 1999.

250. WOLTHERS, M.; CHARLET, L.; VAN CAPPELLEN, P. The surface chemistry of divalent metal carbonate minerals: a critical assessment of surface charge and potential data using the charge distribution multi-site ion complexation model. *Am. J. Sci.*, v. 308, n. 8, p. 905–941, 2008.

251. BALL, J. W.; NORDSTROM, D. K. *User's manual for WATEQ4F, with revised thermodynamic data base and test cases for calculating speciation of major, trace, and redox elements in natural waters*. Menlo Park: U.S. Geological Survey, 2001. Open-File Report 91-183.

252. PETTIT, G.; PETTIT, L.; POWELL, K. J. SC-Database. Versão 5. Otley (UK), 2001. Disponível em: <http://www.acadsoft.co.uk/index.html>. Acesso em: 15 jun. 2018.

253. MAY, P. M.; ROWLAND, D.; MURRAY, K. JESS - Joint Expert Speciation System. Versão 8.6. Perth, 2017. Disponível em: <http://jess.murdoch.edu.au/jess_home.htm>. Acesso em: 15 jun. 2018.

254. WOLERY, T. J. EQ3/6 A Software Package for Geochemical Modeling. Versão 5.0. Livermore, 2010. Disponível em: <https://www.osti.gov/biblio/1231666-eq3-software-package-geochemical-modeling>. Acesso em: 16 jun. 2018.

255. NORDSTROM, D. K. et al. Revised chemical equilibrium data for major water-mineral reactions and their limitations. In: MELCHIOR, D. C.; BASSETT, R. L. (Ed.). *Chemical modeling of aqueous systems II*. Washington, D.C.: American Chemical

Society, 1990. cap. 31, p. 398–413.

256. PAZ-GARCÍA, J. M. et al. Computing multi-species chemical equilibrium with an algorithm based on the reaction extents. *Comput. Chem. Eng.*, v. 58, p. 135–143, 2013.

257. APPELO, C. A. J.; PARKHURST, D. L.; POST, V. E. A. Equations for calculating hydrogeochemical reactions of minerals and gases such as CO_2 at high pressures and temperatures. *Geochim. Cosmochim. Acta*, v. 125, p. 49–67, 2014.

258. REDLICH, O.; MEYER, D. M. The Molal Volumes of Electrolytes. *Chem. Rev.*, v. 64, n. 3, p. 221–227, 1964.

259. BRADY, P. V.; KRUMHANSL, J. L. A surface complexation model of oil-brine-sandstone interfaces at 100°C: low salinity waterflooding. *J. Pet. Sci. Eng.*, v. 81, p. 171–176, 2012.

260. HAYNES, W. M. (Ed.). *CRC Handbook of chemistry and physics*. 97. ed. Boca Raton, FL: CRC Press, 2017.

261. GEORGE, A. K.; SINGH, R. N. Electronic polarizability of light crude oil from optical and dielectric studies. *J. Phys. Conf. Ser.*, v. 869, p. 012016, 2017.

262. LU, Y.; NAJAFABADI, N. F.; FIROOZABADI, A. Effect of temperature on wettability of oil/brine/rock systems. *Energy Fuels*, v. 31, n. 5, p. 4989–4995, 2017.

263. TALANQUER, V.; OXTOBY, D. W. Nucleation on a solid substrate: a density functional approach. *J. Chem. Phys.*, v. 104, n. 4, p. 1483–1492, 1996.

264. BERIM, G. O.; RUCKENSTEIN, E. Contact angle of a nanodrop on a nanorough solid surface. *Nanoscale*, v. 7, p. 3088–3099, 2015.

265. GIACOMELLO, A. et al. Perpetual superhydrophobicity. *Soft Matter*, v. 12, n. 43, p. 8927–8934, 2016.

266. BERIM, G. O.; RUCKENSTEIN, E. Calculation of nanodrop profile from fluid density distribution. *Adv. Colloid Interface Sci.*, v. 231, p. 15–22, 2016.

267. POLYANIN, A. D.; MANZHIROV, A. V. *Handbook of mathematics for engineers*

and scientists. Boca Raton, FL: Chapman & Hall/CRC, 2007.

268. BARBOSA, N. S. V. et al. Electrical double-layer and wettability of brine, calcite and oil interfaces. In: IBEROAMERICAN CONFERENCE ON PHASE EQUILIBRIA AND FLUID PROPERTIES FOR PROCESS DESIGN, 11., 2018, Carlos Paz, Córdoba, Argentina. *Book of Abstracts*... Carlos Paz, Córdoba, Argentina: Universidad Nacional de Córdoba, 2018. p. 139–140.

269. BARBOSA, N. S. V. S. V.; LIMA, E. R. DE A.; TAVARES, F. W. Modelagem de tensões interfaciais e molhabilidade de sistemas contendo solução salina, rocha e óleo. In: CONGRESSO BRASILEIRO DE TERMODINAMICA APLICADA, 9., 2017, Porto Alegre. Universidade Federal do Rio Grande do Sul, 2017. Disponível em: <ttps://www.ufrgs.br/cbtermo2017/R024.pdf>. Acesso em: 20 jan. 2018.

270. MERMIN, N. D. Thermal properties of the inhomogeneous electron gas. *Phys. Rev.*, v. 137, n. 5A, p. A1441–A1443, 1965.

271. BRIGHAM, E. O. *The fast Fourier transform and its applications*. Englewood Cliffs: Prentice-Hall, 1988.

272. FRIGO, M.; JOHNSON, S. G. *FFTW for version 3.3.8*. 2018. Disponível em: <http://www.fftw.org/fftw3.pdf>. Acesso em: 20 jun. 2018.

273. LEBOWITZ, J. L.; PERCUS, J. K. Mean spherical model for lattice gases with extended hard cores and continuum fluids. *Phys. Rev.*, v. 144, n. 1, p. 251–258, 1966.

274. TRIOLO, R.; BLUM, L.; FLORIANO, M. A. Simple electrolytes in the mean spherical approximation. 2. Study of a refined model. *J. Phys. Chem.*, v. 82, n. 12, p. 1368–1370, 1978.

APPENDIX A – Molecular modeling in chemical engineering

BARBOSA, N. S. V.; LIMA, E. R. A.; TAVARES, F. W. Molecular modeling in chemical engineering. In: REEDIJK, J. (Ed.). *Reference module in chemistry, molecular sciences and chemical engineering*. [S.l.]: Elsevier, 2017. Disponível em: <https://doi.org/10.1016/B978-0-12-409547-2.13915-0>. Acesso em: 22 jan. 2018.

Molecular Modeling in Chemical Engineering

Nathalia Salles Vernin Barbosa and Eduardo Rocha de Almeida Lima, Universidade do Estado do Rio de Janeiro, Rio de Janeiro, Brazil
Frederico Wanderley Tavares, Universidade Federal do Rio de Janeiro, Rio de Janeiro, Brazil

Introduction

Molecular modeling studies can provide insight into the microscopic structure and the macroscopic properties of molecular and electrolyte systems, which is fundamental to the comprehension of many phenomena in chemical engineering field. The reliability of such models for predicting the behavior of a material depends strongly on the assumptions used to describe the interactions in the system of interest.

Theoretical and computational methods can be conveniently classified according to the length and time scales to which they are applied or—in case of solvent/solute systems—the way the solvent is modeled. The former classification divides the methods into four main categories depending on the level of detail:

(i) the electronic scale (e.g., ab initio density functional theory), in which matter is described by quantum mechanics and is made up of fundamental particles (i.e., electrons, protons, etc.);
(ii) the atomistic level (e.g., Monte Carlo and molecular dynamics simulation), in which matter is regarded as made up of atoms and is based on statistical mechanic's laws;
(iii) the mesoscale level (e.g., lattice Monte Carlo, lattice Boltzmann, and Monte Carlo and molecular dynamics simulation using coarse grained force field), in which matter is defined as composed of droplets of matter, each representing a number of atoms;
(iv) the continuum level, in which matter is represented as a continuum and is based on the numerical solution of the conservation equations for mass, momentum, and energy. These methods are the most widely known in fundamental engineering.

Regarding the level of detail in solvent's modeling, three groups can be defined: (i) implicit methods; (ii) integral equations and classical density functional theory; and (iii) explicit methods.

The implicit models are mean field approaches and they consider the solvent as a continuous medium described by the dielectric constant. Examples of the implicit methods are: Poisson–Boltzmann equation, Coulomb's law, and Generalized Born model. Conventional implicit methods for electrolytic systems design the ions as point charges without volume.

On the other hand the integral equations (e.g., hipernetted chain closure and reference interactions site model) and classical density functional theory allow a greater level of detail due to the possibility of inclusion of other contributions not conventionally take into account in implicit theories such as the electrostatic and hard sphere correlations between ions, and the formation of chemical or hydrogen bonds in associating fluids. They are very versatile and comprehend a class of methods between implicit and explicit ones.

The explicit methods, which are based on statistical and quantum mechanics, consider the solvent explicitly, that is, as individual molecules characterized by atoms connections (all-atoms model) or super-atoms connections (united atoms and coarse grained models). The molecules are described by force fields that contain information about functional forms and parameter sets used to compute the potential energy of the system. If the essential physical interactions of molecules and/or particles are represented faithfully, explicit methods can reliably predict properties. Examples of these methods are Monte Carlo and molecular dynamics simulations with explicit solvent. Although they present more realistic results, the increase in the degree of freedom also increases the computational time required to compute the microscopic structure and/or macroscopic properties.

In chemical engineering field it is very common to associate molecular simulation methods to explicit solvent models, however it is possible to consider the solvent implicitly. This strategy is widely used in biological field, which contains complex molecules with many atoms and characteristic interactions.

Due to the large number of methods in each category, we limit our scope to three different approaches extensively used in solvent/solute systems: Poisson–Boltzmann equation, classical density functional theory and molecular dynamics simulation. Fig. 1 provides a qualitative comparison among these methods regarding to level of detail and required computational time.

Poisson–Boltzmann Equation

The Poisson–Boltzmann equation (PBE) is a widespread theory for understanding phenomena in systems containing electrolytes. The classical PBE is based on the Gouy–Chapman theory and takes into account only the mean field electrostatic potential, ψ, in order to determine the density profiles of ions close to charged surfaces. As mentioned previously, the ions are considered as point charges embedded in a continuum described by the dielectric constant, ε. The electrochemical potential, μ_i, of ion i with charge, ez_i, is defined as:

$$\mu_i(p,T) = \mu_i^0(p,T) + k_B T \ln c_i + ez_i\psi \tag{1}$$

where μ_i^0 is the standard electrochemical potential of the ion i, k_B is the Boltzmann constant, T is the absolute temperature of the system, c_i is the density of ion i (number of ions per unit volume), e is the elementary charge, and z_i is the charge number of ion i. The term $ez_i\psi$ refers to the electrical energy due to the external electric field generated by the charged surface. For more information about the Gouy–Chapman theory, the article "Electrochemical Double Layer" from Jacob and Sabo can be consult.

At the bulk reservoir, the electrochemical potential of ion i, $\mu_{\infty,i}$, is given by:

$$\mu_{\infty,i}(p,T) = \mu_i^0(p,T) + k_B T \ln c_{\infty,i} + ez_i\psi_\infty \tag{2}$$

where $c_{\infty,i}$ is the bulk density of ion i and ψ_∞ stands for the bulk electrostatic potential, that usually is null. Once the equilibrium is reached, the electrochemical potential remains constant and uniform. Thus, combining Eqs. (1) and (2), we obtain the Boltzmann distribution:

$$c_i = c_{\infty,i} \exp\left[-\frac{z_i e(\psi - \psi_\infty)}{k_B T}\right] \tag{3}$$

The possibility of improvement in the electrical behavior predicted by the classical Poisson–Boltzmann has generated wide interest in the development of modifications in order to take into account several important effects such as dispersion forces, hydration, ion size effects, and electric correlation between ions. These additional contributions may be divided in two classes: external field contributions, for example, those due the interaction with the surface—here represented by U_i—and contributions depending on the interaction among molecules (ions)—here referred as residual chemical potential, μ_i^{res}. These additional terms can be included in the description of the electrochemical potential as follows:[1]

$$\mu_i(p,T) = \mu_i^0(p,T) + k_B T \ln c_i + ez_i\psi + U_i + \mu_i^{res} \tag{4}$$

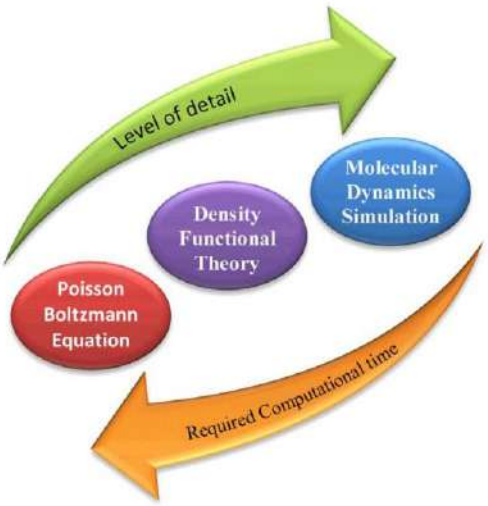

Fig. 1 Level of detail and required computational time for Poisson–Boltzmann equation, classical density functional theory and molecular dynamics simulation.

$$\mu_{\infty,i}(p,T) = \mu_i^0(p,T) + k_B T \ln c_{\infty,i} + e z_i \psi_\infty + \mu_{\infty,i}^{res} \tag{5}$$

where $\mu_{\infty,i}^{res}$ refers to the residual chemical potential at the bulk reservoir and $U_{\infty,i}$ is null. Depending on the additional contribution considered, the non-electrostatic potentials may be function of the distance or even functionals of the ion densities. The modified Boltzmann distribution can be obtained by the combination of Eqs. (4) and (5). Note that the non-electrostatic energy contribution appears at the same level of the electrostatic potential:

$$c_i = c_{\infty,i} \exp\left[-\frac{z_i e(\psi - \psi_\infty) + U_i + \mu_i^{res} - \mu_{\infty,i}^{res}}{k_B T}\right] \tag{6}$$

The augmented PBE is given by the combination of the Poisson equation to the modified Boltzmann distribution:

$$\varepsilon_0 \nabla\cdot(\varepsilon \nabla\psi) = -e\sum_i z_i c_{\infty,i} \exp\left[-\frac{z_i e(\psi - \psi_\infty) + U_i + \mu_i^{res} - \mu_{\infty,i}^{res}}{k_B T}\right] - \rho_f \tag{7}$$

Here ε_0 is the permittivity of vacuum and the term ρ_f represents the volumetric density of fixed charge. Here the term "fixed" refers to charges that are fixed in space (immobile), but not necessarily with a constant value. The augmented PBE also permits the variation of dielectric function in space along the diffuse layer.

The boundary conditions usually associated with Eq. (7) can be of three types: Dirichlet boundary (potential specified at the boundary), Neumann boundary (derivative of the potential specified at the boundary), and Robin boundary (a weighted combination of Dirichlet boundary conditions and Neumann boundary conditions).

Considering one surface, the Dirichlet boundary conditions can be written as:

$$\psi|_{\text{surface}} = \psi_0 \tag{8}$$

$$\psi|_{x\to\infty} = 0 \tag{9}$$

where ψ_0 is the potential at the surface and x is the perpendicular distance to the surface. For two surfaces, the Dirichlet boundary conditions are given by:

$$\psi|_{\text{surface1}} = \psi_{01} \tag{10}$$

$$\psi|_{\text{surface2}} = \psi_{02} \tag{11}$$

where ψ_{01} and ψ_{02} are the potentials at surfaces 1 and 2, respectively. On the other hand, the Neumann boundary conditions for systems with only one surface are defined as:

$$[\varepsilon\nabla\psi]|_{\text{surface}} = -\frac{Q}{\varepsilon_0} \tag{12}$$

$$\nabla\psi|_{x\to\infty} = 0 \tag{13}$$

where Q is the surface charge density; whereas for two surfaces, we have

$$[\varepsilon\nabla\psi]|_{\text{surface1}}\cdot\vec{n} = -\frac{Q_1}{\varepsilon_0} \tag{14}$$

$$[\varepsilon\nabla\psi]|_{\text{surface2}}\cdot\vec{n} = -\frac{Q_2}{\varepsilon_0} \tag{15}$$

where Q_1 and Q_2 are surface charge densities at surfaces 1 and 2, respectively, and $\vec{n}$ is the unit normal vector to the corresponding surface.

The Robin boundary conditions are useful in systems with surface charge density susceptible to pH or the presence of other ions close to the surface. Examples of such surfaces are proteins, carbonate rocks, sandstone rocks, some ionic membranes, etc. Charge regulation models are typically used in these cases.

For numerical convenience, Eq. (7) is usually written in dimensionless form as, for example, the one presented in Eq. (16).

$$\nabla\cdot(\bar{\varepsilon}\nabla\gamma) = -\frac{\sum_i z_i c_{i,\infty} \exp\left(-z_i\gamma + z_i\gamma_\infty - u_i + \bar{\mu}_i^{res} - \bar{\mu}_{\infty,i}^{res}\right)}{\sum_i z_i^2 c_{\infty,i}} - \bar{\rho}_f \tag{16}$$

where $\gamma = e\psi/k_B T$ is the dimensionless electrostatic potential; $\bar{\varepsilon}$ is the normalized dielectric constant, that is equal to $\bar{\varepsilon} = \varepsilon/\varepsilon_{ref}$; ε_{ref} is the dielectric constant of the reference fluid at the system's temperature; $u_i = U_i/k_B T$; $\bar{\mu}_i^{res} = \mu_i^{res}/k_B T$ and $\bar{\rho}_f$ is the dimensionless volumetric density of fixed charges. All spatial variables were scaled by κ^{-1}, the Debye length:

$$\kappa^2 = \frac{e^2\sum_i c_{\infty,i} z_i^2}{\varepsilon_{ref}\varepsilon_0 k_B T} \tag{17}$$

For Cartesian coordinates with one plane surface, constant dielectric constant, symmetrical electrolyte, and Dirichlet boundary condition, classical PBE can be solved analytically. For other coordinates or conditions, different numerical techniques can be used to solve the PBE equation such as finite difference method, finite volume method, second order spline finite elements method, and finite element method.

From the electrostatic potential, the density profiles are obtained which in turn can lead to the calculation of both structural and thermodynamic properties of the system by following standard statistical-mechanical relations.

Non-Electrostatic Potential

Although PBE is a very successful theory which can reproduce many phenomena, considerable researches have been devoted to improve it with the inclusion of non-electrostatic potential.

In order to take into account the specific ion effects, the dispersion potential between ions and macroparticles, U_i^{disp}, in different colloidal systems can be inserted in augmented PBE. This is relevant to explain some phenomena such as adsorption of colloidal particles and surface tension of electrolyte solutions, commonly observed experimentally. One of the methodologies to obtain this potential is based on the Lifshitz theory. In Cartesian coordinates, the expression used to calculate U_i^{disp} is given by:[2]

$$U_i^{disp} = -\frac{G(x)B_i}{x^3} \tag{18}$$

where

$$G(x) = 1 + \frac{2x}{\sqrt{\pi}r_i}\left(\frac{2x^2}{r_i^2} - 1\right)\exp\left(-\frac{x^2}{r_i^2}\right) - \left(1 + \frac{4x^4}{r_i^4}\right)\operatorname{erfc}\left(\frac{x}{r_i}\right) \tag{19}$$

x is the perpendicular distance from the center of the ion i to the interface, r_i is the ion radius, and B_i is the dispersion interaction coefficient of ion i obtained from Lifshitz theory:[1,3]

$$\frac{B_i}{k_BT} = \frac{\alpha_i(0)}{4\varepsilon_w(0)}\left[\frac{\varepsilon_m(0) - \varepsilon_w(0)}{\varepsilon_m(0) + \varepsilon_w(0)}\right] + \frac{h}{4\pi k_BT}\int_{\nu_{min}}^{\infty}\frac{\alpha_i(\nu)}{\varepsilon_w(\nu)}\left[\frac{\varepsilon_m(\nu) - \varepsilon_w(\nu)}{\varepsilon_m(\nu) + \varepsilon_w(\nu)}\right]d\nu \tag{20}$$

where $\alpha_i(0)$ and $\alpha_i(\nu)$ are the effective polarizabilities of ion i at frequencies 0 and ν in the solvent, respectively, h is Planck's constant, $\nu_{min} = 2\pi k_BT/h$ is the first nonzero frequency, $\varepsilon_j(0)$ and $\varepsilon_j(\nu)$ are the dielectric constants of j at frequencies 0 and ν, respectively. The subscript j can be w for the solvent and m for the macroparticle. Usually the polarizability and dielectric constant of a molecule at a frequency ν can be expressed by the harmonic-oscillator model:

$$\alpha(\nu) = \frac{\alpha(0)}{1 + (\nu/\nu^I)^2} \tag{21}$$

$$\varepsilon(\nu) = 1 + \frac{n^2 - 1}{1 + (\nu/\nu^I)^2} \tag{22}$$

where n is the refractive index for the sodium D line. The ionization frequency ν^I of ions in aqueous solution can be estimated from free energy of hydration of ions. At the bulk reservoir, that is, far from the macroparticle, $U_{\infty,i}^{disp}$ tends to zero.

Some modifications have been proposed to include the size effects of the ions, similar to Stern-Gouy-Chapman model. Based on the Boublik-Mansoori-Carnahan-Starling-Leland equation of state (BMCSL EoS) for hard spheres, the residual chemical potential of each ion can be defined as:[4]

$$\begin{aligned}\mu_i^{res,\,\mathrm{BMCSL}} &= w_i[\boldsymbol{c}(x), r] \\ &= \frac{8\left(\xi_0 - \frac{\xi_2^3}{\xi_3^2}\right)r_i^3 + 6\xi_2 r_i + 12\xi_1 r_i^2}{1-\xi_3} + \frac{16\xi_2^3 r_i^3}{\xi_3(1-\xi_3)^3} + \frac{24\xi_1\xi_2 r_i^3 + \left(\frac{12\xi_2^2 r_i^2}{\xi_3}\right) + \left(\frac{8\xi_2^3 r_i^3}{\xi_3^2}\right)}{(1-\xi_3)^2} \\ &\quad + \left(-1 + \frac{12\xi_2^2 r_i^2}{\xi_3^2} + \frac{16\xi_2^3 r_i^3}{\xi_3^3}\right)\ln(1-\xi_3)\end{aligned} \tag{23}$$

where w is the size correlation term and the packing fractions $\xi_k (k = 0, 1, 2 \text{ or } 3)$ are given by:

$$\xi_k = \frac{\pi}{6}\sum\nolimits_i c_i(x)(2r_i)^k \tag{24}$$

Volumetric Density of Fixed Charges

Regularization functions, also known as smoothing functions, are used to join two different functions of the same independent variable. This methodology is important when we use the Poisson–Boltzmann equation to analyze a system characterized by two different but adjacent environments in which we can obtain different responses for each compartment.[5] This strategy ensures that

the Gibbs–Donnan potential automatically arises from the resolution of only one PBE for the whole system. Thus, the regulation function is used to generate a continuous function over the entire range of the spatial variable. One example of function that presents this behavior is the hyperbolic tangent function. Considering two generic functions $g(x)$ and $h(x)$, such that

$$f(x) = \begin{cases} g(x), & for\ x < x^* \\ h(x), & for\ x > x^* \end{cases} \tag{25}$$

the main idea is to convert the discontinuous function $f(x)$ into a continuous function $F(x)$. For this purpose, the adopted tactic applies the hyperbolic tangent function as follows:

$$F(x) = v(x)h(x) + [1 - v(x)]g(x) \tag{26}$$

where

$$v(x) = \frac{1 + \tanh\left(\frac{x-x^*}{\eta}\right)}{2} \tag{27}$$

The parameter η is related to the smoothness of the curve. Large values of η generate smoother curves, while low values generate steep curves.

An interesting point is that $g(x)$ and $h(x)$ can be a function of the position or a functional of the electrostatic potential. The last case was previously used for charge-regulated volume charge density in bacterial wall, for example. It could also be used to estimate some properties in a system with an acidic or basic membrane or porous environment adjacent to an ionic solution.

Fig. 2A shows a typical concentration profile of electrolyte 1:1 with bulk density equal to 0.1 M and bulk pH equal to 7.0, whereas Fig. 2B displays the comparison between zeta potential obtained from PBE with charge-regulated volume charge density and those from experimental data.[5]

The PBE with smoothing strategy reproduced experimental data with good agreement. More information about this topic can be found in our previous work.[5]

Density Functional Theory

The classical density functional theory (DFT) is based on Hohenberg–Kohn theorem and statistical mechanics. The main idea is very similar to the electronic density functional theory for which the ground state energy is a unique functional of the electron density. Conversely in classical DFT, the density functional refers to atoms, molecules, or even polymer units. Special attention should be given to the acronymic conventionally observed in the literature for both theories that unfortunately are the same.

The Hohenberg–Kohn theorem applied to classical DFT establishes that for an open system with temperature T, total volume V and chemical potential for each species μ_i specified (grand canonical ensemble), the one body potential can be uniquely defined by the density profile at equilibrium, that is, the density profile that minimizes the grand potential functional, $\Omega[\{c_i(\mathbf{R})\}]$. A corollary of this theorem suggests that for a classical system, the intrinsic Helmholtz energy F can be expressed as a unique functional of the molecule or block unit profiles independent of the external potential. The grand potential is given by:

$$\Omega[\{c_i(\mathbf{R})\}] = F[\{c_i(\mathbf{R})\}] + \int \sum_i c_i(\mathbf{R})[v_i(\mathbf{R}) - \mu_i]d\mathbf{R} \tag{28}$$

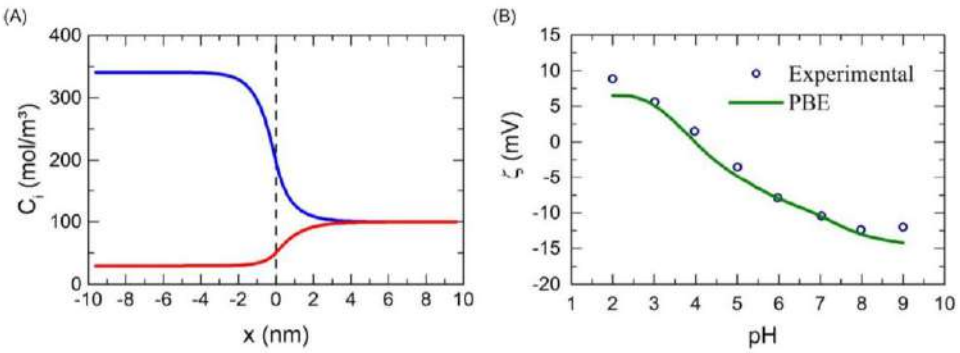

Fig. 2 (A) Ion density profile as function of the distance from an imaginary plane delimiting the two different and adjacent environments at bulk pH 7.0. (B) Zeta potential of *Bacillus brevis* at a solution of 0.1 M NaCl as function of bulk pH ranging from 2.0 to 9.0.[5]

where $c_i(\mathbf{R})$ is the density profile of the specie i at equilibrium, which represents the ensemble average of instantaneous densities, $\mathbf{R}$ denotes the positions of all particles connected (e.g., atoms of a molecule, or monomers of a polymer), and v_i is the external potential. Minimization of the grand potential yields:

$$\frac{\delta\Omega[\{c_i(\mathbf{R})\}]}{\delta c_i(\mathbf{R})} = \frac{\delta F[\{c_i(\mathbf{R})\}]}{\delta c_i(\mathbf{R})} + v_i(\mathbf{R}) - \mu_i = 0 \tag{29}$$

A central issue in DFT is the calculation of the intrinsic Helmholtz energy functional. It can be divided into an ideal part and an excess part. The ideal part, F^{id}, takes into account the contribution of ideal gas where nonbonded interactions are disregarded,

$$\frac{F^{id}[\{c_i(\mathbf{R})\}]}{k_B T} = \sum_{i=1}^{N} \int c_i(\mathbf{R})\{\ln[c_i(\mathbf{R})\lambda_i^3] - 1\}d\mathbf{R} + \sum_{i=1}^{N} \int c_i(\mathbf{R}) \frac{U_{bond,i}(\mathbf{R})}{k_B T} d\mathbf{R} \tag{30}$$

where $U_{bond,i}(\mathbf{R})$ represents the bond potential of a molecule/polymer i with all its atoms/monomers connections in a configuration $\mathbf{R}$. The excess part, F^{ex}, is correlated to the thermodynamic nonideality and can include contributions from short-range repulsions due to the excluded volume effect, van der Waals attractions, electrostatic correlations, weak associations, chain connectivity correlation, etc. In the next section, some of these contributions are exposed.

Knowledge of external potential and excess part of intrinsic Helmholtz energy functional allows the calculation of the density profiles by the resolution of Eq. (29). The non-linear integral equation obtained to each species in the system can be solved by Picard iteration. To avoid divergence, the input density profile of a new iteration ${\rho_{i,in}}^{(k)}(\mathbf{R})$ is computed by mixing the input density profile ${\rho_{i,in}}^{(k-1)}(\mathbf{R})$ with the output profile ${\rho_{i,out}}^{(k-1)}(\mathbf{R})$ from the previous iteration using a mixing parameter α:

$${\rho_{i,in}}^{(k)}(\mathbf{R}) = \alpha\, {\rho_{i,out}}^{(k-1)}(\mathbf{R}) + (1-\alpha)\, {\rho_{i,in}}^{(k-1)}(\mathbf{R}) \tag{31}$$

It is essential to choose $\alpha \in [0, 1]$ large enough to provide fast convergence, but also sufficiently small to avoid divergence due to instability during the iteration process.

Another method also possible to be used to solve nonlinear integral equations is the Newton–Raphson. It requires more computer storage than Picard method once it is necessary to solve an associated integral equation. However, some researches indicate that this method is more efficient than Picard's. For more information about these methods, the book "Statistical Mechanics of phases, interfaces, and thin films" from Ted Davis can be consulted.

Excess Helmholtz Energy Functional

In a typical semi-empirical force field, the short range repulsion between molecules is frequently represented by a hard sphere model, which considers that each molecule has a physical volume and prohibits the overlapping of molecules. The most remarkable methodology used to describe the short range repulsion is the fundamental measure theory (FMT), first proposed by Rosenfeld in 1989.[6] It is based on the idea of interpolation between the limit of high density, where the pair direct correlation function is dominated by the geometric convolutions of single particles and the limit of low density described by the pair exclusion volume. The FMT does not require the bulk density as the input; instead, it can be reduced to a bulk fluid theory as an output. Rosenfeld postulated that the excess free energy functional F_{hs}^{ex} can be written as:[6]

$$\frac{F_{hs}^{ex}}{k_B T} = \int \Phi^{hs}[n_\alpha(\mathbf{R})]d\mathbf{R} \tag{32}$$

where the excess free energy density Φ^{hs} is only a function of the system averaged fundamental geometric measures of the particles, known as weighted densities $n_\alpha(\mathbf{R})$:

$$n_\alpha(\mathbf{R}) = \sum_{i=1}^{N} n_{\alpha,i}(\mathbf{R}) = \sum_{i=1}^{N} \int c_i\left(\mathbf{R}'\right)\omega_i^{(\alpha)}\left(\mathbf{R} - \mathbf{R}'\right)d\mathbf{R}' \tag{33}$$

The weight functions $\omega_i^{(\alpha)}$ characterize the geometry of the particles. In 3D systems, two scalar functions are related to the volume and the surface area respectively:

$$\omega_i^{(3)}(\mathbf{R}) = \theta(r_i - |\mathbf{R}|) \tag{34}$$

$$\omega_i^{(2)}(\mathbf{R}) = \delta(r_i - |\mathbf{R}|) \tag{35}$$

where $\delta(x)$ is the Dirac delta function and $\theta(x)$ is the Heaviside step function, and a surface vector function characterizes the variance across the particle surface:

$$\boldsymbol{\omega}_i^{(V2)}(\mathbf{R}) = \frac{\mathbf{R}}{|\mathbf{R}|}\delta(r_i - |\mathbf{R}|) \tag{36}$$

The other weight functions in 3D are proportional to these three, and are given by:

$$\omega_i^{(1)}(\mathbf{R}) = \frac{\omega_i^{(2)}(\mathbf{R})}{4\pi r_i} \tag{37}$$

$$\omega_i^{(0)}(\mathbf{R}) = \frac{\omega_i^{(2)}(\mathbf{R})}{4\pi r_i^2} \tag{38}$$

$$\boldsymbol{\omega}_i^{(V1)}(\mathbf{R}) = \frac{\boldsymbol{\omega}_i^{(V2)}(\mathbf{R})}{4\pi r_i} \tag{39}$$

In the uniform fluid limit, the scalar weighted densities are reduced to variables of the scaled particle theory, $n_\alpha(\mathbf{R}) = \sum_{i=1}^{N} c_i r_i^\alpha$, while the vector weighted densities vanish.

Since the first publication of the FMT in 1989, some modifications have been proposed in the description of the excess free energy density. One of these versions is based on the BMCSL EoS and denominated White Bear (WB).[7] WB presents better results for confined systems and divides the excess free energy density into scalar and vector contributions:

$$\Phi^{hs} = \Phi^{hs,S} + \Phi^{hs,V} \tag{40}$$

$$\Phi^{hs,S} = -n_0 \ln(1-n_3) + \frac{n_1 n_2}{1-n_3} + \frac{n_2^3}{36\pi n_3^3}\left[n_3 \ln(1-n_3) + \frac{n_3^2}{(1-n_3)^2}\right] \tag{41}$$

$$\Phi^{hs,V} = -\frac{\mathbf{n}_{V1}\mathbf{n}_{V2}}{1-n_3} + \frac{n_2 \mathbf{n}_{V2}\cdot\mathbf{n}_{V2}}{12\pi n_3^3}\left[n_3 \ln(1-n_3) + \frac{n_3^2}{(1-n_3)^2}\right] \tag{42}$$

The van der Waals attraction is an important component in nonbonded interatomic interactions. The most common approaches used to take into account the van der Waals contribution to the excess free energy functional F_{att}^{ex} are the mean field approximation (MFA) and the quadratic density expansion of the excess Helmholtz energy functional relative to that for a uniform fluid. The former is given by:

$$F_{att}^{ex}[\{c_i(\mathbf{R})\}] = \frac{1}{2}\iint \sum_i \sum_j c_i(\mathbf{R}) c_j\left(\mathbf{R}'\right) \Gamma_{ij}^{att}\left(\left|\mathbf{R}-\mathbf{R}'\right|\right) d\mathbf{R} d\mathbf{R}' \tag{43}$$

where the van der Walls potential Γ_{ij}^{att} is usually described by square-well, Yukawa, or Lennard-Jones models.

The quadratic expansion is written as:

$$F_{att}^{ex}[\{c_i(\mathbf{R})\}] = F_{att}^{ex}[\{c_{i,\infty}\}] + \sum_{i=1}^{N} \mu_{att,i}^{ex} \int [c_i(\mathbf{R}) - c_{i,\infty}] d\mathbf{R} - \frac{k_B T}{2}\iint \sum_{i=1}^{N}\sum_{j=1}^{N} \Delta C_{ij}^{(2)att}\left(\left|\mathbf{R}-\mathbf{R}'\right|; \{c_{\infty,i}\}\right)[c_i(\mathbf{R}) - c_{\infty,i}]\left[c_j\left(\mathbf{R}'\right) - c_{\infty,j}\right] d\mathbf{R} d\mathbf{R}' \tag{44}$$

where $F_{att}^{ex}[\{c_{i,\infty}\}]$ is the attractive part of the excess Helmholtz energy of the reference bulk fluid, $\mu_{att,i}^{ex}$ is the excess chemical potential, and $\Delta C_{ij}^{(2)att}(|\mathbf{R}|;\{c_{\infty,i}\})$ is the direct correlation function of a bulk fluid. Analytical correlation functions derived from the first-order mean-spherical approximation are particularly useful to calculate $\mu_{att,i}^{ex}$ and $\Delta C_{ij}^{(2)att}(|\mathbf{R}|;\{c_{\infty,i}\})$.

The Helmholtz energy due to the Coulomb interactions can be divided into two contributions: the direct Coulomb interaction and the contribution due to the correlation of charge distributions. The direct Coulomb contribution F_C^{ex} is defined as:

$$F_C^{ex}[\{c_i(\mathbf{R})\}] = \frac{1}{2}\sum_i \sum_j \iint \frac{e^2 z_i z_j c_i(\mathbf{R}) c_j\left(\mathbf{R}'\right)}{\varepsilon\varepsilon_0\left|\mathbf{R}-\mathbf{R}'\right|} d\mathbf{R} d\mathbf{R}' \tag{45}$$

Since electrostatic correlations often play a dominant role in systems with electric double layers, many approaches have been proposed in the literature to account for them, such as: the bulk fluid density approximation, the reference fluid density approximation, the weighted correlation approximation, and the contact corrected approach. For more information about these theories, one can consult the paper of Jiang et al.[8]

Fig. 3 shows a comparison between the density profiles of ions obtained by PBE, DFT, and Monte Carlo.[9] For the DFT calculation, the excess free energy functional due to the short range repulsion was computed based on White Bear theory and the contribution due to the electrostatic correlations considered the bulk fluid density approximation approach. The system consists of a plane wall with a surface charge density equal to -0.35 C/m^2 in an aqueous solution with 1:1 electrolyte (bulk concentration equal to 2 M) at 298.15 K. The diameters of ions correspond to 4.25 Å.

The results predicted by DFT agree very well with the Monte Carlo data as observed in Fig. 3. On the other hand, as expected, PBE data could not predict the charge inversion.

Molecular Dynamics Simulation

The molecular dynamics simulation (MD) is a computational method that provides the estimation of equilibrium and transport properties of a classical many-body system. Typically the simulation box has around hundreds to thousands of atoms studied over

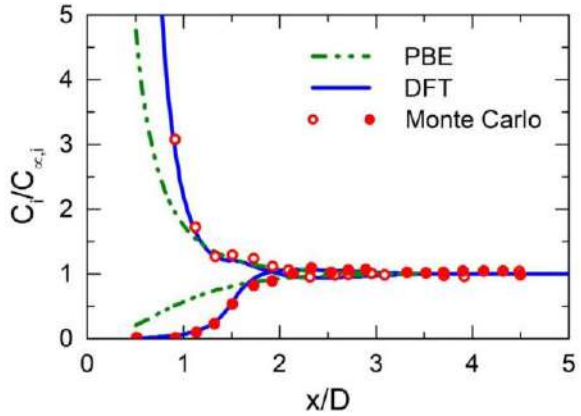

Fig. 3 Density profile of ions as a function of the distance from the surface ($Q = -0.35$ C/m^2) for 1:1 electrolyte solution ($c_\infty = 2$ M) at 298.15 K. Diameter of the ions (D) equal to 4.25 Å. Monte Carlo results from Torrie and Valleau.[9]

time intervals of 10–100 ns. Atoms or molecules interact with each other through a force field, and the predicted results depend strongly on the accuracy of the force field. Many force fields are available in the literature, such as CHARMM (Chemistry at Harvard Macromolecular Mechanics), OPLS-AA (Optimized Potentials for Liquid Simulations, All-Atom), AMBER (Assisted Model Building and Energy Refinement), and GAFF (General AMBER Force Field). These force fields have similar basic functional form, representing bond stretching, angle bending, dihedral torsion, van der Waals, and Coulombic interactions for each molecule:

$$U_{tot} = \sum_{bonds} \frac{k_l}{2}(l - l_{eq})^2 + \sum_{angles} \frac{k_\theta}{2}(\theta - \theta_{eq})^2 + \sum_{dihedrals} \frac{k_\chi}{2}[1 + \cos(n\chi - \delta_\chi)] + \sum_{i=1}^{N-1}\sum_{i<j}^{N}\left\{4\epsilon_{ij}\left[\left(\frac{\sigma_{ij}}{r_{ij}}\right)^{12} - \left(\frac{\sigma_{ij}}{r_{ij}}\right)^{6}\right] + \frac{q_i q_j}{4\pi\varepsilon_0 r_{ij}}\right\} \quad (46)$$

where U_{tot} is the total energy; k_l, k_θ and k_χ are the bond, angle, and dihedral angle force constants, respectively; l_{eq}, θ_{eq}, and χ are the bond length, bond angle, and dihedral angle, respectively, and the subscript eq represents the equilibrium values for the individual terms. Coulomb and Lennard-Jones 6–12 terms contribute to nonbonded interactions where ε_{ij} is the Lennard-Jones well depth and σ_{ij} is the finite distance at which the inter-particle potential is zero, q_i is the partial atomic charge, and r_{ij} is the distance between atoms i and j. The Lennard-Jones parameters between pairs of different atoms are obtained from combination rules, which can be based on the geometric or arithmetic mean depending on the force field.

The basic idea of MD consists on the preparation of a sample by choosing a model containing N particles and solving the Newton's equations of motion for this system until the system properties do not change anymore with the time. This step is known as equilibration. The initial positions of all atoms are chosen such that the system is close to a local potential energy minimum to prevent large forces at the beginning of the simulation. Software specialized in energy minimization techniques can be found elsewhere; one example is the PACKMOL (Initial configurations for Molecular Dynamics Simulations by packing optimization).[10] The initial velocities are usually sampled using a random generator with a specified seed at the specified temperature following a Maxwell–Boltzmann distribution.

At the end of equilibration, all the memory from the initial configuration should be lost. The next step is the production aiming the calculation of equilibrium and nonequilibrium desirable properties based on the position and momentum of molecules over time.

In order to minimize the surface effects, periodic boundary conditions are usually used in MD. The strategy consists in replicate the original simulation box throughout the space to form an infinite lattice. During the simulation, the movement of the atom in the original simulation box promotes the same movement of its periodic image in each of the neighboring boxes. When an atom moves out of the original simulation box, one of its images will move in through the opposite face.

In a conventional MD, the total energy and the total linear momentum are constant, and therefore it is most naturally formulated in microcanonical ensemble (specified number of particles, total volume and energy). Nevertheless it is not an impediment to carry out MD in other ensembles due to the existence of techniques that enable the correlation of the fluctuations in different ensembles. Thermostats can be included to the simulation in order to control the temperature, barostats can control the pressure of the system, and particle baths can control the chemical potential.

Newton's Equations of motion

One of the most fundamental ways to write the Newton's equations of motion is the Lagrangian equation of motion:

$$\frac{d}{dt}\left(\frac{\partial \mathcal{L}}{\partial \dot{q}_k}\right) - \frac{\partial \mathcal{L}}{\partial q_k} = 0 \quad (47)$$

where q_k are the generalized coordinates and $\dot{q}_k$ are their time derivatives. The Lagrangian function $\mathcal{L}(q, \dot{q}, t)$ is defined in terms of kinetic $K(\mathbf{q}\dot{\mathbf{q}}, t)$ and potential $\Gamma(\mathbf{q}\dot{\mathbf{q}}, \mathrm{t})$ energies:

$$\mathcal{L}(\mathbf{q}\dot{\mathbf{q}}, t) \equiv K(\mathbf{q}\dot{\mathbf{q}}, t) + \Gamma(\mathbf{q}\dot{\mathbf{q}}, t) \tag{48}$$

For a system of atoms with Cartesian coordinates $\mathbf{R}_i$, Eq. (47) yields

$$\mathbf{F}_i = m_i\mathbf{a}_i = m_i\ddot{\mathbf{R}}_i = \frac{\partial \mathcal{L}}{\partial \mathbf{R}_i} = \frac{\partial \Gamma}{\partial \mathbf{R}_i} \tag{49}$$

where m_i and $\mathbf{a}_i$ are the mass and acceleration of particle i and $\mathbf{F}_i$ is the force on that particle.

The most common algorithms developed to solve the Newton's equations of motion are based on the simple finite difference method. Given a set of positions and velocities at time t, we attempt to obtain the positions and velocities at a time $t+\delta t$ with enough accuracy. Examples of algorithms developed to integrate the equation of motion are Verlet algorithm, Leap Frog algorithm, velocity Verlet algorithm, Beeman algorithm, and velocity-corrected Verlet algorithm.

In the Verlet algorithm, the position of particle i at time $t+\delta t$ and $t-\delta t$ are related to the position at time t by a Taylor series yielding

$$\mathbf{R}_i(t+\delta t) = \mathbf{R}_i(t) + \delta t\frac{d\mathbf{R}_i(t)}{dt} + \frac{1}{2!}(\delta t)^2\frac{d^2\mathbf{R}_i(t)}{dt^2} + \frac{1}{3!}(\delta t)^3\frac{d^3\mathbf{R}_i(t)}{dt^3} + O(\delta t^4) \tag{50}$$

$$\mathbf{R}_i(t-\delta t) = \mathbf{R}_i(t) - \delta t\frac{d\mathbf{R}_i(t)}{dt} + \frac{1}{2!}(\delta t)^2\frac{d^2\mathbf{R}_i(t)}{dt^2} - \frac{1}{3!}(\delta t)^3\frac{d^3\mathbf{R}_i(t)}{dt^3} + O(\delta t^4) \tag{51}$$

The equation for advancing positions is obtained by adding Eqs. (50) and (51) and substituting Eq. (49)

$$\mathbf{R}_i(t+\delta t) = 2\mathbf{R}_i(t) - \mathbf{R}_i(t-\delta t) + (\delta t)^2\mathbf{a}_i(t) + O(\delta t^4) \tag{52}$$

Although velocities are not necessary to compute the trajectories, their knowledge has a great importance for the estimation of the kinetic and total energy of the system. They can be obtained by subtracting Eq. (50) from Eq. (51)

$$\mathbf{v}_i(t) = \frac{\mathrm{d}\mathbf{R}_i(t)}{\mathrm{d}t} = \frac{\mathbf{R}_i(t+\delta t) - \mathbf{R}_i(t-\delta t)}{2\delta t} \tag{53}$$

Scale Integration

We refer to scale integration as the communication between methods of different length scales. The goal is to take advantage of the high level of detail of sophisticated methods, which are more demanding, and use this information in methods that require low computational time.

For example, the potential of mean force (PMF) of ions at infinite dilution close to a specific surface can be obtained from molecular dynamics simulation and posteriorly inserted as non-electrostatic interaction in augmented PBE or DFT. The PMF includes image charge effects, ion hydration effects, and van der Waals interactions among ions, water, and substrate (Fig. 4A).

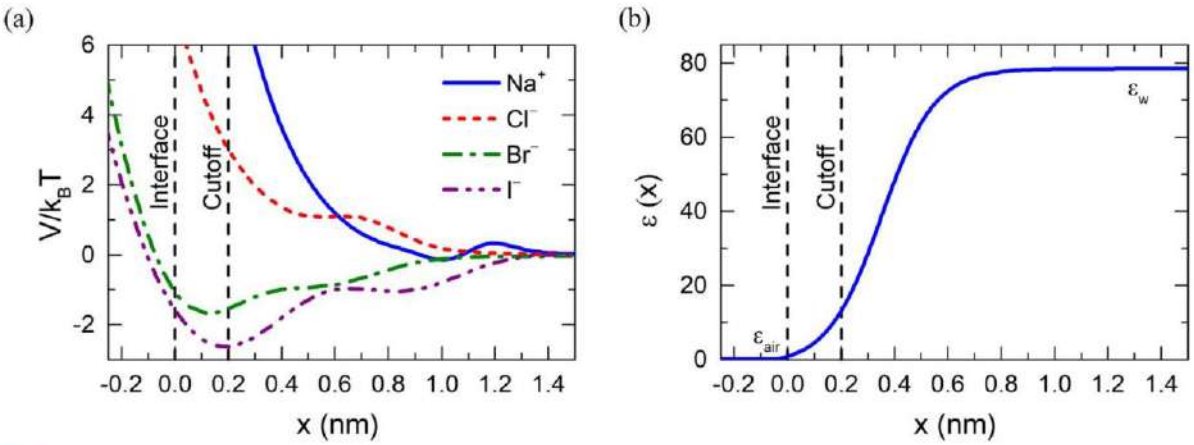

Fig. 4 (A) Potentials of mean force for various ions and (B) local dielectric constant for air-water interface. Here, the zero point is the Gibbs dividing surface, and the cut-off distance is $x = 0.2$ nm.[11]

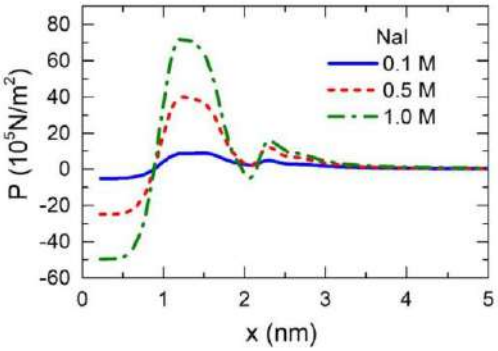

Fig. 5 Double layer pressure between two air-bubbles interacting through 0.1 M, 0.5 M, and 1 M NaI salt solutions, at a temperature of 298.15 K.[11]

The local dielectric function profile $\varepsilon(x)$ can also be estimated based on simulation data and inserted in augmented PBE and DFT calculations (Fig. 4B).

An example of data obtained with the insertion of PMF and dielectric constant profile into the PBE is presented in Fig. 5. The property refers to the double layer pressure between two air-bubbles interacting at 298.15 K through 0.1 M, 0.5 M, and 1 M NaI salt solutions.[11]

Conclusion

Molecular modeling plays a key role in the prediction of structures and properties of different kinds of systems and helps in the understanding of many phenomena experimentally observed.

There are numerous methods and theories that can be used to mimic the behavior of molecules and ions. This work has focused on three methods to exemplify each category of the molecular modeling classification for solvent/solute systems. Even considering a small sampling of methods, the possibilities of modifications available in the literature are enormous.

According to the required computational time, the Poisson Boltzmann equation is the most efficient, however it presents the lowest level of detail. In the other extreme, there is the molecular dynamics simulation that requires a considerable computational time due to the high level of detail. Different from molecular dynamics simulation, density functional theory accounts for the microscopic details of a many-body system without explicitly dealing with thermal fluctuations; its computational efficiency is comparable to PBE.

Acknowledgment

For financial support, we are grateful to PETROBRAS and the Brazilian Agencies "Coordination of Improvement of Higher Education Personnel" (CAPES), "Carlos Chagas Filho Research Support Foundation" (FAPERJ) and "National Council for Scientific and Technological Development" (CNPq).

References

1. Boström, M.; Lima, E. R. A.; Biscaia, E. C., Jr.; Tavares, F. W.; Kunz, W. Modifying the Poisson-Boltzmann Approach to Model Specific Ion Effects. In *Specific Ion Effects*; Kunz, W., Ed.; World Scientific: Singapore, 2010; (Chapter 11).
2. Parsons, D. F.; Ninham, B. W. *Langmuir* **2010**, *26*, 1816–1823.
3. Israelachvili, J. N. Intermolecular and Surface Forces, 3rd ed.; Academic Press: Burlington, 2011.
4. Alijó, P. H. R.; Tavares, F. W.; Biscaia, E. C., Jr. *Colloids Surf. A* **2012**, *412*, 29–35.
5. Barbosa, N. S. V.; Lima, E. R. A.; Tavares, F. W. *Colloids Surf. B* **2015**, *134*, 447–452.
6. Rosenfeld, Y. *Phys. Rev. Lett.* **1989**, *63*, 980–983.
7. Roth, R.; Evans, R.; Lang, A.; Kahl, G. *J. Phys. Condens. Matter* **2002**, *14*, 12063–12078.
8. Jiang, J.; Cao, D.; Henderson, D.; Wu, J. *Phys. Chem. Chem. Phys.* **2014**, *16*, 3934–3938.
9. Torrie, G.; Valleau, J. P. *J. Chem. Phys.* **1980**, *73*, 5807–5816.
10. Martínez, L.; Andrade, R.; Birgin, E. G.; Martínez, J. M. *J. Comput. Chem.* **2009**, *30*, 2157–2164.
11. Lima, E. R. A.; Boström, M.; Sernelius, B. E.; Horinek, D.; Netz, R. R.; Biscaia, E. C., Jr.; Kunz, W.; Tavares, F. W. *Chem. Phys. Lett.* **2008**, *458*, 299–302.

Further Reading

Davis, H. T. *Statistical Mechanics of Phases, Interfaces, and Thin Films*; Wiley-VCH: New York, 1996.
Frenkel, D.; Smit, B. *Understanding Molecular Simulation*; Academic Press: San Diego, 2002.
Henderson, D., Ed.; *Fundamental of Inhomogeneous Fluids*; Marcel Dekker: New York, 1992.
Jacob, T.; Sabo, L. Electrochemical Double Layer. In *Reference Module in Chemistry, Molecular Sciences and Chemical Engineering*; Elsevier, 2015.

Errata:

The Figure 1 of the paper should be:

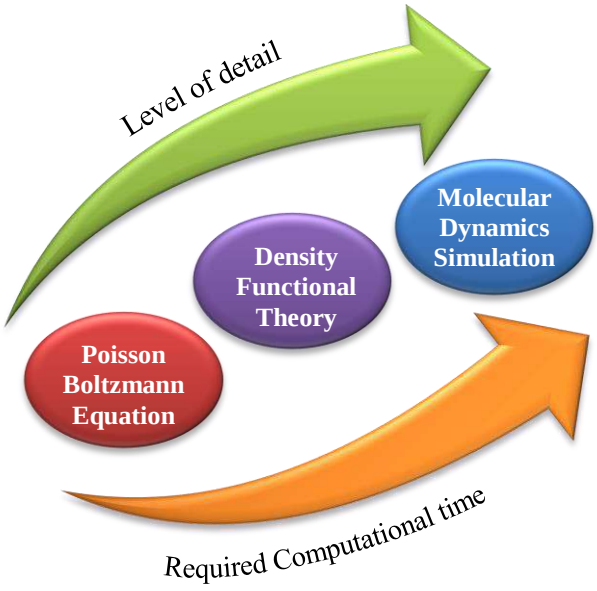

Additionally:

In page 7, lines 4 –5 of the chapter, where it is written:

"In the uniform fluid limit, the scalar weighted densities are reduced to variables of the scaled particle theory, $n_\alpha(\mathbf{R}) = \sum_{i=1}^{N} c_i r_i^\alpha$, while the vector weighted densities vanish.",

read:

"In the uniform fluid limit, the vector weighted densities vanish and the scalar weighted densities are reduced to variables of the scaled particle theory, $n_\alpha = \sum_{i=1}^{N} c_{\infty,i} R_i^{(\alpha)}$, where $R_i^{(\alpha)} = 1, r_i, 4\pi r_i^2, 4\pi r_i^3/3$ for α equal to 0, 1, 2 and 3, respectively."

In page 9, equation 48, where it is written:

"$\mathcal{L}(\mathbf{q}\dot{\mathbf{q}}, t) \equiv K(\mathbf{q}\dot{\mathbf{q}}, t) + \Gamma(\mathbf{q}\dot{\mathbf{q}}, t)$"

read:

"$\mathcal{L}(\mathbf{q}, \dot{\mathbf{q}}, t) \equiv K(\mathbf{q}, \dot{\mathbf{q}}, t) - \Gamma(\mathbf{q}, \dot{\mathbf{q}}, t)$"

APPENDIX B – Hohenberg-Kohn Theorem

The Hohenberg-Kohn theorem was originally developed for quantum mechanics[80,81] and was later adapted by Evans to classical systems.[33,85] According to this theorem, the one body potential can be determined uniquely by the density profile that minimizes the grand potential.

In order to demonstrate the Hohenberg-Kohn theorem, we define a functional of the normalized phase space probability density as[85,270]

$$\Omega[\mathcal{P}] = \sum_N \frac{1}{N!\,h^{3N}} \int \mathcal{P}[\mathcal{H}(\mathbf{r}^N, \mathbf{p}^N) - N\mu + \beta^{-1}\ln \mathcal{P}]\, \mathrm{d}\mathbf{r}^N\, \mathrm{d}\mathbf{p}^N \tag{158}$$

here, for the sake of simplicity, we consider a one-component system, where $\mathcal{P}$ is the probability of finding N molecules at temperature T, independently of the state energy. For a system at equilibrium, the density probability $\mathcal{P}^{eq}$ for the grand canonical ensemble is[100]

$$\mathcal{P}^{eq} = \frac{\exp\{-\beta[\mathcal{H}(\mathbf{r}^N, \mathbf{p}^N) - N\mu]\}}{\Xi} \tag{159}$$

As a result, the functional of the normalized phase space probability density at equilibrium is equal to the grand potential:

$$\Omega[\mathcal{P}^{eq}] = -\sum_N \frac{1}{N!\,h^{3N}} \int \mathcal{P}_0(\beta^{-1}\ln \Xi)\, \mathrm{d}\mathbf{r}^N\, \mathrm{d}\mathbf{p}^N = -\beta^{-1}\ln \Xi \equiv \Omega \tag{160}$$

In order to proof the theorem, we consider a test density $\rho'(\mathbf{r}) \neq \rho^{eq}(\mathbf{r})$ associated with a probability distribution equal to $\mathcal{P}'$, in which the one body potential $\varphi'(\mathbf{r})$ originates the density profile $\rho'(\mathbf{r})$. Thus, we can write that[85,87]

$$\Omega[\mathcal{P}'] - \Omega[\mathcal{P}^{eq}] = \beta^{-1}\left[\sum_N \frac{1}{N!\,h^{3N}} \int \mathcal{P}' \ln \mathcal{P}'\, \mathrm{d}\mathbf{r}^N\, \mathrm{d}\mathbf{p}^N - \sum_N \frac{1}{N!\,h^{3N}} \int \mathcal{P}' \ln \mathcal{P}^{eq}\, \mathrm{d}\mathbf{r}^N\, \mathrm{d}\mathbf{p}^N\right] \tag{161}$$

which is equivalent to

$$\Omega[\mathcal{P}'] - \Omega[\mathcal{P}^{eq}] = \beta^{-1}\left[\sum_N \frac{1}{N!\,h^{3N}}\int \mathcal{P}^{eq}\left[\frac{\mathcal{P}'}{\mathcal{P}^{eq}}\ln\left(\frac{\mathcal{P}'}{\mathcal{P}^{eq}}\right) - \frac{\mathcal{P}'}{\mathcal{P}^{eq}} + 1\right]\mathrm{d}\mathbf{r}^N\,\mathrm{d}\mathbf{p}^N\right] \geq 0 \qquad (162)$$

The right hand side is always non-negative, since $x\ln x \geq x - 1$ for any $x > 0$. Therefore, the grand potential at equilibrium is always the minimum of $\Omega[\mathcal{P}]$.

Now, let us assume that a specific density profile $\rho^{eq}(\mathbf{r})$ can be obtained by two different external potentials, $v'(\mathbf{r}) \neq v(\mathbf{r})$ for an open system with temperature and volume specified. For the external potential $v'(\mathbf{r})$, we have the Hamiltonian $\mathcal{H}'(\mathbf{r}^N, \mathbf{p}^N) = K(\mathbf{p}^N) + \mathcal{U}(\mathbf{r}^N) + \sum_{j=1}^N v'(\mathbf{r}_j)$ which is associated with the probability distribution $\mathcal{P}'^{eq}$ and the grand potential

$$\Omega' \equiv \Omega'[\mathcal{P}'^{eq}] = \sum_N \frac{1}{N!\,h^{3N}}\int \mathcal{P}'^{eq}[\mathcal{H}' - N\mu + \beta^{-1}\ln\mathcal{P}'^{eq}]\,\mathrm{d}\mathbf{r}^N\mathrm{d}\mathbf{p}^N \qquad (163)$$

According to the Gibbs-Bogoliubov inequality – Eq. (162) – we find[85,87]

$$\begin{aligned}\Omega'[\mathcal{P}'^{eq}] &\leq \sum_N \frac{1}{N!\,h^{3N}}\int \mathcal{P}^{eq}[\mathcal{H}' - N\mu + \beta^{-1}\ln\mathcal{P}^{eq}]\,\mathrm{d}\mathbf{r}^N\mathrm{d}\mathbf{p}^N \\ &= \Omega + \sum_N \frac{1}{N!\,h^{3N}}\int \mathcal{P}^{eq}\left[\sum_{j=1}^N v'(\mathbf{r}_j) - \sum_{j=1}^N v(\mathbf{r}_j)\right]\mathrm{d}\mathbf{r}^N\mathrm{d}\mathbf{p}^N\end{aligned} \qquad (164)$$

which in turn can be expressed as function of the one body potential, yielding

$$\Omega' \leq \Omega + \int \rho^{eq}(\mathbf{r})[\varphi'(\mathbf{r}) - \varphi(\mathbf{r})]\mathrm{d}\mathbf{r} \qquad (165)$$

Interchanging prime and unprimed quantities, we have

$$\Omega \leq \Omega' + \int \rho^{eq}(\mathbf{r})[\varphi(\mathbf{r}) - \varphi'(\mathbf{r})]\mathrm{d}\mathbf{r} \qquad (166)$$

Consequently, the hypothesis that two different external potentials give rise to a given equilibrium density is false, since Ω' must be equal to Ω to satisfy both equations, *i.e.* for a given chemical potential there is a unique external potential to a specific density profile at equilibrium. Since $\mathcal{P}^{eq}$ is a functional of $\varphi(\mathbf{r})$, it follows that it is also a functional of the equilibrium density. Hence, the equilibrium density corresponds to the minimum of the functional $\Omega[\rho(\boldsymbol{r})]$, as presented in Eq. (24).

B.1 Density as a functional derivative of the Grand canonical partition function

An integral part of the relation between the density and the grand partition function is the formal definition of the functional derivative of $\mathcal{F}$ as

$$\int \frac{\delta\mathcal{F}(\{y\})}{\delta y(\mathbf{r})}\phi(\mathbf{r})\mathrm{d}\mathbf{r} \equiv \left[\frac{\mathrm{d}\mathcal{F}(\{y+\epsilon\phi\})}{\mathrm{d}\epsilon}\right]_{\epsilon=0} \tag{167}$$

which can be evaluate to give the functional derivative of $\exp\left[-\beta\varphi\left(\mathbf{r}_j^{(i)}\right)\right]$ with respect to $\varphi_i(\mathbf{r})$ as [107]

$$\frac{\delta \exp\left[-\beta\varphi\left(\mathbf{r}_j^{(i)}\right)\right]}{\delta\varphi_i(\mathbf{r})} = -\beta \exp\left[-\beta\varphi\left(\mathbf{r}_j^{(i)}\right)\right]\delta\left(\mathbf{r}-\mathbf{r}_j^{(i)}\right) \tag{168}$$

Applying Eq. (168) to get $\delta\Xi/\delta\varphi_i(\mathbf{r})$, it results in

$$\begin{aligned}\frac{\delta\,\Xi}{\delta\varphi_i(\mathbf{r})} = -\beta \sum_{N_1,N_2\ldots N_n}\left[\prod_{k=1}^{n}\frac{1}{N_k!\,\Lambda_k^{3N_k}}\right]\int\left[\sum_{j=1}^{N_i}\delta\left(\mathbf{r}-\mathbf{r}_j^{(i)}\right)\right]\times \\ \exp\left[-\beta\left(\mathcal{U}(\mathbf{r})+\sum_{j=1}^{N}\varphi(\mathbf{r}_j)\right)\right]\mathrm{d}\mathbf{r}^N\end{aligned} \tag{169}$$

Comparing to Eq. (19), it is possible to verify that $\rho_i(\mathbf{r}) = -\frac{1}{\beta\Xi}\frac{\delta\Xi}{\delta\varphi_i(\mathbf{r})}$.

APPENDIX C – Weighting functions in the real and reciprocal space

The one-dimensional weight functions in Cartesian coordinates and real space are:

$$\omega_i^{(0)}(x) = \frac{\omega_i^{(2)}(x)}{\pi {\sigma_i}^2} \tag{170}$$

$$\omega_i^{(1)}(x) = \frac{\omega_i^{(2)}(x)}{2\pi\sigma_i} \tag{171}$$

$$\omega_i^{(2)}(x) = \pi\sigma_i\, \theta\left(\frac{\sigma_i}{2} - |x|\right) \tag{172}$$

$$\omega_i^{(3)}(x) = \pi\left[\left(\frac{\sigma_i}{2}\right)^2 - x^2\right] \theta\left(\frac{\sigma_i}{2} - |x|\right) \tag{173}$$

$$\boldsymbol{\omega}_i^{(V1)}(x) = \frac{\boldsymbol{\omega}_i^{(V2)}(x)}{2\pi\sigma_i} \tag{174}$$

$$\boldsymbol{\omega}_i^{(V2)}(x) = 2\pi x\, \theta\left(\frac{\sigma_i}{2} - |x|\right) \hat{\mathbf{x}} \tag{175}$$

Regarding the weighting functions in reciprocal space, first, it is important to define the correlation between the discrete Fourier transform and the continuous Fourier transform, since we are interested in the computation of the Fourier transform of the weighting functions $\widehat{\omega}_i^{(\alpha)}$ analytically to multiply them *a posteriori* by the Fourier transform of the densities obtained by FFT. Herein we assume the definitions proposed by Brigham[271], Frigo and Johnson[272], in which the continuous Fourier transform H of a function $\hbar$ is equal to

$$H(\not{f}) = \int_{-\infty}^{\infty} \hbar(x) \exp(-2\pi i \not{f} x)\, \mathrm{d}x \tag{176}$$

where $\not{f}$ is the inverse wavelength and $i = \sqrt{-1}$. Sampling the function $\hbar(x)$ at evenly spaced intervals in real domain, we have:

$$\hbar_j = \hbar(x_j) \qquad x_j = j\Delta \qquad j = 0, 1, 2, \cdots, \mathcal{N}_x - 1 \tag{177}$$

where Δ denotes the interval between consecutive samples and $\mathcal{N}_x$ is the total number of samples. On the other hand, the reciprocal space grid is characterized by

$$\not{f}_k \equiv \frac{k}{\mathcal{N}_x \Delta} \qquad k = -\frac{\mathcal{N}_x}{2}, \frac{\mathcal{N}_x}{2} + 1 \cdots, \frac{\mathcal{N}_x}{2} \tag{178}$$

with $\mathcal{N}_x + 1$ values of $\not{f}_k$; however, the two extremes are equal, reducing the number of $\not{f}_k$ to $\mathcal{N}_x$. It is worthwhile to note that the discrete Fourier transform of a function is periodic in k, with period $\mathcal{N}_x$. Therefore, Eq. (178) can be expressed with k varying from 0 to $\mathcal{N}_x - 1$, similar to Eq. (177), with zero frequency corresponding to $k = 0$, positive frequencies in the range between $1 \leq k \leq \mathcal{N}_x/2 - 1$, negative frequencies between $\mathcal{N}_x/2 + 1 \leq k \leq \mathcal{N}_x - 1$, and finally, $k = \mathcal{N}_x/2$ corresponding to both positive and negative frequencies. For a system with d dimensions, $\not{f}_{k_d}$ is given by

$$\not{f}_{k_d} = \begin{cases} \dfrac{k_d}{\mathcal{N}_d \Delta_d} & \text{for} \quad k_d \leq \dfrac{\mathcal{N}_d}{2} \\ \dfrac{-(\mathcal{N}_d - k_d)}{N_d \Delta_d} & \text{for} \quad k_d > \dfrac{\mathcal{N}_d}{2} \end{cases} \tag{179}$$

This convention is used in the FFTW algorithm developed by Frigo and Johnson[272].

Approximating the integral in Eq. (176) by a discrete sum yields

$$H(\not{f}_k) \approx \sum_{j=0}^{\mathcal{N}_x - 1} \not{h}_j \exp\left(-2\pi i \not{f}_k x_j\right) \Delta = \Delta \sum_{j=0}^{\mathcal{N}_x - 1} \not{h}_j \exp(-2\pi i k j / \mathcal{N}_x) \tag{180}$$

in which the final summation is called the discrete Fourier transform (H_k) of the $\mathcal{N}_x$ points h_j:

$$H_k \equiv \sum_{j=0}^{\mathcal{N}_x - 1} \not{h}_j \exp(-2\pi i k j / \mathcal{N}_x) \tag{181}$$

The formula for the discrete inverse Fourier transform, which recovers the set of $\not{h}_j$ exactly from H_k is[271]

$$h_j = \frac{1}{\mathcal{N}_x} \sum_{k=0}^{\mathcal{N}_x - 1} H_k \exp(2\pi i k j / \mathcal{N}_x) \tag{182}$$

After these brief comments about Fourier transform, we are able to compute the analytical Fourier transform of the weighting functions, represented here with a hat $\widehat{\omega}_i^{(\alpha)}$.

We start with the Fourier transform of $\omega_i^{(2)}$ by applying Eq. (42) in Eq. (176):[108,124]

$$\begin{aligned} \widehat{\omega}_i^{(2)} &= \int_0^{2\pi} \mathrm{d}\phi \int_0^{\pi} \mathrm{d}\theta \sin\theta \int_0^{\infty} \mathrm{d}r r^2 \delta\left(\frac{\sigma_i}{2} - |\mathbf{r}|\right) \exp(-2\pi i \mathbf{r} \cdot \boldsymbol{\mathbb{f}}) \\ &= 2\pi \int_0^{\pi} \mathrm{d}\theta \sin\theta \left(\frac{\sigma_i}{2}\right)^2 \exp\left(-2\pi i \frac{\sigma_i}{2} \hat{\mathbf{r}} \cdot \boldsymbol{\mathbb{f}}\right) \end{aligned} \tag{183}$$

where $\hat{\mathbf{r}}$ is the versor. In order to facilitate the integration, we adopted the spherical coordinates. The dot product $\hat{\mathbf{r}} \cdot \boldsymbol{\mathbb{f}}$ is equal to $\sin\theta\cos\phi\, \mathbb{f}_x + \sin\theta\sin\phi\, \mathbb{f}_y + \cos\theta\, \mathbb{f}_z$; however, taking advantage of the rotational symmetry, we can consider that $\boldsymbol{\mathbb{f}}$ points purely in $\hat{\mathbf{z}}'$ direction, resulting in $\hat{\mathbf{r}} \cdot \boldsymbol{\mathbb{f}} = \cos\theta'\, \mathbb{f}_z'$, where prime indicates the hypothetical coordinate system. Performing this assumption in Eq. (183) and integrating by parts, we obtain

$$\widehat{\omega}_i^{(2)} = 2\pi \int_0^{\pi} \mathrm{d}\theta' \sin\theta' \left(\frac{\sigma_i}{2}\right)^2 \exp\left(-2\pi i \frac{\sigma_i}{2} \cos\theta'\, \mathbb{f}_z'\right) = \frac{\sigma_i}{f_z'} \sin(\pi \sigma_i \mathbb{f}_z') \tag{184}$$

which, in the original coordinate system is

$$\widehat{\omega}_i^{(2)} = \frac{\sigma_i}{|\boldsymbol{\mathbb{f}}|} \sin(\pi \sigma_i |\boldsymbol{\mathbb{f}}|) \tag{185}$$

The two first weighting functions can be obtained straightforwardly through Eqs. (40) and (41) as

$$\widehat{\omega}_i^{(0)} = \frac{\sin(\pi \sigma_i |\boldsymbol{\mathbb{f}}|)}{\pi \sigma_i |\boldsymbol{\mathbb{f}}|} \tag{186}$$

$$\widehat{\omega}_i^{(1)} = \frac{\sin(\pi \sigma_i |\boldsymbol{\mathbb{f}}|)}{2\pi |\boldsymbol{\mathbb{f}}|} \tag{187}$$

For $\widehat{\omega}_i^{(3)}$ we use the property that the Heaviside function can be obtained as the integral of the Dirac delta function, thus:

$$\widehat{\omega}_i^{(3)} = \int_0^{\frac{\sigma_i}{2}} \mathrm{d}r\, \widehat{\omega}_i^{(2)}\Big|_{\frac{\sigma_i}{2}=r} = \frac{\sin(\pi\sigma_i|\boldsymbol{\mathbb{f}}|)}{2\pi^2|\boldsymbol{\mathbb{f}}|^3} - \frac{\sigma_i\cos(\pi\sigma_i|\boldsymbol{\mathbb{f}}|)}{2\pi|\boldsymbol{\mathbb{f}}|^2} \tag{188}$$

For the vector weighting functions, a procedure similar to $\widehat{\omega}_i^{(2)}$ is followed, keeping in mind, however, the vector nature of these functions.[108] Applying Eq. (45) in Eq. (176) yields

$$\begin{aligned}\widehat{\boldsymbol{\omega}}_i^{(V2)} &= \int_0^{2\pi}\mathrm{d}\phi\int_0^{\pi}\mathrm{d}\theta\sin\theta\int_0^{\infty}\mathrm{d}r\,\frac{\mathbf{r}}{|\mathbf{r}|}r^2\delta\left(\frac{\sigma_i}{2}-|\mathbf{r}|\right)\exp(-2\pi i\mathbf{r}\cdot\boldsymbol{\mathbb{f}}) \\ &= \int_0^{2\pi}\mathrm{d}\phi\int_0^{\pi}\mathrm{d}\theta\sin\theta\left(\frac{\sigma_i}{2}\right)^2\exp\left(-2\pi i\frac{\sigma_i}{2}\hat{\mathbf{r}}\cdot\boldsymbol{\mathbb{f}}\right)\hat{\mathbf{r}}\end{aligned} \tag{189}$$

In addition, for the integration over the polar angle, it is necessary to expand $\hat{\mathbf{r}}$ on its vector form:

$$\hat{\mathbf{r}} = \sin\theta\cos\phi\,\hat{\mathbf{x}} + \sin\theta\sin\phi\,\hat{\mathbf{y}} + \cos\theta\,\hat{\mathbf{z}} \tag{190}$$

and consider a hypothetical rotate coordinate system in which $\boldsymbol{\mathbb{f}}$ points purely in $\hat{\mathbf{z}}$ direction, resulting in

$$\widehat{\boldsymbol{\omega}}_i^{(V2)} = 2\pi\left(\frac{\sigma_i}{2}\right)^2\int_0^{\pi}\mathrm{d}\theta'\sin\theta'\cos\theta'\exp[-\pi i\sigma_i\cos\theta'\,\mathbb{f}_z']\,\hat{\mathbf{z}} \tag{191}$$

Finally, the integration over the azimuth gives

$$\widehat{\boldsymbol{\omega}}_i^{(V2)} = -\frac{i}{\pi\mathbb{f}_z'^2}[\sin(\pi\sigma_i\mathbb{f}_z') - \pi\sigma_i\mathbb{f}_z'\cos(\pi\sigma_i\mathbb{f}_z')]\hat{\mathbf{z}} \tag{192}$$

which, in the original coordinate system, is

$$\widehat{\boldsymbol{\omega}}_i^{(V2)} = -\frac{i}{\pi|\boldsymbol{\mathbb{f}}|^2}[\sin(\pi\sigma_i|\boldsymbol{\mathbb{f}}|) - \pi\sigma_i|\boldsymbol{\mathbb{f}}|\cos(\pi\sigma_i|\boldsymbol{\mathbb{f}}|)]\widehat{\boldsymbol{\mathbb{f}}} \tag{193}$$

Here, $\widehat{\boldsymbol{\mathfrak{f}}}$ is the versor of $\boldsymbol{\mathfrak{f}}$. As shown in Eq. (44), the $\widehat{\omega}_i^{V1}$ weighting function can be obtained from Eq. (193) as

$$\widehat{\boldsymbol{\omega}}_i^{(V1)} = -\frac{i}{2\pi^2\sigma_i|\boldsymbol{\mathfrak{f}}|^2}[\sin(\pi\sigma_i|\boldsymbol{\mathfrak{f}}|) - \pi\sigma_i|\boldsymbol{\mathfrak{f}}|\cos(\pi\sigma_i|\boldsymbol{\mathfrak{f}}|)]\widehat{\boldsymbol{\mathfrak{f}}} \tag{194}$$

When $|\boldsymbol{\mathfrak{f}}| \to 0$, the weighting functions in reciprocal space are evaluated using the L'Hôpital's rule in order to obtain:

$$\lim_{|\boldsymbol{\mathfrak{f}}|\to 0} \widehat{\omega}_i^{(0)} = \lim_{|\boldsymbol{\mathfrak{f}}|\to 0} \frac{1}{\pi\sigma_i|\boldsymbol{\mathfrak{f}}|}\sin(\pi\sigma_i|\boldsymbol{\mathfrak{f}}|) = \frac{\pi\sigma_i\cos(0)}{\pi\sigma_i} = 1 \tag{195}$$

$$\lim_{|\boldsymbol{\mathfrak{f}}|\to 0} \widehat{\omega}_i^{(1)} = \lim_{|\boldsymbol{\mathfrak{f}}|\to 0} \frac{1}{2\pi|\boldsymbol{\mathfrak{f}}|}\sin(\pi\sigma_i|\boldsymbol{\mathfrak{f}}|) = \frac{\pi\sigma_i\cos(0)}{2\pi} = \frac{\sigma_i}{2} \tag{196}$$

$$\lim_{|\boldsymbol{\mathfrak{f}}|\to 0} \widehat{\omega}_i^{(2)} = \lim_{|\boldsymbol{\mathfrak{f}}|\to 0} \frac{\sigma_i}{|\boldsymbol{\mathfrak{f}}|}\sin(\pi\sigma_i|\boldsymbol{\mathfrak{f}}|) = \pi\sigma_i^2\cos(0) = \pi\sigma_i^2 \tag{197}$$

$$\lim_{|\boldsymbol{\mathfrak{f}}|\to 0} \widehat{\omega}_i^{(3)} = \lim_{|\boldsymbol{\mathfrak{f}}|\to 0} \left[\frac{\sin(\pi\sigma_i|\boldsymbol{\mathfrak{f}}|)}{2\pi^2|\boldsymbol{\mathfrak{f}}|^3} - \frac{\sigma_i\cos(\pi\sigma_i|\boldsymbol{\mathfrak{f}}|)}{2\pi|\boldsymbol{\mathfrak{f}}|^2}\right] = \frac{\pi\sigma_i^3}{6} \tag{198}$$

$$\lim_{|\boldsymbol{\mathfrak{f}}|\to 0} \widehat{\boldsymbol{\omega}}_i^{(V1)} = \lim_{|\boldsymbol{\mathfrak{f}}|\to 0} \left\{-\frac{i}{2\pi^2\sigma_i|\boldsymbol{\mathfrak{f}}|^2}[\sin(\pi\sigma_i|\boldsymbol{\mathfrak{f}}|) - \pi\sigma_i|\boldsymbol{\mathfrak{f}}|\cos(\pi\sigma_i|\boldsymbol{\mathfrak{f}}|)]\widehat{\boldsymbol{\mathfrak{f}}}\right\} = 0 \tag{199}$$

$$\lim_{|\boldsymbol{\mathfrak{f}}|\to 0} \widehat{\boldsymbol{\omega}}_i^{(V2)} = \lim_{|\boldsymbol{\mathfrak{f}}|\to 0} \left\{-\frac{i}{\pi|\boldsymbol{\mathfrak{f}}|^2}[\sin(\pi\sigma_i|\boldsymbol{\mathfrak{f}}|) - \pi\sigma_i|\boldsymbol{\mathfrak{f}}|\cos(\pi\sigma_i|\boldsymbol{\mathfrak{f}}|)]\widehat{\boldsymbol{\mathfrak{f}}}\right\} = 0 \tag{200}$$

Note that these are the limits expected, since the fundamental measures of the sphere are recovery, *i.e.* the Euler characteristic, radius, surface area, and volume of the sphere.

APPENDIX D – Mean electrostatic potential close to a charged surface

The Poisson equation in its differential form can be solved semi-analytically for a system containing a charged wall in one or both boundaries at the same direction. For this case, we consider the symmetry and solve the one-dimension Poisson equation in Cartesian coordinate.

For the presence on a single wall located at $x = 0$, we take advantage of the Neumann boundary condition at $x \to \infty$

$$\left.\frac{\mathrm{d}\psi}{\mathrm{d}x'}\right|_{x'\to\infty} = 0 \tag{201}$$

and integrate the Poisson equation from x'' to ∞, yielding

$$\frac{\mathrm{d}\psi(x'')}{\mathrm{d}x''} = \frac{e}{\varepsilon_0 \varepsilon}\sum_i \int_{x''}^{\infty} z_i \rho_i(x')\mathrm{d}x' \tag{202}$$

The resulting equation can be integrated again; but now from z to ∞ and using the Dirichlet boundary condition $\psi|_{x\to\infty} = 0$:

$$\psi(x) = -\frac{e}{\varepsilon_0 \varepsilon}\sum_i \int_{x}^{\infty} \int_{x''}^{\infty} z_i \rho_i(x')\mathrm{d}x'\,\mathrm{d}x'' \tag{203}$$

In addition, a change in the integration order is made to get a better numerical convenience. Thus, we can write

$$\psi(x) = -\frac{e}{\varepsilon_0 \varepsilon}\sum_i \int_{x}^{\infty} \int_{x}^{x'} z_i \rho_i(x')\mathrm{d}x''\,\mathrm{d}x' = -\frac{e}{\varepsilon_0 \varepsilon}\sum_i \int_{x}^{\infty} (x' - x) z_i \rho_i(x')\mathrm{d}x' \tag{204}$$

For $x = 0$, the mean electrostatic potential is given by:

$$\psi(0) = -\frac{e}{\varepsilon_0 \varepsilon}\sum_i \int_0^\infty x' z_i \rho_i(x')\mathrm{d}x' \tag{205}$$

which in turn can be combined with Eq. (204) yielding

$$\psi(x) = \psi(0) + \frac{ex}{\varepsilon_0 \varepsilon}\sum_i \int_x^\infty z_i \rho_i(x')\mathrm{d}x' + \frac{e}{\varepsilon_0 \varepsilon}\sum_i \int_0^x x' z_i \rho_i(x')\mathrm{d}x' \tag{206}$$

Eq. (206) might be integrated numerically resulting in the mean electric potential.

For an electrolyte confined within a slit pore, we integrate the Poisson equation in two different domains: one from the surface on the left to the midplane (x_m) and other from the midplane to the surface on the right. For $x < x_m$, we integrate the Poisson equation from x'' to x_m, with the boundary condition:

$$\left.\frac{\mathrm{d}\psi}{\mathrm{d}x'}\right|_{x_m} = \hbar \tag{207}$$

yielding:

$$\hbar - \frac{\mathrm{d}\psi(x'')}{\mathrm{d}x''} = -\frac{e}{\varepsilon_0 \varepsilon}\sum_i \int_{x''}^{x_m} z_i \rho_i(x')\mathrm{d}x' \tag{208}$$

Now, Eq. (208) is integrated from x to x_m with Dirichlet boundary condition $\psi|_{x_m} = \psi_m$:

$$\psi_m - \psi(x) = \int_x^{x_m} \hbar \mathrm{d}x'' + \frac{e}{\varepsilon_0 \varepsilon}\sum_i \int_x^{x_m} \int_{x''}^{x_m} z_i \rho_i(x')\mathrm{d}x'\,\mathrm{d}x'' \tag{209}$$

Similar to the system with one surface, we chance the integration order as

$$\begin{aligned}\psi(x) &= -(x_m - x)\hbar + \psi_m - \frac{e}{\varepsilon_0 \varepsilon}\sum_i \int_x^{x_m} \int_x^{x'} z_i \rho_i(x')\mathrm{d}x''\,\mathrm{d}x' \\ &= -(x_m - x)\hbar + \psi_m - \frac{e}{\varepsilon_0 \varepsilon}\sum_i \int_x^{x_m} (x' - x) z_i \rho_i(x')\mathrm{d}x'\end{aligned} \tag{210}$$

Assuming that the surface on the left is located at the origin ($x = x_{s1} = 0$), we have:

$$\psi(x_{s1}) = -x_m \mathcal{k} + \psi_m - \frac{e}{\varepsilon_0 \varepsilon} \sum_i \int_0^{x_m} x' z_i \rho_i(x') \mathrm{d}x' \tag{211}$$

which in turn can be combined with Eq. (210) yielding

$$\psi(x) = \psi(x_{s1}) + x\mathcal{k} + \frac{ex}{\varepsilon_0 \varepsilon} \sum_i \int_x^{x_m} z_i \rho_i(x') \mathrm{d}x' + \frac{e}{\varepsilon_0 \varepsilon} \sum_i \int_0^{x} x' z_i \rho_i(x') \mathrm{d}x' \tag{212}$$

The second half of the domain can be treated in analogous fashion providing:

$$\begin{aligned} \psi(x) = \psi(x_{s2}) + (x - x_{s2})\mathcal{k} + \frac{e}{\varepsilon_0 \varepsilon} \sum_i \int_{x_m}^{x} (x_{s2} - x) z_i \rho_i(x') \mathrm{d}x' \\ + \frac{e}{\varepsilon_0 \varepsilon} \sum_i \int_x^{x_{s2}} (x_{s2} - x') z_i \rho_i(x') \mathrm{d}x' \end{aligned} \tag{213}$$

The constant $\mathcal{k}$ is determined by the combination of Eqs. (212) and (213) at $x = x_m$:

$$\mathcal{k} = \frac{\psi(x_{s2}) - \psi(x_{s1})}{x_{s2}} - \frac{e}{\varepsilon_0 \varepsilon} \sum_i \int_0^{x_{s2}} \frac{x'}{x_{s2}} z_i \rho_i(x') \mathrm{d}x' + \frac{e}{\varepsilon_0 \varepsilon} \sum_i \int_{x_m}^{x_{s2}} z_i \rho_i(x') \mathrm{d}x' \tag{214}$$

APPENDIX E – Mean-Spherical Approximation

The mean spherical approximation (MSA), which was initially developed by Lebowitz and Percus,[273] considers the core exclusion *i.e.*, the ions are not allowed to overlap. It has the advantage of being analytically solvable.[146,147,274] However, the only restriction is the electroneutrality condition.

Here, we used the MSA to compute the second order direct correlation function due to the electrostatic screening, which can be written as

$$c_{ij}^{(2)el}(\mathbf{r}) = c_{ij}^{(2)}(\mathbf{r}) + \frac{\lambda_B z_i z_j}{|\mathbf{r}|} - c_{ij}^{(2)hs}(\mathbf{r}) \tag{215}$$

According to Hiroike,[146] when $\sigma_i < \sigma_j$ and $0 \leq |\mathbf{r}| < \frac{\sigma_i+\sigma_j}{2}$, the difference between the total direct correlation function and the DCF due the hard sphere exclusion volume is

$$c_{ij}^{(2)}(\mathbf{r}) - c_{ij}^{(2)hs}(\mathbf{r}) = -2\lambda_B\left[-z_i \mathrm{N}_j + X_i(\mathrm{N}_i + \Gamma X_i) - \frac{\sigma_i}{3}(\mathrm{N}_i + \Gamma X_i)^2\right] \tag{216}$$

On the other hand, when $\left|\frac{\sigma_j-\sigma_i}{2}\right| \leq |\mathbf{r}| < \frac{\sigma_j+\sigma_i}{2}$, we have[146]

$$\begin{aligned} & c_{ij}^{(2)}(\mathbf{r}) - c_{ij}^{(2)hs}(\mathbf{r}) \\ & = \lambda_B \left\{ \begin{array}{l} \frac{(\sigma_i-\sigma_j)}{|\mathbf{r}|}\left[\begin{array}{c} \frac{(X_i+X_j)}{4}\left[(\mathrm{N}_i+\Gamma X_i)-(\mathrm{N}_j+\Gamma X_j)\right] \\ -\frac{\sigma_i-\sigma_j}{16}\left[(\mathrm{N}_i+\Gamma X_i+\mathrm{N}_j+\Gamma X_j)^2-4\mathrm{N}_i\mathrm{N}_j\right] \end{array}\right] \\ -\left[\begin{array}{c} (X_i-X_j)(\mathrm{N}_i-\mathrm{N}_j)+(X_i^2+X_j^2)\Gamma+(\sigma_i+\sigma_j)\mathrm{N}_i\mathrm{N}_j \\ -\frac{1}{3}\left[\sigma_i(\mathrm{N}_i+\Gamma X_i)^2+\sigma_j(\mathrm{N}_j+\Gamma X_j)^2\right] \end{array}\right] \\ +|\mathbf{r}|\left[\begin{array}{c} \frac{X_i}{\sigma_i}(\mathrm{N}_i+\Gamma X_i)+\frac{X_j}{\sigma_j}(\mathrm{N}_j+\Gamma X_j)+\mathrm{N}_i\mathrm{N}_j \\ -\frac{1}{2}\left[(\mathrm{N}_i+\Gamma X_i)^2+(\mathrm{N}_j+\Gamma X_j)^2\right] \end{array}\right] \\ +|\mathbf{r}|^3\left[\frac{(\mathrm{N}_i+\Gamma X_i)^2}{6{\sigma_i}^2}+\frac{(\mathrm{N}_j+\Gamma X_j)^2}{6{\sigma_j}^2}\right] \end{array} \right\} \end{aligned} \tag{217}$$

where X_i, N_i and Γ are computed numerically as

$$X_i = \frac{z_i}{1+\Gamma\sigma_i} - \frac{c{\sigma_i}^2}{1+\Gamma\sigma_i}\frac{\sum_j \rho_j\sigma_j z_j\left(1+\Gamma\sigma_j\right)^{-1}}{1+c\sum_j \rho_j{\sigma_i}^3\left(1+\Gamma\sigma_j\right)^{-1}} \tag{218}$$

$$X_i = z_i + \mathrm{N}_i\sigma_i \tag{219}$$

$$\Gamma^2 = \frac{\beta\pi e^2}{\varepsilon}\sum_i \rho_i {X_i}^2 \tag{220}$$

and

$$c = \frac{\pi}{2\left[1-\frac{\pi}{6}\right]\sum_i \rho_i{\sigma_i}^3} \tag{221}$$

Blum and Rosenfeld[147] reported a different derivation path and arrived in a DCF similar to the one proposed by Hiroike, nevertheless, simpler:

$$c_{ij}^{(2)}(\mathbf{r}) - c_{ij}^{(2)hs}(\mathbf{r}) = -\frac{\lambda_B}{2}\left[\frac{\mathscr{b}_i+\mathscr{b}_j}{\mathscr{b}_i\mathscr{b}_j} - \frac{|\mathbf{r}|}{2\mathscr{b}_i\mathscr{b}_j} - \frac{\left(\mathscr{b}_i-\mathscr{b}_j\right)^2}{2\mathscr{b}_i\mathscr{b}_j}\right] \tag{222}$$

where $\mathscr{b}_i$ is the effective characteristic radius defined by[147]

$$\mathscr{b}_i = \frac{\sigma_i + \Gamma^{-1}}{2} \tag{223}$$

APPENDIX F – The electrostatic behavior of the bacterial cell wall using a smoothing function to describe the charge-regulated volume charge density profile

BARBOSA, N. S. V.; LIMA, E. R. A.; TAVARES, F. W. The electrostatic behavior of the bacterial cell wall using a smoothing function to describe the charge-regulated volume charge density profile. *Colloids Surf. B* , v. 134, p. 447–452, 2015. doi: 10.1016/j.colsurfb.2015.06.066.

Colloids and Surfaces B: Biointerfaces 134 (2015) 447–452

Contents lists available at ScienceDirect

Colloids and Surfaces B: Biointerfaces

journal homepage: www.elsevier.com/locate/colsurfb

The electrostatic behavior of the bacterial cell wall using a smoothing function to describe the charge-regulated volume charge density profile

Nathalia S.V. Barbosa[a], Eduardo R.A. Lima[a], Frederico W. Tavares[b,c,*]

[a] Programa de Pós-graduação em Engenharia Química, Universidade do Estado do Rio de Janeiro, CEP 20550-013, Rio de Janeiro, RJ, Brazil
[b] Escola de Química, Universidade Federal do Rio de Janeiro, CEP 21949-900, Rio de Janeiro, RJ, Brazil
[c] Programa de Engenharia Química, COPPE, Universidade Federal do Rio de Janeiro, CEP 21945-970, Rio de Janeiro, RJ, Brazil

ARTICLE INFO

Article history:
Received 7 March 2015
Received in revised form 25 May 2015
Accepted 30 June 2015
Available online 10 July 2015

Keywords:
Donnan potential
Poisson–Boltzmann equation
Fixed charge
Regularization function

ABSTRACT

The Donnan potential can be observed in many biological systems due to the presence of polyelectrolytes as proteins and nucleic acids. The aim of this work was to present a useful tool to describe the fixed and charge-regulated volume charge density profile through the use of a smoothing function and to obtain the electrostatic potential profile as well as the Donnan potential of this system by solving Poisson–Boltzmann (PB) equation. When we use the smoothing function, the Donnan potential arises automatically from the solution of only one Poisson–Boltzmann equation and it is not necessary to impose this potential for treating charged system in the presence of a membrane. The electrostatic behavior across the *Bacillus brevis* wall considering the dependence on the ionization of the cell wall functional groups as a function of the solution pH was analyzed. An important issue was to show that potentiometric titration data could be used together with the Poisson–Boltzmann equation to predict the electrostatic behavior (e.g., zeta potential) of the bacterial cell surface.

1. Introduction

The electrical properties of bacterial cells are determined by the type and concentration of specific functional groups on bacterial cell walls, pH value, composition and ionic strength of the electrolyte, and separation distance from nearby surfaces [1–10]. These properties induce important environment characteristics of the bacteria such as mobility [1–5], zeta potential [1–4,6], metal binding [3–5,11–18] and adhesion to surfaces [19–23]. The bacterial cell surface charge is originated from the acidic and basic functional groups, including carboxyl, phosphoryl, hydroxyl, and amine groups [11–13]. In the cell walls of the Gram-positive bacteria, these functional groups are associated with rigid and relatively thick peptidoglycan layer adjacent anionic polymers (teichoic acid and theichuronic acid) [24–28]. On the other hand, the cell walls of Gram-negative bacteria have an outer membrane covering a thin layer of peptidoglycan. This outer membrane is composed of phospholipids, proteins, and polysaccharides [26–28].

The concentrations of anionic and cationic groups in the bacterial cell wall can be quantified by an acid–base titration of a bacterial suspension [25–28]. The presence of these groups gives the bacterial wall amphoteric properties, thereby depending on the pH, the net charge in the wall can be either positive, negative or zero [28]. However under most physiological conditions, the bacterial cell surface carries a net negative charge.

The electrical potential in the bacterial wall can be obtained by solving the Poisson equation, taking into account the fixed volume charge density of the cell wall together with the volume densities of mobile charges [28]. Here the term "fixed" refers to charges that are fixed in space (immobile), but not necessarily with a constant value. Some usual approximations are: fixed cell wall charge uniformly distributed and cell wall thickness much greater than the Debye length [28–30]. This means that, inside the wall, the potential is approximately constant and equal to the Donnan potential. The gram-positive cell wall is usually between 20 and 80 nm thick while the gram-negative cell wall is usually between 5 and 10 nm thick.

The Donnan potential occurs (i) when non-permeable ions are unequally distributed between two electrolyte solutions separated by a selectively permeable membrane, which allows certain ions to move freely between the two solutions; (ii) between regions of a solution and the charged membrane (or charged macromolecules). The distribution of ions obeys the laws of thermodynamics and the principle of electroneutrality between the two compartments

* Corresponding author at: Escola de Química, Universidade Federal do Rio de Janeiro, CEP 21949-900, Rio de Janeiro, RJ, Brazil.
E-mail address: tavares@eq.ufrj.br (F.W. Tavares).

http://dx.doi.org/10.1016/j.colsurfb.2015.06.066
0927-7765/

separated by the membrane [31,32]. In such situations, an asymmetric distribution of small ions (mobile ions) can be observed. The Donnan effect refers not only to the membrane equilibria but to any situation in which there is a tendency to produce an ion partitioning.

The electric potential is present in many biological systems and may be originated from several sources such as the existence of free ions, the ionized molecular groups or the electrical polarization of biomolecules and the occurrence of electron transfer reactions in certain biochemical reaction systems.

The current study aimed to obtain the electrostatic potential in a system with fixed charge solving the Poisson–Boltzmann equation with the inclusion of fixed volume charge density. In the present contribution, we showed that the use of a smoothing function to describe the charged-regulated or fixed volume charge density profile can be a useful tool to analyze the electrostatic potential and the concentration profiles in systems containing polyelectrolytes dispersed distinctively between two phases. With this strategy, the Donnan potential automatically arises from the resolution of the Poisson–Boltzmann equation for the two environments (with and without the polyelectrolytes) simultaneously.

We here analyzed two situations: one was a general case with polyelectrolytes uniformly distributed on one side of a selectively permeable membrane in an aqueous system containing NaCl and KCl. Another case was an applied example: the potential profile across the *Bacillus brevis* cell wall was calculated as a function of the solution pH, depending on the ionization of the cell wall function groups. An important issue was to show that the potentiometric titration and the zeta potential data can be used together with the Poisson–Boltzmann equation to predict the electrostatic behavior of the bacterial cell surface.

2. Theory

The classical treatment of the Donnan potential is considered to be accompanied by a discontinuous potential gap across the membrane surface [29]. This difference in electrical potential ($\Delta\psi$) is given by the Nernst equation [33]:

$$\Delta\psi = \frac{RT}{Fz_i} \ln \frac{a_i^{\beta}}{a_i^{\alpha}} \tag{1}$$

where R is the universal gas constant, T is the absolute temperature, F is the Faraday constant, z_i is the valence of ion i, and a_i is the activity of ion i in a phase (α or β).

Mauro [32] suggested a continuous Donnan potential using the Poisson–Boltzmann equation applied to two regions adjacent to each other: one containing fixed charge completely ionized and another one without fixed charge. It is possible to demonstrate that the Donnan potential calculated via the Poisson–Boltzmann equation for remote regions is equal to the difference in the potential provided for the Nernst equation [32,34].

In the classical form, the Poisson–Boltzmann equation is obtained from the Poisson equation assuming that the mobile charges follow a Boltzmann distribution in the mean field approximation. This distribution is affected by the electrostatic potential ψ and the temperature, following the Gouy–Chapman approach to describe the electrical double layer.

The Poisson–Boltzmann equation with the presence of fixed charges can be written as:

$$\epsilon_0 \frac{\mathrm{d}}{\mathrm{d}x}\left(\epsilon \frac{\mathrm{d}\psi(x)}{\mathrm{d}x}\right) = -e\sum_i z_i c_{i,\infty} \exp\left(\frac{-ez_i\psi(x)}{k_B T}\right) - \rho_f \tag{2}$$

where ϵ_0 is the permittivity of vacuum, ϵ is the dielectric constant of the environment, ψ is the electrostatic potential, $c_{i,\infty}$ is the concentration of ion i (number of ions per unit volume) at an infinitely large distance from the interface (in the bulk solution, $\psi_\infty = 0$), e is the elementary charge, z_i is the valence of ion i, k_B is the Boltzmann constant, T is the absolute temperature of the system, and ρ_f is the volume density of fixed charge.

The boundary conditions usually associated with Eq. (2) can be of two types: Dirichlet boundary condition (potential specified at the boundary) or Neumann boundary condition (derivative of the potential specified at the boundary). In this work, we applied Neumann boundary conditions, by specifying the surface charge density at $x \to \infty$ and $x \to -\infty$ being equal to 0, according to Eqs. (3) and (4).

$$\left.\frac{\mathrm{d}\psi(x)}{\mathrm{d}x}\right|_{x\to\infty} = 0 \tag{3}$$

$$\left.\frac{\mathrm{d}\psi(x)}{\mathrm{d}x}\right|_{x\to-\infty} = 0 \tag{4}$$

It is noteworthy that in the Mauro's model [32], the boundary conditions are equal to Eqs. (3) and (4) together with other two conditions: $\psi(x)|_{x\to 0_-} = \psi(x)|_{x\to 0_+}$ and $\nabla\psi(x)|_{x\to 0_-} = \nabla\psi(x)|_{x\to 0_+}$. The interface is at $x = 0$. Ohshima and Ohki used a similar approach considering a planar charged membrane in equilibrium with a large volume of a symmetrical electrolyte solution [29]. Another way [35,36] is using the Dirichlet boundary condition when $x \to \infty$ (considering the solution located on the right side from the interface without polyelectrolytes), the Neumann boundary condition when $x \to -\infty$ (considering the solution located on the left side from the interface with polyelectrolytes), and the continuity conditions for and $\nabla\psi(x)$ and $\psi(x)$. This approach assumes that the electric potential far inside the phase with fixed charge remains constant at the Donnan potential, independent of the membrane separation. This is equivalent to the condition of electroneutrality in the bulk phase inside the membrane [36–39].

Thus, the strategies often found in literature consist of solving the Poisson–Boltzmann equation for each side of the interface with boundary conditions that ensure the continuity of the electrostatic potential between the two phases. In this work, instead of solving the Poisson–Boltzmann equation twice (one for each side of the interface), we propose the use of a smoothing function to describe the fixed volume charge density profile.

Smoothing functions – also known as regularization functions – are used to join two different functions of the same independent variable. This methodology is important when we use the Poisson–Boltzmann equation for two environments simultaneously, in which we can obtain different responses for each compartment. The smoothing function is used to generate a continuous function over the entire range of the spatial variable [40].

Considering two generic functions $g(x)$ and $h(x)$, such that:

$$f(x) = \begin{cases} g(x), & \text{for} \quad x \le x^* \\ h(x), & \text{for} \quad x > x^* \end{cases} \tag{5}$$

the goal is to convert the discontinuous function $f(x)$ into a continuous function. In order to reconcile the two solutions and turn the function into a continuous function $F(x)$, we used a hyperbolic tangent function as follows:

$$F(x, \eta) = \nu(x, \eta)h(x) + [1 - \nu(x, \eta)]g(x) \tag{6}$$

where:

$$\nu(x, \eta) = \frac{1 + \tanh\left(\frac{x - x^*}{\eta}\right)}{2} \tag{7}$$

The parameter η is related to the smoothness of the curve. High values of η generate smoother curves, while low values generate steep curves. We used a value equal to 0.1 for η. This is the greatest value that generates a steep curve without affecting the electro-

static profile calculated, in other words lower values of parameter η produce the same fixed volume charge density profile.

Other smoothing functions could be used. The choice of a hyperbolic tangent function was due to the generality in the treatment of several discontinuous functions. A key feature for choosing a hyperbolic tangent function was the following property:

$$\nu(x,\eta) \cong \begin{cases} 0 & \text{for } x < x^* \\ 1 & \text{for } x \geq x^* \end{cases} \quad (8)$$

For numerical convenience, we write Eq. (2) in the dimensionless form as:

$$\frac{d}{d\chi}\left(\bar{\epsilon}\frac{dy}{d\chi}\right) = -\frac{\sum_i z_i c_{i,\infty} \exp(-z_i y)}{\sum_i z_i^2 c_{i,\infty}} - \bar{\rho}_f \quad (9)$$

where χ is the dimensionless spatial variable, $y = e\psi/k_B T$ is the dimensionless electrostatic potential, $\bar{\epsilon}$ is the normalized dielectric constant, that is equal to $\bar{\epsilon} = \epsilon/\epsilon_W$, ϵ_W is the dielectric constant of water at the system's temperature, and $\bar{\rho}_f$ is the dimensionless fixed volume charge density:

$$\bar{\rho}_f = \frac{\rho_f}{e\sum_i z_i^2 c_{i,\infty}} \quad (10)$$

In Eq. (9), spatial variables x from Eq. (2) are scaled by the Debye length κ^{-1}:

$$\chi = \kappa x \quad (11)$$

where:

$$\kappa^2 = \frac{e^2 \sum_i c_{i,\infty} z_i^2}{\epsilon_W \epsilon_0 k_B T} \quad (12)$$

The Poisson–Boltzmann equation was solved in its dimensionless form (Eq. (9)) by a second order spline finite elements method in a steady one-dimensional Cartesian coordinate system. This method consists in the division of the domain, which defines the problem that we want to model into smaller subdomains. In each of these subdivisions, the dependent variables involved in the problem are approximated by interpolating its values fixed in the boundaries of the subdomain. Thus, the discretization of the differential equation results in algebraic equations whose unknowns are the values of these variables on the boundary of various subdivisions (nodes of the finite elements) [41]. The nonlinear term of Poisson–Boltzmann equation was linearized around the previous iteration value of y at the collocation point of the finite element. Thus, the solution should be iterative, i.e., the linearized equations are solved at each iteration and, therefore, the solution of the nonlinear equations are obtained after the convergence of consecutive iterations. It is noteworthy that the linear system obtained is a sparse system. The method used to solve the linear algebraic system is a generalized Thomas method for solving heptadiagonal systems.

Currently in the literature, besides the boundary conditions mentioned above [29,32,35–39], it is common the use of semi analytical methods, in which the Poisson-Boltzmann equation is integrated once, and subsequently, numerical methods are used to find the solution [32,42]. However, these methods are not general methods, i.e., they are applicable to differential equations similar to Poisson-Boltzmann equation with only diffusive and source terms. Our idea in this work was to use a method that can be applied to every differential equation, focusing on systems with two regions with different properties.

2.1. Charged-regulated volume charge density in bacterial wall

The charge of the bacterial cell wall originates from the dissociation or protonation of carboxyl, phosphoryl, hydroxyl, and amino groups and consequently depends on pH. We consider the cell wall as a fixed polyelectrolytes layer in which charges vary as a function of the ionization of the functional groups.

Considering both acidic and basic sites on the cell wall, the volume charge density of fixed sites ρ_f is controlled by the following dissociation equilibria [12,13]:

$$R_{aj}H \leftrightarrow R_{aj}^- + H^+ \quad (13)$$

$$R_{bm}H^+ \leftrightarrow R_{bm} + H^+ \quad (14)$$

where R_{aj} is the acidic ionizable site of type j which can be represented by phosphoryl, carboxyl and hydroxyl groups, and R_{bm} is the basic ionizable site of type m, represented by the amine group.

The dissociation constants of each functional group (K_{aj} and K_{bm}) can be expressed as [42,43]:

$$K_{aj} = \frac{c_{R_{aj}^-} c_{H^+}}{c_{R_{aj}H}} \quad (15)$$

$$K_{bm} = \frac{c_{R_{bm}} c_{H^+}}{c_{R_{bm}H^+}} \quad (16)$$

The concentration of H^+ can be expressed by the Boltzmann distribution as:

$$c_{H^+} = c_{H^+,\infty} \exp\left(\frac{-e z_{H^+}\psi}{k_B T}\right) \quad (17)$$

According to the general notion, cations display a less important specific ion effect on biological surfaces than anions. Many studies have shown that the binding constants of monovalent ions onto biological surfaces are negligible [44–46]. Although we have not considered the specific cation effect, it is important to highlight that Medda et al. [47] have investigated the cation specific effects on the aggregation of hemoglobin at low and physiological salt concentration in the pH range 4.5–9.5. An anomalous cation effect, attributed to kosmotropic cation binding to carboxylate groups, has been observed at pH approximately equal to 7.1 [47].

N_{aj} and N_{bm} are defined as the number of acidic sites of type j and basic sites of type m per unit of volume, respectively:

$$N_{aj} = c_{R_{aj}^-} + c_{R_{aj}H} \quad (18)$$

$$N_{bm} = c_{R_{bm}} + c_{R_{bm}H^+} \quad (19)$$

We assumed that the sites are uniformly distributed in the wall (i.e., number of acidic sites of type j and basic sites of type m per unit of volume are constant inside the bacteria cell wall).

To express the change of $N_{aj}(x)$ and $N_{bm}(x)$ between the cell wall and the surrounding electrolyte solution, we used a smoothing function, in order to ensure continuity and to eliminate possible numerical problems.

The volume charge density of fixed sites is proportional to the number of positively charge sites minus the total number of negatively charged sites [19]:

$$\frac{\rho_f(x)}{e} = [1 - \nu(x)]\left[\sum_m c_{R_{bm}H^+}(x) - \sum_j c_{R_{aj}^-}(x)\right] \quad (20)$$

From Eqs. (15)–(19), we can write Eq. (20) as:

$$\frac{\rho_f(x)}{e} = [1 - \nu(x)]\left[\sum_m \frac{10^{-pH_\infty} N_{bm}(x)}{10^{-pH_\infty} + K_{bm}\exp\left(\frac{e z_{H^+}\psi(x)}{k_B T}\right)} - \sum_j \frac{K_{aj} N_{aj}(x)}{K_{aj} + 10^{-pH_\infty}\exp\left(\frac{-e z_{H^+}\psi(x)}{k_B T}\right)}\right] \quad (21)$$

where 10^{-pH_∞} is equal to the concentration of H^+ at an infinitely large distance from the interface (in the bulk solution, $\psi_\infty = 0$).

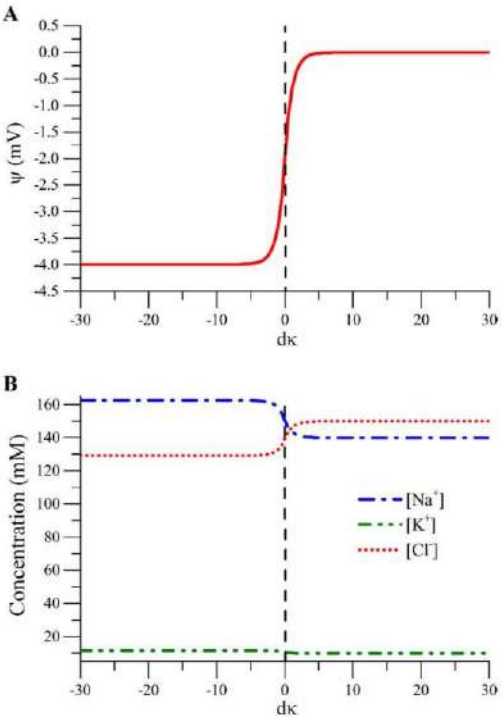

Fig. 1. Electric potential profile (A) and ionic concentration profile (B) near a selectively permeable membrane. The dashed black line refers to the membrane localization. In protein compartment, the concentrations of protein is 45 mEq/L, and the bulk concentration in non-protein compartment are 140 mM NaCl and 10 mM KCl. $d\kappa$ is the dimensionless distance from the membrane.

3. Results and discussion

The classical one-dimensional Poisson–Boltzmann equation in Cartesian coordinates in the presence of fixed charges was solved in order to compare its results with those obtained by the Donnan equilibrium calculations and to evaluate the use of a smoothing function to describe the volume density of fixed charge.

The system being modeled consists of two compartments with an aqueous electrolyte solution containing NaCl and KCl at 310.15 K, separated by a selectively permeable membrane. The dielectric constant of the medium was considered equal to 74.16. In addition, the semipermeable membrane had no charge. In one compartment separated by the permeable selective membrane, there was negative net charge of protein equal to -4.34 MCm^{-3} (equivalent concentration of 45 mEq) in the bulk solution. The concentrations of Na^+, K^+ and Cl^- in the bulk solution of non-protein compartment are equal to 140 mM, 10 mM and 150 mM, respectively.

According to the principle of electroneutrality and the laws of thermodynamics, the concentrations of Na^+, K^+ and Cl^- in the bulk solution of the protein compartment are equal to 162.57 mM, 11.61 mM and 129.18 mM, respectively. The Donnan potential between the two compartments separated by the membrane calculated from the Nernst equation is equal to -3.99 mV.

Using Poisson–Boltzmann equation, we obtained a potential difference between the bulk solutions of the compartments equal to that predicted by the Donnan potential (Fig. 1A); the same happened to the concentrations of Na^+, K^+ and Cl^- in the bulk solution of protein compartment (Fig. 1B).

Thus, it is possible to observe that the Donnan potential arises automatically from the solution of only one Poisson–Boltzmann equation and it is not necessary to impose this potential for treating charged system in the presence of membrane when we use the smoothing function.

Table 1
Dissociation constants and site concentrations for the cell surface of *B. brevis*.

	Ac_1[a]	Ac_2[a]	Ac_3[a]	Ac_4[a,b]	B[a,b]
Dissociation Constant (pK)[c]	3.81	5.31	7.01	9.81	9.81
Site concentrations (10^{-4} mol/g)	3.77	1.53	2.19	1.14	2.36
Site concentrations (10^2 mol/m^3)	2.94	1.19	1.71	0.89	1.84

[a] Ac_i refers to acidic site *i* and *B* refers to basic site.
[b] $N_{o4}+N_b = N_4$ and $pK_{a4} = pK_b = pK_4$, where N_4 is the overall site concentrations for the fourth pK value given in Hong and Brown [25]. N_{o4} and N_b were calculated through the isoelectric point.
[c] Data from Hong and Brown [25].

3.1. Smoothing function to describe the charge-regulated volume charge density in bacterial system

In order to obtain the electrostatic potential profile for *Bacillus brevis* (a gram-positive bacteria), we use the data from Hong and Brown's study [25]. These authors demonstrated the presence of four pK_a values of 3.81, 5.81, 7.01 and 9.81 with corresponding site concentrations of 3.77, 1.53, 2.19 and 3.50×10^{-4} mol/g (Table 1), respectively for the bacterial cultures grown in a minimal media consisted of 5.44 g KH_2PO_4 and 0.6 mL of salt solution (10.0 g/L $MgSO_4 \cdot 7H_2O$, 0.1 g/L $CaCl_2 \cdot 2H_2O$, 0.4 g/L $FeSO_4 \cdot 7H_2O$, and 1.0 g/L $MnCl_2 \cdot 2H_2O$) in 1 L of water with the addition of 2.0 g glucose and 0.5 g NH_4Cl.

The first three pK values are associated with functional groups that can be negatively charged, the fourth pK value is associated with functional groups that can be either negatively charged (hydroxyl) or positively charged (amine). On the basis of the isoelectric point of *B.brevis*, approximately 4.0 [4], it was possible to estimate the concentration of hydroxyl and amine groups.

We assumed that the site numbers are uniformly smeared out over the cell wall with thickness of 75 nm for *B. brevis* [2]. Cell wall thickness was used to estimate the cell wall volume together with the cell dimensions (1.60±0.31 μm length and 0.60±0.05 μm width [4]). To calculate the site concentration in mol per m^3 (Table 1), we used the cell wall volume and the ratio of cell numbers to dry mass (4.0×10^{12} cell/g for *B. brevis* [4]).

The Poisson–Boltzmann equation (Eq. (9)) together with volume charge density function of fixed sites (Eq. (21)) and boundary conditions (Eqs. (3) and (4)) were solved using a second order spline finite elements method in a steady one-dimensional Cartesian coordinate system for various bulk pH values. In Fig. 2, we can observe the electrostatic potential as a function of distance from the cell surface. At

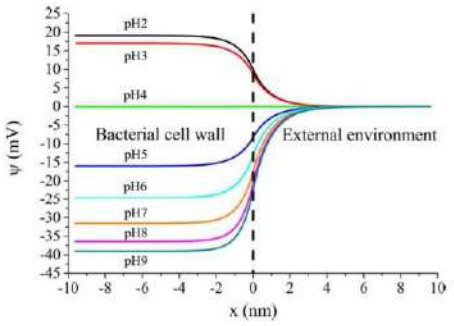

Fig. 2. Electrostatic potential as a function of the distance from the cell surface ($x = 0$) for *B. brevis* at bulk pH ranging from 2.0 to 9.0 (indicated as pH2 to pH9) and bulk NaCl concentration of 0.1 M.

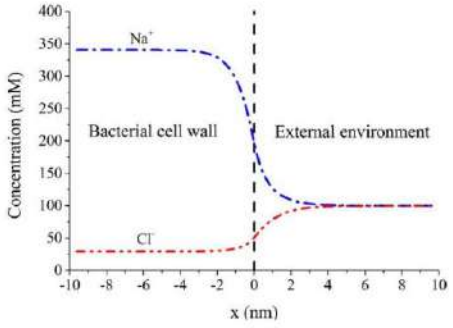

Fig. 3. Ionic concentration as a function of distance from the cell surface ($x = 0$) for *B. brevis* at bulk pH 7.0 and bulk NaCl concentration of 0.1 M.

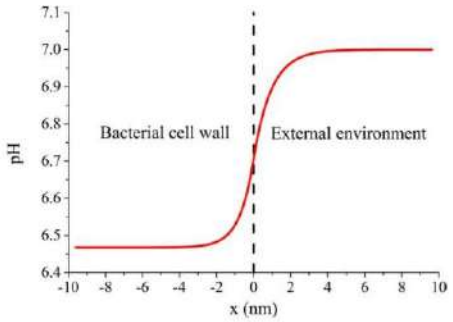

Fig. 4. Local pH as a function of distance from the cell surface ($x = 0$) for *B. brevis* at bulk pH 7.0 and bulk NaCl concentration of 0.1 M.

pH values lower than the isoelectric point (IEP), the potential inside the cell wall is positive. On the other hand, at pH values greater than IEP, the potential is negative inside cell wall. Because the thickness of bacterial wall is much greater than the Debye length $1/\kappa$, the potential deep inside the surface layer becomes the Donnan potential [35].

A similar study has been carried out by Wasserman and Felmy [48]. These authors analyzed the electrostatic potential profile for some bacteria and the theoretical impact of trace amounts of divalent and trivalent cations at very low concentrations (10^{-6}M) in the electrostatic profile. To obtain the electrostatic profile, they solved Poisson–Boltzmann equation (without considering the fixed charge of cell wall as a function of the ionization of the functional groups) for the membrane and solution, using continuity conditions in the boundary of the two environments (membrane and surrounding electrolyte solution) [48].

Hong and Brown proposed the location of all sites on the surface of the cell and found the effective site numbers by an iterative method: the real density of the acid/base groups has been uniformly reduced until the surface potential was equal to zeta potential [4].

The ionic concentration profiles at bulk pH 7.0 and bulk NaCl concentration of 0.1 M are shown in Fig. 3. Due to the negative net charge of the cell wall at this pH, we can observe a greater concentration of Na^+ than Cl^- within the layer. Fig. 4 presents a similar behavior, with pH inside cell wall smaller than in the bulk solution.

The potential at the surface of shear between the charged surface and the electrolyte solution is known as zeta potential (ζ). The shear plane is characterized by being a region of rapidly changing viscosity [49]. Considering the average size of ions and molecules we defined the shear plate at a distance of 0.4 nm from the interface. Based on this data, we compared the zeta potential estimated by Smoluchowski equation according to experimental electrophoretic

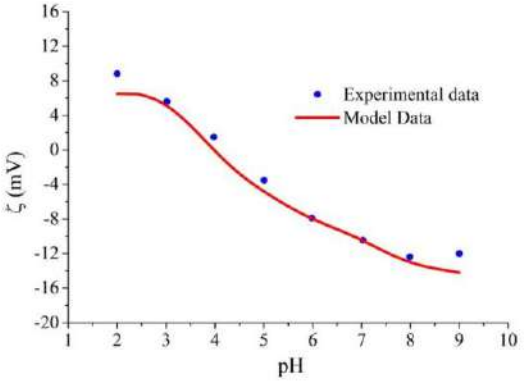

Fig. 5. Zeta Potential of *B. brevis* as a function of bulk pH ranging from 2.0 to 9.0 and bulk NaCl concentration of 0.1 M. Circles are data from Hong and Brown [4] and line refers to the model.

mobility data [4] with the electrostatic potential at the distance 0.4 nm from the interface calculated here. Fig. 5 shows that our calculations are in good agreement with experimental data for ζ potential as a function of pH (ranging from 2.0 to 9.0).

4. Conclusions

On the basis of these results, we conclude that the Poisson–Boltzmann equation with the inclusion of fixed charge using a smoothing function can be a useful tool to analyze potential and ionic concentrations in systems where the Donnan potential is present. Using this strategy, the Donnan potential automatically arises from the resolution of the Poisson–Boltzmann equation simultaneously from both sides of the interface.

The potential profile across the *Bacillus brevis* wall considering the ionization of the cell wall functional groups as a function of solution pH has been analyzed. Using data from potentiometric titration, we can predict *zeta* potential of *Bacillus brevis* wall for various pH values in agreement with experimental data.

Acknowledgments

For financial support, we are grateful to the Brazilian Agencies, Coordenação de Aperfeiçoamento de Pessoal de Nível Superior (CAPES), Fundação Carlos Chagas Filho de Amparo à Pesquisa do Estado do Rio de Janeiro (FAPERJ) and Conselho Nacional de Desenvolvimento Científico e Tecnológico (CNPq).

References

[1] E. Dziubakiewicz, K. Hrynkiewicz, M. Walczyk, B. Buszewski, Colloids Surf. B. Biointerfaces 104 (2013) 122–127, http://dx.doi.org/10.1016/j.colsurfb.2012.11.018
[2] A. van der Wal, M. Minor, W. Norde, A.J.B. Zehnder, J. Lyklema, Langmuir 13 (1997) 165–171, http://dx.doi.org/10.1021/la960386k
[3] A.G. González, L.S. Shirokova, O.S. Pokrovsky, E.E. Emnova, R.E. Martínez, J.M. Santana-Casiano, M. González-Davila, G.S. Pokrovski, J. Colloid Interface Sci. 350 (2010) 305–314, http://dx.doi.org/10.1016/j.jcis.2010.06.020
[4] Y. Hong, D.G. Brown, Langmuir 24 (2008) 5003–5009, http://dx.doi.org/10.1021/la703564q
[5] P.-G. Burnett, H. Heinrich, D. Peak, P.J. Bremer, A.J. McQuillan, C.J. Daughney, Geochim. Cosmochim. Acta 70 (2006) 1914–1927, http://dx.doi.org/10.1016/j.gca.2006.01.009
[6] R.E. Martinez, O.S. Pokrovsky, J. Schott, E.H. Oelkers, J. Colloid Interface Sci. 323 (2008) 317–325, http://dx.doi.org/10.1016/j.jcis.2008.04.041
[7] X. Sheng, Y.P. Ting, S.O. Pehkonen, J. Colloid Interface Sci. 321 (2008) 256–264, http://dx.doi.org/10.1016/j.jcis.2008.02.038
[8] W. Zhao, S.L. Walker, Q. Huang, P. Cai, Water Res. 53 (2014) 35–46, http://dx.doi.org/10.1016/j.watres.2014.01.009

[9] H.H.M. Rijnaarts, W. Norde, J. Lyklema, A.J.B. Zehnder, Colloids Surf. B Biointerfaces 14 (1999) 179–195, http://dx.doi.org/10.1016/S0927-7765(99)00035-1
[10] M. Ramstedt, L. Leone, P. Persson, A. Shchukarev, Langmuir 30 (2014) 4367–4374, http://dx.doi.org/10.1021/la5002573
[11] C.J. Daughney, J.B. Fein, J. Colloid Interface Sci. 198 (1998) 53–77, http://dx.doi.org/10.1006/jcis.1997.5266
[12] N. Yee, J. Fein, Geochim. Cosmochim. Acta 65 (2001) 2037–2042, http://dx.doi.org/10.1016/S0016-7037(01)00587-7
[13] J.B. Fein, C.J. Daughney, N. Yee, T.A. Davis, Geochim Cosmochim. Acta 61 (1997) 3319–3328, http://dx.doi.org/10.1016/S0016-7037(97)00166-X
[14] D.D. Fowle, J.B. Fein, Geochim. Cosmochim. Acta 63 (1999) 3059–3067, http://dx.doi.org/10.1016/S0016-7037(99)00233-1
[15] D. Borrok, J. Fein, M. Tischler, E. O'loughlin, H. Meyer, M. Liss, K.M. Kemner, Chem. Geol. 209 (2004) 107–119, http://dx.doi.org/10.1016/j.chemgeo.2004.04.025
[16] B.T. Ngwenya, I.W. Sutherland, L. Kennedy, Appl Geochemistry. 18 (2003) 527–538, http://dx.doi.org/10.1016/S0883-2927(02)00118-X
[17] T.J. Beveridge, R.G. Murray, J. Bacteriol. 141 (1980) 876–887.
[18] A.G. González, O.S. Pokrovsky, F. Jiménez-Villacorta, L.S. Shirokova, J.M. Santana-Casiano, M. González-Davila, E.E. Emnova, Chem. Geol. 372 (2014) 32–45, http://dx.doi.org/10.1016/j.chemgeo.2014.02.013
[19] A.T. Poortinga, R. Bos, W. Norde, H.J. Busscher, Surf. Sci. Rep. 47 (2002) 1–32, http://dx.doi.org/10.1016/S0167-5729(02)00032-8
[20] S. Bayoudh, A. Othmane, L. Mora, H. Ben Ouada, Colloids Surf. B. Biointerfaces 73 (2009) 1–9, http://dx.doi.org/10.1016/j.colsurfb.2009.04.030
[21] J. Azeredo, J. Visser, R. Oliveira, Colloids Surfaces B Biointerfaces 14 (1999) 141–148, http://dx.doi.org/10.1016/S0927-7765(99)00031-4
[22] G. Hwang, I.-S. Ahn, B.J. Mhin, J.-Y. Kim, Colloids Surf. B. Biointerfaces 97 (2012) 138–144, http://dx.doi.org/10.1016/j.colsurfb.2012.04.031
[23] S. Tsuneda, H. Aikawa, H. Hayashi, A. Yuasa, A. Hirata, FEMS Microbiol. Lett. 223 (2003) 287–292, http://dx.doi.org/10.1016/S0378-1097(03)00399-9
[24] J. Ubbink, P. Schär-Zammaretti, Curr. Opin. Colloid Interface Sci. 12 (2007) 263–270, http://dx.doi.org/10.1016/j.cocis.2007.08.004
[25] Y. Hong, D.G. Brown, Colloids Surf. B. Biointerfaces 50 (2006) 112–119, http://dx.doi.org/10.1016/j.colsurfb.2006.05.001
[26] M. Dittrich, S. Sibler, J. Colloid Interface Sci. 286 (2005) 487–495, http://dx.doi.org/10.1016/j.jcis.2005.01.029
[27] R.E. Martinez, D.S. Smith, E. Kulczycki, F.G. Ferris, J. Colloid Interface Sci. 253 (2002) 130–139, http://dx.doi.org/10.1006/jcis.2002.8541
[28] A. van der Wal, W. Norde, A.J.B. Zehnder, J. Lyklema, Colloids Surfaces B Biointerfaces. 9 (1997) 81–100, http://dx.doi.org/10.1016/S0927-7765(96)01340-9
[29] H. Ohshima, S. Ohki, Biophys. J. 47 (1985) 673–678, http://dx.doi.org/10.1016/S0006-3495(85)83963-1
[30] J.H.A.M. Wonders, H.P. Van Leeuwen, J. Lyklema, Colloids Surfaces A Physicochem. Eng. Asp. 120 (1997) 221–233, http://dx.doi.org/10.1016/S0927-7757(96)03680-1
[31] P. Krysinski, H. Ti Tien, Prog. Surf. Sci. 23 (1986) 317–412.
[32] A. Mauro, Biophys. J. 2 (1962) 179–198, http://dx.doi.org/10.1016/S0006-3495(62)86848-9
[33] J.M. Prausnitz, R.N. Lichtenthaler, E.G. Azevedo, Molecular Thermodynamics of Fluid-phase Equilibria, 3rd ed., Prentice Hall, Upper Saddle River, 1999.
[34] R. Chein, H. Chen, C. Liao, J. Membr. Sci. 342 (2009) 121–130, http://dx.doi.org/10.1016/j.memsci.2009.06.033
[35] H. Ohshima, J. Colloid Interface Sci. 323 (2008) 313–316, http://dx.doi.org/10.1016/j.jcis.2008.04.027
[36] H. Ohshima, Double layer interaction between soft particles, in: H. Ohshima (Ed.), Theory of Colloid and Interfacial Electric Phenomena, Elsevier, London, 2006, pp. 390–408.
[37] H. Ohshima, T. Kondo, J. Theor. Biol. 128 (1987) 187–194, http://dx.doi.org/10.1016/S0022-5193(87)80168-6
[38] J.F.L. Duval, Langmuir 21 (2005) 3247–3258, http://dx.doi.org/10.1021/la040108i
[39] H. Ohshima, T. Kondo, J. Colloid Interface Sci. 123 (1988) 136–142, http://dx.doi.org/10.1016/0021-9797(88)90 230-5
[40] T.C. Freitas, T.C. Quinto, A.R. Secchi, E.C. Biscaia, An Efficient adjoint-free dynamic optimization methodology for batch processing using Pontryagin's formulation, in: I.D.L. Bogle, M. Fairweather (Eds.), 22nd Eur. Symp. Comput. Aided Process Eng, Elsevier, Amsterdam, 2012, pp. 1297–1301.
[41] G. Dhatt, G. Touzot, E. Lefrançois, Finite Element Method, John Wiley & Sons, Inc., Hoboken, 2012.
[42] E. Wasserman, A.R. Felmy, Appl. Environ. Microbiol. 64 (1998) 2295–2300.
[43] S. Dunham-Cheatham, B. Farrell, B. Mishra, S. Myneni, J.B. Fein, Chem. Geol. 373 (2014) 106–114, http://dx.doi.org/10.1016/j.chemgeo.2014.02.030
[44] Y.-I. Chang, J.-P. Hsu, Colloids Surfaces A Physicochem. Eng. Asp 96 (1995) 155–163, http://dx.doi.org/10.1016/0927-7757(94)03050-A
[45] S. Ohki, H. Ohshima, Colloids Surfaces B Biointerfaces 5 (1996) 307–317, http://dx.doi.org/10.1016/0927-7757(96)03538-8
[46] J.A. Cohen, M. Cohen, Biophys. J. 36 (1981) 623–651, http://dx.doi.org/10.1016/S0006-3495(81)84756-X
[47] D. Huster, K. Arnold, K. Gawrisch, Biophys. J. 78 (2000) 3011–3018, http://dx.doi.org/10.1016/S0006-3495(00)76839-1
[48] L. Medda, C. Carucci, D.F. Parsons, B.W. Ninham, M. Monduzzi, A. Salis, Langmuir 29 (2013) 15350–15358, http://dx.doi.org/10.1021/la404249n
[49] D.J. Shaw, Introduction to Colloid & Surface Chemistry, 4th ed., Butterworth-Heinemann, Oxford, 2000.

APPENDIX G – Membrane potential and ion partitioning in an erythrocyte using the Poisson–Boltzmann equation

BARBOSA, N. S. V. *et al.* Membrane potential and ion partitioning in an erythrocyte using the Poisson–Boltzmann equation. *J. Phys. Chem. B*, v. 119, n. 21, p. 6379–6388, 2015. doi: 10.1021/acs.jpcb.5b02215

THE JOURNAL OF PHYSICAL CHEMISTRY B

Article

pubs.acs.org/JPCB

Membrane Potential and Ion Partitioning in an Erythrocyte Using the Poisson−Boltzmann Equation

Nathalia S. V. Barbosa,[†] Eduardo R. A. Lima,[†] Mathias Boström,[‡] and Frederico W. Tavares*[,§,∥]

[†]Programa de Pós-graduação em Engenharia Química, Universidade do Estado do Rio de Janeiro, 20550-013, Rio de Janeiro, Brazil

[‡]Centre for Materials Science and Nanotechnology, University of Oslo, P.O. Box 1048, Blindern, NO-0316 Oslo, Norway

[§]Escola de Química, Universidade Federal do Rio de Janeiro, 21945-970, Rio de Janeiro, Brazil

[∥]Programa de Engenharia Química, COPPE, Universidade Federal do Rio de Janeiro, 21945-970, Rio de Janeiro, Brazil

ABSTRACT: In virtually all mammal cells, we can observe a much higher concentration of potassium ions inside the cell and vice versa for sodium ions. Classical theories ignore the specific ion effects and the difference in the thermodynamic reference states between intracellular and extracellular environments. Usually, this differential ion partitioning across a cell membrane is attributed exclusively to the active ion transport. Our aim is to investigate how much the dispersion forces contribute to active ion pumps in an erythrocyte (red blood cell) as well as the correction of chemical potential reference states between intracellular and extracellular environments. The ionic partition and the membrane potential in an erythrocyte are analyzed by the modified Poisson−Boltzmann equation, considering nonelectrostatic interactions between ions and macromolecules. Results show that the nonelectrostatic potential calculated by Lifshitz theory has only a small influence with respect to the high concentration of K^+ in the intracellular environment in comparison with Na^+.

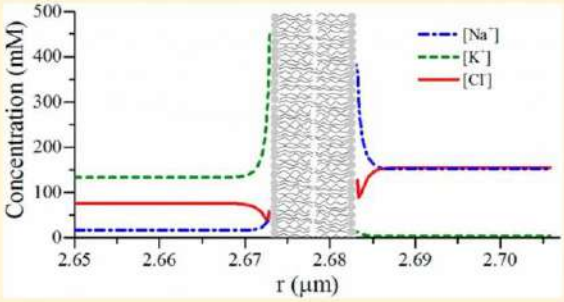

1. INTRODUCTION

Membranes define the external boundaries of biological cells and regulate the molecular transport across these boundaries. Membranes are selectively permeable; i.e., they retain certain compounds and ions within cells while excluding others.[1,2]

The ionic composition of cytosol (intracellular fluid) usually differs greatly from that of the extracellular environment (Table 1). In virtually all cells, the cytosolic concentration of K^+ is much higher than that of Na^+ (the concentration of K^+ is about 30 times higher in cells than in the blood, while the concentration of Na^+ is 10 times lower in cells than in the blood).[1,3]

Table 1. Comparison of Ion Concentrations inside and outside a Typical Mammalian Cell

ion	intracellular concentration[a] (mM)	extracellular concentration[a] (mM)
Na^+	5−15	145
K^+	140	5
Mg^{2+}	0.5	1−2
Ca^{2+}	10^{-4}	1−2
H^+	7×10^{-5} (pH 7.2)	4×10^{-5} (pH 7.4)
Cl^-	5−15	110

[a]From Alberts et al.[2] The cell must contain equal quantities of positive and negative charges. Thus, in addition to Cl^-, the cell contains many other anions like HCO_3^-, PO_4^{3-}, proteins, nucleic acid, etc.

A central issue in molecular biology is that membranes are not merely passive barriers. They include an array of proteins specialized in moving specific organic solutes and inorganic ions across the membrane. In this way, according to the biological literature, ion gradients across membranes are established due to the activity of these specialized membrane proteins. Thus, there is a balance between active and passive transport processes.[1,4] In this context, an active ion transporter stands out: Na^+K^+ATPase. This transporter couples phosphorylation−dephosphorylation of an amino acid residue to simultaneous movement of two K^+ ions inward and three Na^+ ions outward across the plasma membrane (the ions are moved against their electrochemical gradients).[3,5] The transmembrane potential that is characteristic of most cells is assigned to the Na^+K^+ATPase, once it is an electrogenic transporter, i.e., it creates a net separation of charge across the membrane.[1,3,4]

In the classical theories of physical chemistry of electrolytes, ionic interactions are attributed to electrostatic forces alone, whether among ions or between ions and biomolecules.[6] Therefore, the specific ion or Hofmeister effects are not accounted for by these theories.[7−9] Specific ion effects occur in bulk solutions and at interfaces. In biological systems,

Received: March 6, 2015
Revised: May 1, 2015
Published: May 5, 2015

DOI: 10.1021/acs.jpcb.5b02215
J. Phys. Chem. B 2015, 119, 6379−6388

Hofmeister effects are ubiquitous due to the presence of electrolytes and biomolecules in aqueous systems. According to Lo Nostro and Ninham,[9] the concentration at which specific ion effects occur is typically around or above that of physiological solutions.

The specific ion effect has been observed in water dispersions of short chain phospholipids (dioctanoyl-phosphatidylcholine).[10] In this system, an asymmetric distribution of the anions occurs in a finite volume that contains the two phases in equilibrium due to different ion adsorption at the micellar interface. This effect depends on the nature of the electrolyte. Boström et al.[6] studied the same system in order to show theoretically how different anions accumulate in a specific way in the micellar phase. They showed that anions with higher polarizability accumulate in a much higher degree in the phase with phospholipid micelles than anions with lower polarizability. This effect can be quantified taking into account the nonelectrostatic ion binding to micelle surfaces. The same mechanism can be expected to operate in any system of lipids, proteins, or polymers, compartmentalized by a membrane or segregated by equilibrium phase separation due to ion-specific nonelectrostatic (NES) forces.[6]

The partitioning of electrolytes has also been studied in a more realistic biological experiment:[8] several sodium salts were used to analyze the asymmetric partitioning of ions between two equilibrium phases of a surfactant/protein complex (sodium dodecyl sulfate/lysozyme). A reversed Hofmeister series was observed which suggested the importance of specific ion−protein dispersion interactions. Once the two phases are separated, the protein rich phase can either accumulate or exclude most of the present ions, depending on the electrolyte.[8]

These observations indicate that specific ion binding can occur in any finite volume that comprehends two phases in equilibrium, containing different concentrations of lipids, proteins, or polymers. In this way, the specific ion effects can play an important role in ion partitioning that occurs in biological cells; once within the cell, there is a higher protein concentration than in the extracellular environment. A good example of this situation occurs in human erythrocytes.

Human erythrocytes (also denominated red blood cells) are cells responsible for carrying nearly all the oxygen required by the cells from the lungs to the tissues.[1] They are anucleate cells with biconcave discoidal shape in their mature form, free of intracellular organelles. Due to the lack of a nucleus and other organelles, they are considered classic model systems for studying how ions and other compounds in solution go through the plasma membrane.[11]

The cytoplasm of erythrocytes comprises nearly close-packed hemoglobin.[7,11] The distance between the surfaces of neighboring proteins averages only about 20 Å.[12] The hemoglobin is one of the most soluble of all proteins and constitutes more than 98% of erythrocyte protein by mass.[11] It is important to highlight also that hemoglobin is a protein of high surface area.[7]

According to molecular biology, the Na^+K^+ATPase is responsible for maintaining low Na^+ and high K^+ concentrations in the cell relative to the extracellular fluid.[1−3] Electrogenic transport, like Na^+K^+ATPase, contributes to the membrane potential that is characteristic of most cells and is essential to the conduction of action potentials in neurons.[1]

The value of the transmembrane potential of human erythrocyte in physiological solution (about −8 to −13.8 mV) has been estimated with different techniques such as microelectrodes,[13,14] fluorescent dyes,[15,16] and measurements of the distribution of chloride ions[11,17,18] and radioactive lipophilic ions.[19]

Considering that both phenomena—active transport by Na^+K^+ATPase and specific ion effects—occur in mammal cells, the aim of this work is to investigate how much the specific ion effects contribute to ion partitioning in erythrocytes. We use Lifshitz theory to quantify the dispersion interactions between ions and macromolecules. In addition, we propose an extra potential that takes into account the energy involved in the difference in chemical potential reference states between the intracellular and extracellular environments and the difference in ion permeability of the erythrocyte membrane and the presence of active transporters at the plasma membrane. To correct the change of the reference state from the intracellular composition to the extracellular environment, we use the Born equation. The system containing an erythrocyte is analyzed using a modified Poisson−Boltzmann theory in Cartesian coordinates.

2. MODELING AND THEORY

In the classical theory, the Poisson−Boltzmann equation takes into account only the electrostatic potential. The inclusion of the dispersion potential between ions and macroparticles in different colloid systems is relevant to explain some phenomena such as adsorption of colloidal particles and surface tension of electrolyte solutions, commonly observed experimentally.[7,20] Aiming at the inclusion of other interactions beyond the electrostatic interactions, we use a modified Poisson−Boltzmann equation[21−23]

$$\varepsilon_0 \nabla\cdot(\varepsilon\nabla\psi) = -e\sum_i z_i c_{i,\infty}\exp\left(-\frac{z_i e\psi + U_i}{k_B T}\right) - \rho_f \tag{1}$$

where ε_0 is the permittivity of the vacuum, ε is the dielectric constant of the medium, $c_{i,\infty}$ is the concentration of ion i (number of ions per unit volume) at an infinitely large distance from the interface (in the bulk solution, $\psi_\infty = 0$), e is the elementary charge, z_i is the charge number of ion i, ψ is the electrostatic potential, k_B is the Boltzmann constant, T is the absolute temperature of the system, ρ_f is the volumetric density of fixed charge, and U_i is the nonelectrostatic energetic contribution of ion i. Nonelectrostatic interactions can be, for example, van der Waals interactions between ion i and the interface and hydration interactions.

The boundary conditions usually associated with eq 1 can be of two types: Dirichlet boundary (potential specified at the boundary) or Neumann boundary (derivative of the potential specified at the boundary). In this work, we apply Neumann boundary conditions, by specifying the surface charge density at $x \to \infty$ and $x \to -\infty$, or $x = x_{surface}$ and $x \to \infty$, or $x \to -\infty$ and $x = x_{surface}$, depending on the system, according to eqs 2 and 3.

$$\left.\frac{d\psi(x)}{dx}\right|_{x\to\pm\infty} = 0 \tag{2}$$

$$\left[\varepsilon\left.\frac{d\psi(x)}{dx}\right|_{interface}\right]\cdot\vec{n} = -\frac{\sigma}{\varepsilon_0} \tag{3}$$

For numerical convenience, we write eq 1 in dimensionless form as

DOI: 10.1021/acs.jpcb.5b02215
J. Phys. Chem. B 2015, 119, 6379−6388

$$\nabla\cdot(\bar{\varepsilon}\nabla y) = -\frac{\sum_i z_i c_{i,\infty} \exp(-z_i y - u_i)}{\sum_i z_i^2 c_{i,\infty}} - \bar{\rho}_f \quad (4)$$

where $y = e\psi/k_B T$ is the dimensionless electrostatic potential; $\bar{\varepsilon}$ is the normalized dielectric constant, that is equal to $\bar{\varepsilon} = \varepsilon/\varepsilon_w$; ε_w is the dielectric constant of water at the system's temperature; $u_i = U_i/k_B T$ are the dimensionless nonelectrostatic potentials; and $\bar{\rho}_f$ is the dimensionless volumetric density of fixed charges.

In eq 4, all spatial variables are scaled by κ^{-1}, the Debye length:

$$\kappa^2 = \frac{e^2 \sum_i c_{i,\infty} z_i^2}{\varepsilon_w \varepsilon_0 k_B T} \quad (5)$$

The Poisson−Boltzmann equation was solved in its dimensionless form (eq 4) by a second order spline finite elements method in a steady one-dimensional Cartesian coordinate system. This method consists of the division of the domain, which defines the problem that we want to model into smaller subdomains. In each of these subdivisions, the dependent variables involved in the problem are approximated by interpolating its values fixed in the boundaries of the subdomain. Thus, the discretization of the differential equation results in algebraic equations whose unknowns are the values of these variables on the boundary of various subdivisions (nodes of the finite elements).[24] The nonlinear term of the Poisson−Boltzmann equation was linearized around the previous iteration value of y at the collocation point of finite element. Thus, the solution should be iterative; i.e., the linearized equations are solved at each iteration and, therefore, the solution of nonlinear equations is obtained after the convergence of consecutive iterations. It is noteworthy that the linear system obtained is a sparse system. The method used to solve the linear algebraic system is a generalized Thomas method for solving heptadiagonal systems.

Considering the equilibrium between the intracellular and extracellular environments, the transmembrane potential between these two compartments is equivalent to the Donnan potential.

The Donnan potential occurs (i) when nonpermeable ions are unequally distributed between two electrolyte solutions separated by a selectively permeable membrane, which allows certain ions to move freely between the two solutions, and (ii) between regions of solution and charged membrane (or charged macromolecules) with a fixed charge interface.[25,26]

In the classical treatment, the Gibbs−Donnan potential is considered to be accompanied by a (discontinuous) potential gap across the membrane surface[27] described by the Nernst equation. Mauro[26] suggested a continuous Donnan potential using the Poisson−Boltzmann equation applied to two regions: one containing fixed charge completely ionized and another one without fixed charge. It is possible to demonstrate that the Donnan potential calculated via the Poisson−Boltzmann equation for remote regions is equal to the difference in potential provided for the Nernst equation.[26,28] In the literature, we can observe two common ways of treating the Donnan potential with the Poisson−Boltzmann equation. One way consists of using Neumann's boundary conditions as in eq 2, together with other conditions: $\psi(x)|_{x\to 0_-} = \psi(x)|_{x\to 0_+}$ and $\nabla\psi(x)|_{x\to 0_-} = \nabla\psi(x)|_{x\to 0_+}$, where the interface is at $x = 0$.[26,27] The other way is using Dirichlet boundary conditions when $x \to -\infty$, Neumann boundary conditions when $x \to \infty$, and the continuity conditions for $\psi(x)$ and $\nabla\psi(x)$.[29,30] The value of the electrostatic potential in $x \to -\infty$ is considered equal to zero.

In this work, the modified Poisson−Boltzmann equation is solved for both environments (intracellular and extracellular) simultaneously, using regularization functions in order to ensure continuity and to eliminate possible numerical problems. These regularization functions were applied to express the volumetric density of fixed charge, the nonelectrostatic energetic contribution of ions, and the dielectric function between intracellular and extracellular environments.

The use of a regularization function to describe volumetric density of fixed charge is a strategy to ensure that the Gibbs−Donnan potential automatically arises from the resolution of the Poisson−Boltzmann equation, solving only one equation for the system.

Regularization functions are used to join two different functions of the same independent variable. This methodology is important when we use the Poisson−Boltzmann equation for two environments simultaneously, in which we can obtain different responses in each compartment. The regularization function is used to generate a continuous function over the entire range of the spatial variable.[31]

We use a hyperbolic tangent function as the regularization function. We consider two generic functions $g(x)$ and $h(x)$, such that

$$f(x) = \begin{cases} g(x), & \text{for } x \le x^* \\ h(x), & \text{for } x > x^* \end{cases} \quad (6)$$

where $f(x)$ is a discontinuous function. In order to reconcile the two solutions and turn the function into a continuous function $F(x)$, we apply the following equation

$$F(x) = \nu(x)h(x) + [1 - \nu(x)]g(x) \quad (7)$$

where

$$\nu(x) = \frac{1 + \tanh\left(\frac{x - x^*}{\eta}\right)}{2} \quad (8)$$

The parameter η is related to the smoothness of the curve. High values of η generate smoother curves, while low values generate stiff curves.

2.1. van der Waals Dispersion. The NES potential corresponds to the van der Waals dispersion interactions obtained from Lifshitz theory.[32] In Cartesian coordinates, the expression used to calculate U_i is[7,32,33]

$$U_i = -\frac{B_i}{x^3}, \quad \text{for } x \ge r_i \quad (9)$$

where x is the perpendicular distance from the center of the ion i to the interface and B_i is the dispersion interaction coefficient of ion i, obtained from Lifshitz theory:

$$\frac{B_i}{k_B T} = \frac{\alpha_i(0)}{4\varepsilon_w(0)}\left[\frac{\varepsilon_m(0) - \varepsilon_w(0)}{\varepsilon_m(0) + \varepsilon_w(0)}\right] + \frac{h}{4\pi k_B T} \int_{\nu_{min}}^{\infty} \frac{\alpha_i(\nu)}{\varepsilon_w(\nu)}\left[\frac{\varepsilon_m(\nu) - \varepsilon_w(\nu)}{\varepsilon_m(\nu) + \varepsilon_w(\nu)}\right] d\nu \quad (10)$$

where $\alpha_i(0)$ and $\alpha_i(\nu)$ are the effective polarizabilities in water of ion i at frequencies 0 and ν, respectively, h is Planck's constant, $\nu_{min} = 2\pi k_B T/h$ is the first nonzero frequency, and

DOI: 10.1021/acs.jpcb.5b02215
J. Phys. Chem. B 2015, 119, 6379−6388

$\varepsilon_j(0)$ and $\varepsilon_j(\nu)$ are the dielectric constants of j at frequencies 0 and ν, respectively. The subscript j can be w for water and m for the macroparticle.

In order to calculate B_j, one needs to know how the effective polarizabilities of ions and the dielectric constants for the macroparticle and the solvent vary with frequency. The polarizability and dielectric constant of a molecule at a frequency ν can be expressed by the harmonic-oscillator model[7,32,33]

$$\alpha(\upsilon) = \frac{\alpha(0)}{1 + (\nu/\nu^{\mathrm{I}})^2} \tag{11}$$

$$\varepsilon(\upsilon) = 1 + \frac{n^2 - 1}{1 + (\nu/\nu^{\mathrm{I}})^2} \tag{12}$$

where n is the refractive index for the sodium D line. The ionization frequency ν^{I} of ions in aqueous solution can be estimated from the free energy of hydration of ions.[32]

2.2. Born Correction Contribution. In situations where two different liquid phases in equilibrium exist in the presence of electrolytes, special attention must be given to reference states. The total environment effect on the transfer of an ion from a finite concentration in one liquid phase to a similar concentration in another phase takes into account two main contributions. One results from a difference in ion−ion interactions in the two solvents, while the other one results from a difference in ion−medium interactions. In implicit models, different environments are characterized mainly by their dielectric response, so both medium effect contributions should largely depend on the dielectric constant. In this way, the Born term correction can be used to capture the effects of ion−medium interactions due to the change in the dielectric constant[34,35]

$$\frac{\Delta G_i^{\mathrm{ex,Born}}}{k_{\mathrm{B}}T} = \frac{e^2 z_i^{\,2}}{8\pi k_{\mathrm{B}} T \varepsilon_0}\left[\frac{1}{\varepsilon_{\mathrm{mix}}} - \frac{1}{\varepsilon_{\mathrm{ref}}}\right]\frac{1}{r_{\mathrm{B},i}} \tag{13}$$

where $\Delta G_i^{\mathrm{ex,Born}}$ is the energy of transfer of an ion i with Born radius $r_{\mathrm{B},i}$ from an environment with dielectric constant $\varepsilon_{\mathrm{ref}}$ to another one with $\varepsilon_{\mathrm{mix}}$. The subscript ref indicates the solution chosen as a reference state.

The Born energy is equivalent to the electrostatic contribution for the solvation energies. This excess free energy is found by discharging a sphere (represented by an ion) in the first environment, transferring this neutral sphere, and then charging up this sphere in the other environment.[36]

Considering the problem studied here, if the extracellular solution is chosen as the reference state, we need to correct the change of the reference state from the intracellular composition to extracellular solution.

2.3. Erythrocyte Model. The main assumptions used in the model proposed to emulate an erythrocyte are the following:

(a) Temperatures are equal to 310.15 K (same temperature in both sides).
(b) Erythrocyte is considered as a sphere with an equivalent radius of 2.673 μm.
(c) The thickness of the plasma membrane plus glycocalyx is equal to 10 nm.
(d) The surface charge density on the outer surface (glycocalyx) is equal to 0.02 C/m^2.[37]
(e) The surface charge density on the inner membrane surface is equal to that of the outer membrane plus glycocalyx; i.e., the asymmetric distribution of lipids and proteins in cell membranes was not considered.
(f) The intracellular dielectric constant is equal to 65.22.[38]
(g) The extracellular dielectric constant is equal to the aqueous dielectric constant at the system's temperature (considering that more than 90% by mass of the blood is water[39]).
(h) The presence of proteins in the blood is neglected.
(i) Only Na^+, K^+, and Cl^- ions are present.
(j) The plasma membrane is considered as a flat plane.
(k) The average distance between ions and cytoplasm proteins is equal to 5 Å.
(m) Equilibrium between intracellular and extracellular environments.
(n) The Born radii of Na^+, K^+, and Cl^- are considered equal to 1.68, 2.17, and 1.94 Å, respectively.[40]

The bulk concentrations used in the simulation for Na^+, K^+, and Cl^- are shown in Table 2. The sodium and potassium concentrations in the intracellular and extracellular environments as well as intracellular chloride are in accordance with the experimental data obtained by Funder and Wieth[41,42] and Aribi and collaborators.[43] The chloride concentration in the extracellular environment was obtained through the principle of electroneutrality. As we consider only the presence of chloride anion in the extracellular environment, this concentration must be equal to the sum of the concentrations of all cations in the extracellular environment.

Table 2. Ionic Concentration in the Model System Containing an Erythrocyte

ion	intracellular concentration (mequiv/L of H_2O)	extracellular concentration (mequiv/L of H_2O)
Na^+	16.5[a]	151.6[a]
K^+	133.7[a]	4.1[a]
Cl^-	75.7[b]	155.7[c]

[a]From refs 41 and 43. [b]From ref 42. [c]According to the principle of electroneutrality in an extracellular environment.

On the basis of the principle of electroneutrality, the equivalent protein concentration in the cell was considered equal to 74.5 mequiv/L.

3. RESULTS AND DISCUSSION

The dispersion interaction coefficients between ions and plasma membrane (B_{m}) and between ions and cytoplasmic protein (B_{p}) were calculated using Lifshitz theory.[32] Table 3 shows the static dielectric constants, ionization energies, and refractive indices for water, protein, and plasma membrane used

Table 3. Physical Properties for Water, Protein, and Plasma Membrane

physical properties	water	protein	plasma membrane
n[a]	1.3313[d]	1.6[d]	1.48[d]
$\varepsilon(0)$[b]	74.16[e]	2.56[f]	5.0[g]
$h\nu^{\mathrm{Ic}}$ (10^{12} erg)	20[f]	20[f]	20[f]

[a]Refractive index (sodium D line). [b]Dielectric constant. [c]Ionization energy. [d]From ref 33. [e]From ref 44. [f]From ref 32. [g]From ref 45.

DOI: 10.1021/acs.jpcb.5b02215
J. Phys. Chem. B 2015, 119, 6379−6388

to calculate the dispersion interaction coefficients presented in Table 4.

Table 4. Van der Waals Dispersion Interaction Coefficients between Ions and Plasma Membrane and between Ions and Cytoplasmic Protein at 310.15 K

ion	B_m[a] (10^{-50} J m^3)	B_p[b] (10^{-50} J m^3)
Na^+	0.257	0.459
K^+	1.083	1.918
Cl^-	2.076	3.631

[a]Dispersion interaction coefficients between ions and plasma membrane. [b]Dispersion interaction coefficients between ions and cytoplasmic protein.

Using the Poisson−Boltzmann equation with Neumann boundary conditions in a discontinuous system that mimics an erythrocyte immersed in an infinite bath with bulk salt concentrations equal to that of the extracellular medium (Table 2), we obtain a membrane potential equal to −6.88 mV (Figure 1A). This value is lower than (but close to) that

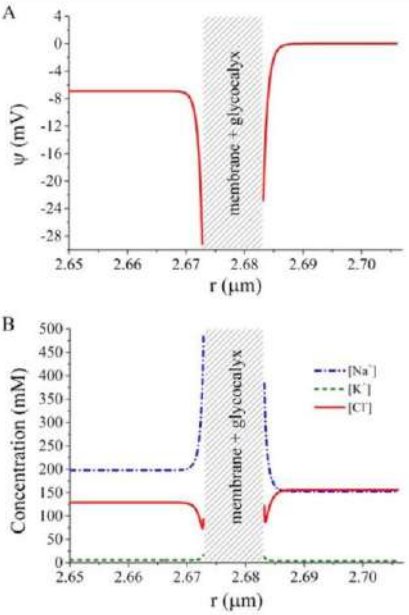

Figure 1. Electrostatic potential profile (A) and ion concentration profile (B) near erythrocyte plasma membrane in a discontinuous system between the intracellular and extracellular environments. Surface charge densities equal to −0.02 C/m^2 and bulk concentration of ions equal to the extracellular concentration shown in Table 2. Plasma membrane plus glycocalyx are represented by hatching.

reported in the literature for an erythrocyte (about −8 to −13 mV),[11,13−19] which can be attributed to the approximations and assumptions used in the model. In this case, we consider the reference bulk concentration of ions equal to their extracellular concentration. In Figure 1B, we show the ion profiles for this system. Near the cell membrane and glycocalyx, there are higher ion concentrations due to the adsorption of ions on these surfaces, including Cl^- (Figure 1B). Although Cl^- and the membrane have like charges, the peak of the Cl^- concentration close to the interface is because of the dispersion interaction between the ion and plasma membrane. It is worth noting that the value of B_m for Cl^- is higher than the values for the other ions. This effect is best observed at the interface membrane/extracellular solution once the absolute value of the electrostatic potential at the membrane/extracellular interface is smaller than that at the intracellular/membrane interface. We can note that the intracellular concentrations predicted by the model are different from experimental data. As previously mentioned, the intracellular environment has a higher K^+ concentration when compared to Na^+.[41] The disagreement between computational and experimental data may be occurring due to the difference in reference states between the intracellular and extracellular environments, the difference in ion permeability of the erythrocyte membrane, and/or the presence of active transporters at the plasma membrane.

Analyzing the normalized ion concentration profile within the cell, we can observe that K^+ has a slightly greater tendency of concentrating within the cell than Na^+ (Figure 2). This is

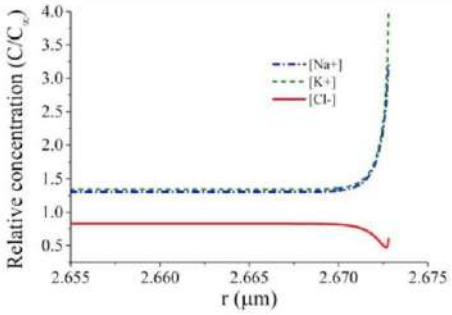

Figure 2. Normalized concentration profile within the cell. K^+ has a slightly greater tendency to concentrate within the cell than Na^+. Surface charge density equal to −0.02 C/m^2 and bulk concentration of ions equal to the extracellular concentration shown in Table 2.

due to nonelectrostatic interactions. Since there is a large amount of proteins within the cell, K^+ that is more polarizable tends to adsorb more to the proteins than Na^+. However, nonelectrostatic interactions are not sufficient to explain the higher K^+ concentration within the cell observed experimentally. Nevertheless, in this first study, we consider the same overall concentration in the two environments, taking the concentration of extracellular medium as a reference. Had we imposed the bulk concentration of the intracellular medium, we would be imposing the Donnan potential indirectly.

In the literature, this differential ion partitioning of Na^+ and K^+ is generally attributed to the action of the pump Na^+K^+ATPase. In order to analyze the potential required to describe experimental ion partitioning, we proposed the inclusion of a potential β in the modified Poisson−Boltzmann equation (eq 1). The algorithm developed for this specific step has an outer loop, in order to reproduce the experimental intracellular concentration values shown in Table 2. For each iteration, new values of β for each ion are obtained until the absolute difference between the intracellular concentration shown in Table 2 and the intracellular concentration calculated for a given estimated β potential is smaller than the tolerance. New values of β for each ion i are calculated according to

$$\beta_i = \ln\left(\frac{c_{i,\infty}}{c_{i,\mathrm{int}}}\right) - z_i y|_{x\to-\infty} - u_i|_{x\to-\infty} \quad (14)$$

DOI: 10.1021/acs.jpcb.5b02215
J. Phys. Chem. B 2015, 119, 6379−6388

where $c_{i,in}$ is the intracellular concentration of ion i, $y|_{x\to-\infty}$ is the dimensionless electrostatic potential inside the cell at an infinitely large distance from the interface, and $u_i|_{x\to-\infty}$ is the dimensionless nonelectrostatic potential of ion i inside the cell at an infinitely large distance from the interface.

The β potential takes into account the difference in reference states between intracellular and extracellular environments, the difference in ion permeability of the erythrocyte membrane, and short-range hydration forces.

Figure 3A shows the electrostatic potential profile obtained by solving the modified Poisson–Boltzmann equation with the

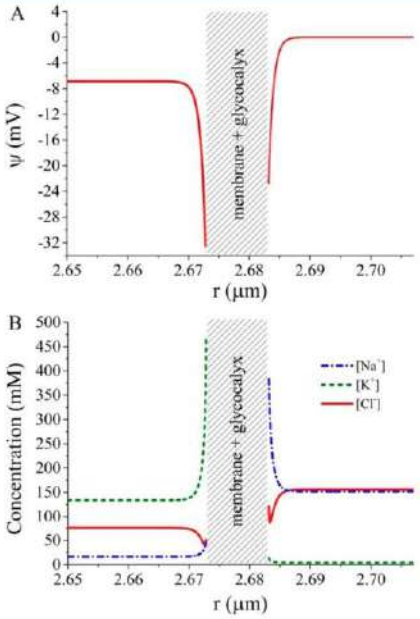

Figure 3. (A) Electrostatic potential profile and (B) ion concentration profile near the erythrocyte plasma membrane in a discontinuous system between the intracellular and extracellular environments considering β potential. Surface charge densities equal to −0.02 C/m^2 and bulk concentration of ions equal to the extracellular concentration shown in Table 2. Plasma membrane plus glycocalyx are represented by hatching.

inclusion of β potential. Extracellular β potentials for all ions are considered equal to zero. Intracellular values of β for each ion can be seen in Table 5. Comparing the membrane potential in the absence and the presence of β potential, we can observe that it is virtually invariable. Figure 3B shows the ion profiles analyzed in the presence of β potential. As expected, inside the cell, there is more K^+ than Na^+, and outside the cell, the inverse occurs.

As previously mentioned, the dielectric constants of the intracellular and extracellular environments are not the same. Then, it is necessary to introduce a correction due to the change of the reference state, which is connected with dielectric constants of both environments. In this context, it is noteworthy that different values of intracellular dielectric constant for normal erythrocytes have been reported in the literature such as 57[46] and 65.22.[38] We analyzed the contribution of this correction in ion–medium interaction for these two different values of intracellular dielectric constant using the Born equation (eq 12). Table 5 shows the values of the Born term for Na^+, K^+, and Cl^-. Comparing the Born correction term for each ion using both intracellular dielectric constant values reported in the literature, it is possible to note that, despite the influence of the dielectric constant in the correction term, the order of magnitude is the same. The values of the β potential and Born term for Cl^- are similar with respect to the order of magnitude, suggesting that the difference between the intracellular concentration of Cl^- observed experimentally and theoretically in this work can be due to the change of the thermodynamic reference state.

According to Bernhardt and Weiss,[4] under physiological conditions, the net ion movement of K^+ and Na^+ in comparison to Cl^- across the erythrocyte membrane is very small (about 2 orders of magnitude lower); i.e., the net Cl^- permeability across the membrane is larger than the K^+ and Na^+ permeability. Therefore, we expect an equilibrium distribution of Cl^- between intracellular and extracellular environments, which can be observed comparing β_{Cl^-} with the Born term for this ion. The difference between these terms can be attributed to the consideration of all anions present in the extracellular environment as chloride (including bicarbonates, sulfates, organic phosphates, proteins, etc.), as well as the real value of the intracellular dielectric constant.

If nonelectrostatic interactions between the ions and macromolecules are not explicitly considered in the modified Poisson–Boltzmann equation, the β value for each ion becomes also responsible for expressing the nonelectrostatic potential. The values of β potential for each ion in the system considering or not the nonelectrostatic interactions can be observed in Table 6.

Table 5. Intracellular Values of β and the Born Term for Na^+, K^+, and Cl^-

		$\Delta G_i^{ex,Born}/(k_BT)$	
ion	nondimensional β potential	$\varepsilon_{in} = 65.22^a$	$\varepsilon_{in} = 57^b$
Na^+	2.484	0.296	0.651
K^+	−3.191	0.230	0.503
Cl^-	0.531	0.257	0.564

[a]Dielectric constant of the intracellular environment equal to 65.22.[38] [b]Dielectric constant of the intracellular environment equal to 57.[46]

Table 6. Comparison between the β Potential for Na^+, K^+, and Cl^- Considering or Not the Nonelectrostatic Interactions

ion	β potential (system with NES), nondimensional	β potential (system without NES), nondimensional
Na^+	2.484	2.475
K^+	−3.191	−3.227
Cl^-	0.531	0.464

Comparing the values presented in both columns of Table 6, we can see that the contribution of the nonelectrostatic potential to the ion partitioning of sodium and potassium when compared to β potential is very small (0.4% for Na^+, 1.1% for K^+).

We can observe that the contribution of the Born correction term is more evident than nonelectrostatic interaction, at least with respect to Cl^-. It is worth noting that the magnitude of the Born correction term for Na^+ and K^+ is different from β_{Na^+} and

DOI: 10.1021/acs.jpcb.5b02215
J. Phys. Chem. B 2015, 119, 6379–6388

β_{K^+}, respectively. This fact suggests that neither nonelectrostatic interactions nor the Born correction term can explain intracellular K^+ and Na^+ concentrations. Then, the presence of Na^+K^+ATPase is clear.

Bernhardt and Weiss[4] have calculated the ratio between K^+ and Na^+ permeability using the Goldman–Hodgkin–Katz equation. According to their calculation, this ratio was equal to 1.5. Considering β is a term related to ion permeability across the cell membrane, we can calculate the absolute ratio of β_{K^+}/β_{Na^+}. The value obtained is equal to 1.3, close to that predicted by Bernhardt and Weiss. However, we must have in mind that this is an equilibrium calculation and the real cell is not in equilibrium, so this β potential may be related to the extra work done by the active transporters in order to keep the ion concentrations as they are in nature. This extra work is proportional to the permeability of the ions.

The free energy required to move 1 mol of solute across the plasma membrane (toward the extracellular environment to the intracellular) is given by $-RT\ln(C_{ex}/C_{in})$, where R is the universal gas constant, C_{ex} is the extracellular concentration, and C_{in} is the intracellular concentration. This free energy to move an ion i must be equal to $z_iF\delta\psi + RT\delta u_i + RT\delta\beta_i$, where F is the Faraday constant, $\delta\psi$ is the transmembrane potential, δu_i is the difference in transmembrane nonelectrostatic potential, and $\delta\beta_i$ is the difference in transmembrane β potential. This way, we can calculate the free energy required to move 1 mol of ions across the plasma membrane, as presented in Table 7.

Table 7. Free Energy Necessary to Move 1 mol of an Ion across the Plasma Membrane (toward the Extracellular Environment to the Intracellular)

ion	ΔG (kJ/mol)
Na^+	−5.72
K^+	8.99
Cl^-	−1.86

The standard free-energy change for the hydrolysis of ATP is equal to −30.5 kJ/mol. In human erythrocytes, the average concentrations of ATP, ADP, and P_i present in the cytoplasm are equal to 2.25, 0.25, and 1.65 mM, respectively. At pH 7.0 and 25 °C, the free energy change for the hydrolysis of ATP in erythrocytes is equal to −51.8 kJ/mol.[1]

At physiological concentrations of reactants and products, about 11 kcal/mol might be released by the hydrolysis of the terminal phosphate bond in ATP,[47] which corresponds to 46.1 kJ/mol. Sen and Post (1964)[47] found a ratio of active transport cycles of Na^+K^+ATPase equal to $3Na^+:2K^+:(1.16 \pm 0.04)$ATP.

On the basis of the data from Table 7, one transport cycle of Na^+K^+ATPase on a molar basis requires 35.14 kJ (free energy necessary to move 3 mol of Na^+ and 2 mol of K^+ against the electrochemical gradient). In order to compare this energy in terms of ATP, it is necessary to consider the efficiency of the transporter. According to Skou[5] for the transport of Na^+ and K^+ across the plasma membrane, the transporter uses 70–85% of the free energy of the hydrolysis of ATP. Considering 70% efficiency, 50.20 kJ of energy is necessary for the carrying of these ions, equivalent to 0.97 ATP. This value is close to that reported by Sen and Post.[47]

In order to model a continuous system encompassing intracellular and extracellular environments, a peak of volumetric density of fixed charge was estimated and inserted at the interfaces between the electrolyte solutions and plasma membrane to represent each face of the plasma membrane in order to reproduce the electrostatic potential profile of the discontinuous system. The volumetric density of fixed charge at the cytoplasmic face (cytoplasm–membrane interface) shows a minimum value of -1.16×10^8 C/m^3, while, at the external face, this value is equal to -9.85×10^7 C/m^3.

Figure 4 shows a comparison between continuous and discontinuous systems for the electrostatic potential profile. It is

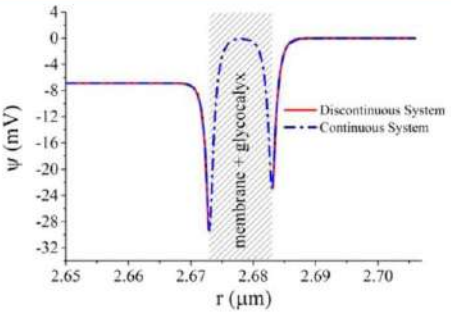

Figure 4. Comparison between continuous and discontinuous systems for the electrostatic potential profile. For the continuous system, the surface charge densities are equal to −0.02 C/m^2, and for the discontinuous system, the volumetric density of fixed charge at the cytoplasmic face (cytoplasm–membrane interface) shows a minimum value of -1.16×10^8 C/m^3, while, at the external face, this value is equal to -9.85×10^7 C/m^3. The bulk concentration of ions for both systems is equal to the extracellular concentration shown in Table 2.

noteworthy that the electrostatic potential and concentration profiles within the membrane are not real, being a numerical strategy to ensure the continuity.

The β potential was inserted in the regularization function such that in the extracellular environment this potential for all ions is equal to zero and in the intracellular environment the β potential has a particular value for each ion.

Two situations were analyzed. The first one considers x^*—the parameter used to represent the boundary between the two regions in the regularization function of the β potential—at the interface between the cytoplasm and the plasma membrane, and the other one considers x^* in the middle plane of the plasma membrane.

Figure 5A shows the electrostatic potential profile for the first case. The transmembrane potential is equal to that found for the discontinuous system; nevertheless, the potential of the cytoplasm–membrane interface is lower. However, in the discontinuous system, the potential of the cytoplasm–membrane interface is −32.5 mV, and in the continuous system with x^* at the interface, this potential is equal to −43.0 mV.

In Figure 5B, we observe the ion concentration profile of the first case. We can note that there is an increase of sodium ion concentration near the cytoplasm–membrane interface as well as an increase and a subsequent decrease of the concentration of potassium ion due to the regularization function of the β potential.

Analyzing the same case but for x^* in the middle plane of the plasma membrane, the potential of the cytoplasm–membrane interface is equal to −31.3 mV (Figure 6A), which is closest to that observed in the discontinuous system. The variance in electrostatic potential inside the plasma membrane refers to the impact of the β potential. Therefore, the position of x^* impacts

DOI: 10.1021/acs.jpcb.5b02215
J. Phys. Chem. B 2015, 119, 6379–6388

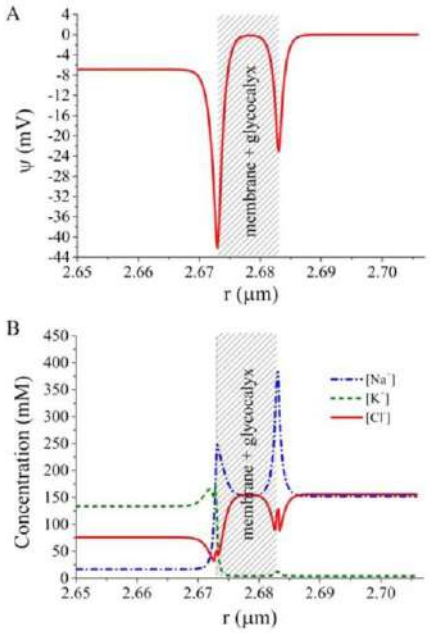

Figure 5. (A) Electrostatic potential profile and (B) ion concentration profile near the erythrocyte plasma membrane in a continuous system between the intracellular and extracellular environments considering x^* relative to the β potential at the cytoplasm−membrane interface. The volumetric density of fixed charge at the cytoplasmic face shows a minimum value of -1.16×10^8 C/m^3, while, at the external face, this value is equal to -9.85×10^7 C/m^3 and the bulk concentration of ions is equal to the extracellular concentration shown in Table 2. Plasma membrane plus glycocalyx are represented by hatching.

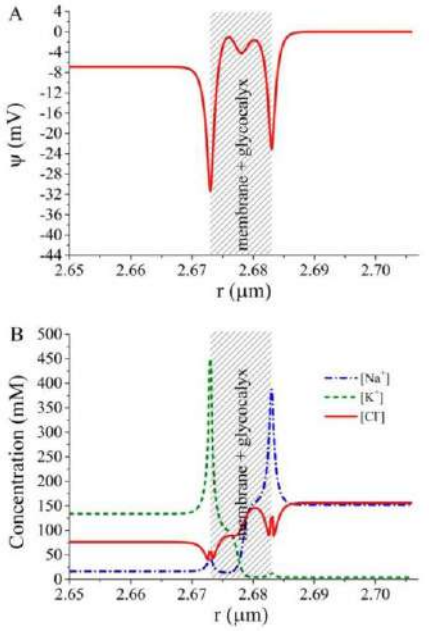

Figure 6. Electrostatic potential profile (A) and ion concentration profile (B) near the erythrocyte plasma membrane in a continuous system between the intracellular and extracellular environments considering x^* relative to the β potential in the middle of the plasma membrane. The volumetric density of fixed charge at the cytoplasmic face shows a minimum value of -1.16×10^8 C/m^3, while, at the external face, this value is equal to -9.85×10^7 C/m^3 and the bulk concentration of ions is equal to the extracellular concentration shown in Table 2. Plasma membrane plus glycocalyx are represented by hatching.

the β potential profiles, which strongly influences the electrostatic potential profile near this point.

Figure 6B presents a similar behavior in comparison with the discontinuous system (Figure 3B), in which there is an increase in the ion concentrations near the membrane interface due to nonelectrostatic interactions with the membrane.

Comparing the ion concentration profiles present in Figures 5B and 6B, we can observe that the latter is more consistent with what is expected, since it presents a peak of K^+ concentration near the cytoplasm−membrane interface and a subtle increase in the concentration of Na^+ near this interface (Na^+ peak in Figure 6B in accordance with the concentration of this ion in the intracellular environment).

4. CONCLUSIONS

The nonelectrostatic potential calculated by Lifshitz theory has only a small influence with respect to the high concentration of K^+ in the intracellular environment in comparison with Na^+. Despite that the intracellular environment has a larger surface area due to the presence of proteins, it is not sufficient by itself to explain the higher ion partitioning observed experimentally.

The insertion of a Born correction term in the modified Poisson−Boltzmann equation allows analyzing the energy involved in the difference in chemical potential reference states between intracellular and extracellular environments. Although this term cannot explain cation partitioning in erythrocytes, it has a correlation with Cl^- partitioning.

Regarding the membrane potential, the value obtained is lower than that reported in the literature for an erythrocyte. This fact can be attributed to the approximations and assumptions used in the model. The membrane potential in an erythrocyte, according to the literature, is directly related to the concentration of chloride, since this ion has a high permeability across the plasma membrane due to passive ion channels and transporters present. However, the analysis performed in this work considers all other anions present in the system, mainly in the extracellular environment, as chloride.

The electrostatic potential profile analyzed does not include the interior of the plasma membrane which is governed mainly by the dipole potential due to the anisotropic distribution of the lipid headgroup orientation. For the analysis of the potential dipole, it is necessary to use explicit or hybrid techniques.

Two continuous approaches have been proposed for solving a system containing the intracellular and extracellular environments. The advantage of the continuous system involves obtaining the electrostatic potential and concentration profiles of the intracellular and extracellular environments simultaneously using the same algorithm.

AUTHOR INFORMATION

Corresponding Author

*E-mail: tavares@eq.ufrj.br.

Notes

The authors declare no competing financial interest.

DOI: 10.1021/acs.jpcb.5b02215
J. Phys. Chem. B 2015, 119, 6379−6388

■ ACKNOWLEDGMENTS

For financial support, we are grateful to the Brazilian Agencies, Coordenação de Aperfeiçoamento de Pessoal de Nível Superior (CAPES), Fundação Carlos Chagas Filho de Amparo à Pesquisa do Estado do Rio de Janeiro (FAPERJ), and Conselho Nacional de Desenvolvimento Científico e Tecnológico (CNPq).

■ REFERENCES

(1) Nelson, D. L.; Cox, M. M. *Lehninger: Principles of Biochemistry*, 5th ed.; W. H. Freeman and Company: New York, 2008.
(2) Alberts, B.; Jonhson, A.; Lewis, J.; Raff, M.; Roberts, K.; Walter, P. *Molecular Biology of the Cell*, 5th ed.; Garland Science: New York, 2008.
(3) Lodish, H.; Berk, A.; Kaiser, C. A.; Krieger, M.; Scott, M. P.; Bretscher, A.; Ploegh, H.; Matsudaira, P. *Molecular Cell Biology*, 4th ed.; W. H. Freeman and Company: New York, 2000.
(4) Bernhardt, I.; Weiss, E. Passive Membrane Permeability for Ions and Membrane Potential. In *Red cell membrane transport in health and disease*; Bernhardt, I., Ellory, J. C., Eds.; Springer: Heidelberg, Germany, 2003; pp 83−119.
(5) Skou, J. C. The Identification of the Sodium-Potassium Pump (Nobel Lecture). *Biosci. Rep.* **1998**, *18*, 155−169.
(6) Boström, M.; Lima, E. R. A.; Biscaia, E. C.; Tavares, F. W.; Lo Nostro, P.; Parsons, D. F.; Deniz, V.; Ninham, B. W. Anion-Specific Partitioning in Two-Phase Finite Volume Systems: Possible Implications for Mechanisms of Ion Pumps. *J. Phys. Chem. B* **2009**, *113*, 8124−8127.
(7) Ninham, B. W.; Lo Nostro, P. *Molecular Forces and Self Assembly*; Cambridge University Press: Cambridge, U.K., 2010.
(8) Lo Nostro, P.; Peruzzi, N.; Severi, M.; Ninham, B. W.; Baglioni, P. Asymmetric Partitioning of Anions in Lysozyme Dispersions. *J. Am. Chem. Soc.* **2010**, *132*, 6571−6577.
(9) Lo Nostro, P.; Ninham, B. W. Hofmeister Phenomena: An Update on Ion Specificity in Biology. *Chem. Rev.* **2012**, *112*, 2286−2322.
(10) Lagi, M.; Lo Nostro, P.; Fratini, E.; Ninham, B. W.; Baglioni, P. Insights into Hofmeister Mechanisms: Anion and Degassing Effects on the Cloud Point of Dioctanoylphosphatidylcholine/Water Systems. *J. Phys. Chem. B* **2007**, *111*, 589−597.
(11) Freedman, J. Membrane Transport in Red Blood Cells. In *Cell Physiology Sourcebook: A Molecular Approach*; Sperelakis, N., Ed.; Academic Press: San Diego, CA, 2001; pp 377−392.
(12) Ponder, E. *Hemolysis and Related Phenomena*; Grune and Stratton: New York, 1948.
(13) Lassen, U. V.; Sten-Knudsen, O. Direct Measurements of Membrane Potential and Membrane Resistance of Human Red Cells. *J. Physiol.* **1968**, *195*, 681−696.
(14) Jay, A. W. L.; Burton, A. C. Direct Measurement of Potencial Difference across the Human Red Blood Cell Membrane. *Biophys. J.* **1969**, *9*, 115−121.
(15) Hoffman, J. F.; Laris, P. C. Determination of Membrane Potentials in Human and Amphiuma Red Blood Cells by Means of Fluorescent Probe. *J. Physiol.* **1974**, *239*, 519−552.
(16) Moersdorf, D.; Egee, S.; Hahn, C.; Hanf, B.; Ellory, C.; Thomas, S.; Bernhardt, I. Transmembrane Potential of Red Blood Cells under Low Ionic Strength Conditions. *Cell. Physiol. Biochem.* **2013**, *31*, 875−882.
(17) Beauge, L. Non-Pumped Sodium Fluxes in Human Red Blood Cells: Evidence for Facilitated Diffusion. *Biochim. Biophys. Acta* **1975**, *401*, 95−108.
(18) Cotterrell, D.; Whittam, R. The Influence of the Chloride Gradient across Red Cell Membranes on Sodium and Potassium Movements. *J. Physiol.* **1971**, *214*, 509−536.
(19) Cheng, K.; Haspel, H. C.; Vallano, M. Lou; Osotimehin, B.; Sonenberg, M. Measurement of Membrane Potentials (ψ) of Erythrocytes and White Adipocytes by the Accumulation of Triphenylmethylphosphonium Cation. *J. Membr. Biol.* **1980**, *56*, 191−201.
(20) Ninham, B. W.; Yaminsky, V. Ion Binding and Ion Specificity: The Hofmeister Effect and Onsager and Lifshitz Theories. *Langmuir* **1997**, *13*, 2097−2108.
(21) Boström, M.; Williams, D. R. M.; Ninham, B. W. Specific Ion Effects: Role of Salt and Buffer in Protonation of Cytochrome c. *Eur. Phys. J. E* **2004**, *13*, 239−245.
(22) Boström, M.; Williams, D. R. M.; Ninham, B. W. Ion Specificity of Micelles Explained by Ionic Dispersion Forces. *Langmuir* **2002**, *18*, 6010−6014.
(23) Boström, M.; Lima, E. R. A.; Tavares, F. W.; Ninham, B. W. The Influence of Ion Binding and Ion Specific Potentials on the Double Layer Pressure between Charged Bilayers at Low Salt Concentrations. *J. Chem. Phys.* **2008**, *128*, 135104.
(24) Dhatt, G.; Touzot, G.; Lefrançois, E. *Finite Element Method*; John Wiley & Sons, Inc.: Hoboken, NJ, 2012.
(25) Krysinski, P.; Ti Tien, H. Membrane Electrochemistry. *Prog. Surf. Sci.* **1986**, *23*, 317−412.
(26) Mauro, A. Space Charge Regions in Fixed Charge Membranes and the Associated Property of Capacitance. *Biophys. J.* **1962**, *2*, 179−198.
(27) Ohshima, H.; Ohki, S. Donnan Potential and Surface Potential of a Charged Membrane. *Biophys. J.* **1985**, *47*, 673−678.
(28) Chein, R.; Chen, H.; Liao, C. Investigation of Ion Concentration and Electric Potential Distributions in Charged Membrane/electrolyte Systems. *J. Membr. Sci.* **2009**, *342*, 121−130.
(29) Ohshima, H. The Donnan Potential-Surface Potential Relationship for a Cylindrical Soft Particle in an Electrolyte Solution. *J. Colloid Interface Sci.* **2008**, *323*, 313−316.
(30) Ohshima, H. Double Layer Interaction between Soft Particles. In *Theory of Colloid and Interfacial Electric Phenomena*; Ohshima, H., Ed.; Elsevier: London, 2006; pp 390−408.
(31) Freitas, T. C.; Quinto, T. C.; Secchi, A. R.; Biscaia, E. C. An Efficient Adjoint-Free Dynamic Optimization Methodology for Batch Processing Using Pontryagin's Formulation. In *22nd European Symposium on Computer Aided Process Engineering*; Bogle, I. D. L., Fairweather, M., Eds.; Elsevier: Amsterdam, The Netherlands, 2012; pp 1297−1301.
(32) Tavares, F. W.; Bratko, D.; Blanch, H. W.; Prausnitz, J. M. Ion-Specific Effects in the Colloid-Colloid or Protein-Protein Potential of Mean Force: Role of Salt-Macroion van der Waals Interactions. *J. Phys. Chem. B* **2004**, *108*, 9228−9235.
(33) Israelachvili, J. N. *Intermolecular and Surface Forces*, 3rd ed.; Academic Press: Burlington, MA, 2011.
(34) Robinson, R. A.; Stokes, R. H. *Electrolyte Solutions*; Dover: New York, 2002.
(35) Chen, C.; Song, Y. Generalized Electrolyte-NRTL Model for Mixed-Solvent Electrolyte Systems. *AIChE J.* **2004**, *50*, 1928−1941.
(36) Dill, K. A. *Molecular Driving Forces: Statistical Thermodynamics in Chemistry and Biology*; Garland Science: New York, 2003.
(37) Donath, E.; Lerche, D. 309 - Electrostatic and Structural Properties of the Surface of Human Erythrocytes. I-Cell-Electrophoretic Studies Following Neuraminidase Treatment. *Bioelectrochem. Bioenerg.* **1980**, *7*, 41−53.
(38) Di Biasio, A.; Cametti, C. On the Dielectric Relaxation of Biological Cell Suspensions: The Effect of the Membrane Electrical Conductivity. *Colloids Surf., B* **2011**, *84*, 433−441.
(39) Feher, J. J. Plasma and Red Blood Cells. In *Quantitative Human Physiology: An Introduction*; Feher, J. J., Ed.; Academic Press: San Diego, CA, 2012; pp 428−436.
(40) Rashin, A. A.; Honig, B. Reevaluation of the Born Model of Ion Hydration. *J. Phys. Chem.* **1985**, *89*, 5588−5593.
(41) Funder, J.; Weith, J. Potassium, Sodium and Water in Normal Human Red Blood Cells. *Scand. J. Clin. Lab. Invest.* **1966**, *18*, 167−180.
(42) Funder, J.; Weith, J. Chloride and Hydrogen Ions Distribution between Human Red Cell and Plasma. *Acta Physiol. Scand.* **1966**, *98*, 234−245.

DOI: 10.1021/acs.jpcb.5b02215
J. Phys. Chem. B 2015, 119, 6379−6388

(43) Aribi, M.; Haddouche, M.; Benyoucef, M.; Taleb, A.; Kendoucitani, M.; Merzouk, S. A.; Meziane, A. Clinical Evaluation of Lipids, Lipoproteins and Red Blood Cells Sodium and Potassium in Patients with Different Grades of Hypertension. *Clin. Biochem.* **2010**, *43*, 942−947.
(44) Malmberg, C. G.; Maryott, A. A. Dielectric Constant of Water from 0° a 100°C. *J. Res. Natl. Bur. Stand. (U. S.)* **1956**, *56*, 1−6.
(45) Sperelakis, N. *Cell Physiology Source Book: A Molecular Approach*, 3rd ed.; Academic Press: San Diego, CA, 2001.
(46) Gascoyne, P.; Pethig, R.; Satayavivad, J.; Becker, F. F.; Ruchirawat, M. Dielectrophoretic Detection of Changes in Erythrocyte Membranes Following Malarial Infection. *Biochim. Biophys. Acta* **1997**, *1323*, 240−252.
(47) Sen, A. K.; Post, R. L. Stoichiometry and Localization of Adenosine Triphosphate-Dependent Sodium and Potassium Transport in the Erythrocyte. *J. Biol. Chem.* **1964**, *239*, 345−352.

DOI: 10.1021/acs.jpcb.5b02215
J. Phys. Chem. B 2015, 119, 6379−6388

APPENDIX H – Wettability of rock, oil and brine system based on density functional theory

BARBOSA, N. S. V.; LIMA, E. R. A.; TAVARES, F. W. Wettability of rock, oil and brine system based on density functional theory. *Fluid Phase Equilib.*, v. 479, n. 1, p. 99–105, 2019. doi: 10.1016/j.fluid.2018.09.01

Fluid Phase Equilibria 479 (2019) 99–105

Contents lists available at ScienceDirect

Fluid Phase Equilibria

journal homepage: www.elsevier.com/locate/fluid

Wettability of rock, oil and brine system based on density functional theory

Nathalia S.V. Barbosa [a], Eduardo R.A. Lima [a, *], Frederico W. Tavares [b, c]

[a] Programa de Pós-graduação em Engenharia Química, Universidade do Estado do Rio de Janeiro, Rio de Janeiro, RJ 20550-013, Brazil
[b] Escola de Química, Universidade Federal do Rio de Janeiro, Rio de Janeiro, RJ 21941-909, Brazil
[c] Programa de Engenharia Química, COPPE, Universidade Federal do Rio de Janeiro, Rio de Janeiro, RJ 21941-914, Brazil

ARTICLE INFO

Article history:
Received 11 May 2018
Received in revised form
16 September 2018
Accepted 22 September 2018
Available online 1 October 2018

Keywords:
Wettability
Contact angle
DFT
Electrolyte
Dispersion interaction

ABSTRACT

The composition of an ionic aqueous solution can modify the wettability behavior of a liquid/liquid/solid system. This behavior is of great importance for oil extraction and some separation processes. Here we model the contact angle and wettability on the basis of a tridimensional classical density functional theory (DFT) and Young equation for a brine/oil/solid surface system. We propose the inclusion of dispersion interaction between surface-ion and oil-ion. The equilibrium contact angle is found through the minimization of the grand potential. The approach presented here is promising and due to its versatility can be expanded to systems with some peculiarities such as roughness and thin film.

1. Introduction

The growing interest in the wettability of systems involving two liquids and a solid surface is well documented in the literature specially in the context of separation processes and oil extraction [1–8]. By definition wettability, which is often expressed as the macroscopic contact angle, refers to the relative preference of one liquid over another to spread on a surface [9] due to the interplay of molecular and ionic interactions among three phases. It can be altered thermally [5,6], or chemically using low-salinity brine, selective ions [3–5], surfactants [7], and nanoparticles [8], for example. Smart-water waterflooding – which is characterized by the injection of a specific composition of aqueous electrolyte solution into oil reservoir in order to enhance the oil recovery – is an example of system where the knowledge of the wettability is crucial for the efficiency of the process [3–5]. Depending on the concentration and type of salts, the brine solution may have profound effects on the wetting state (e.g. alteration of rock property from oil-wet to water-wet).

Classical density functional theory (DFT) has been used to investigate the wettability in vapor/liquid/solid substrate systems because of its versatility to determine the equilibrium structure and corresponding thermodynamic quantities of systems subjected to external potentials [10–16]. However, the application of DFT to study the wettability and contact angle of liquid/liquid/solid substrate as far as we could track has not been performed.

The aim of this work is the determination of the most probable contact angle of a system characterized by an oil phase, ionic aqueous solution and a planar solid surface using DFT. More than expose a quantitative value, we are interested in providing a different approach to study these kind of systems using classical tridimensional DFT. Here the characteristics of the oil and the solid surface are defined by external potentials between them and the ions in solution.

The paper is arranged as follows. Section 2 summarizes the description of the system under consideration and the formalism of density functional theory and other main equations necessary to calculate the free energy of the system and the contact angle. In Section 3, the density profiles of the brine solution in the vicinity of an oil droplet is presented, as well as, the equilibrium contact angle. The conclusions are presented in Section 4.

* Corresponding author.
E-mail address: lima.eduardo@uerj.br (E.R.A. Lima).

https://doi.org/10.1016/j.fluid.2018.09.019
0378-3812/

2. Theory

In the following derivations, we consider a liquid droplet of oil resting on a flat solid surface surrounded by ionic aqueous solution as presented in Fig. 1. It is assumed that the chemical and physical characteristics of the substrate are not changed because of the contact with the fluid molecules.

Neglecting the gravitation field, the shape of the droplet may be visualized rather close to a spherical cap. If θ is the contact angle between the droplet of volume V_d and the solid, then the radius R, the height h of the cap and the area of the droplet in contact with the solid (A_{so}) can be written as (Fig. 2) [10,17].

$$R^3 = \frac{3V_d}{\pi(2-\cos\theta)(1+\cos\theta)^2} \tag{1}$$

$$h = R(1+\cos\theta) \tag{2}$$

$$A_{so} = \pi R^2\left(\sin^2\theta\right) \tag{3}$$

For the sake of simplicity, we consider for the time being the mean density inside the droplet to be uniform, *i.e.*, the oil droplet is incompressible.

We also assume, *a priori*, the absence of thin brine film between the solid surface and the oil.

Given an infinitesimal change in area dA, the change in the surface free energy dE of the system in Fig. 1 is given by

$$\mathrm{d}E = (\gamma_{so} - \gamma_{sb} - \gamma_{bo}\cos\theta)\mathrm{d}A \tag{4}$$

where γ_{sb}, γ_{so}, and γ_{bo} are the solid-brine, solid-oil, and brine-oil interfacial free energy per unit area, respectively. The balance of forces in the x direction correlates the interfacial tensions with the contact angle by the Young equation

$$\cos\theta = \frac{\gamma_{so} - \gamma_{sb}}{\gamma_{bo}} \tag{5}$$

The nature of the contact angle is determined by the relative affinity of the two liquid phases for the solid defined by their interfacial tensions. For the wettability regime, we consider the contact angle between 0° and 70° as water-wet, from 70° to 110° as neutral and from 110° to 180° as oil-wet, following the definition adopted by Santos *et al.*. [18].

2.1. Density functional theory

Our approach is based on a classical DFT of inhomogeneous fluids in three dimensions [19,20] which treats the rock and the oil as external potentials acting on the brine. DFT is based on the Hohenberg-Kohn theorem and statistical mechanics. For an open system with temperature T, total volume V and chemical potential for each species μ_i specified, the grand potential Ω_{DFT} may be expressed as functional of the local density distribution of the species ρ_i [21].

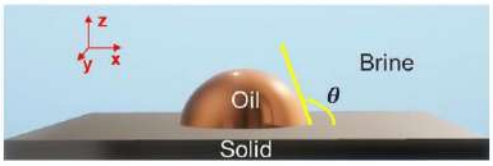

Fig. 1. Sketch of the oil droplet immersed in brine resting on a flat solid particle.

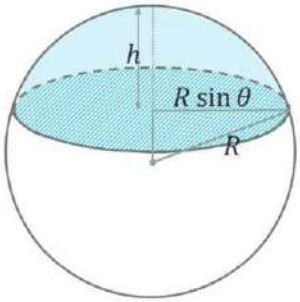

Fig. 2. Geometric measure representation of spherical cap (in blue). θ, R, and h are the contact angle, the radius and the height, respectively. The hatched area corresponds to the area of the base circle of the cap (A_{so}). (For interpretation of the references to colour in this figure legend, the reader is referred to the Web version of this article.)

$$\Omega_{\mathrm{DFT}}[\{\rho_i(\mathbf{r})\}] = F[\{\rho_i(\mathbf{r})\}] + \int\sum_i \rho_i(\mathbf{r})[\nu_i(\mathbf{r}) - \mu_i]\mathbf{dr} \tag{6}$$

where $F[\{\rho_i(\mathbf{r})\}]$ is the intrinsic Helmholtz energy functional and ν_i is the external potential relative to the species i. In order to determine the structure of the fluid, DFT minimizes the grand potential with respect to the local density by solving the Euler-Lagrange equation:

$$\frac{\delta\Omega_{\mathrm{DFT}}[\{\rho_i(\mathbf{r})\}]}{\delta\rho_i(\mathbf{r})} = \frac{\delta F[\{\rho_i(\mathbf{r})\}]}{\delta\rho_i(\mathbf{r})} + \nu_i(\mathbf{r}) - \mu_i = 0 \tag{7}$$

The derivation of analytical equations to compute the intrinsic Helmholtz energy functional is a central issue in DFT. It can be decomposed into an ideal part and an excess part. Whereas the ideal part is well-know,

$$\beta F^{id}[\{\rho_i(\mathbf{r})\}] = \sum_i \int \rho_i(\mathbf{r})\left[\ln\left[\rho_i(\mathbf{r})\lambda_i^3\right] - 1\right]\mathbf{dr}, \tag{8}$$

the excess part splits into diverse contributions. In Eq. (8), λ is the thermal wavelength, $\beta = 1/(k_BT)$, and k_B is the Boltzmann constant. Here we consider the contributions from short-range repulsions (F_{hs}^{ex}), direct Coulomb energy (F_C^{ex}), and electrostatic correlations (F_{el}^{ex}) for the excess Helmholtz energy functional:

$$F[\{\rho_i(\mathbf{r})\}] = F^{id}[\{\rho_i(\mathbf{r})\}] + F_{hs}^{ex}[\{\rho_i(\mathbf{r})\}] + F_C^{ex}[\{\rho_i(\mathbf{r})\}] + F_{el}^{ex}[\{\rho_i(\mathbf{r})\}] \tag{9}$$

To model the contribution from short-range repulsions, we use the White-Bear version of the fundamental measure theory (WB-FMT). According to WB-FMT, F_{hs}^{ex} is given by [22,23]

$$\beta F_{hs}^{ex}[\{\rho_i(\mathbf{r})\}] = \int \Phi^{hs}[n_\alpha(\mathbf{r})]\mathbf{dr} \tag{10}$$

where Φ^{hs} is the reduced free energy density due to the hard-sphere repulsion and $n_\alpha(\mathbf{r})$ is the weighted density defined by

$$n_\alpha(\mathbf{r}) = \sum_i \int \rho_i(\mathbf{r}')\omega_i^\alpha(\mathbf{r}' - \mathbf{r})\mathbf{dr}', \tag{11}$$

with $\alpha \in \{0, 1, 2, 3, V1, V2\}$. The weight functions ω_i^α are expressed by

$$\omega_i^0(\mathbf{r}) = \frac{\omega_i^2(\mathbf{r})}{\pi\sigma_i^2} \tag{12}$$

$$\omega_i^1(\mathbf{r}) = \frac{\omega_i^2(\mathbf{r})}{2\pi\sigma_i} \tag{13}$$

$$\omega_i^2(\mathbf{r}) = \delta\left(\frac{\sigma_i}{2} - |\mathbf{r}|\right) \tag{14}$$

$$\omega_i^3(\mathbf{r}) = \Theta\left(\frac{\sigma_i}{2} - |\mathbf{r}|\right) \tag{15}$$

$$\boldsymbol{\omega}_i^{V1}(\mathbf{r}) = \frac{\boldsymbol{\omega}_i^{V2}(\mathbf{r})}{2\pi\sigma_i} \tag{16}$$

$$\boldsymbol{\omega}_i^{V2}(\mathbf{r}) = \left(\frac{\mathbf{r}}{|r|}\right)\delta\left(\frac{\sigma_i}{2} - |\mathbf{r}|\right) \tag{17}$$

where $\delta(r)$ is the Dirac function, $\Theta(r)$ is the Heaviside step function, and both $\boldsymbol{\omega}_i^{V1}$ and $\boldsymbol{\omega}_i^{V2}$ are vectors. Integration over $\omega_i^3(\mathbf{r})$, $\omega_i^2(\mathbf{r})$, $\omega_i^1(\mathbf{r})$, and $\omega_i^0(\mathbf{r})$ recovers the volume, surface area, mean radius of curvature, and Euler characteristics, respectively, *i.e.* the fundamental geometrical measures of a sphere of species i in tridimensional space. Based on the Boublik-Mansoori-Carnahan-Starling-Leland equation of state, $\Phi^{hs}[n_\alpha(\mathbf{r})]$ is given by [22,23]

$$\Phi^{hs}(n_\alpha) = -n_0\ln(1-n_3) + \frac{n_1 n_2 - \mathbf{n}_{V1}\cdot\mathbf{n}_{V2}}{1-n_3} + \left(n_2^3 - 3n_2\mathbf{n}_{V2}\cdot\mathbf{n}_{V2}\right)\times\frac{n_3 + (1-n_3)^2\ln(1-n_3)}{36\pi n_3^2(1-n_3)^2} \tag{18}$$

To calculate the convolution in Eq. (11), we solve it in Fourier space in order to reduce the number of operations from $\mathcal{O}(N^2)$ to $\mathcal{O}(N\log N)$, where N is the number of grid points [19,20,24,25]. The weight functions are computed analytically [20,26], whereas, for the density profile, we use the fast Fourier transform (FFT) [19,20]. Some advantages of the Fourier space over the real space to compute the weighted density, as well as, the motivation to calculate the Fourier transform of each weight function analytically can be found in elsewhere [19,20,24,25]. According to Knepley *et al* [19], the fundamental geometrical measures of a sphere are not recovered with straightforward real space methods.

The direct Coulomb contribution F_C^{ex} is defined as

$$\beta F_C^{ex}[\{\rho_i(\mathbf{r})\}] = \frac{1}{2}\iint\sum_{i,j}\frac{\psi_{ij}(\mathbf{r},\mathbf{r}')\rho_i(\mathbf{r})\rho_j(\mathbf{r}')}{k_BT}\mathrm{d}\mathbf{r}\mathrm{d}\mathbf{r}' \tag{19}$$

where

$$\psi_{ij}(\mathbf{r},\mathbf{r}') = \frac{Z_iZ_je^2}{4\pi\varepsilon\varepsilon_0|\mathbf{r}-\mathbf{r}'|} \tag{20}$$

is the interaction potential of two point particles with charges Z_ie and Z_je located at $\mathbf{r}$ and $\mathbf{r}'$, respectively, e is the elementary charge, Z_i is the valence of ion i, ε is the dielectric constant, and ε_0 is the permittivity of vacuum. Here we assume uniform dielectric constant in each phase. It is worthwhile to note that the dielectric constant can also be considered as function of the position local dielectric permittivity [27].

Several approaches are available in the literature to take into account the contributions from electrostatic correlations [26,28–34]. For the sake of simplicity, here we use the "bulk fluid density" model (BFD) [26], although it presents well-known limitations [30,35–37]. It is a classical approximation and as previously mentioned we are interested in present a strategy to calculate the contact angle of a liquid/liquid/solid system, independently of the functionals used to describe the excess Helmholtz energy. According to BFD, the excess Helmholtz energy functional due to the electrostatic correlations F_{el}^{ex} is expressed by a quadratic functional Taylor expansion around bulk densities $\{\rho_i^b\}$ [26]:

$$\beta F_{el}^{ex}[\{\rho_i(\mathbf{r})\}] = \beta F_{el}^{ex}\left(\left\{\rho_i^b\right\}\right) - \int\sum_i\Delta C_i^{(1)}\left[\rho_i(\mathbf{r}) - \rho_i^b\right]\mathrm{d}\mathbf{r} - \frac{1}{2}\iint\sum_{i,j}\Delta C_{ij}^{(2)}(|\mathbf{r}-\mathbf{r}'|)\times\left[\rho_i(\mathbf{r}) - \rho_i^b\right]\left[\rho_j(\mathbf{r}) - \rho_j^b\right]\mathrm{d}\mathbf{r}\mathrm{d}\mathbf{r}' \tag{21}$$

where $\Delta C_i^{(1)}$ and $\Delta C_{ij}^{(2)}(\mathbf{r},\mathbf{r}')$ are the direct correlation functions. The latter is given by

$$\Delta C_{ij}^{(2)}(\mathbf{r},\mathbf{r}') = C_{ij}(\mathbf{r},\mathbf{r}') + \beta\psi_{ij}(\mathbf{r},\mathbf{r}') - C_{ij}^{hs}(\mathbf{r},\mathbf{r}') \tag{22}$$

and calculated based on the analytical bulk mean spherical approximation (MSA) correlation functional derived by Blum and Rosenfeld [38].

As well as the contributions from hard sphere interactions, the convolutions of $\delta F_{el}^{ex}/\delta\rho_i$ and the Poisson equation are calculated in the Fourier domain following the strategy of Knepley *et al.* [19].

Eq. (7) is solved using Picard iterative method [19].

2.2. External potential

Different functions to express the surface-fluid (external) potential – mainly for the interaction between surface with molecules or uncharged particles – have been used over the years such as: hard-wall [23], Yukawa [11,12], and Lennard-Jones [13,39] potentials. With respect to ions or charged particles, the hard-wall potential,

$$v_i^{hw}(\mathbf{r}) = \begin{cases}\infty & \text{if } \eta(\mathbf{r}) < \sigma_i/2,\\ 0 & \text{otherwise}\end{cases} \tag{23}$$

along with the electrostatic interaction between wall and the fluid has been the most popular choice [29,30,35,40], where $\eta(\mathbf{r})$ represents the closest distance from the point $\mathbf{r}$ to the surface. However, little progress has been made in DFT with the inclusion of disperse interaction of an ion with a surface. It is worth mentioning that studies applying mean-field methods like modified Poisson-Boltzmann equation demonstrated that the ion-specific surface interactions play an important role in the total surface excess near interfaces [41]. One option to address this issue is the inclusion of the dispersion interaction between an ion and an interface with Hamaker constant B described by Lifshitz theory [41–44].

$$v^{disp}(\mathbf{r}) = -\frac{B}{[\eta(\mathbf{r})]^3} \tag{24}$$

In Eq. (24), B and v^{disp} depend on the ion and on the interface. According to Lifshitz theory, the dispersion coefficient B can be written as [43,44].

$$\beta B = \frac{1}{2}\sum_m{}'\frac{\alpha^*(i\omega_m)}{\varepsilon_b(i\omega_m)}\frac{\varepsilon_s(i\omega_m) - \varepsilon_b(i\omega_m)}{\varepsilon_s(i\omega_m) + \varepsilon_b(i\omega_m)} \tag{25}$$

where the excess polarizability $\alpha^*(i\omega_m)$ of an ion and the dielectric spectra of the solvent $\varepsilon_b(i\omega_m)$ and the surface $\varepsilon_s(i\omega_m)$ vary in the

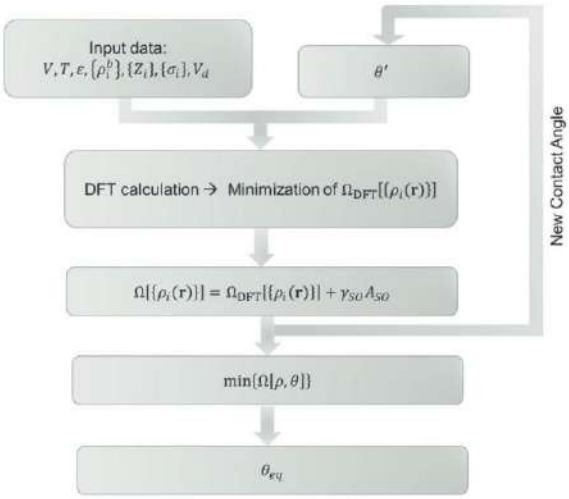

Fig. 3. Computational strategy used to compute the equilibrium contact angle.

frequency ($\omega_m = 2\pi m k_B T/\hbar$). The prime indicates that at zero frequency, the component should be taken with a factor 1/2. The polarizability and dielectric constant varies with frequency much in the same way as a harmonic-oscillator model [44]:

$$\alpha(i\omega) = \frac{\alpha(0)}{1 + (\omega^2/\omega_I^2)} \tag{26}$$

$$\varepsilon(i\omega) = 1 + \frac{n^2 - 1}{1 + (\omega^2/\omega_e^2)} \tag{27}$$

where ω_I is the ionization frequency, ω_e is the main electronic absorption frequency in the UV, and n is the refractive index of the medium in the visible.

2.3. Simulation details

The oil droplet and the brine adopt the configuration that minimizes the grand potential $\Omega = -pV + \gamma_{sb}A_{sb} + \gamma_{so}A_{so} + \gamma_{bo}A_{bo}$, which is conveniently divided into bulk and surface contributions, where p is the bulk pressure, A_{ij} is the surface area between phases i and j, and the subscripts s, b, and o correspond to the solid, brine and oil phases, respectively. The line tension was neglected. In order to provide the equilibrium contact angle θ_{eq} among the three phases, we simulated a set of systems with a constant droplet volume varying the contact angle θ' (Figs. 3 and 4). An increase in the droplet radius with increasing θ' is observed to maintain the constant volume. Thus, θ' is an input data for each simulation in a set along with the volume, temperature, dielectric constant, bulk densities, ionic valences, ionic diameters, and droplet volume, whereas the density distribution of ions outside the droplet and the grand potential provided by DFT are the output data. The latter does not include the free energy due to the interaction between solid-oil ($\gamma_{so}A_{so}$), being necessary to add it *a posteriori* as shown in Fig. 3. We assume, for the sake of simplicity, that the density of oil inside the droplet is uniform for all the systems in a set. With these information, θ_{eq} is calculated by the analysis of the angle that minimizes Ω.

3. Results and discussion

For our simulations, we examined an aqueous NaCl solution (1:1) at 298.15 K. The ionic diameters are equal to 0.198 nm and 0.362 nm for cation (σ_+) and anion (σ_-), respectively [45]. The simulation cell has the dimensions of $6 \times 6 \times 6$ nm^3 and the flat surface is placed at z. equal to 0 nm. The volume of the droplet was set to 3.0 nm^3. The dielectric constant of the solvent is equal to 78.5. The main model parameters are summarized in Table 1. Periodic

Table 1
Model parameters.

Parameters	Values
temperature [K]	298.15
dielectric constant of the solvent	78.15
cation diameter [nm]	0.198
anion diameter [nm]	0.362
volume of the droplet [nm^3]	3.0

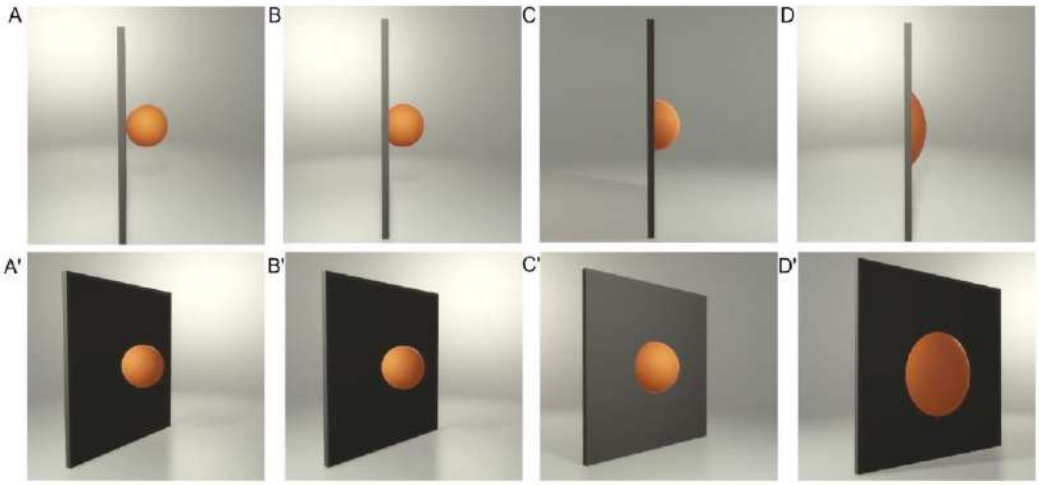

Fig. 4. Variation of the radius with the contact angle for a constant droplet volume. Note that the upper and lower drawings in each column are equivalent, only the perspective of the observer changes. The contact angles are 0°, 45°, 90°, and 135°, respectively.

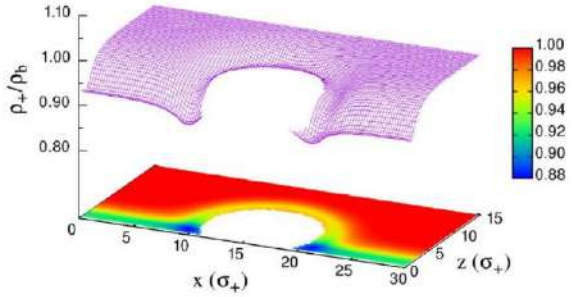

Fig. 5. Density profile of cations near a droplet for a bulk ionic strength of 1000 mol/m^3. Contact angle between the rock and droplet equal to 0.6 rad (34.4°).

boundary conditions were considered in xy directions, whereas in z direction both boundaries are delimited by the presence of planar surfaces.

Figs. 5 and 6 show the density profiles of cations and anions, respectively, near to the droplet and solid surface with contact angle equal to 34.4° and bulk ionic strength (ρ_b) of 1000 mol/m^3. To evidence the vicinity of the droplet, Figs. 5 and 6 only present half of z axis. The distances are adimensionalized by the cationic diameter. We used the hard wall potential to take into account the interactions between brine/solid surface and brine/oil droplet. The discrete increase of the cation concentration close to the interfaces (see Fig. 5) is due to the bulk fluid density theory used to describe the electrostatic correlation. Comparatively with data from molecular simulation, this increase is qualitatively incorrect and has motivated the development of other theories to compute the electrostatic correlations as mentioned in Section 2.1 [30,35–37]. It is interesting to note that because the cation is smaller than the anion by a factor of 0.55, the former can get closer to the interfaces. Consequently, a more pronounced increase in concentration of anions can be observed in the vicinity of the interfaces (Fig. 6). It is important to remember that in this study both surfaces are supposed to be neutral, so there is no electrostatic interaction between ions and surfaces.

We analyzed a range of contact angle from 0.1 to 2.4 rad (5.7° to 137.5°) for bulk ionic strength equal to 500 and 1000 mol/m^3, and the grand potential provided by DFT (Ω_{DFT}) was determined in this process. In order to find the contact angle, it is necessary to add the contribution of oil/solid surface to the grand potential:

$$\Omega[\{\rho_i(\mathbf{r})\}] = \Omega_{DFT}[\{\rho_i(\mathbf{r})\}] + \gamma_{so}A_{so} \tag{28}$$

Increasing the contact angle increases the basal area of the spherical cap (A_{so}). Therefore, depending on the magnitude of γ_{so},

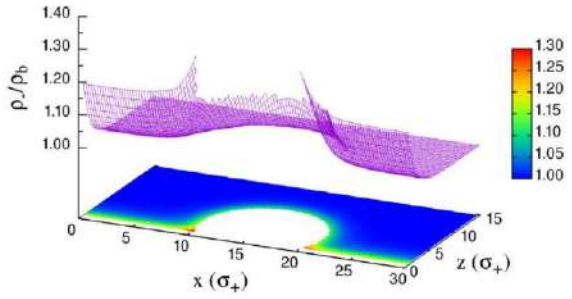

Fig. 6. Density profile of anions near a droplet for a bulk ionic strength of 1000 mol/m^3. Contact angle between the rock and droplet equal to 0.6 rad (34.4°).

Table 2
Summary of equilibrium contact angle (in degrees) for different concentrations and external potentials.

γ_{so} [mN/m]	Hard Wall		Lifshitz	
	0.5 M	1.0 M	0.5 M	1.0 M
0.5	103	126	103	130
1.0	69	103	66	105
2.0	<5	69	<5	69

the profile of $\Omega[\{\rho_i(\mathbf{r})\}]$ presents a minimum within the range of contact angle analyzed. The impact of different values of γ_{so} (0.5, 1.0 and 2.0 mN/m) is showed in Table 2 and Figs. 7 and 8 for bulk ionic strength equal to 500 and 1000 mol/m^3, respectively. Considerable differences are observed between systems with different γ_{so}. Hence, the interaction oil/solid surface is fundamental to the definition of the contact angle. Considering γ_{so}, equal to 2.0 mN/m the system is completely water-wet for ρ_b equal to 500 mol/m^3 as observed in Fig. 7.

Table 3 gives the constants necessary to calculate the Hamaker constant by Lifshitz theory for Na^+ and Cl^- interacting with silica and n-pentane. According to the value of Hamaker constant both ions are attracted by silica. However, this effect is about 7 times stronger for chloride. Dispersion coefficients are presented in Table 4.

As it can be seen in Table 2, the dispersion interactions has little effect on the equilibrium contact angle compared to the hard wall potential considering the ions, solid and oil analyzed. Other components could provide different results, mainly if we consider charge on surfaces.

4. Conclusions

There are also several avenues for improvement of the model here proposed. The assumption of constant density and, hence, of a constant volume of oil droplet containing a given number of molecules was employed, however it is possible to refine the model aiming to consider the oil molecules explicitly inside the droplet. In such analysis the contribution due to the oil/solid surface interactions would be automatically included into the Ω_{DFT}. Another important contribution is the inclusion of charge on the solid surface, or even, on the oil surface.

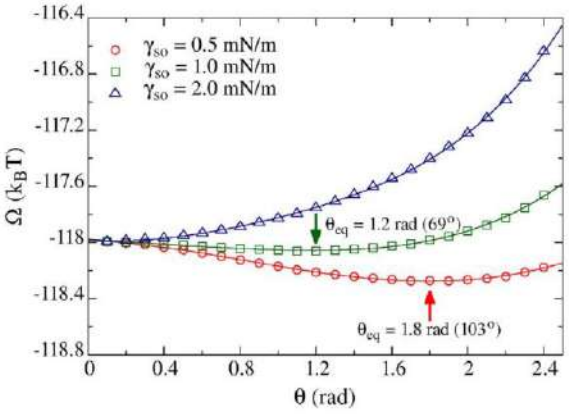

Fig. 7. Grand potential for the oil/brine (ρ^b = 0.5M)/rock system with nonelectrostatic interaction between brine and rock. The arrows refer to the equilibrium contact angle.

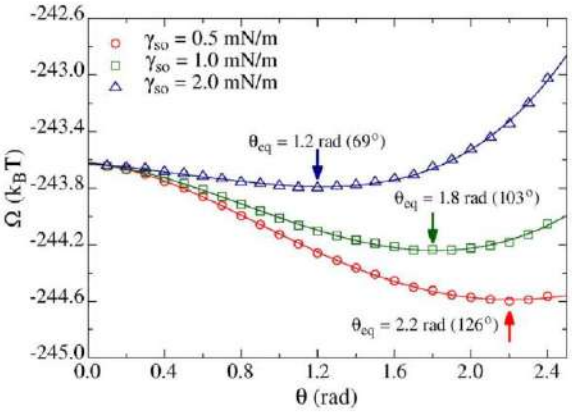

Fig. 8. Grand potential for the oil/brine (ρ^b = 1.0M)/rock system with nonelectrostatic interaction between brine and rock. The arrows refer to the equilibrium contact angle.

Table 3
Physical properties for water, silica, n-pentane and ions.

	dielectric constant	refractive index	polarizability [Å^3]	absorption frequency [10^{12} erg]
water	78.5[a]	1.333[a]	–	20[a]
pentane	1.84[a]	1.349[a]	–	20[a]
silica	3.8[a]	1.448[a]	–	20[a]
Na^+	–	–	0.1485[b]	54.7[b]
Cl^-	–	–	3.764[b]	9.15[b]

[a] From ref. [41].
[b] From ref. [44].

Table 4
Hamaker coefficients for ions.

ion	$\frac{B_{ion-pentane}}{k_BT}$ [Å^3]	$\frac{B_{ion-silica}}{k_BT}$ [Å^3]
Na^+	0.0678	0.578
Cl^-	0.552	4.248

The description of electrostatic correlation by more sophisticated theories is straightforward. Nevertheless it is important to evaluate the advantages of this change for each particular system, because, in general, they demand more computation time, specially for tridimensional DFT (3D-DFT).

We conclude that the approach presented here is promising to investigate the contact angle of different electrolyte solutions and the impact of the bulk concentration and ionic valence on the wettability. The tridimensional treatment turns the method versatile and provides options for inclusion of some peculiarities such as roughness on the solid surface and the presence of a thin film of brine between the oil and the solid.

Acknowledgement

For financial support, we are grateful to Petrobras and the Brazilian Agencies Coordination of Improvement of Higher Education Personnel (CAPES), Carlos Chagas Filho Research Support Foundation (FAPERJ) and National Council for Scientific and Technological Development (CNPq). We also thank the Brazilian National Laboratory for Scientific Computing (LNCC) and the Advanced High Performance Computing Center (NACAD) of the Federal University of Rio de Janeiro for the computational resources.

References

[1] Z. Xue, S. Wang, L. Lin, L. Chen, M. Liu, L. Feng, L. Jiang, A novel superhydrophilic and underwater superoleophobic hydrogel-coated mesh for oil/water separation, Adv. Mater. 23 (37) (2011) 4270–4273, https://doi.org/10.1002/adma.201102616.
[2] Z. Xue, Y. Cao, N. Liu, L. Feng, L. Jiang, Special wettable materials for oil/water separation, J. Mater. Chem. A 2 (8) (2014) 2445–2460, https://doi.org/10.1039/C3TA13397D.
[3] S. Aslan, N.F. Najafabadi, A. Firoozabadi, Non-monotonicity of the contact angle from NaCl and $MgCl_2$ concentrations in two petroleum fluids on atomistically smooth surfaces, Energy Fuels 30 (4) (2016) 2858–2864, https://doi.org/10.1021/acs.energyfuels.6b00175.
[4] S.J. Fathi, T. Austad, S. Strand, "Smart water" as a wettability modifier in chalk: the effect of salinity and ionic composition, Energy Fuels 24 (4) (2010) 2514–2519, https://doi.org/10.1021/ef901304m.
[5] P. Zhang, T. Austad, Wettability and oil recovery from carbonates: effects of temperature and potential determining ions, Colloids Surf., A 279 (1–3) (2006) 179–187, https://doi.org/10.1016/j.colsurfa.2006.01.009.
[6] H. Jabbari, K. Afsari, M. Rabiei, A. Monk, Thermally-induced wettability alteration from hot-water imbibition in naturally fractured reservoirs – Part 1: numerical model development & 1D models, Fuel 208 (2017) 682–691, https://doi.org/10.1016/j.fuel.2017.07.016.
[7] M. Amirpour, S.R. Shadizadeh, H. Esfandyari, S. Ahmadi, Experimental investigation of wettability alteration on residual oil saturation using nonionic surfactants: capillary pressure measurement, Petroleum 1 (4) (2015) 289–299, https://doi.org/10.1016/j.petlm.2015.11.003.
[8] A. Maghzi, S. Mohammadi, M.H. Ghazanfari, R. Kharrat, M. Masihi, Monitoring wettability alteration by silica nanoparticles during water flooding to heavy oils in five-spot systems: a pore-level investigation, Exp. Therm. Fluid Sci. 40 (2012) 168–176, https://doi.org/10.1016/j.expthermflusci.2012.03.004.
[9] N.R. Morrow (Ed.), Interfacial Phenomena in Petroleum Recovery, Marcel Dekker, New York (NY), 1991.
[10] V. Talanquer, D.W. Oxtoby, Nucleation on a solid substrate: a density functional approach, J. Chem. Phys. 104 (4) (1996) 1483–1492, https://doi.org/10.1063/1.470914.
[11] R. Evans, U.M.B. Marconi, P. Tarazona, Capillary condensation and adsorption in cylindrical and slit-like pores, J. Chem. Soc., Faraday Trans. 2 82 (1986) 1763–1787, https://doi.org/10.1039/f29868201763.
[12] P. Röcken, A. Somoza, P. Tarazona, G. Findenegg, Two-stage capillary condensation in pores with structured walls: a nonlocal density functional study, J. Chem. Phys. 108 (20) (1998) 8689–8697, https://doi.org/10.1063/1.476297.
[13] L. Wang, W. Zhang, X. Wang, J. Mi, J. Ma, Z. Du, The mechanism of roughness-induced CO_2 microbubble nucleation in polypropylene foaming, Phys. Chem. Chem. Phys. 19 (31) (2017) 21069–21077, https://doi.org/10.1039/C7CP02988H.
[14] G.O. Berim, E. Ruckenstein, Contact angle of a nanodrop on a nanorough solid surface, Nanoscale 7 (7) (2015) 3088–3099, https://doi.org/10.1039/C4NR06591C.
[15] A. Giacomello, L. Schimmele, S. Dietrich, M. Tasinkevych, Perpetual superhydrophobicity, Soft Matter 12 (43) (2016) 8927–8934, https://doi.org/10.1039/C6SM01727D.
[16] G.O. Berim, E. Ruckenstein, Calculation of nanodrop profile from fluid density distribution, Adv. Colloid Interface Sci. 231 (2016) 15–22, https://doi.org/10.1016/j.cis.2016.02.004.
[17] A.D. Polyanin, A.V. Manzhirov, Handbook of Mathematics for Engineers and Scientists, Chapman & Hall/CRC, Boca Raton, FL, 2007.
[18] R.G. dos Santos, R.S. Mohamed, A.C. Bannwart, W. Loh, Contact angle measurements and wetting behavior of inner surfaces of pipelines exposed to heavy crude oil and water, J. Pet. Sci. Eng. 51 (1–2) (2006) 9–16, https://doi.org/10.1016/j.petrol.2005.11.005.
[19] M.G. Knepley, D.A. Karpeev, S. Davidovits, R.S. Eisenberg, D. Gillespie, An efficient algorithm for classical density functional theory in three dimensions: ionic solutions, J. Chem. Phys. 132 (12) (2010) 124101, https://doi.org/10.1063/1.3357981.
[20] L.J.D. Frink, A.G. Salinger, M.P. Sears, J.D. Weinhold, A.L. Frischknecht, Numerical challenges in the application of density functional theory to biology and nanotechnology, J. Phys.: Condens. Matter 14 (2002) 12167–12187, https://doi.org/10.1088/0953-8984/14/46/320.
[21] J. Wu, Density functional theory for chemical engineering: from capillarity to soft materials, AIChE J. 52 (3) (2006) 1169–1193, https://doi.org/10.1002/aic.10713.
[22] R. Roth, R. Evans, A. Lang, G. Kahl, Fundamental measure theory for hard-sphere mixtures revisited: the White Bear version, J. Phys.: Condens. Matter 14 (46) (2002) 12063–12078, https://doi.org/10.1088/0953-8984/14/46/313.
[23] Y.-X. Yu, J. Wu, Structures of hard-sphere fluids from a modified fundamental-measure theory, J. Chem. Phys. 117 (22) (2002) 10156–10164, https://doi.org/10.1063/1.1520530.
[24] R. Roth, S. Dietrich, Binary hard-sphere fluids near a hard wall, Phys. Rev. E 62 (5) (2000) 6926–6936, https://doi.org/10.1103/PhysRevE.62.6926.
[25] M.P. Sears, L.J.D. Frink, A new efficient method for density functional theory calculations of inhomogeneous fluids, J. Comput. Phys. 190 (1) (2003) 184–200, https://doi.org/10.1016/S0021-9991(03)00270-5.

[26] Y. Rosenfeld, Free energy model for inhomogeneous fluid mixtures: Yukawa-charged hard spheres, general interactions, and plasmas, J. Chem. Phys. 98 (10) (1993) 8126–8148, https://doi.org/10.1063/1.464569.
[27] A. Oleksy, J.-P. Hansen, Microscopic density functional theory of wetting and drying of a solid substrate by an explicit solvent model of ionic solutions, Mol. Phys. 107 (23–24) (2009) 2609–2624, https://doi.org/10.1080/00268970903469022.
[28] D. Gillespie, W. Nonner, R.S. Eisenberg, Coupling Poisson–Nernst–Planck and density functional theory to calculate ion flux, J. Phys.: Condens. Matter 14 (2002) 12129–12145, https://doi.org/10.1088/0953-8984/14/46/317.
[29] Z. Wang, L. Liu, I. Neretnieks, The weighted correlation approach for density functional theory: a study on the structure of the electric double layer, J. Phys.: Condens. Matter 23 (17) (2011) 175002, https://doi.org/10.1088/0953-8984/23/17/175002.
[30] J. Jiang, D. Cao, D. Henderson, J. Wu, Revisiting density functionals for the primitive model of electric double layers, J. Chem. Phys. 140 (4) (2014) 044714, https://doi.org/10.1063/1.4862990.
[31] B. Groh, R. Evans, S. Dietrich, Liquid-vapor interface of an ionic fluid, Phys. Rev. E 57 (6) (1998) 6944–6954, https://doi.org/10.1103/PhysRevE.57.6944.
[32] O. Pizio, A. Patrykiejew, S. Sokołowski, Phase behavior of ionic fluids in slitlike pores: a density functional approach for the restricted primitive model, J. Chem. Phys. 121 (23) (2004) 11957–11964, https://doi.org/10.1063/1.1818677.
[33] O. Pizio, S. Sokołowski, Phase behavior of the restricted primitive model of ionic fluids with association in slitlike pores. Density-functional approach, J. Chem. Phys. 122 (14) (2005) 11957–11964. https://doi.org/10.1063/1.1883165.
[34] A. Patrykiejew, S. Sokołowski, O. Pizio, The liquid-vapor interface of the restricted primitive model of ionic fluids from a density functional approach, Condens. Matter Phys. 14 (1) (2011) 13603, https://doi.org/10.5488/CMP.14.13603.
[35] Y.-X. Yu, J. Wu, G.-H. Gao, Density-functional theory of spherical electric double layers and ζ potentials of colloidal particles in restricted-primitive-model electrolyte solutions, J. Chem. Phys. 120 (15) (2004) 7223–7233, https://doi.org/10.1063/1.1676121.
[36] L.B. Bhuiyan, S. Lamperski, J. Wu, D. Henderson, Monte Carlo simulation for the double layer structure of an ionic liquid using a dimer model: a comparison with the density functional theory, J. Phys. Chem. B 116 (34) (2012) 10364–10370, https://doi.org/10.1021/jp304362y.
[37] D. Henderson, S. Lamperski, Z. Jin, J. Wu, Density functional study of the electric double layer formed by a high density electrolyte, J. Phys. Chem. B 115 (44) (2011) 12911–12914, https://doi.org/10.1021/jp2078105.
[38] L. Blum, Y. Rosenfeld, Relation between the free energy and the direct correlation function in the mean spherical approximation, J. Stat. Phys. 63 (5–6) (1991) 1177–1190, https://doi.org/10.1007/BF01030005.
[39] Z. Li, J. Wu, Toward a quantitative theory of ultrasmall liquid droplets and vapor-liquid nucleation, Ind. Eng. Chem. Res. 47 (15) (2008) 4988–4995, https://doi.org/10.1021/ie070578i.
[40] K. Liu, J. Wu, Boosting the performance of ionic-liquid-based supercapacitors with polar additives, J. Phys. Chem. C 120 (2016) 24041–24047, https://doi.org/10.1021/acs.jpcc.6b09161.
[41] J.N. Israelachvili, Intermolecular and Surface Forces, 3rd Edition, Academic Press, Burlington, 2011.
[42] V. Deniz, D.F. Parsons, Effect of nonelectrostatic ion interactions on surface forces involving ion adsorption equilibria, J. Phys. Chem. C 117 (32) (2013) 16416–16428, https://doi.org/10.1021/jp404086u.
[43] B.W. Ninham, P. Lo Nostro, Molecular Forces and Self Assembly, Cambridge University Press, Cambrigde, 2010.
[44] F.W. Tavares, D. Bratko, H.W. Blanch, J.M. Prausnitz, Ion-specific effects in the Colloid–Colloid or Protein–Protein potential of mean force: role of Salt–Macroion van der Waals interactions, J. Phys. Chem. B 108 (26) (2004) 9228–9235, https://doi.org/10.1021/jp037809t.
[45] W.M. Haynes (Ed.), CRC Handbook of Chemistry and Physics, 97th Edition, CRC Press, Boca Raton, 2017.

APPENDIX I – Development of an AMBER-compatible transferable force field for poly(ethylene glycol) ethers (glymes)

BARBOSA, N. S. V.; ZHANG; Y. LIMA, E. R. A.; TAVARES, F. W; MAGINN, E. Development of an AMBER-compatible transferable force field for poly(ethylene glycol) ethers (glymes). *J. Mol. Model.*, v. 23, n. 6, p. 194, 2017.

J Mol Model (2017) 23:194
DOI 10.1007/s00894-017-3355-3

ORIGINAL PAPER

Development of an AMBER-compatible transferable force field for poly(ethylene glycol) ethers (glymes)

Nathalia S. V. Barbosa[1] · Yong Zhang[2,3] · Eduardo R. A. Lima[1] · Frederico W. Tavares[4,5] · Edward J. Maginn[2,3]

Received: 10 February 2017 / Accepted: 24 April 2017

Abstract An all-atom force field consistent with the general AMBER force field (GAFF) format for poly(ethylene glycol) dimethyl ether (diglyme or G2) was developed by fitting to experimental liquid densities and dielectric constants. Not surprisingly, the new force field gives excellent agreement with experimental liquid phase densities and dielectric constants over a wide temperature range. Other dynamic and thermodynamic properties of liquid G2 such as its self-diffusion coefficient, shear viscosity, and vaporization enthalpy were also calculated and compared to experimental data. For all of the properties studied, the performance of the proposed new force field is better than that of the standard GAFF force field. The force field parameters were transferred to model two other poly(ethylene glycol) ethers: monoglyme (G1) and tetraglyme (G4). The predictive ability of the modified force field for G1 and G4 was significantly better than that of the original GAFF force field. The proposed force field provides an alternative option for the simulation of mixtures containing glymes using GAFF-compatible force fields, particularly for electrochemical applications. The accuracy of a previously published force field based on the OPLS-AA format and the accuracies of two modified versions of that force field were also examined for G1, G2, and G4. It was found that the original OPLS-AA force field is superior to the modified versions of it, and that it has a similar accuracy to the proposed new GAFF-compatible force field.

Keywords Glymes · Transferability · General AMBER force field · Dielectric constant

Electronic supplementary material The online version of this article (doi:10.1007/s00894-017-3355-3) contains supplementary material, which is available to authorized users.

✉ Frederico W. Tavares
tavares@eq.ufrj.br

✉ Edward J. Maginn
ed@nd.edu

[1] Programa de Pós-graduação em Engenharia Química, Universidade do Estado do Rio de Janeiro, Rio de Janeiro, RJ 20550-013, Brazil

[2] Department of Chemical and Biomolecular Engineering, University of Notre Dame, Notre Dame, IN 46556, USA

[3] Joint Center for Energy Storage Research, University of Notre Dame, Notre Dame, IN 46556, USA

[4] Escola de Química, Universidade Federal do Rio de Janeiro, Rio de Janeiro, RJ 21941-909, Brazil

[5] Programa de Engenharia Química, COPPE, Universidade Federal do Rio de Janeiro, Rio de Janeiro, RJ 21941-914, Brazil

Introduction

Glymes (also known as glycol diethers) are aprotic saturated polyethers containing no other functional groups. Most glymes present a large liquid range, high electrochemical stability, a relatively low vapor pressure, high solubility in water and organic solvents, and strong solvating power towards alkali metal ions [1–5]. They have been used as solvents in many laboratory and industrial applications, including reactions (e.g., organometallic reactions, polymerization, reactions involving alkali metals, oxidation, and reduction), extraction, gas scrubbing, refrigeration, adhesive and coating formulations, electronics industry, and pharmaceutical formulations [2, 6–8].

Recently, due to the high donor numbers and relatively strong Lewis basicities of glymes, mixtures of them with alkali metal salts have been widely investigated as potential electrolytes for batteries [2, 6–8]. Molecular modeling studies using classical force fields can provide insight into the energy storage capacities of these systems [6, 9–11]. The reliability of such atomistic computer simulations for predicting the

Published online: 26 May 2017

behavior of a material depends strongly on the accuracy of the force fields that are used to describe the interactions in the system of interest. If the essential physical interactions of molecules are represented faithfully, molecular simulations can reliably predict properties.

In 1993, Smith, Jaffe, and Yoon constructed a force field [12] specifically for monoglyme (G1) and poly(ethylene oxide), based on the results of ab initio orbital calculations performed at the MP2 level using the D95 + (2df,p) basis set and geometries optimized at the SCF level using the D95** basis set for G1 [13]. The nonbonded interactions were described by the Coulomb–Buckingham potential with Buckingham parameters taken from a force field used to describe the crystal structures and energetics of polyoxymethylene. In this force field, bond and angle terms are treated harmonically, and dihedral terms [12, 14] are compatible with the CHARMM force field [15]. This force field has been used in a number of simulations involving G1 in an aqueous environment [16–20]. However, because the force fields most commonly employed for organic molecules use Lennard-Jones and Coulombic potentials to describe nonbonded interactions, these force fields often lead to compatibility problems when applied to mixtures, as the force fields for some species use different approaches to nonbonded interactions.

One force field commonly used in classical simulations of organic molecules is the OPLS-AA (Optimized Potentials for Liquid Simulations—All Atom) developed by Jorgensen and coworkers [21]. The OPLS-AA force field with constrained lengths of bonds that include hydrogen atoms was used in recent simulations of triglyme (G3) and tetraglyme (G4) mixed with equimolar amounts of lithium salts [8].

Over the years, some modifications to the OPLS-AA force field have been proposed in order to achieve more accurate descriptions of glyme molecules [6, 9, 22]. When using the original OPLS-AA force field [21], the population of the *tgg'* conformation of G1 molecules was found to be underestimated, whereas that of the *tgt* conformation was overestimated. Underestimation of the population of the *tgg'* conformation was also observed when using the force field of Smith and coworkers [12, 23]. In order to improve the agreement between the simulated conformer population of G1 in the bulk liquid and experimental Raman spectroscopic results [24], Anderson and Wilson proposed two different force fields in which the torsion angle parameters were revised based on either MP2/6–31++G′(d,p) ab initio calculations of G1 or an extensive reverse-engineering procedure [22].

Watanabe and coworkers proposed modifications to the OPLS-AA force field for glymes that involved assigning the partial atomic charges based on molecular orbital calculations at the MP2/cc-pvTZ(−f) // HF/6-31G(d) level of theory [6]. All of the other parameters were taken from the original OPLS-AA force field [21], with the exception of the torsion angle parameters, which were taken from [22]. However, Watanabe and coworkers did not specify which set of torsion angle parameters suggested by Anderson and Wilson were adopted. In addition, instead of the geometric combining rule typically used in the OPLS-AA force field, Watanabe and coworkers suggested the use of the Lorentz–Berthelot combining rule for the Lennard-Jones parameters [6].

A different version of the modified OPLS-AA force field [21] was also proposed by Watanabe and coworkers in a separate study of G3 and G4 molecules [9]. In that force field, modifications were made to the bond-stretching, angle-bending, torsion-angle, and nonbonded parameters. All of the C–H bonds were held rigid in this force field [9].

Other force fields that are widely used in simulations of organic molecules include the AMBER force field [25] and the general AMBER force field (GAFF) [26]. Due to differences in, for example, the mixing rule used for the Lennard-Jones parameters, the scaling factors for 1–4 nonbonded Coulombic interactions, and the functional form of torsional angles, AMBER and GAFF are usually not compatible with OPLS-AA-based force fields. Using the first version of the AMBER force field (AMBER94) [25], Dong and coworkers performed studies of amorphous G4 at 300 K with constrained bond lengths [27]. The experimental density at this temperature was reproduced with an error of <1%. However, parameters such as the atomic partial charges and the procedure used to derive the atomic partial charges were not provided in their paper.

The GAFF model [26] with partial atomic charges derived using the restrained electrostatic potential (RESP) method [28] has been shown to be a convenient and reliable force field, and has been widely used for the simulation of various organic molecules [29, 30]. Note that, unlike some force fields, the convention in GAFF is to derive unique partial charges for individual molecules. However, GAFF was found to be inaccurate when used to simulate glymes; for example, when the partial charges derived at the B3LYP/6–311++G(d,p) level were used, the density in the range 288.15–423.15 K was overestimated by ~6.5% and the dielectric constant was overestimated by ~20%.

In addition to all-atom models, other types of force fields for glymes can also be found in the literature. For example, Cordeiro, Zschunke, and Müller-Plathe developed a coarse-grained force field [31] for polyglymes based on Smith and coworkers' all-atom force field [12]. In this force field, the superatom was defined as CH_n—O—CH_2, where n was either 2 or 3. Electrostatic interactions were not explicitly considered in this model [31]. The Transferrable Potential for Phase Equilibria force field (TraPPE-UA) is a united atom force field originally developed by Siepmann and coworkers [32]. A modified version of the TraPPE-UA force field for poly(oxyethylene) oligomers [33, 34] has been shown to more accurately describe the conformer population of G1 in water than the original TraPPE-UA force field does.

Given these developments, and considering the popularity of GAFF in simulations of organic molecules that include ionic systems, it is unfortunate that there is not an accurate GAFF-compatible force field for glymes. Therefore, the aim of the work reported in the present paper was to develop an all-atom force field for diglyme (G2) that is compatible with GAFF [26]. Considering the importance of glymes as solvents for batteries, efforts were made to reproduce experimental densities and dielectric constants over a wide temperature range. Values for the enthalpy of vaporization, self-diffusion coefficient, and shear viscosity were also computed and compared with available experimental data. Transferability to other glymes such as G1 and G4 was evaluated. The accuracies of several existing glyme force fields were also assessed.

Given an accurate force field for simulating pure glymes, it will be possible in future studies to examine mixtures of glymes with other compounds that are modeled accurately using GAFF, such as ionic liquids and alkali halide salts for electrochemical applications.

Computational methods

Molecular dynamics simulation

Unless otherwise specified, the following MD simulation procedures were used. The simulation box was built by putting 200 glyme molecules randomly in a cubic box using the package Packmol [35, 36]. This system was simulated in the isothermal-isobaric (NPT) ensemble. Periodic boundary conditions were applied, and a time step of 1 fs was used. The temperature T and the pressure P were maintained via the Nosé–Hoover thermostat [37] and the extended Lagrangian approach [38], respectively. The latter was always set to atmospheric pressure. The cutoff for nonbonded interactions was set to 12 Å, with a long-range van der Waals tail correction. The long-range Coulombic interactions were estimated using the particle-particle particle-mesh (PPPM) method [39] to a precision of 10^{-4}. Each simulation was run for 10 ns, while configurations were recorded every 0.2 ps. The first 0.5 ns of each trajectory was treated as equilibration and was not considered in the equilibrium averages. All simulations were performed with the LAMMPS simulation package [40].

Force field

The following GAFF functional form was used to describe the intra- and intermolecular interactions [26]:

$$U_{\mathrm{tot}} = \sum_{\mathrm{bonds}} k_r\left(r-r_{\mathrm{eq}}\right)^2 + \sum_{\mathrm{angles}} k_\theta\left(\theta-\theta_{\mathrm{eq}}\right)^2 + \sum_{\mathrm{dihedrals}} k_\chi\left[1+\cos\left(n\chi-\delta_\chi\right)\right] + \sum_{i=1}^{N-1}\sum_{i<j}^{N}\left\{4\varepsilon_{ij}\left[\left(\frac{\sigma_{ij}}{r_{ij}}\right)^{12}-\left(\frac{\sigma_{ij}}{r_{ij}}\right)^{6}\right]+\frac{q_i q_i}{4\pi\varepsilon_0 r_{ij}}\right\}, \quad (1)$$

where the total energy is expressed in terms of bond stretching, angle bending, dihedral torsion, and both Lennard-Jones and electrostatic interactions. Arithmetic and geometric combining rules were used for σ_{ij} and ε_{ij}, respectively. Furthermore, intramolecular pairwise Lennard-Jones and Coulombic interactions that were separated by one and two bonds (so-called 1–2 and 1–3 interactions) were set to 0.0, whereas intramolecular interactions separated by three bonds (so-called 1–4 interactions) were scaled by 0.5 and 5/6 for Lennard-Jones and Coulombic interactions, respectively.

The atomic partial charge on each atom was derived with the RESP method [28], based on the optimized structure of each isolated molecule calculated at the B3LYP/ 6–311++ G(d,p) level using the Gaussian 09 package [41].

In order to improve the accuracy of the calculated density and the dielectric constant of G2, the Lennard-Jones parameters of the original GAFF were modified with all the other parameters untouched. To make the modification proposed for G2 easily transferable to other glymes, the same scaling factors of σ^{LJ} and ϵ^{LJ} were used for other glyme atoms.

Calculation of bulk properties

Static dielectric constant

According to the Ewald approach using conducting metal (tinfoil) boundary conditions, the static dielectric constant ε is given by [42]

$$\varepsilon = 1 + \frac{\left(\langle \boldsymbol{M}^2\rangle - \langle \boldsymbol{M}\rangle^2\right)}{3\langle V\rangle \varepsilon_0 k_{\mathrm{B}} T}, \quad (2)$$

where $\langle \boldsymbol{M}^2\rangle - \langle \boldsymbol{M}\rangle^2$ is the fluctuation of the total dipole moment of the system and,

$$\boldsymbol{M} = \sum_{i=1}^{N} \boldsymbol{\mu}_i, \quad (3)$$

where $\boldsymbol{\mu}_i$ is the dipole moment of molecule i in the system, ε_0 is the vacuum permittivity, k_{B} is the Boltzmann constant, and $\langle V\rangle$ is the average volume of the simulation system. At low temperatures, the convergence of $\langle \boldsymbol{M}^2\rangle - \langle \boldsymbol{M}\rangle^2$ can be rather slow due to the long fluctuation autocorrelation times.

Self-diffusion coefficient

The self-diffusion coefficient D was computed from the slope of the mean squared displacement (MSD) as a function of time according to the Einstein equation

$$D = \frac{1}{6}\lim_{t\to\infty}\frac{d}{dt}\langle\left[\boldsymbol{r}(t_0+t)-\boldsymbol{r}(t_0)\right]^2\rangle, \quad (4)$$

where $r(t)$ is the position of the center of mass of a molecule at time t, and the brackets $\langle\cdots\rangle$ denote an average over both time origins and individual molecules.

Viscosity

The shear viscosity was calculated from the integral over time of the stress tensor autocorrelation function according to the Green–Kubo relation:

$$\eta = \frac{V}{k_B T}\int_0^\infty \langle \tau_{\alpha\beta}(t_0 + t)\cdot\tau_{\alpha\beta}(t_0)\rangle \mathrm{d}t, \quad (5)$$

where $\tau_{\alpha\beta}$ denotes the $\alpha\beta$ component of the stress tensor. Six independent terms of the stress tensor, i.e., τ_{xy}, τ_{yz}, τ_{zx}, $0.5(\tau_{xx}-\tau_{yy})$, $0.5(\tau_{yy}-\tau_{zz})$, and $0.5(\tau_{xx}-\tau_{zz})$, are averaged in Eq. 5 [43]. The shear viscosity must be estimated from a finite time plateau region of the integral, but identifying the constant region can be difficult when only one trajectory is considered [44]. To avoid this problem, the time-decomposition method [44–46] was used. Thirty independent trajectories of 5 ns in the canonical (NVT) ensemble were generated at a given temperature T. The stress tensor was saved every 5 fs for each trajectory. The first 1 ns of each trajectory was considered equilibration and discarded, while the rest of the trajectory was used to calculate the integral in Eq. 5. The average of the running integrals over the 30 trajectories $\langle\eta(t)\rangle$ and the standard deviation as a function of time,

$$\sigma(t) = \sqrt{\frac{1}{m-1}\sum_{i=1}^{m}\left(\eta(t)_i - \langle\eta(t)\rangle\right)^2}, \quad (6)$$

where m is the number of independent trajectories, were computed. The standard deviation was fitted to a power function $\sigma(t) = A \times t^b$.

An empirical double-decay exponential function of the form

$$\eta(t) = A\alpha\tau_1\left(1-\mathrm{e}^{-t/\tau_1}\right) + A(1-\alpha)\tau_2\left(1-e^{-t/\tau_2}\right) \quad (7)$$

was used to fit the average running integral up to a cutoff time t_{cut}, where $1/t^b$ is the weighting function and A, α, τ_1, and τ_2 are fitting parameters. The parameter t_{cut} is the time required for the standard deviation to reach 30% of the estimated viscosity of the system [44–46].

Enthalpy of vaporization

The molar enthalpy of vaporization Δh_{vap} can be calculated via

$$\Delta h_{vap}(T,P) = \langle h_{gas}(T,P)\rangle - \langle h_{liq}(T,P)\rangle, \quad (8)$$

where $\langle h_{gas}(T,P)\rangle$ and $\langle h_{liq}(T,P)\rangle$ are the molar average enthalpies in the gas and liquid phases, respectively, at temperature T and pressure P. The molar average enthalpy in the liquid phase is

$$\langle h_{liq}(T,P)\rangle = \langle u_{liq}(T,P)\rangle + Pv_{liq}, \quad (9)$$

and, assuming that the gas is ideal, the average molar enthalpy in the gas phase is

$$\langle h_{gas}(T)\rangle = \langle u_{gas}(T)\rangle + Pv_{gas} = \langle u_{gas}(T)\rangle + RT, \quad (10)$$

where u is the molar internal energy, R is the gas constant, and v is the molar volume.

The term Pv_{liq} is negligible because the magnitude of this term is much smaller than the molar internal energy in the liquid phase. Equation 8 can then be written as

$$\Delta h_{vap}(T,P) = \langle u_{gas}(T)\rangle + RT - \langle u_{liq}(T,P)\rangle. \quad (11)$$

The simulations of the gas phase were performed with one molecule of glyme in the canonical ensemble in a large, nonperiodic box to prevent edge effects.

Results and discussion

Development of a general AMBER force field (GAFF)-compatible force field for diglyme

To improve the prediction of the liquid density and the dielectric constant at temperatures between 288.15 K and 423.15 K, the Lennard-Jones parameters σ^{LJ} and ϵ^{LJ} of G2 in the original GAFF force field were systematically modified by applying the scaling parameters f^σ and f^ε, respectively. The 3D graphic in Fig. 1 shows the correlation between the values of the scaling parameters f^σ and f^ε and the computed liquid density

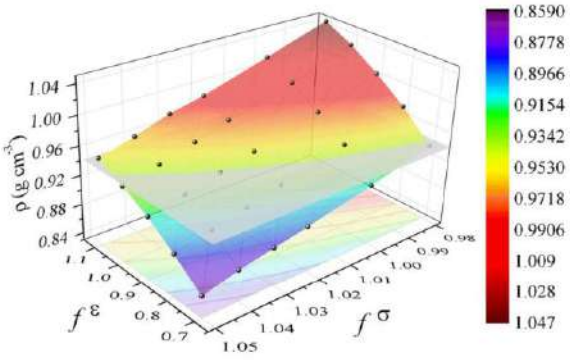

Fig. 1 Correlation between different values of the Lennard-Jones scaling parameters f^σ and f^ε for G2 and the calculated liquid density at 298.15 K. The *gray plane* represents the experimental density of G2 at this temperature [47]

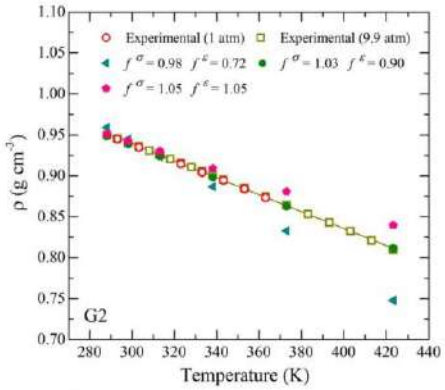

Fig. 2 Comparison of experimental [47, 48] (*open symbols*) and computed (*filled symbols*) values of the density of liquid G2 as functions of temperature. The density values computed using three different combinations of f^{σ} and f^{ε} are provided. All three combinations were found to be able to reproduce the experimental density of G2 at 298 K

of G2 at 298.15 K. The density decreases with increasing f^{σ} and decreasing f^{ε}. Intuitively it makes sense that the atoms tend to be further apart when the interparticle potentials are zero (σ^{LJ}); as they get closer, the well depth (ϵ^{LJ}) increases because the attraction between the atoms strengthens. The gray plane in Fig. 1 represents the experimental density of G2 at 298.15 K: 939.61 kg m^{-3} [47]. The intersection of the two planes defines a line where the experimental density is exactly reproduced by combinations of f^{σ} and f^{ε}.

The temperature dependence of the density was also studied for the scaling parameter combinations that reproduce the liquid density at 298 K. The calculated density values of G2 obtained with three combinations of f^{σ} and f^{ε} are shown in Fig. 2. Also provided in the figure are two sets of experimental density values of G2: those obtained at 1 atm [47] and 9.9 atm [48]. It can be seen in Fig. 2 that the density of liquid G2 is insensitive to pressure in this pressure range, and that the density values obtained under the two pressures are almost

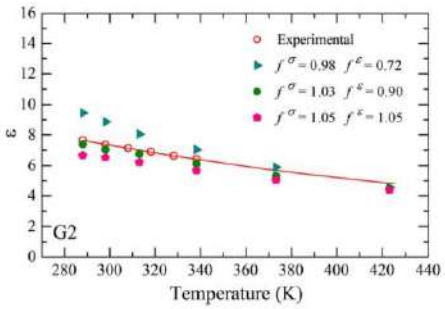

Fig. 3 Comparison of experimental [49] (*open symbols*) and computed (*filled symbols*) values of the dielectric constant for G2 molecules as functions of temperature. The computed dielectric constant values obtained using three different combinations of f^{σ} and f^{ε} are provided

Table 1 Bond parameter values from GAFF [26]

Bond	k_r/k_B (K/Å^2)	r_{eq} (Å)
C—C	152,526.0	1.535
C—O	151,721.0	1.439
C—H	169,031.0	1.093

the same at the same temperature. Therefore, the experimental density at 9.9 atm was compared with the computed density at high temperature. For f^{σ} = 0.98 and f^{ε} = 0.72, the computed density values underestimate the experimental values obtained at high temperature, whereas those obtained at low temperatures match each other. On the other hand, the experimental density values were overestimated at high temperature with f^{σ} = 1.05 and f^{ε} = 1.05. The combination of f^{σ} = 1.03 and f^{ε} = 0.9 was found to reproduce the experimental density values across the entire temperature range.

The effects of the scaling parameters f^{σ} and f^{ε} on the dielectric constant were also studied. The calculated dielectric constant values as a function of temperature obtained using the same three sets of f^{σ} and f^{ε} are shown in Fig. 3. Each point in the plot corresponds to an average of four independent trajectories. Qualitatively, the dielectric constant decreases with increasing f^{σ}. The impact of f^{ε} on the slope of the dielectric constant versus temperature curve is very small compared to that of f^{σ}. For f^{σ} = 0.98 and f^{ε} = 0.72, the calculated dielectric constant values at low temperatures overestimate the experimental values. On the other hand, the computed dielectric constant values at low temperatures underestimate the experimental values with f^{σ} = 1.05 and f^{ε} = 1.05. Combining the results for both the liquid density and the dielectric constant, the combination of f^{σ} = 1.03 and f^{ε} = 0.9 was found to be able to reproduce the experimental values accurately over the entire temperature range studied in this work. This combination of scaling parameters was chosen for use in subsequent simulations of liquid G2.

As previously mentioned, the bond, angle, and dihedral parameter values of the new force field are the same as those of the original GAFF model [26]. These parameter values are summarized in Tables 1, 2, and 3, respectively. The modified values of the Lennard-Jones parameters are shown in Table 4. In Fig. 4, the partial charges on the atoms of G2 derived using the RESP method [28] based on the optimized structure of the isolated molecule calculated at the B3LYP/ 6–311++G(d,p) level are presented.

Table 2 Angle parameter values from GAFF [26]

Angle	k_θ/k_B (K/rad^2)	θ_{eq} (deg)
C—O—C	31,396.0	112.45
H—C—H	19,716.0	109.55
H—C—O	25,584.0	108.82
C—C—O	34,108.0	108.42
C—C—H	23,329.0	110.07

Table 3 Dihedral parameter values from GAFF [26]

Dihedral	n_i	k_χ/k_B (K)	δ_χ (deg)
H–C–O–C	3	192.730	0.0
C–C–O–C	3	192.730	0.0
C–C–O–C	2	50.320	180.0
H–C–C–O	1	125.800	0.0
O–C–C–O	3	72.460	0.0
O–C–C–O	2	591.280	0.0
H–C–C–H	3	78.500	0.0

Figure 5 presents a comparison of the experimental [47, 48] and computed liquid density values of G2 as a function of temperature obtained using the original GAFF model [26] with charges from B3LYP/ 6–311++G(d,p) (labeled "GAFF") and the modified force field proposed here (labeled "modified GAFF").

The original GAFF systematically overestimates the experimental density values in the studied temperature range with a relative error of around 6.5%. On the other hand, the density values calculated using the modified GAFF force field proposed in the current work agree very well with the experimental values over the whole temperature range (relative error <0.5%).

The thermal expansivity, defined as

$$\alpha_P = \frac{1}{V}\left(\frac{\partial V}{\partial T}\right)_P = -\frac{1}{\rho}\left(\frac{\partial \rho}{\partial T}\right)_P, \quad (12)$$

was calculated using each force field. The result obtained using the modified GAFF proposed in the current work is in excellent agreement with experimental values (the result obtained with the modified GAFF is overlaid on the experimental result in Fig. 6b).

The dielectric constant values of liquid G2 computed using original and modified GAFF force fields are presented in Fig. 7 as functions of temperature. Each point in the plot corresponds to an average of four independent trajectories. Figure 7 shows that the dielectric constant values computed using the original GAFF force field are overestimated relative to the experimental values [49] by 9–21%. The accuracy is significantly improved by using the modified GAFF, which yields errors of 5%.

Table 4 Lennard-Jones parameter values in the modified force field of G2

Atom	ϵ^{LJ}/k_B (K)	σ^{LJ} (Å)
C	49.547	3.502
O	76.992	3.090
H	7.111	2.545

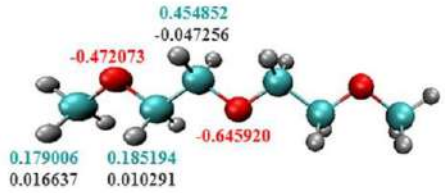

Fig. 4 Partial charge (in e) on each atom, as obtained from the RESP method [28] based on the optimized structure of an isolated G2 molecule calculated at the B3LYP/ 6-311++G(d,p) level

Other properties of diglyme

As described in the previous section, the force field parameters developed for G2 in the current work were optimized to reproduce the experimental density and dielectric constant as functions of temperature. Other properties were also studied using the newly developed parameters to check their performance.

Self-diffusion coefficient

Figure 8 shows the self-diffusion coefficient values of G2 calculated using the original and modified GAFF force fields as functions of temperature. Each point in the plot corresponds to an average over four different 10-ns trajectories.

The data were fitted to the Arrhenius equation

$$D = D_0 exp\left(-\frac{E_D}{RT}\right), \quad (13)$$

with weighting equal to $1/\sigma^2$, where E_D is the activation energy for self-diffusion and σ is the standard deviation. The activation energy values calculated based on the experimental and computed self-diffusion coefficients are listed in Table 5.

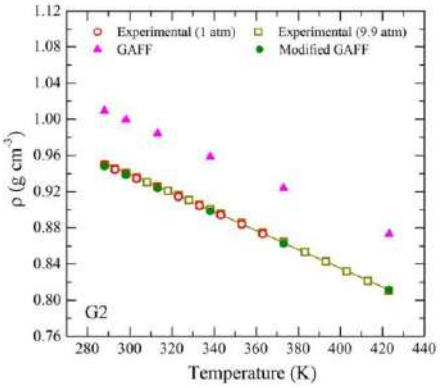

Fig. 5 Experimental [47, 48] (*open symbols*) and computed (*filled symbols*) values of the density of liquid G2 as functions of temperature

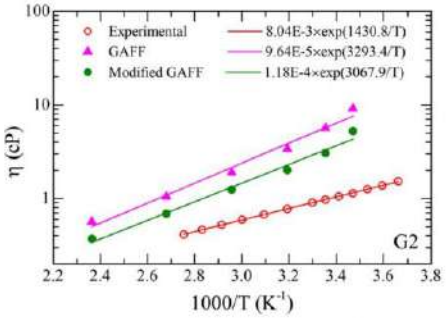

Fig. 9 Viscosity of G2 as a function of temperature. Simulation data are shown as *filled symbols* and experimental data [47] as *open symbols*

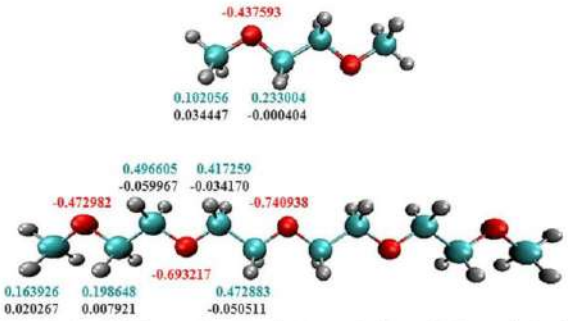

Fig. 10 Partial charges (in *e*) on the atoms in G1 and G4, as obtained using the RESP method [28] based on the optimized structure of each isolated molecule calculated at the B3LYP/ 6-311++G(d,p) level

obtained by uniformly scaling the σ^{LJ} and ϵ^{LJ} parameters from the original GAFF. This transferability was tested by studying the G1 and G4 systems using the same values of the scaling parameters (f^{σ} = 1.03 and f^{ε} = 0.9) as those found to be optimal for G2.

Following the same procedure applied to G2, the partial charges on the atoms in G1 and G4 were derived from the RESP method [28] based on the optimized structure of each isolated molecule calculated at the B3LYP/ 6-311++G(d,p) level. The results are presented in Fig. 10.

Density and thermal expansivity

The densities of G1 and G4 were calculated using the modified GAFF force field with the same values of the scaling parameters f^{σ} = 1.03 and f^{ε} = 0.9 as those found to be optimal for G2. The results are provided in Fig. 11. Deviations between the simulated and experimental [47, 48] densities are around 2% when using the modified GAFF for both G1 and G4 (Fig. 11b, e), whereas the relative error was found to be 5% and 8% when the original GAFF was used for G1 and G4, respectively. In addition, the thermal expansivity values calculated using the modified GAFF proposed in the current work also agree very well with the experimental values (Fig. 11c, f).

Table 6 Experimental [1] and computed values for the molar enthalpy of vaporization ΔH_{vap} of G2 at 298.15 K

	ΔH_{vap} (kJ/mol)	Relative error (%)
Experimental	44.69[a]	-
GAFF	64.34	44.0
Modified GAFF	60.25	34.8

[a] From [1]

Static dielectric constant

Figure 12 shows a comparison of experimental and computed dielectric constant values obtained using the original and modified GAFF force fields for G1 and G4. For the modified GAFF, the errors are consistently around 11% and 10% for G1 and G4, respectively, whereas the original GAFF [26] predicts an accurate dielectric constant for G1 (relative error <4.6%) but yields a much higher error of 17% in the dielectric constant for G4.

It is worth mentioning that, in the simulations of G4 (Fig. 12b), the error appears to increase significantly at low temperatures. A decrease in the calculated dielectric constant with decreasing temperature at temperatures <313.15 K is also observed, which contrasts with the experimental trend. Such behavior is probably due to the fact that the convergence can be rather slow because of very long fluctuation autocorrelation times in larger molecules, and because the dynamics of G4 at low temperatures are slower than those of G1 and G2.

Self-diffusion coefficient

Figure 13 shows values for the the self-diffusion coefficients and Table 7 presents values for the activation energies calculated by fitting the Arrhenius expression to self-diffusion coefficient data obtained at various temperatures for G1 and G4. Experimental self-diffusivity data could not be found in the literature for G1. The calculated self-diffusion coefficients obtained using both force fields are rather similar, as illustrated by Fig. 13a and Table 7 (the activation energy values of G1 calculated using both GAFF-based force fields are very similar).

For G4, the self-diffusion coefficient was only calculated at high temperatures due to slow dynamics at low temperatures. In Fig. 13b, it is apparent that both force fields underestimate the experimental self-diffusivity [52], as also seen for G2. The results calculated using the modified GAFF have relatively large errors, but it still performs better than the original GAFF.

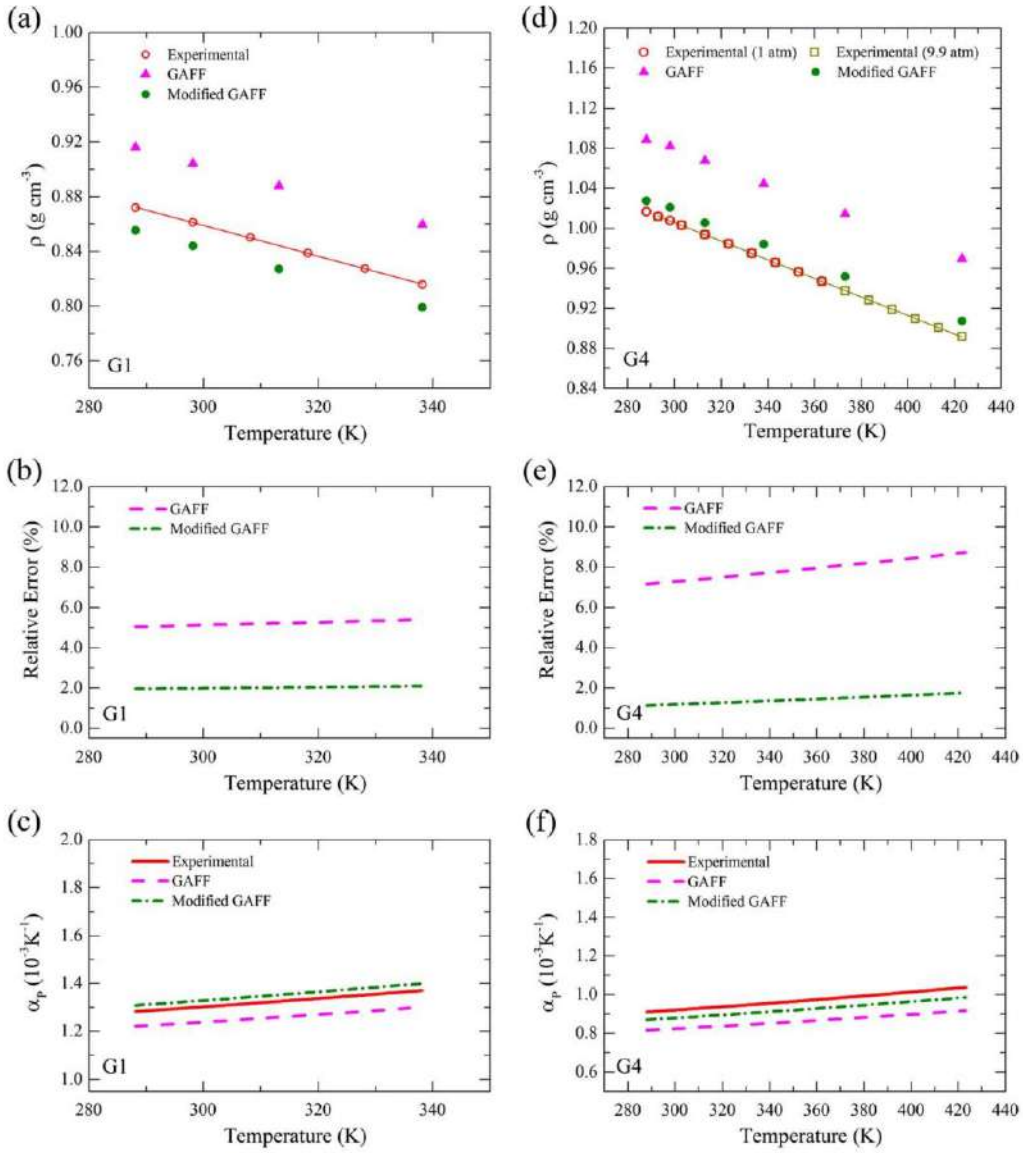

Fig. 11a–f Plots of experimental [47, 48] (*open symbols*) and computed (*filled symbols*) values of the density (**a** and **d**), relative errors in the computed density values (**b** and **e**), and thermal expansivity values (**c** and **f**) for G1 (*left column*) and G4 (*right column*) molecules versus temperature

Shear viscosity

An improvement in the accuracy of the shear viscosity calculated using the modified GAFF compared to that calculated with the original GAFF can be seen for G1 and G4 (Fig. 14). For G1, the slope of the logη versus 1000/T curve, where η was calculated using the modified GAFF force field developed in this work, is very close to the slope obtained using the corresponding experimental shear viscosity data [53] (Fig. 14a), with the simulation results consistently overestimating the shear viscosity by a factor of ~1.5. For G4, however, the viscosity values calculated using the modified GAFF force field are 2.5–7.1 times the experimental data.

Enthalpy of vaporization

The calculated enthalpies of vaporization are summarized in Table 8 together with available experimental data. Similar to what was seen for G2, both GAFF-based force fields overestimate the molar enthalpy of vaporization for both G1 and G4.

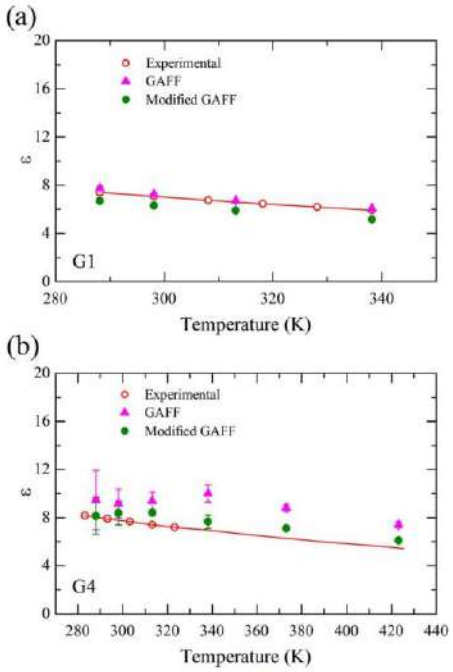

Fig. 12a–b Plots of experimental [49, 51] (*open circles*) and computed (*filled symbols*) values for the dielectric constants of G1 (**a**) and G4 (**b**) versus temperature

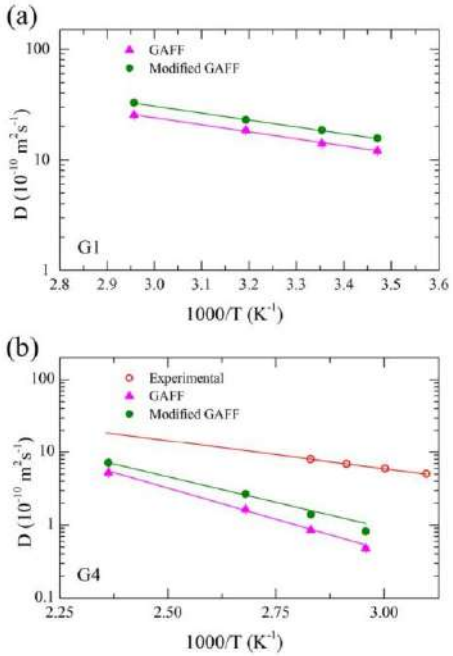

Fig. 13a–b Plots of the self-diffusion coefficients of G1 (**a**) and G4 (**b**) versus temperature. Simulation data are shown by *filled symbols* and available experimental data [52] are depicted as *open symbols*. *Lines* are fits to the Arrhenius expression

Table 7 Activation energies of G1 and G4 calculated by fitting the Arrhenius expression to self-diffusion coefficient data obtained at various temperatures

	$E_D^{G_1}$ (kJ/mol)	$E_D^{G_4}$ (kJ/mol)
Experimental	—	14.84[a]
GAFF	12.21	32.91
Modified GAFF	12.01	27.34

[a] From [52]

Compared to the experimental values, the results obtained using the original GAFF force field have relative errors of 9.6% for G1 and 46.7% for G4, respectively. Using the modified GAFF, the agreement with the experimental values is improved for both G1 (relative error of 3.8%) and G4 (relative error of 36.4%).

Conformer population distribution

The G1 conformer population distribution in the liquid phase was studied in the simulations. The calculated distribution of the five most populated conformers of G1 (*ttt*, *tgt*, *ttg*, *tgg*, and *tgg'*) was compared with the experimental distribution obtained using Raman spectroscopy [24]; see Fig. 15. The populations of the *ttt*, *ttg*, and *tgg'* conformations are slightly underestimated by both the original GAFF and the modified GAFF, whereas that of the *tgt* conformer was slightly

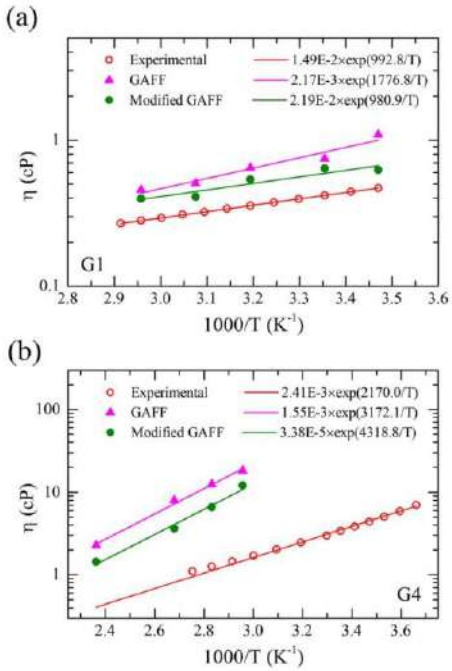

Fig. 14a–b Plots of experimental and calculated viscosity values for G1 (**a**) and G4 (**b**) versus temperature. Simulation data are shown as *filled symbols* and experimental data [47, 53] as *open symbols*

Table 8 Experimental and computed values of the molar enthalpy of vaporization ΔH_{vap} for G1 and G4 at 298.15 K

	Monoglyme		Tetraglyme	
	ΔH_{vap} (kJ/mol)	Error (%)	ΔH_{vap} (kJ/mol)	Error (%)
Experimental	36.39[a]	—	76.9[b]	—
GAFF	39.89	9.6	112.81	46.7
Modified GAFF	37.79	3.8	104.91	36.4

[a] From [1]

[b] From [54]

overestimated. The modified GAFF very accurately predicts the *tgg* population, but the original GAFF performs better than the modified version for the two most abundant conformers, *tgt* and *tgg'*. Although, as we have seen, the modified force field generally shows improved agreement with experiment, the original GAFF is better for this particular property.

In summary, the modified GAFF force field for G1 and G4 that uses the scaling parameters optimized for the density and dielectric constant of G2 predicts a range of properties of liquid G1 and G4 more accurately than the original GAFF model.

OPLS-AA-based force fields

As mentioned above, the OPLS-AA force field is also a popular force field for organic molecules [21], and two modified versions of this force field have recently been proposed for glyme molecules [6, 9]. The performance of each of these force fields was also evaluated in the current work.

Figure 16 presents a comparison of the experimental [47, 48] and computed values of the liquid density of G2 as a function of temperature, where the computed values were obtained using OPLS-AA [21], the modified OPLS-AA developed by Tsuzuki et al. [9] (Tsuzuki2015), and the modified OPLS-AA developed by Saito et al. [6] (Saito2016) using the DMEFF torsion parameters proposed by Anderson and Wilson [22]. Interestingly, the original version of the OPLS-AA force field appears to give more accurate results than the two modified versions of this force field. At room temperature, the results from the OPLS-AA force field present excellent agreement with the experimental density measurements (relative error <1%). At high temperatures, the agreement becomes slightly worse (at 423.15 K, the relative error is around 2%). The results from the two modified OPLS-AA force fields show deviations from the experimental values of between 1 and 4% across the entire temperature range, as shown in Fig. S1 of the ESM. It is worth noting that, in spite of the rather small errors generated by the use of the OPLS-AA force field to predict the density, the computed thermal expansivity values deviate significantly from the corresponding experimental values (Fig. 16b)

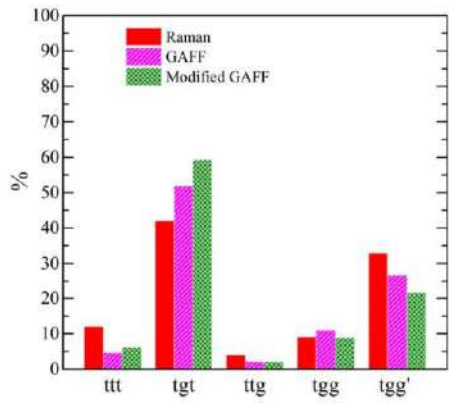

Fig. 15 Distribution of the five most populated conformers of G1 in the pure liquid phase at 298 K

The temperature dependence of the dielectric constant computed for liquid G2 using each OPLS-AA-based force field is presented in Fig. 16c. The OPLS-AA force field yields an error of around 15%, whereas the modified OPLS-AA force fields overestimate the true values considerably across the whole temperature range.

Figure 16d shows that all of the OPLS-AA-based force fields underestimate the self-diffusivity, just as seen for the GAFF-based force fields. Nevertheless, the modified OPLS-AA force fields are—surprisingly—less accurate than the original OPLS-AA model (Fig. 16d and Table S2 in the ESM).

In summary, among the OPLS-AA-based force fields tested in this work, the original version was surprisingly found to perform better than the two modified versions for G2. The same trend was noticed for G1 and G4, as shown in the ESM.

Conclusions

Mixtures of glymes with alkali metal salts have been widely investigated as electrolyte solvents for batteries due to their high donor numbers, relatively strong Lewis basicities, and the high electrochemical stabilities of these solvents. In this context, molecular simulation studies can be useful for understanding and improving the energy storage capacities of these devices if the force fields used to describe the molecules in the system yield accurate results. Different force fields and

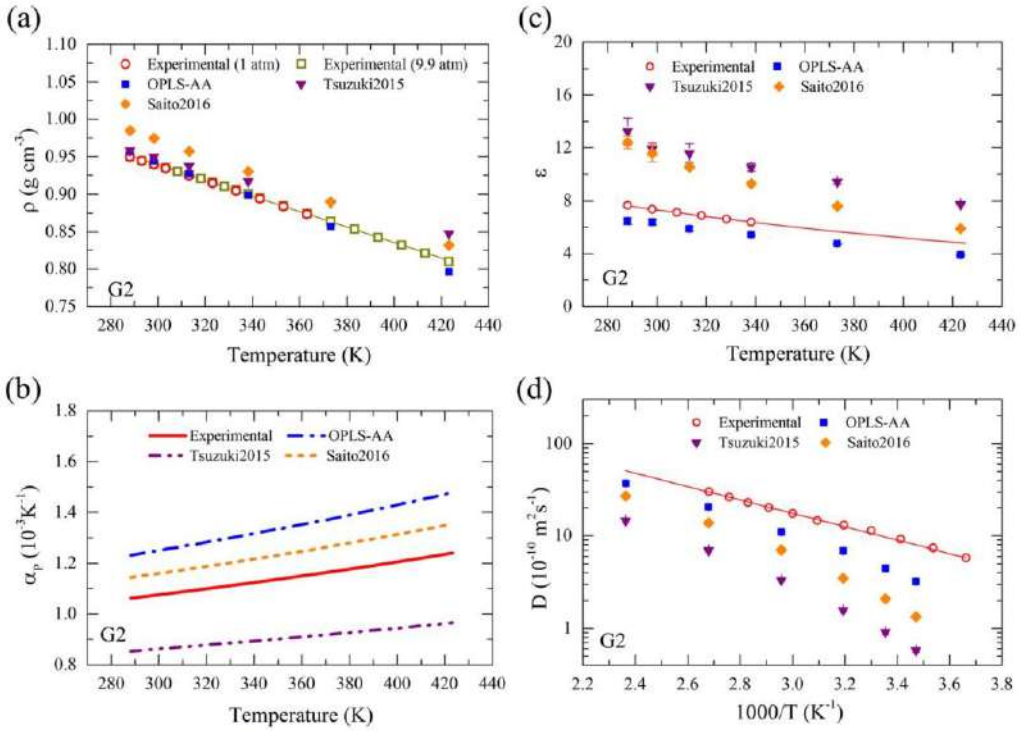

Fig. 16a–d Plots of the experimental [47, 48] and computed density (**a**), thermal expansivity (**b**), experimental [49] and computed dielectric constant (**c**), and experimental and computed self-diffusion coefficient [50] (**d**) of G2 as functions of temperature. Experimental data are shown as *open symbols* and data computed using OPLS-AA-based force fields as *filled symbols*

modifications of them have been proposed over the years. Among nonpolarizable all-atom force fields, the Optimized Potentials for Liquid Simulations—All Atom (OPLS-AA) force field and the generalized AMBER force field (GAFF) are widely used. Both of these were developed for the general study of organic systems and are usually not compatible. When applied to glyme systems, the accuracies of these force fields are sometimes limited and need to be improved. Modified versions of the OPLS-AA force field have been reported and applied in simulations including glymes. On the other hand, it was found that the GAFF force fields tend to significantly overestimate the densities of liquid glyme systems, but no revised force fields have been suggested so far. Considering the popularity of the GAFF force field for studying related systems, it is desirable to have a compatible force field that exhibits greater accuracy. Therefore, in the current work, a revised GAFF force field was developed for glymes.

Based on the GAFF force field, the Lennard-Jones parameters σ^{LJ} and ϵ^{LJ} were uniformly scaled with all the other parameters untouched so that the revised force field was compatible with the original GAFF. The scaling factors were optimized to reproduce the experimental density and dielectric constant of G2 (diglyme) over a wide temperature range. The final scaling parameters were found to be $f^{\sigma} = 1.03$ and $f^{\epsilon} = 0.9$. Besides the density and dielectric constant, the revised force field was used to calculate the dynamic and thermodynamic properties of G2; better agreement with experimental data was obtained using the modified GAFF than when applying the original GAFF parameters.

The revised force field was developed by simply scaling the Lennard-Jones parameters σ^{LJ} and ϵ^{LJ} by a factor. It is possible that additional improvements to the force field could be made by scaling the partial charges, but these parameters were kept fixed at the values obtained from the RESP calculations. Therefore, the optimized scaling parameters can be easily transferred to other glymes. The transferability of the scaling parameters was tested on G1 and G4. For both liquids, improved performance over the original GAFF was observed, suggesting that the same optimized scaling factors can be applied to other glymes as well.

The accuracies of the OPLS-AA and two modified versions of this force field were also evaluated in the current work. It was found that for almost all of the properties studied here, the original OPLS-AA performs better than the modified versions. For most of the properties studied in the current work, the performance of the original OPLS-AA force field is comparable to that of the revised GAFF force field, and both can

be used with equivalent accuracy and compatible force fields in related studies.

The new GAFF-compatible force field for poly(ethylene glycol) ethers provides an alternative to the OPLS and CHARMM force fields for simulating glymes and their mixtures with other compounds. The proposed model is superior to the existing GAFF force field for a wide variety of properties and can be used with other GAFF-compatible models for computing properties.

Acknowledgments N.S.V. Barbosa, E.R.A. Lima, and F.W. Tavares are grateful to several Brazilian agencies—the National Counsel of Technological and Scientific Development (CNPq) and the Carlos Chagas Filho Foundation for Research Support in the State of Rio de Janeiro (FAPERJ)—for financial support. Computational resources were provided by the Center for Research Computing (CRC) at the University of Notre Dame. Y. Zhang and E. Maginn are supported by the U.S. Department of Energy, Basic Energy Science, Joint Center for Energy Storage Research under contract no. DE-AC02-06CH11357.

References

1. Haynes WM (ed) (2015) CRC handbook of chemistry and physics, 96th edn. CRC Press, Boca Raton
2. Tang S, Zhao H (2014) Glymes as versatile solvents for chemical reactions and processes: from the laboratory to industry. RSC Adv 4:11251–11287. doi:10.1039/c3ra47191h
3. Yoshida K, Tsuchiya M, Tachikawa N, Dokko K, Watanabe M (2011) Change from glyme solutions to quasi-ionic liquids for binary mixtures consisting of lithium bis(trifluoromethanesulfonyl)amide and glymes. J Phys Chem C 115:18384–18394. doi:10.1021/jp206881t
4. Frech R, Huang W (1995) Conformational changes in diethylene glycol dimethyl ether and poly(ethylene oxide) induced by lithium ion complexation. Macromolecules 28:1246–1251. doi:10.1021/ma00108a063
5. Flick EW (ed)(1998) Glycol ethers. In: Industrial solvents handbook, 5th edn. William Andrew/Noyes, Westwood, pp 496–624
6. Saito S, Watanabe H, Ueno K, Mandai T, Seki S, Tsuzuki S, Kameda Y, Dokko K, Watanabe M, Umebayashi Y (2016) Li^+ local structure in hydrofluoroether diluted Li-glyme solvate ionic liquid. J Phys Chem B 120:3378–3387. doi:10.1021/acs.jpcb.5b12354
7. Ueno K, Murai J, Moon H, Dokko K, Watanabe M (2017) A design approach to lithium-ion battery electrolyte based on diluted solvate ionic liquids. J Electrochem Soc 164:A6088–A6094. doi:10.1149/2.0121701jes
8. Shimizu K, Freitas AA, Atkin R, Warr GG, FitzGerald PA, Doi H, Saito S, Ueno K, Umebayashi Y, Watanabe M, Canongia Lopes JL (2015) Structural and aggregate analyses of (Li salt + glyme) mixtures: the complex nature of solvate ionic liquids. Phys Chem Chem Phys 17:22321–22335. doi:10.1039/C5CP03414K
9. Tsuzuki S, Shinoda W, Matsugami M, Umebayashi Y, Ueno K, Mandai T, Seki S, Dokko K, Watanabe M (2015) Structures of $[Li(glyme)]^+$ complexes and their interactions with anions in equimolar mixtures of glymes and Li[TFSA]: analysis by molecular dynamics simulations. Phys Chem Chem Phys 17:126–129. doi:10.1039/C4CP04718D
10. Mahurin SM, Mamontov E, Thompson MW, Zhang P, Turner CH, Cummings PT, Dai S (2016) Relationship between pore size and reversible and irreversible immobilization of ionic liquid electrolytes in porous carbon under applied electric potential. Appl Phys Lett 109:143111. doi:10.1063/1.4964130
11. Feng G, Li S, Zhao W, Cummings PT (2015) Microstructure of room temperature ionic liquids at stepped graphite electrodes. AICHE J 61:3022–3028. doi:10.1002/aic.14927
12. Smith GD, Jaffe RL, Yoon DY (1993) A force field for simulations of 1,2-dimethoxyethane and poly(oxyethylene) based upon ab initio electronic structure calculations on model molecules. J Phys Chem 97:12752–12759. doi:10.1021/j100151a021
13. Jaffe RL, Smith GD, Yoon DY (1993) Conformations of 1,2-dimethoxyethane from ab initio electronic structure calculations. J Phys Chem 97:12745–12751. doi:10.1021/j100151a020
14. Sorensen RA, Liau WB, Kesner L, Boyd RH (1988) Prediction of polymer crystal structures and properties: polyethylene and poly(oxymethylene). Macromolecules 21:200–208. doi:10.1021/ma00179a039
15. MacKerell AD, Bashford D, Bellott M, et al (1998) All-atom empirical potential for molecular modeling and dynamics studies of proteins. J Phys Chem B 102:3586–3616. doi:10.1021/jp973084f
16. Bedrov D, Borodin O, Smith GD (1998) Molecular dynamics simulations of 1,2-dimethoxyethane/water solutions. 1. Conformational and structural properties. J Phys Chem B 102:5683–5690. doi:10.1021/jp981009e
17. Bedrov D, Borodin O, Smith GD (1998) Molecular dynamics simulation of 1,2-dimethoxyethane/water solutions. 2. Dynamical properties. J Phys Chem B 102:9565–9570. doi:10.1021/jp982161j
18. Bedrov D, Pekny M, Smith GD (1998) Quantum-chemistry-based force field for 1,2-dimethoxyethane and poly(ethylene oxide) in aqueous solution. J Phys Chem B 102:996–1001. doi:10.1021/jp972545u
19. Bedrov D, Smith GD (1999) Molecular dynamics simulations of 1,2-dimethoxyethane in aqueous solution: influence of the water potential. J Phys Chem B 103:3791–3796. doi:10.1021/jp984613y
20. Smith GD, Borodin O, Bedrov D (2002) A revised quantum chemistry-based potential for poly(ethylene oxide) and its oligomers in aqueous solution. J Comput Chem 23:1480–1488. doi:10.1002/jcc.10166
21. Jorgensen WL, Maxwell DS, Tirado-Rives J (1996) Development and testing of the OLPS all-atom force field on conformational energetics and properties of organic liquids. J Am Chem Soc 118:11225–11236. doi:10.1021/ja9621760
22. Anderson PM, Wilson MR (2005) Developing a force field for simulation of poly(ethylene oxide) based upon ab initio calculations of 1,2-dimethoxyethane. Mol Phys 103:89–97. doi:10.1080/00268970412331293811
23. Smith GD, Jaffe RL, Yoon DY (1995) Conformations of 1,2-dimethoxyethane in the gas and liquid phases from molecular dynamics simulations. J Am Chem Soc 117:530–531. doi:10.1021/ja00106a061
24. Goutev N, Ohno K, Matsuura H (2000) Raman spectroscopic study on the conformation of 1,2-dimethoxyethane in the liquid phase and in aqueous solutions. J Phys Chem A 104:9226–9232. doi:10.1021/jp001340+
25. Cornell WD, Cieplak P, Bayly CI, Gould IR, Merz Jr KM, Ferguson DM, Spellmeyer DC, Fox T, Caldwell JW, Kollman PA (1995) A second generation force field for the simulation of proteins, nucleic acids, and organic molecules. J Am Chem Soc 117:5179–5197. doi:10.1021/ja00124a002
26. Wang J, Wolf RM, Caldwell JW, Kollman PA, Case DA (2004) Development and testing of a general amber force field. J Comput Chem 25:1157–1174. doi:10.1002/jcc.20035
27. Dong H, Hyun J-K, Durham C, Wheeler RA (2001) Molecular dynamics simulations and structural comparisons of amorphous poly(ethylene oxide) and poly(ethylenimine) models. Polymer 42:7809–7817. doi:10.1016/S0032-3861(01)00234-8

28. Bayly CI, Cieplak P, Cornell WD, Kollman PA (1993) A well-behaved electrostatic potential based method using charge restraints for deriving atomic charges: the RESP model. J Phys Chem 97: 10269–10280. doi:10.1021/j100142a004
29. Sprenger KG, Jaeger VW, Pfaendtner J (2015) The general AMBER force field (GAFF) can accurately predict thermodynamic and transport properties of many ionic liquids. J Phys Chem B 119: 5882–5895. doi:10.1021/acs.jpcb.5b00689
30. Zhang Y, Maginn EJ (2012) A simple AIMD approach to derive atomic charges for condensed phase simulation of ionic liquids. J Phys Chem B 116:10036–10048. doi:10.1021/jp3037999
31. Cordeiro RM, Zschunke F, Müller-Plathe F (2010) Mesoscale molecular dynamics simulations of the force between surfaces with grafted poly(ethylene oxide) chains derived from atomistic simulations. Macromolecules 43:1583–1591. doi:10.1021/ma902060k
32. Stubbs JM, Potoff JJ, Siepmann JI (2004) Transferable potentials for phase equilibria. 6. United-atom description for ethers, glycols, ketones, and aldehydes. J Phys Chem B 108:17596–17605. doi:10.1021/jp049459w
33. Fischer J, Paschek D, Geiger A, Sadowski G (2008) Modeling of aqueous poly(oxyethylene) solutions. 2. Mesoscale simulations. J Phys Chem B 112:13561–13571. doi:10.1021/jp805770q
34. Fischer J, Paschek D, Geiger A, Sadowski G (2008) Modeling of aqueous poly (oxyethylene) solutions: 1. Atomistic simulations. J Phys Chem B 112:2388–2398. doi:10.1021/jp0765345
35. Martínez L, Andrade R, Birgin EG, Martínez JM (2009) PACKMOL: a package for building initial configurations for molecular dynamics simulations. J Comput Chem 30:2157–2164. doi:10.1002/jcc.21224
36. Martinez JM, Martínez L (2003) Packing optimization for automated generation of complex system's initial configurations for molecular dynamics and docking. J Comput Chem 24:819–825. doi:10.1002/jcc.10216
37. Hoover WG (1985) Canonical dynamics: equilibrium phase-space distributions. Phys Rev A 31:1695–1697. doi:10.1103/PhysRevA.31.1695
38. Shinoda W, Shiga M, Mikami M (2004) Rapid estimation of elastic constants by molecular dynamics simulation under constant stress. Phys Rev B 69:134103. doi:10.1103/PhysRevB.69.134103
39. Hockney RW, Eastwood JW (1988) Computer simulation using particles. Taylor & Francis, New York
40. Plimpton S (1995) Fast parallel algorithms for short-range molecular dynamics. J Comput Phys 117:1–19. doi:10.1006/jcph.1995.1039
41. Frisch MJ, Trucks GW, Schlegel HB, et al (2009) Gaussian 09, revision a.1. Gaussian, Inc., Wallingford
42. Neumann M (1983) Dipole moment fluctuation formulas in computer simulations of polar systems. Mol Phys 50:841–858. doi:10.1080/00268978300102721
43. Holian BL, Evans DJ (1983) Shear viscosities away from the melting line: a comparison of equilibrium and nonequilibrium molecular dynamics. J Chem Phys 78:5147–5150. doi:10.1063/1.445384
44. Zhang Y, Otani A, Maginn EJ (2015) Reliable viscosity calculation from equilibrium molecular dynamics simulations: a time decomposition method. J Chem Theory Comput 11:3537–3546. doi:10.1021/acs.jctc.5b00351
45. Zhang Y, Xue L, Khabaz F, Doerfler R, Quitevis EL, Khare R, Maginn EJ (2015) Molecular topology and local dynamics govern the viscosity of imidazolium-based ionic liquids. J Phys Chem B 119:14934–14944. doi:10.1021/acs.jpcb.5b08245
46. Otani A, Zhang Y, Matsuki T, Kamio E, Matsuyama H, Maginn EJ (2016) Molecular design of high CO_2 reactivity and low viscosity ionic liquids for CO_2 separative facilitated transport membranes. Ind Eng Chem Res 55:2821–2830. doi:10.1021/acs.iecr.6b00188
47. Kodama D, Kanakubo M, Kokubo M, Hashimoto S, Nanjo H, Kato M (2011) Density, viscosity, and solubility of carbon dioxide in glymes. Fluid Phase Equilib 302:103–108. doi:10.1016/j.fluid.2010.08.014
48. Conesa A, Shen S, Coronas A (1998) Liquid densities, kinematic viscosities, and heat capacities of some ethylene glycol dimethyl ethers at temperatures from 283.15 to 423.15 K. Int J Thermophys 19:1343–1358. doi:10.1023/A:1021927417610
49. Lago A, Rivas MA, Legido J, Iglesias TP (2009) Study of static permittivity and density of the systems {(*n*-nonane + monoglyme or diglyme)} at various temperatures. J Chem Thermodyn 41:257–264. doi:10.1016/j.jct.2008.09.006
50. Hayamizu K, Price WS (2004) A new type of sample tube for reducing convection effects in PGSE-NMR measurements of self-diffusion coefficients of liquid samples. J Magn Reson 167:328–333. doi:10.1016/j.jmr.2004.01.006
51. Pereira SM, Iglesias TP, Legido JL, Rivas MA, Real JN (2001) Relative permittivity increments for $\{xCH_3OH + (1-x)CH_3OCH_2(CH_2OCH_2)_3CH_2OCH_3\}$ from $T = 283.15$ K to $T = 323.15$ K. J Chem Thermodyn 33:433–440. doi:10.1006/jcht.2000.0746
52. Hayamizu K, Akiba E, Bando T, Aihara Y (2002) ^{1}H, ^{7}Li, and ^{19}F nuclear magnetic resonance and ionic conductivity studies for liquid electrolytes composed of glymes and polyetheneglycol dimethyl ethers of $CH_3O(CH_2CH_2O)_nCH_3$ ($n = 3-50$) doped with $LiN(SO_2CF_3)_2$. J Chem Phys 117:5929–5939. doi:10.1063/1.1501279
53. Ku H-C, Tu C-H (2000) Densities and viscosities of seven glycol ethers from 288.15 K to 343.15 K. J Chem Eng Data 45:391–394. doi:10.1021/je990281u
54. Nichols G, Orf J, Reiter SM, Chickos J, Gokel GW (2000) The vaporization enthalpies of some crown and polyethers by correlation gas chromatography. Thermochim Acta 346:15–28. doi:10.1016/S0040-6031(99)00405-0